

CRACK-PARTICLE INTERACTIONS IN BRITTLE COMPOSITES

CRACK-PARTICLE INTERACTIONS IN BRITTLE COMPOSITES

by

DAVID JOHN GREEN, M.Sc., B.Sc.

A[^]Thesis

Submitted to the School of Graduate Studies

in Partial Fulfilment of the Requirements

for the Degree

Doctor of Philosophy

McMaster University

October 1976

DOCTOR OF PHILOSOPHY
(Metallurgy and Materials Science)

MCMASTER UNIVERSITY
Hamilton, Ontario

TITLE: Crack-Particle Interactions in Brittle Composites

AUTHOR: David John Green, B.Sc. (University of Liverpool)
M.Sc. (McMaster University)

SUPERVISOR: Dr. P.S. Nicholson

NUMBER OF PAGES: (viii), 422

ABSTRACT

A study was made of the fracture in a model composite containing nickel spheres in a glass matrix. The macroscopic fracture characteristics of the system were determined by fracture surface energy, strength and elastic modulus measurements. The microstructures of the composites were defined carefully using quantitative microscopy and the fracture processes were studied using fractographic techniques. In particular, the technique of ultrasonic fractography was used to study the crack-particle interactions in detail.

It was found that for a non-bonded S glass-nickel system, the crack shape changes were similar to those observed for a glass-pore system. Theoretical models were used to explain the crack shape variations and their effect on properties. These models were based on the interaction of the stress field of the crack and the particles by local crack blunting and image stresses. Good agreement was obtained between theoretical predictions and experimental measurements of crack shape at breakaway and the fracture surface energy variations.

ACKNOWLEDGEMENTS

The idea for this work was initially conceived by Drs. J.D. Embury and P.S. Nicholson and the author is indebted to them for this and their continued supervision. This thesis provided an exceptional opportunity to study the fracture of brittle materials in a basic fashion, while allowing the practical macroscopic behaviour to be better understood. In this way, the thesis provided a good example of the material science philosophy, which deals with the 'psychology' of materials.

The phenomenon of brittle failure has influenced man's existence from the beginning in both positive and negative ways. For this work, the interest was in the structural applications of brittle materials and in particular their safety with respect to design. Sudden catastrophic failures have provided many instances for the danger of poor design and lack of knowledge. It was interesting to note, that one of the earliest examples of these failures was the falling of a mill in Oldham, England, the town of my origin, in 1844. This accident was caused by the failure of cast-iron beams and led to the death of 20 workers.

The author would particularly like to acknowledge the discussion with Martin Schinker and Dr. Frank Kerkhof of Freiburg, Germany, who helped immensely with setting-up the ultrasonic fractographic technique. The correspondence with Dr. Field in Cambridge was also very useful in this respect. The ultrasonic transmitter was built by Charlie McKay and Jim Hutcheson, and the transducer was produced by the Senior Science

Workshop at McMaster. The novel idea for plating the copper wire was suggested by Jim Faithurst.

The author would also like to thank Dr. J.D. Duncan for his help on the supervisory committee, Dick Hoagland for his useful discussions on fracture over the occasional beer, Colin Sargent for helping with the computer programming and all the technicians and support staff at McMaster for their help and co-operation. The modulus measurements were made very carefully by J. Van den An del of Westinghouse, Hamilton and Bob Millsop and Eugene Parsons of Stelco Research, Hamilton were most helpful in the quantitative microscopy. Thanks are also in accord to Judy Bath, who did a splendid job of reading my writing to type the thesis. The work was sponsored by the Atomic Energy of Canada, Ltd..

Finally, I am indebted to the patience and love of my wife, Trish, who helped me through some hard times and to the kids for their smiles. This thesis marks my exit from McMaster and student life and as a new phase starts, I can appreciate the last, as it filled out my life in many ways.

THIS THESIS IS
DEDICATED TO TRISH

Spinning carousel slows
Searching
Down symmetric, scientific streets,
Or winding, twisting paths of thought,
For the cause.

Two parallel lines
Meeting only at
Infinity.
Between the cosmos
And the
Heart

Sept. 15, 1976

TABLE OF CONTENTS

	<u>Page</u>
INTRODUCTION	1
CHAPTER 1 LITERATURE REVIEW: THE PRODUCTION AND DEFINITION OF A MODEL BRITTLE COMPOSITE SYSTEM	3
1.1 Overview	3
1.2 The Vitreous State	3
1.2.1 The Melting of Glass	4
1.2.2 The Nature of the Glassy State	12
1.2.3 Glass Formation	15
1.2.4 The Structure of Glass	18
1.2.5 Optical Properties	21
1.2.6 Characteristic Reference Temperatures	29
1.3 Hot Pressing	31
1.3.1 Introduction	31
1.3.2 The Hot Pressing Process	31
1.3.3 Hot Pressing Mechanisms	34
1.4 Quantitative Microscopy	36
1.4.1 Symbols and Measurements	37
1.4.2 Basic Equations	37
1.4.3 Particle Size Distributions	40
1.4.4 Contiguity of Two-Phase Systems	46
1.4.5 Interparticle Spacing	47
CHAPTER 2 ENERGY ABSORBING PROCESSES IN THE FRACTURE OF HIGHLY BRITTLE MATERIALS	57
2.1 Overview	57
2.2 The Continuum Approach to Fracture	58
2.2.1 Stress Concentrations and the Griffith Approach	59
2.2.2 Linear Elastic Fracture Mechanics	64
2.2.3 Crack Paths	72
2.2.4 Fracture Mechanics of Particulate Composites	76
2.2.5 The Non-Linear Crack Tip Field	81
2.3 Microstructural Aspects of Crack Propagation	84
2.3.1 Surface Roughness	86

	<u>Page</u>
2.3.2 Microcrack Zones	91
2.3.3 Fracture Surface Steps	94
2.3.4 Crack Blunting	98
2.3.5 Brittle Particulate Composites	102
 CHAPTER 3	
THEORETICAL ASPECTS OF THE EXPERIMENTAL PROCEDURE	
3.1 Determination of Young's Modulus	126
3.1.1 Measurement Techniques	126
3.1.2 Elastic Moduli of Particulate Composites	128
3.2 Fracture Surface Energy Determination: Double Cantilever Beam (DCB) Test	133
3.3 Fracture Stress Determination: Four-Point Bend Test	145
3.3.1 Strength Testing of Brittle Materials	145
3.3.2 Strength of Particulate Composites	154
3.4 Determination of Critical Flaw Size	159
3.5 Fractology	165
3.5.1 Ultrasonic Fractography	168
 CHAPTER 4	
EXPERIMENTAL PROCEDURE	183
4.1 Materials	183
4.1.1 S Glass	183
4.1.2 Nickel	185
4.1.3 Other Materials	186
4.2 Fabrication and Machining	186
4.2.1 Hot Pressing	186
4.2.2 Machining	190
4.3 Determination of Young's Modulus	193
4.4 Determination of Room Temperature Fracture Energy	196
4.5 Strength Measurements	201
4.6 Ultrasonic Modulation of Fracture Surfaces	201
4.7 Fractography	211

	<u>Page</u>	
CHAPTER 5	RESULTS AND DISCUSSION	215
5.1	Starting Materials	215
5.1.1	Nickel Powder	215
5.1.2	S Glass Powder	220
5.2	Microstructural Characterization of the Fabricated Composites	223
5.2.1	Detection of Internal Stress	223
5.2.2	Quantitative Microscopy	226
5.3	Fracture Surface Energy Standard- ization Tests	244
5.3.1	Stress Analysis Approach	244
5.3.2	Compliance Analysis	250
5.3.3	Comparison Between Two Approaches and Literature Values of K_{IC} for Pyrex	251
5.4	Determination of Young's Modulus	255
5.4.1	Four-Point Flexure Data	255
5.4.2	Ultrasonic Measurements	256
5.5	Fracture Toughness of S Glass-Nickel Composites	260
5.5.1	Areal Contribution	260
5.5.2	Plastic Deformation	262
5.5.3	Surface Roughness	263
5.5.4	Fracture Surface Steps	266
5.5.5	Decohesion Zone	269
5.5.6	Crack Shape	270
5.5.7	Crack Blunting	273
5.6	Strength of the S Glass-Nickel Composites	275
5.7	Fractographic Observations	292
5.7.1	Basic Fractography	292
5.7.2	General Fractography	297
5.7.3	Ultrasonic Fractography	302
5.8	Theoretical Aspects	319
5.8.1	Crack Approach to an Elastic Disturbance	321
5.8.2	The By-Pass Process	326
5.8.3	Fracture Surface Steps	343
CHAPTER 6	CONCLUSIONS	344
	SUMMARY FOR FUTURE WORK	349
	REFERENCES	351
	APPENDIX	366

INTRODUCTION

Fracture is the ultimate catastrophe that occurs in the deformation of materials. In the last few decades a greater understanding of the fracture properties of materials has been developed. In particular, a scientific approach known as fracture mechanics has recognized the energetics involved in this process.

Historically, fracture mechanics was founded on a theoretical and experimental study of brittle materials because these materials are amenable to mathematical formulation. In these materials the response to stress is essentially linear, especially in the macroscopic sense. A fracture criterion can then be developed which recognizes that a critical point should occur when the stored elastic energy release rate is at least equivalent to the force necessary to produce the required fracture surface. Extrapolations to sub-critical and super-critical fracture behaviour have proved to be rather more illusive. Fracture mechanics is essentially a continuum approach to the fracture problem but the material scientist must also be concerned with the atomistic and microstructural aspects of the process. The solution to problems such as the exact details of the energy absorbing mechanisms and crack trajectories have proved more intractable.

Fracture mechanics, even with its limitations, has enjoyed a reasonable success with its extrapolation to non-brittle materials. Indeed the emphasis of the development has been on metals due to their structural importance. In recent years, however, it has been recognized that brittle ceramics possess attractive properties especially in high

temperature applications. In the search for energy-saving and energy production devices, ceramics will play an essential role. Furthermore, it has been recognized that the fracture process in brittle materials is not simple; fracture is often the result of the competition of several different processes and not simply the production of new planar surfaces. Improved resistance to fracture in ceramics was initially sought in pure single phase materials where enhanced ductility was thought possible. More recently, the search has turned to composite materials wherein the presence of dispersed phases disturb the fracture process.

It is the aim of this thesis to study a model brittle composite system and in particular to determine the basic physical processes that occur when a crack interacts with a particle of different phase. It is hoped that such a study will help in the understanding of the fracture processes that occur in more complex systems and aid in improved design of simple composite microstructures.

CHAPTER I

LITERATURE REVIEW: THE PRODUCTION AND DEFINITION OF A MODEL BRITTLE COMPOSITE SYSTEM

1.1 Overview

A model brittle particulate composite can be produced by hot pressing (pressure sintering) glass powder with the second phase particles. This process allows well-dispersed samples of high density to be formed at temperatures less than those required by conventional fabrication techniques (provided the powder characteristics and structures are understood). The lower temperatures allow control of chemical reactions that may occur between the matrix and the dispersed phase. The microstructures of such composites are simple and can be defined in quantitative terms.

Since glass is generally considered an ideal brittle solid, glass-matrix composites should allow the fracture processes occurring to be studied in a basic fashion.

This first chapter reviews the relevant structure and properties of glass, the hot-pressing technique for fabrication and the quantitative microscopy needed to define composite microstructures.

1.2 The Vitreous State

Glass is a versatile material. The fabrication of which has been exploited since the time of the Roman Empire. The diversity of the properties of glass can be attributed to several factors. Firstly,

the composition of glasses can vary over wide limits and can include sixty of the chemical elements. Within the compositional limits, the properties of glass often vary continuously in a predictable manner. Secondly, the free energy of a glass is almost always greater than that of its crystalline counterpart thereby increasing the possibility of further solid state reactions such as precipitation or decomposition. Finally, glass is isotropic and can be made extremely pure and homogeneous.

The exploitation of glass properties has been achieved by viewing it as a substance continuous with the liquid state yet rigid. At intermediate temperatures glass often behaves like a viscous liquid, allowing simple forming operations. In this state, chemical reactions are sensitive to time and temperature and therefore easily controlled. This ease of formation and structural control has led to glasses being used as precursors for derivative materials such as glass-ceramics.

The definition that 'glass is a non-crystalline solid'[1] seems to include most known features of this material, but is somewhat nebulous. Presumably, the transition from non-crystalline to crystalline is just a matter of degree. It would seem that the diverse nature of glass is reflected not only in the difficulty to find uniform theories to describe its structure and properties but even in its definition.

1.2.1 The Melting of Glass

The main process in the industrial manufacture of glass is the melting of inorganic oxides or salts. The section discusses the production of silicate glasses with special reference to soda aluminosilicate glasses, the system utilized in this thesis.

During the melting process, the batch is raised to 1350°C - 1600°C (depending on the composition) and many complex physical and chemical changes occur. The principal chemical reactions of decomposition and dissolution take place during the melting stage. Glasses must also pass through a "refining" stage, which allows chemical homogenization and dissolved gas and gas bubbles to escape. On the lab scale the refining process is often aided by stirring.

(i) Melting Reactions

Silica is the major constituent of most commercial glasses with oxides added as fluxes. These additions allow control of viscosity, chemical resistance, optical and special properties. For example, the soda-aluminosilicate glass used in this work was chosen with special reference to its chemical stability and thermal expansion coefficient.

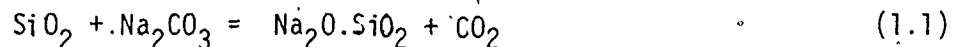
The choice of raw material to supply a given component depends on factors such as:

- a) availability
- b) cost
- c) impurity contents
- d) particle size
- e) desirability of specific reaction paths and
- f) volatilization characteristics and associated safety or pollution considerations.

Silica is added as natural sand or sandstone unless high purity is important. It is also added in the form of minerals containing the other oxides. For example, in cases where both alumina and alkali oxides are required, spodumene, petalite or other feldspar-related

minerals have been used. In compositions where the impurity levels of natural minerals are not tolerable, alumina is added in the calcined or hydrated forms. The alkali oxides are commonly added as the carbonates (soda ash and potash). For specific control of the melting process sodium nitrate and sulphate are sometimes added.

A comprehensive study of the melting reactions can only be made in terms of a specific composition (e.g. soda-alumina-silica). Although solid-state reactions often occur before any liquid phase develops these reactions are thought not to be of major importance. The first significant step is generally the appearance of the lowest melting liquid phase. Referring to Figure 1, the primary liquid phase in the $\text{Na}_2\text{O} - \text{SiO}_2$ system corresponds to the eutectic between sodium disilicate and silica $\sim 800^\circ\text{C}$. This eutectic liquid can react with more soda to precipitate the metasilicate at temperatures less than 840°C . The sodium carbonate (soda ash) decomposes at 850°C , giving a rapid and violent reaction [3]:



This reaction allows substantial refinement to occur and exerts an important mixing effect [4]. The final stage of melting involves the dissolution of the remaining silica residues. This dissolution occurs in the viscous silica-rich melt and proceeds slowly, making it the limiting step of the process. To speed this process salt cake is often added to the batch. The rate of disappearance of the silicate residues will depend on the diffusion kinetics of silica in the melt and factors such as particle or agglomeration size play an important role. As the final remnants dissolve, bubbles of carbon dioxide are

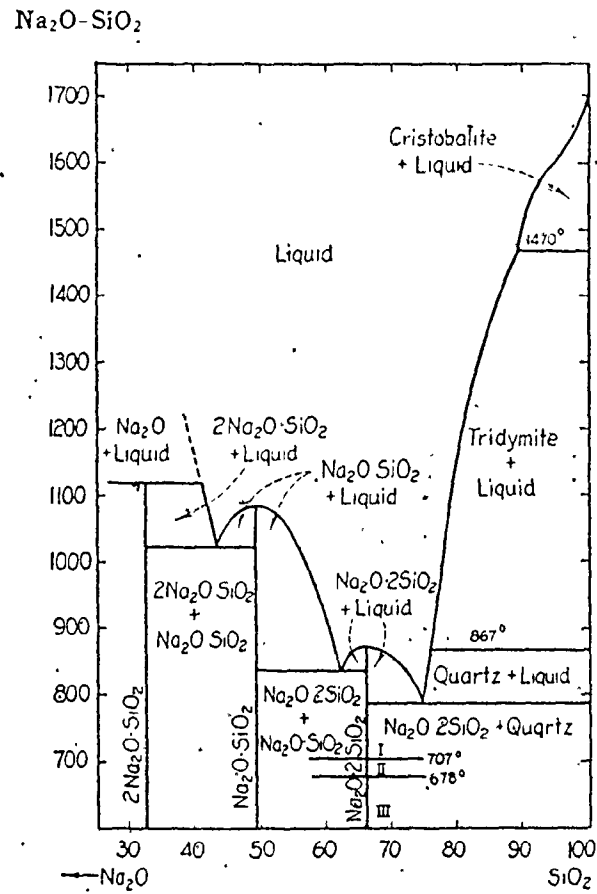


Figure 1. Phase Diagram for the System $\text{SiO}_2-2\text{Na}_2\text{O} \cdot \text{SiO}_2$ (Reference 2)

nucleated at the glass-residue interface, reflecting the decrease in solubility of carbon dioxide with increase in silica content.

The introduction of alumina complicates the process of glass formation. The characteristics of the melt will be different especially the viscosity. The phase diagram for the system $\text{SiO}_2 - \text{Al}_2\text{O}_3 - \text{Na}_2\text{O}$ is shown as Figure 2. The dominant feature of this ternary diagram involves the presence of two ternary compounds, one binary compound and one pure oxide on the $\text{Na}_2\text{O}/\text{Al}_2\text{O}_3 = 1.0$ line. The topographical results of this alignment is to produce two ternary eutectics and one peritectic on that line as well as at least four ternary eutectics between that line and the $\text{Na}_2\text{O}/\text{Al}_2\text{O}_3$ binary. The compounds present on the $\text{Na}_2\text{O}/\text{SiO}_2 = 1.0$ line all possess stable three-dimensional arrays of MO_4 tetrahedra. Large amounts of Na_2O or Al_2O_3 would tend to disrupt the silica network by the formation of NaO_6 and AlO_6 octahedra. This behaviour is reflected by high viscosities along the $\text{Al}_2\text{O}_3/\text{Na}_2\text{O} = 1.0$ line in liquid melts [5].

The rate of melting and reaction paths depend on the range and distribution of particle sizes in the batch. Finer particle sizes and more uniform mixing will permit rapid reaction initially but sintering may complicate the escape of the carbon dioxide. The liquid phase will be uniformly produced in this case and will tend to close any open channels, thus suppressing the decomposition reaction [6]. If the alkali carbonate has a smaller particle size than the silica, melting may be accelerated. The finer carbonate probably distributes itself more evenly over the surface of the silica grains, allowing the carbon dioxide to escape more easily. Other factors that will affect the

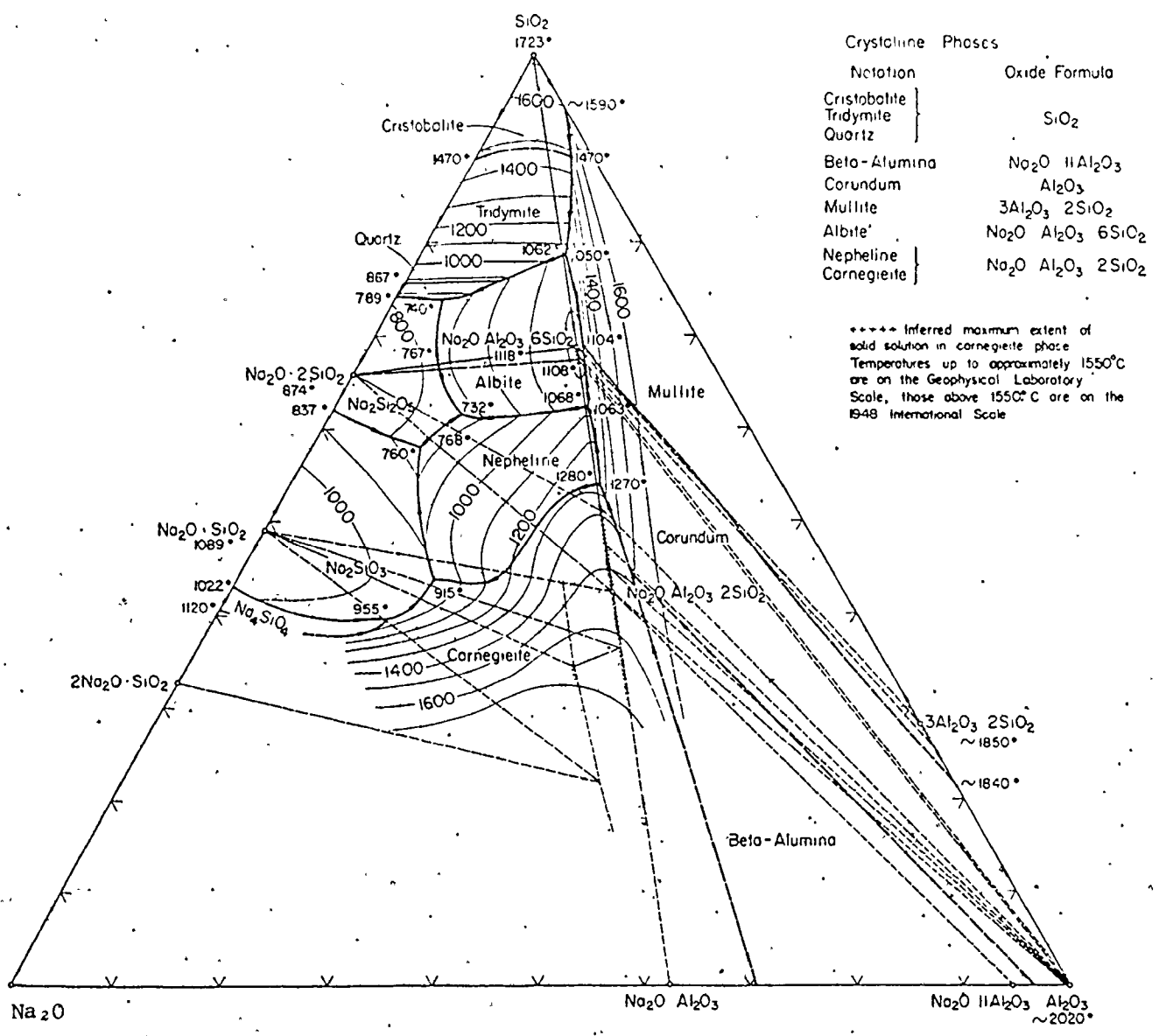


Figure 2. Phase Diagram for the System Na₂O-Al₂O₃-SiO₂ (Reference 2)

melting rate are segregation of the batch materials and melt viscosities. Numerous techniques have been employed to accelerate the melting process such as [7]:

- (a) additions of water, sulphates etc.
- (b) replacement of soda ash by caustic soda
- (c) use of low-melting frit
- (d) use of silica gels
- (e) precompaction of batch materials
- (f) addition of cullet (scrap glass), and
- (g) mode of heating.

The melting process is complex and other considerations such as redox potentials, heat transfer and fluid flow should be included in a comprehensive review. Such an undertaking is beyond the scope of this thesis.

(ii) Refining

This stage of glass-making refers to the removal of bubbles from the molten glass. These bubbles may originate from the furnace atmosphere, the decomposition of the batch materials, at the glass/refractory interface or by nucleation and growth from supersaturated solution. During refinement, these bubbles must disappear by either escaping or dissolving in the glass. These processes are aided by reduced viscosities, the use of volatile materials, dissolution by specific chemical reactions and by control of surface tension.

The rise of gas bubbles in a melt can generally be described by the classical Stokes relation.

$$v = \frac{2gr^2}{9\eta} \quad (1.2)$$

where v = velocity of rise
 g = acceleration due to gravity
 r = bubble radius
 ρ = glass density
 η = glass viscosity

Obviously control of temperature (hence viscosity), diffusion rate and solubility will be important in this process. Clearly, the bubble size will also be a determining factor. Several techniques, such as bubbling of helium through the melt, could be used to accelerate the refining process.

The rate of disappearance of gas bubbles is not just dependant on flotation but dissolution also occurs. For small bubbles the surface tension may be sufficient to favour dissolution of the bubbles. Dissolution also depends on the specific gaseous species involved.

(a) Carbon dioxide: The solubility of CO_2 is sensitive to composition. For example, it increases substantially with increasing alkali content in soda-silica glass. This solubility probably occurs by formation of carbonate ions as in the equilibrium



Above 1200°C , however, dissolved CO_2 is minimized but the capacity for further dissolution is still possible during the cooling process. It is interesting to note that CO_2 has a relatively high diffusion coefficient at temperatures in the range $1100 - 1300^\circ\text{C}$ [8], which allows dissolution to occur quite rapidly.

(b) Water vapour: Water solubility increases with increasing alkali content and increasing temperature and occurs through the incorporation of hydroxyl ions within the glass structure.

(c) Oxygen: Solubility of oxygen is possible within melts especially under oxidizing conditions.

(d) Nitrogen: Nitrogen does have affinity for molten glass especially under reducing conditions and is generally considered the most difficult gas to eliminate.

An interesting problem in glassmaking is the potential for some glasses to "reboil", i.e. bubbles reappear during cooling or changes in melt conditions. Certainly the decrease of solubility of nitrogen and water vapour with decreasing temperature could initiate reboil. This tendency for reboil may be important when glass powders are vacuum hot-pressed. Lange [9] showed that evolution of gases such as water vapour occurs at temperatures up to 800°C.

The final stage of glass melting is homogenization. Inhomogeneity may arise from various sources, e.g. poor batch mixing reactions at the glass/refractory interface, surface reactions, etc. Reduction in inhomogeneity will depend on the diffusional characteristics of the melt and occasionally the process is aided by mechanical mixing or special furnace designs.

1.2.2 The Nature of the Glassy State

At melting temperatures, glasses are highly viscous liquids (~ 10 Pa.s). The viscosity increases progressively as the melt is cooled until it becomes rigid (10^{12} Pa.s). This continuous transition

from liquid to solid provides a distinction between glasses and crystalline solids. There is no evolution of latent heat during the liquid to solid transition indicating that no structural transformation occurs. Just below its nominal melting point, the supercooled liquid is metastable but as the temperature decreases further the viscosity increases until it is too high to permit structural rearrangements. The liquid converts to a solid whose free energy is greater than the corresponding crystalline phases. The departure from metastability is sensitive to the cooling rate and gives rise to two important factors, i.e.,

- (i) failure to evolve heat consistent with the melt temperature, and
- (ii) failure to equilibrate dimensionally.

These two factors are illustrated in Figure 3 showing a sharp change from linearity as the liquid is cooled. Furthermore, this departure is sensitive to the cooling rate employed, giving rise to a transformation "range". If a glass is reheated into this range it will tend to equilibrate at a rate dependent on its thermal history. This pseudo-equilibrium is indicated by the fact that the physical characteristics of the glass such as refractive index, viscosity, density, etc. tend towards a unique value at a given temperature. The temperature in the transformation region at which the structure of a given piece of glass would be stable is called the fictive temperature. For example, a rapidly-cooled sample has a high specific volume, reflecting its more open structure, corresponding to a high fictive temperature. This concept has its limitations. For example it has been shown [10] that the average thermal expansion coefficient varies

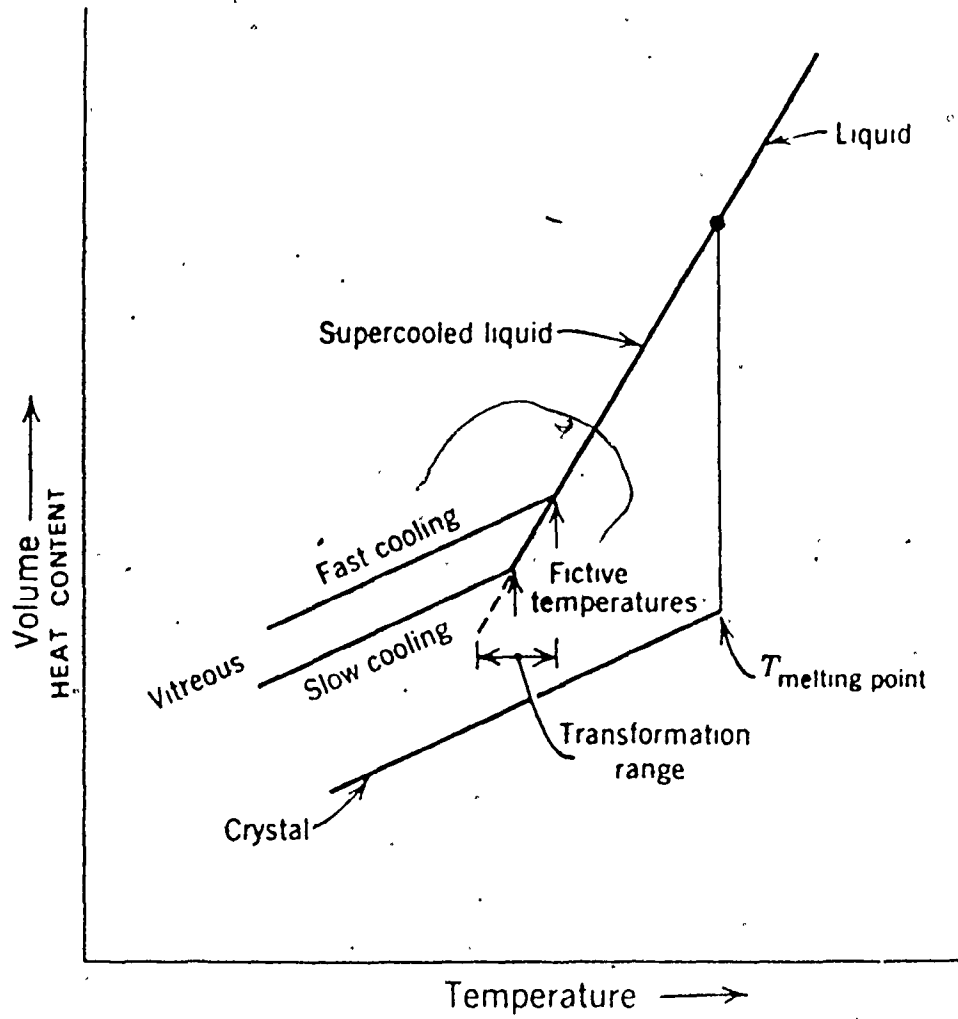


Figure 3. Relationship between Liquid, Crystalline, and Vitreous States.

markedly with index of refraction depending on whether or not the glass was soaked at a given temperature or cooled at constant rate. It may be that the subtle effects of thermal history cannot be formalized into such a concept since each equilibrium density may not necessarily be characteristic of a unique structure.

1.2.3 Glass Formation

The formation of a stable, homogeneous glass requires that the melt temperature be reduced in such a way as to avoid crystallization. Unfortunately, a complete understanding of glass formation is elusive. Glass formation is not a simple function of energy or structural differences. Table 1 indicates that such differences do not show a clear relationship to glass formation. This may be surprising as large structural differences might hinder crystallization and thereby enhance glass formation. For some systems such as sulphur and phosphorous pentoxide this may seem true but, in contrast, vitreous silica has a structure which closely resembles that of cristobalite. There is evidence that the melt structure does relate directly to glass formation. For example, if the liquid is a complex network structure, crystallization would involve the breaking of relatively strong bonds making glass formation easier.

The thermal energy available to activate crystallization is also important. For example, a low temperature eutectic mixture of CaO and Al_2O_3 will form a glass while neither component in itself is a glass former. Another approach to the study of glass-forming ability, is to consider the dynamics of the crystal nucleation and growth process.

The stability of glasses formed by cooling a melt depends on the quench-rate because crystallization and quenching are competitive processes.

The quench-rate has associated variables such as melt size, temperature and the method of quenching. An increased quenching-rate will enlarge the glass-forming region and new methods such as splat cooling have produced glasses from TeO_2 , V_2O_5 , MoO_3 and, more recently, metals.

Crystal nucleation and growth rates will depend in detail on the types of structural adjustments that must take place. The kinetics of these processes, however, will further depend on the mobility of species within the melt. For this reason, high viscosity is often cited as the major parameter in studying glass formation.

Glass formation can also be studied from a crystal chemical viewpoint. Initially, attempts were made to correlate glass formation with bond type as many glass forming oxides are highly covalent. This type of classification is unsatisfactory as each bond type class contains glass forming substances, e.g. the ionic compound BeF_2 readily forms a glass.

A better correlation results when the bond strength is compared to the glass forming ability. This concept implies that glass formation is aided when strong bonds are present making structural changes difficult. A summary of the work of Sun [11] as shown in Table 2 and allows the oxides to be classified according to whether they form glasses, promote glass formation (intermediates) or alter the glass properties (modifiers).

TABLE 1. Molar Heats of Fusion and Entropy for Several Substances.

Substance	Melting Point (°K)	Heat of Fusion (kJ/mole)	Entropy of Fusion. (J/°)
<u>Se</u>	491	5.0	10.5
Na	371	2.6	7.1
<u>SiO₂</u>	1980	5.4	2.9
<u>S</u>	394	1.2	3.1
LiCl	887	19.7	22.2
<u>B₂O₃</u>	733	22.2	30.1
<u>GeO₂</u>	1388	41.8	29.3
<u>K₂O.4SiO₂</u>	1073	49.0	45.6
Al ₂ O ₃	2318	108.	4.6

Glass formers are underlined.

TABLE 2. Relationship of Glass Formation to Dissociation Energy as suggested by Sun (Ref 11)

M in MO _x	Dissociation Energy per MO _x (MJ/mole)	Coordination Number	Single Bond Strength (kJ/m)
<u>Glass Formers</u>			
B	1.49	3	500
Si	1.77	4	440
Ge	1.80	4	450
Al	1.33-1.68	4	330-420
B	1.49	4	370
P	1.85	4	370-460
<u>Intermediates.</u>			
Ti	1.82	6	305
Zn	0.60	2	301
Pb	0.61	2	305
Al	1.33-1.68	6	220-280
Be	1.05	8	260
<u>Modifiers.</u>			
Mg	0.93	6	150
Ba	1.09	8	140
Ca	1.06	8	130
Li	0.60	4	150
Na	0.50	6	83
K	0.48	9	53
Rb	0.48	10	48
Cs	0.48	12	42

1.2.4 The Structure of Glass

Historically, the structure of glass has been approached from two directions. In the first case, the basic co-ordination unit is fixed but the location of atoms outside this unit becomes less and less defined with distance. The second approach is to consider the glass as composed of small crystallites arranged in different orientations.

The Zachariasen model for the structure of silica glass is based on the former approach and is generally called the "random-network" theory. This crystal chemical approach predicts not only the structure of glass but also their glass-forming tendencies (Section 1.2.3).

The basic structural unit is assumed to be the (SiO_4^{2-}) tetrahedron and the joining of other tetrahedra to it is done in such a way as to allow flexibility of relative orientation. To form a network structure, Zachariasen [12, 13] laid down specific geometrical rules. Warren and his co-workers [14, 15] calculated the theoretical x-ray diffraction curves from such structural models and found good agreement with experiment. For vitreous silica, it was shown that on average each silicon is surrounded by four oxygens and each oxygen bridges between two silicons. The angle of the Si-O-Si bridge was shown to follow a distribution with the most probable angle being 144 degrees. The structure of vitreous silica under these conditions leads to an open network. Figure 4 illustrates the difference between crystalline and vitreous silica.

The addition of other ions to this silica network can be considered by their role in either joining in the network (intermediates)

or by breaking up the network (modifiers). For example, the addition of soda disrupts the continuity of the network because it will not be possible for every oxygen ion to be joined to two silicon ions. The sodium ions give rise to non-bridging oxygens and occupy spaces in the network near these oxygens in order to preserve electrical neutrality. This disruption of the network structure is illustrated in Figure 5. The addition of soda therefore gives rise to marked changes in the physical properties of glass by breaking up the network. For example, the viscosity of soda-silica glasses is much less than vitreous silica for a given temperature. X-ray diffraction data shows that the sodium ions are not distributed randomly. On average each sodium is surrounded by five oxygens and the network must adhere to this type of co-ordination rather than simply placing the sodium ions in random holes. The earlier ideas of crystallites now begin to reappear and indeed the diffraction data can be interpreted in this way. For instance, the diffraction patterns of soda-silica glasses can be described by superposition of the pure vitreous silica and the vitreous $\text{Na}_2\text{O} \cdot \text{SiO}_2$ curves appropriately weighted. This evidence led Russian workers to hypothesize that glass is micro-heterogeneous with regions of different composition. Evidence for such heterogeneity has been found in electron microscopic studies of some glasses but interpretation is ambiguous. Such behaviour could be linked with phase separation as observed on a larger scale.

Another approach to the problem was taken by Eckstein [16] who considered increasing the number of defects in a crystal until the deformed regions around defects overlap, i.e. the structure of glasses is viewed in a continuous fashion from crystallinity to non-crystallinity.

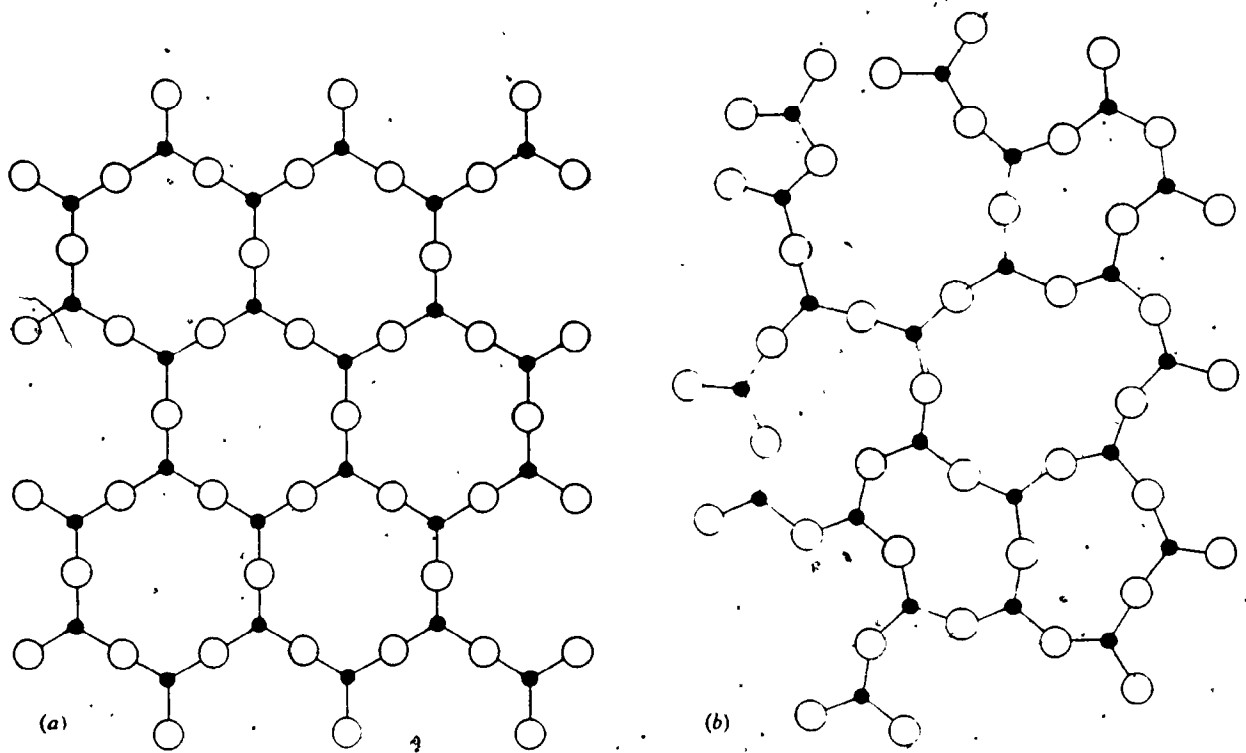


Figure 4. Two-dimensional Analogue of a) the Crystalline and b) the Glassy Form of a Substance R_2X_3 . (Open circles = X, Filled circles = R)

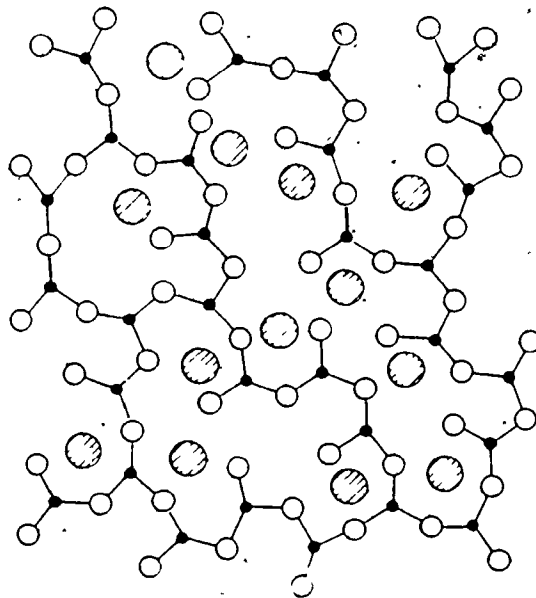


Figure 5. Two-dimensional Analogue of a Modified Glass; R_2X_3 modified by the Addition of some M_2X . (Shaded circles = M)

The random network theory is simplistic but still remains a useful qualitative guide to the physical properties of oxide glasses. Practical glasses contain a variety of oxides and the random network theory has been used to characterize their role in the structure. The classification into network formers, modifiers and intermediates has proved a useful concept. In the case of alumina, the aluminium ion can substitute for a silicon ion to form an AlO_4 tetrahedron, which can join the network, provided an additional cation is located nearby to preserve electrical neutrality. (Fig. 6). The inorganic oxides commonly used in glass making are listed in Table 3 along with their influence on the properties of the glasses.

1.2.5 Optical Properties

The purpose of this section is to discuss the development of colours in glass and stress-optical effects.

In the simplest terms, colours occur in glass because the spectrum of light which is incident upon a piece of glass is altered as it interacts with the glass. The incident beam may be reflected, absorbed or scattered. If a glass absorbs or scatters light in one part of the visible spectrum more strongly than another, then the glass transmits light more readily in the remaining regions. The optical properties of solids are not directly dependent on the form or existence of long range order but rather on the local arrangement of the constituent atoms or ions. The optical properties of glasses are, therefore, not sharply distinguished from those of crystals which contain the same ions in comparable local groupings. The variety of ions that can be

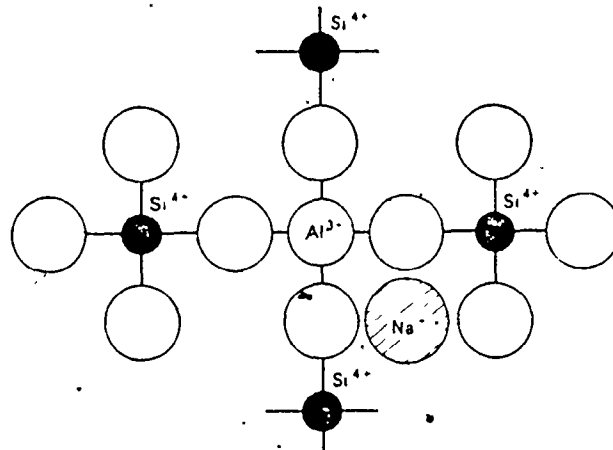


Figure 6. Schematic Representation of Al_2O_3 in a Silica Network.

TABLE 3. Common Constituents of Glasses and their Influences on Properties.

SiO_2	Basic glass former (network former). Crystalline silica has very high melting point and liquid silica very high viscosity. High concentration of silica in a glass confers high softening temperature, low thermal expansion, good chemical durability.
B_2O_3	Network former. Will join network structure of silica glasses reducing viscosity without producing adverse changes in thermal expansion and durability. Is a component of all heat-resisting and 'chemical' glasses.
PbO	Not a network former but can link SiO_4 tetrahedra. Widely used for high dielectric constant, refractive index, and resistivity. Expensive. Needs oxidizing furnace atmosphere.
Na_2O	Network modifier. Markedly lowers softening point. Raises thermal expansion and ionic conductivity. Reduces durability.
K_2O	Network modifier-similar to Na_2O but larger K^+ ion less mobile.
Li_2O	Network modifier-similar to Na_2O but smaller Li^+ ion more mobile. Promotes devitrification.
CaO	Network modifier. Inhibits mobility of alkali ions, hence increases resistivity and durability of alkali glasses. Shortens working range.
MgO	Network modifier- as CaO
ZnO	
BaO	Cheaper substitute for PbO ,
Al_2O_3	Intermediate. Can join network in AlO_4 tetrahedra which are a different size from SiO_4 . Strongly suppresses devitrification; increases viscosity making melting and fining more difficult.

incorporated into a silicate glass network yield a range of refractive indices and colours.

(i) Colours due to the scattering of Light

Commercial glass colours that depend on the scattering of light are generally those that contain minute crystallites of one phase suspended in a glassy matrix. These crystallites range from metals to compounds, including gold, copper, fluorides, phosphates and sulphides. The particle size must be comparable to the wavelength of the incident light, which suffers a combination of diffraction, diffuse reflection and scattering. Production of these coloured glasses involve careful control not only of the nucleation and growth process and redox conditions, but also of the final particle size. Glasses containing a dispersion of colloidal particles often exhibit rich colours. Common glasses coloured by light scattering are the opals and rubies.

(ii) Absorption Colours

For absorption to occur, electrons must undergo transitions between energy levels within the constituent atoms or ions. The periodic table of elements when drawn up according to the filling of the quantum mechanical energy states gives rise to different energy levels, which become energetically closer as the distance from the nucleus increases. In the transition metal series the 4s level is slightly more stable than the 3d level and the series is characterized by an incomplete 3d electron shell. The transition element series provides many of the colouring ions important in glass technology. Similar electronic structures are also found in the rare earths and

actinides. The importance of these incomplete inner shells is that electron transfer can take place within them under certain conditions. For ions in solution, the energy levels can be "split" by the interaction of the surrounding ions, allowing electron transfer to take place. This gives rise to weak absorption. Thermal fluctuations and the random nature of the glass structure broaden this behaviour into absorption bands by producing variations in the local electric fields. In the lanthanide and actinide series similar electron transfer can occur. The absorption peaks in these cases are sharper as the incomplete shells are more deeply buried than those of the transition element series and therefore less affected by the surrounding electric fields. The coordination of the surrounding ions will influence the position of the absorption bands since their influence depends on the symmetry and strength of their electric fields. For example, cobalt ions in a borosilicate glass give a pink colour due to (CoO_6) groups while in potash-silica glass cobalt ions give a purple colour associated with (CoO_4) and (CoO_6) coordination groups. The situation is further complicated by the variable valency states of the transition elements. In soda-lime-silica glass, Mn^{3+} gives a deep purple but Mn^{2+} gives a faint pink. Control of the redox conditions is an essential facet in the development of specific colours in glass. The most important colourant in commercial glass is iron. The ferrous ion has a strong absorption band in the infra-red and the tail of this band runs into the red end of the visible spectrum producing a blue/green glass. The ferric ion is a weaker colourant. In the production of colourless glass, the deleterious effect of the ferrous ions are eliminated by melting under oxidizing conditions or by using decolourizing agents which absorb in

those regions of the visible spectrum where the ferrous ion transmits. Control is essential since this decolourization process reduces the total transmittance of the glass. In the production of amber glass control of the ferrous ion concentration is guaranteed by adjustment of the oxygen partial pressure in the glass melt.

A comprehensive review of the colours that can be produced in glass has been written by Weyl [17].

Except under certain conditions [17], nickel absorbs almost the entire visible spectrum. Figure 7 shows the absorption due to Ni^{2+} in both tetrahedral and octahedral co-ordination. Because nickel exists in both these coordinations in most silicate glasses, absorption generally extends across the entire visible spectrum. Nickel is a powerful colorant and one part in 50,000 produces a recognizable tint.

Other processes which can produce colours in glass are fluorescence, defect centres and ultra-violet radiation.

(iii) Stress Optical Effects in Glass

Anisotropy in the atomic packing or electron distribution can cause the speed of light and hence the refractive index to vary with direction in a material. This phenomena is called birefringence. Many transparent materials, including glasses and plastics are isotropic but become birefringent when subjected to mechanical stresses. This effect is the basis of a useful experimental technique, photoelasticity, which is used to determine the distribution of strains in complex engineering structures. In glass science, however, it is more generally used to detect strain developed by uneven cooling or stresses due to

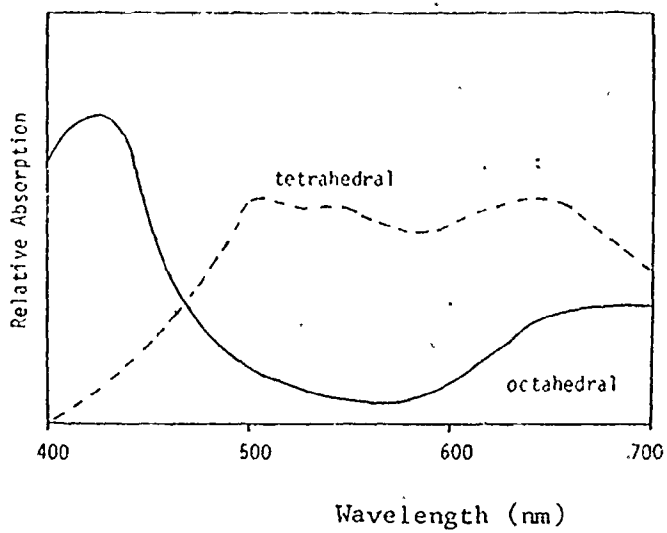


Figure 7. Absorption Spectra for Ni²⁺ in Tetrahedral and Octahedral Co-ordination in Glass.

mismatch in thermal expansion coefficients (e.g. glass to metal seals). When a photoelastic material is analyzed in polarized light that part of the wave with its wave vector parallel to the applied stress will move at a different velocity to that at right angles. These transmitted components when viewed through a second crossed polarizer recombine to give a resultant light wave. If the relative retardation is equal to the wave length of the light used, optical interference will result in extinction of the transmitted light. If white light is used, the colour whose wavelength is equal to the relative retardation is extinguished giving a coloured beam. The relative retardation (r) between the two transmitted waves is [18]

$$r = R(\sigma_p - \sigma_q)d \quad (1.4)$$

where R is the stress-optical coefficient σ_p and σ_q are the principal stresses and d is the thickness of the material. For a stressed plate viewed in white light the sequence of colours observed as the stress increases is shown in Table 4. The stress-optical coefficient for glasses is relatively small (Table 5) and large stresses are required to reach the first order dark fringe in monochromatic light. In glass-working operations, it is essential to detect the presence of stresses much smaller than this. The greater sensitivity is achieved using white light and a 'sensitive tint' plate between the polarizer and the analyser. This plate is a thin plate of birefringent material such as mica. This mica plate has a thickness and orientation such that, in the absence of an additional birefringent specimen, first order destructive interference occurs within the yellow part of the spectrum and the

TABLE 4. Colour Sequence in Photoelastic Material viewed in White Light.

Approx. Relative Retardation (nm)	Colours Extinguished	Colour Observed	Order
50	-	Grey	} 1st
200	-	White	
400	Violet	Yellow	
450	Blue	Orange	
500	Green	Red	
590	Yellow	Purple	
650	Orange	Blue	
700	Red	Green	} 2nd
800	Deep red(1st) Violet(2nd)	Yellow	
900	Blue	Orange	
1000	Green	Red	
1180	Yellow(2nd)Violet(3rd)	Purple	
1300	Orange-red(2nd)Indigo(3rd)	Emerald Green	
1400	Red(2nd)Blue(3rd)	Pale Yellow	
1550	Deep-red(2nd)Green(3rd)	} 3rd	
	Violet(4th)		Pink
1700	Yellow(3rd)Indigo(4th)		Pale Green
1900	Orange(3rd)Blue(4th)	White	} 4th
2100	Red(3rd)Green(4th)	Pale Pink	
	Violet(5th)	Pale Green	
2400	Deep-red(3rd)Yellow(4th)	Pale Green	
	Blue(5th)Violet(6th)	Pale Green	
2500	Orange(4th)Green(5th)	White	
	Indigo(6th)	White	

Above the 3rd order overlapping becomes more and more pronounced, being a repetition of white, pink and green, getting paler each time until at about the 7th order, the transmitted light is practically white

TABLE 5. Stress Optical Coefficients.

Soda-lime-silica glass	2.5
Silica glass	3.4
Perspex	5
Epoxy resin	7
Bakelite	53
Gelatin	2,000-14,000

, Units are μm path difference per m of path length per MPa

light emerging from the analyser is magenta in colour. When additional birefringence is introduced, the missing absorption band moves and the colour changes towards blue or red. The eye is more sensitive to changes of hue in this part of the spectrum and so small stresses can then be detected.

1.2.6 Characteristic Reference Temperatures

For glasses there is no sharp discontinuous transition from the solid to the liquid state but a progressive decrease occurs in viscosity through the transformation range. The width and position of this transformation range varies from glass to glass so a series of reference conditions have been defined in terms of the viscosity changes. These reference points roughly correspond to specific arbitrary tests, e.g. the fibre softening point.

The viscosity of glass in the melting tank is ~ 10 Pa.s. When being pressed into moulds or drawn into tubes or rods, the viscosity (η) ranges from 10^2 to 10^5 Pa.s and arbitrarily the temperature at which $\eta = 10^3$ Pa.s is called the working point. The strain point ($\eta = 10^{13.5}$ Pa.s) is the highest temperature from which a glass can be rapidly cooled without introducing serious internal stress. The annealing point ($\eta = 10^{13.4}$ poise) is the temperature at which any internal stress will be relieved in a few minutes. The change in viscosity with temperature for various glasses and their characteristic reference points are shown in Figure 8. As a final note to this section on materials, a comprehensive review should make mention of the structure and properties of nickel. The important physical properties of nickel are presented in Table 6.

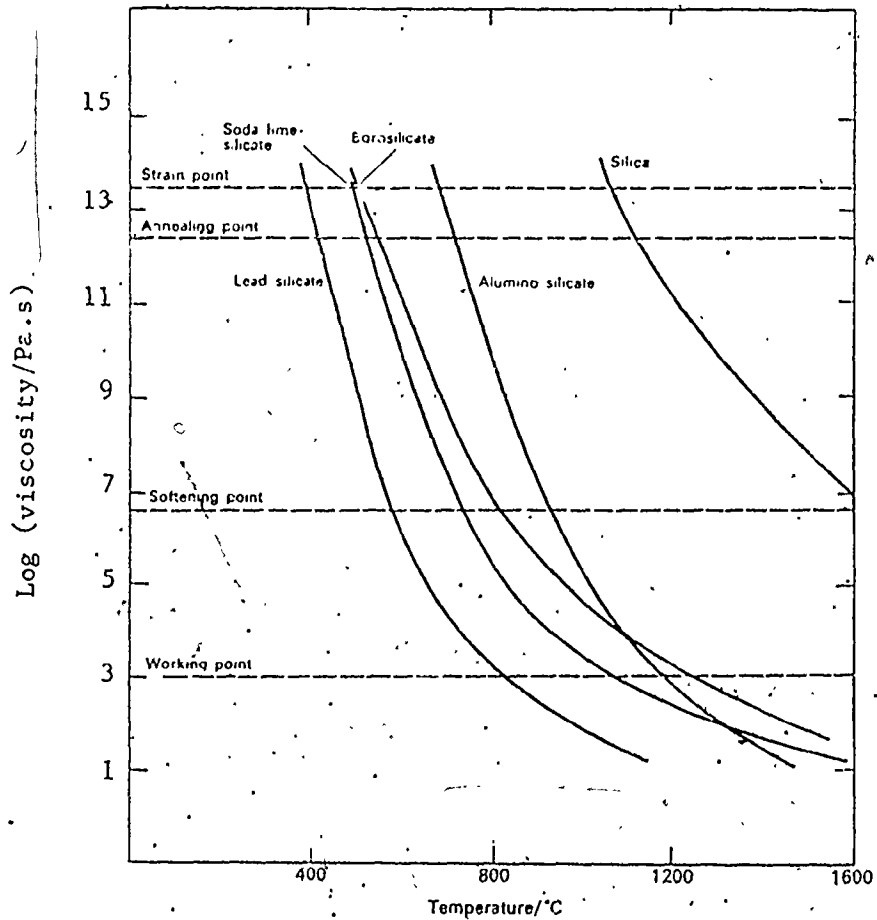


Figure 8. Variation of Viscosity with Temperature for some Commercial Glasses.

TABLE 6. Physical Properties of Nickel.

Density (kg/m^3)	8.90×10^3
Young's Modulus (MPa)	20.4×10^4
Poisson's Ratio.	0.280
Thermal Expansion Coeff. ($\text{m/m}^\circ\text{C}$)	13.9×10^{-6}
Resistivity 0°C ($\Omega\text{-m}$)	6.14×10^2
Melting Point ($^\circ\text{C}$)	1453
Boiling Point ($^\circ\text{C}$)	2820
Atomic Weight	58.7
Electron Configuration	$1s^2 2s^2 2p^6 3s^2 3p^6 3d^8 4s^2$

1.3 Hot Pressing

1.3.1 Introduction

The development of high performance ceramic materials with controlled microstructures, high densities and improved properties is an important area in ceramic processing. The simultaneous application of temperature and pressure to powder compacts, known as hot pressing or pressure-sintering has proved an important technique for the fabrication of such materials. For materials that have low atomic mobility, exhibit rapid or discontinuous grain growth or have high vapour or decomposition pressures at normal sintering temperatures, fabrication by hot pressing may be the only practical means of producing fully dense materials with minimum grain growth. Such hot-pressed materials often exhibit high strength, have smooth wear-resistant surfaces and are transparent to electromagnetic radiation.

Despite its technological importance, there is still little fundamental information on the kinetics and mechanisms of densification which occur during hot pressing.

For this thesis, fully dense glass/nickel composites with well-dispersed nickel phase were hot-pressed at temperatures where minimal reaction occurs between the nickel and glass and thermal stresses during cooling were minimized. Comprehensive reviews of the hot pressing process have been published by Spriggs [19] and Sahm [20].

1.3.2 The Hot Pressing Process

The hot pressing process consists of applying pressure to a powder or cold-pressed compact in a refractory die at a temperature

which gives reasonable densification rates while minimizing such effects as grain growth. The pressure may be applied uniaxially, biaxially or triaxially but most work has been performed uniaxially. The refractory die consists of a hollow cylinder into which cylindrical plungers are inserted. For uniformity of density, it is best to press from both directions and if possible to reduce the die-wall friction. Density gradients will exist in samples with a length to diameter ratio greater than four.

Graphite is the most commonly used die and plunger material as it is inexpensive, easy to machine and refractory. Graphite can be heated by induction or electrical resistance. Induction heating has disadvantages as it is difficult to control the temperature and the die temperature profile. The die design is important for the production of an integral sample. Die stress analysis is based on the standard elastic formulae for thick-walled cylinders with internal pressures. Pressures employed range from 7 to 70 MPa (1000 to 10,000 psi). The use of liners, spacers and coatings eliminate adverse reactions between the sample and the die body [19]. Increased pressures and smaller contamination and wear can be obtained with non-graphite dies (though machining and thermal shock difficulties are often encountered) or by reinforcement of the graphite [19].

The die assembly is placed between hydraulic rams with insulating plates between the plungers and the platens. Insulation can be placed between the die and the induction coil or heating elements. The atmosphere is controlled and inert gases or vacuum are used to prevent oxidation of the die material. The use of vacuum is thought to aid

densification by the removal of final-stage entrapped porosity [19]. Temperatures range up to 2500°C and the pressure is applied at a selected temperature or during the heating cycle. Use of controlled densification rates or special heating cycles is not common although recently, Gazza and Dutta [21] employed a step-heating technique to fabricate transparent spinel without additives at moderate temperatures and pressures. The importance of initial powder characterisation has often been overlooked. Indeed, the processing variables associated with hot pressing have only been recognized in recent times.

As a commercial process, hot pressing still has many limitations though boron carbide lightweight armour has been produced on a commercial scale [19]. The production of complex sizes and shapes is a difficult engineering problem especially if uniformity in density and microstructure is needed. The process is essentially a batch-type operation with its associated increased cost over a continuous process. There has been some attempts recently to make hot pressing a continuous process. Finally, until the processing variables and the densification kinetics and mechanisms are understood improvement in the process may lack direction. There have been several modifications of the hot pressing process which deserve mention. One of these is termed "reactive" hot pressing [22], in which the powders are pressed while undergoing phase transformations, decomposition or dissociation reactions. Increased powder reactivity is associated with these physiochemical changes and dense bodies of materials such as ZrO_2 , Al_2O_3 , UO_2 and certain clay minerals have been produced. A second process is liquid phase hot pressing where enhanced densification is produced by the presence of a liquid. Addi-

tives such as lithium fluoride promote the production of a liquid which then 'distills' off with a post-fabrication anneal. Finally, thermo-mechanical processes such as hot extrusion and hot forging have been used and were reviewed recently by Rice [23]. These processes tend to promote textured and recrystallized materials often with superior properties to those produced by more conventional hot pressing.

1.3.3 Hot Pressing Mechanisms

Comprehensive literature reviews of the densification kinetics and mechanisms during hot pressing have been discussed by Spriggs [19], Sahm [20], Ramquist [24], Coble [25], Chaklader [22] and Spriggs and Dutta [26].

Initial attempts at theoretical evaluation of hot pressing suggested plastic flow (viscous) as a mechanism of hot pressing. The theories were generally considered from a phenomenological standpoint. The material was considered as an elastic continuum with physical constants assigned to its behaviour so as to conform to some idealized model. These models are largely ignored in the current literature though the Murray-Livey-Williams [27] equations should still hold true for some systems particularly in relation to the hot pressing of non-crystalline materials. The work of Vasilos [28] showed that this model applied to the hot pressing kinetics of fused silica. In its simplest form the densification rate ($d\rho/dt$) is given by

$$\frac{d\rho}{dt} = \frac{3}{4} \frac{\sigma}{\eta} (1 - \rho) \quad (1.5)$$

where σ = the applied stress and η is the Bingham solid viscosity.

Other investigators such as Chang and Rhodes [29], Felton [30] and Hashimoto [31] suggest that the early stages of hot pressing are controlled by a combination of particle rearrangement and fragmentation.

Since the early sixties, attempts have been made to derive models for hot pressing based on stress enhancement of the diffusion process. The role of plastic flow was assumed minimal except at high pressure and/or temperatures. Rossi and Fulrath [32] demonstrated that final stage densification of alumina was consistent with the Nabarro-Herring diffusional creep model. Spriggs and Atteraaas [33] suggested that it was likely that more than one mechanism was operating.

The analysis of hot pressing kinetics using creep kinetic models is increasing. This approach generates apparent diffusion coefficients, activation energies and stress dependencies based on the creep equations. At constant temperature, all diffusional creep models are described [19] by the general equation.

$$\dot{\epsilon} = \frac{\sigma^n D}{(GS)^m} \quad (1.6)$$

where $\dot{\epsilon}$ = steady state creep rate

σ = applied stress

GS = grain size

and D = applicable diffusion coefficient.

The stress and grain size exponents can be related to various mechanisms [19]. Corrections are often made for the effect of porosity on the driving force. Coble [34] has pointed out that the creep equations are inapplicable to final stage densification and he has derived an explicit diffusion model for this stage. Unfortunately, the model involves excessive assumptions.

There are some consistent observations that can be made about hot pressing, i.e.

- (i) densification rates increase with decreasing particle size, other factors being constant
- (ii) densification rates increase with increasing temperature and pressure.

The factors controlling the ultimate densification are interdependent and not easily resolved. Particle characteristics and ionic mobility are interrelated while diffusion phenomena, plastic flow and particle rearrangement concurrent with pore removal and grain growth, are sensitive to temperature and pressure. Specific understanding of these complex interrelationships is unavailable and requires more explicit and complex analysis.

Glass-crystal composites have been produced by hot pressing by several workers in their research though none have analysed the hot pressing technique in detail. Lange [9] indicated that there was a tendency for glass evolution from glass powders under vacuum. Lange corrected these problems by using a pre-calcination stage and slow heating rates. In cases where there is a large difference in thermal expansion between the two phases, samples may often crack as they are cooled after fabrication.

1.4 Quantitative Microscopy

In the fracture of brittle particulate composites, the dispersed phase can have a pronounced influence on the fracture resistance. The magnitude of these effects depend partly on the size and spacing of

the dispersed particles (Chapter 2). For theoretical evaluation of the microstructural parameters and their influence on the mechanical properties, quantitative measurements on the microstructure are necessary. Such parameters as, interparticle spacing, mean free path, particle shape, size and distribution volume fraction and degree of dispersion must be determined.

1.4.1 Symbols and Measurements

Microstructural features can be thought of in terms of their dimensionality - i.e., zero-, one-, two- and three-dimensional points, lines, surfaces and volumes. A uniform and self consistent set of symbols [35] are presented in Table 7. The symbol P is associated with points or intersections, L with lines, A with area, S with surface and N with objects. Compound symbols represent fractional quantities, e.g. P_A is equivalent to P/A . The numerator refers to the microstructural parameter and the denominator to the test quantity. In grain size measurements, the number of grain boundaries intersected by a line of fixed length is used to determine N_L or P_L . Measurements are made on random polished sections. All features must be clearly visible and relief polishing should be avoided and special care taken to examine representative samples and random fields of view.

1.4.2 Basic Equations

The basic equations for points, lines, surfaces and volumes in a microstructure are given in Table 8. The measurements are made by scanning a section for areal and lineal features. Measurements of P_A and P_L allow determination of all the parameters shown in Table 8.

TABLE 7. Basic Symbols Used in Quantitative Microscopy and their Definitions.

Symbol	Dimensions	Definition
P	—	Number of point elements or test points
P_p	—	Point fraction. Number of points (in areal feature) per test point
P_l	mm^{-1}	Number of points (intersections) per unit length of test line
P_a	mm^{-2}	Number of points per unit test area
P_v	mm^{-3}	Number of points per unit test volume
L	mm	Length of lineal elements or test line
L_l	mm/mm	Lineal fraction. Length of lineal intercepts per unit length of test line
L_a	mm/mm ²	Length of lineal elements per unit test area
L_v	mm/mm ³	Length of lineal elements per unit test volume
A	mm ²	Planar area of intercepted features or test area.
S	mm ²	Surface or interface area (not necessarily planar)
A_l	mm ² /mm ²	Area fraction. Area of intercepted features per unit test area
S_v	mm ² /mm ³	Surface area per unit test volume
V	mm ³	Volume of 3-dimensional features or test volume
V_l	mm ³ /mm ³	Volume fraction. Volume of features per unit test volume
N	—	Number of features (as opposed to points)
N_l	mm ⁻¹	Number of features intersected per unit length of test line
N_a	mm ⁻²	Number of features intersected per unit test area
N_v	mm ⁻³	Number of features per unit test volume
\bar{L}	mm	Average lineal intercept, L_l/N_l
\bar{A}	mm ²	Average areal intercept, A_l/N_a
\bar{S}	mm ²	Average surface area, S_v/N_v
\bar{V}	mm ³	Average volume, V_l/N_v

TABLE 8. Basic Stereological Parameters and their Inter-relations (Measured quantities are circles and calculated quantities are squares)

Microstructural Feature	Dimensions of Symbols (arbitrarily expressed in terms of millimeters)			
	mm ⁰	mm ⁻¹	mm ⁻²	mm ⁻³
Points	P_p	P_l	P_a	P_v
Lines	L_l	L_l	L_l	—
Surfaces	A_l	S_v	—	—
Volumes	V_l	—	—	—

Basic Equations

- (1) $V_l = A_l = L_l = P_p$ mm⁰
- (2) $S_v = (4/\pi) L_l = 2P_l$ mm⁻¹
- (3) $L_l = 2P_l$ mm⁻²
- (4) $P_l = (1/2) L_l S_v = 2P_l P_l$ mm⁻³

Lineal analysis is usually performed by scanning the planar features along a straight line of fixed length. Areal analysis can be performed using special graticules and comparing the image with a set of standard images. Such techniques are time-consuming and recently automatic scanning and image analysers have become available. It should be noted that all the symbols in Table 8 except those in the first column are interrelated. This gap can be bridged with a simple but powerful choice of grain or particle diameter. The relationship between the parameters are simple and no assumptions are made about particle shape. The derivation of these equations has been discussed by Underwood [36]. Two other important parameters can be derived for these microstructures. The first shows that the mean free path, λ , (the mean edge-to-edge distance along a straight line between particles or separated second phase regions) can be written as [37]

$$\lambda = \frac{1 - V_v}{N_L} \quad (1.7)$$

This parameter makes no assumptions about size, shape and location of the second phase. Furthermore, the parameter is a true three-dimensional parameter [37] even though it is obtained from the plane of polish. The second is the mean intercept length \bar{L}_3 , often used as a grain or particle 'diameter'. This measurement is equal to $1/N_L$ for space-filling grains and to V_v/N for non space-filling particles. It is, for a particular system, independent of the degree of convexity or concavity and has no assumptions about size or shape. From the relationships in Table 8, \bar{L}_3 must also equal $2/S_v$ for space-filling grains,

substitution of the mean intercept length into equation (1.7) gives

$$\lambda = \frac{\bar{L}_3(1 - V_v)}{V_v} \quad (1.8)$$

which, in terms of the specific area per unit volume, becomes

$$\bar{L}_3 = \frac{4V_v}{S_v} \quad (1.9)$$

Equation (1.8) has been verified [36] using independent methods of evaluating V_v . Equation (1.9) connects the two sets of equations in Table 8 and all the stereological parameters are interrelated. The analysis of projected images is more complex and will not be dealt with at this time. Figure 9 provides a complete and consistent set of equations for quantities observed on the plane of polish or on the projected image and their relationship to the true three-dimensional structure. These relationships are general in nature with the proviso that particle overlap and truncation are negligible. There are two interesting results among these equations, i.e. the mean projected intercept length, \bar{L}_2' is equal to the main tangent diameter \bar{d} on a section and secondly $\bar{L}_2 = \bar{L}_3$. The expressions in Figure 9 can be verified easily for the case of spheres and are sometimes used as approximations for real particles. The subscripts 2 and 3 refer to planar and volumetric measurements respectively.

1.4.3 Particle Size Distributions

Size distribution of real particles with irregular shapes are incapable of exact solutions. In general, analyses are based on the assumption that the particles or grains are spherical and that the distribution can be represented in a discontinuous fashion. If the

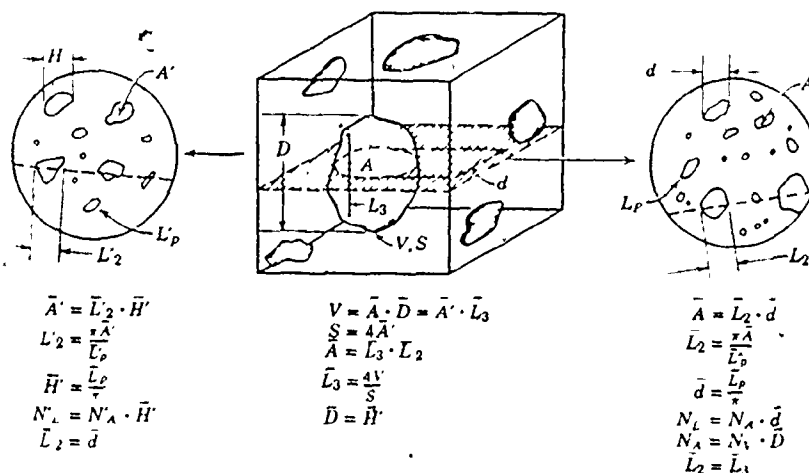


Figure 9. Relations between Convex Particles in Space, their Section, and their Projections.

TABLE 9. Selected Characteristics of Convex Alumina Particles in Cu as determined by Various Methods.

Method.	Mean Particle Diameter (μm)	Surface Area (m^2/g)	Volume Fraction.
Quantitative Stereology.	6.01 (embedded spheres)	0.25	0.149 (point) 0.145 (lineal)
Coulter Counter	5.0 (number basis) 6.5 (weight basis)	—	—
BET	8.7	0.69	—
Micromerigraph.	7.1	—	—
Optical	8.2 (tangent diam.)	—	—
Nominal	—	—	0.10
Chemical Analysis.	—	—	0.095

class intervals are not too big, the greatest inaccuracies should result from the deviation of the particles from spherical shapes and this may be reasonable for equi-axed grains or convex particles. Measurements are generally made from the frequency distribution of section diameters, areas and chords which can be converted to the true three-dimensional frequency distribution. Several methods are available for this conversion. In particular the Schwartz-Saltykov method of analysis is accurate [36, 38, 39] especially where particles are small or poorly resolved. The measurement and detection of the smallest particles is the major practical problem. The distribution of any polydispersed system can be completely defined by the mean diameter, standard deviation and the number of particles per unit volume.

(i) Particle Size Distribution from a Distribution of Section Diameters

There are several methods that can be used to convert a distribution of section diameters into a particle size distribution. These methods have several features in common. Firstly, the section diameters are classified into discrete groups, with the particles in each group considered to have the same diameter. If the spheres are all of one size, then a simple equation relates the number of sections observed per unit area (N_A) to the number of spheres per unit volume (N_V) [39].

$$N_V = \frac{N_A}{D_i} \quad (1.10)$$

where D_i is the diameter of the spheres. When sections of a particular size are counted an appropriate probability factor to account for this arbitrary restriction must be introduced. Equation (1.10) then becomes,

$$N_V = \frac{N_A(i,j)}{p} \frac{1}{D_j} \quad (1.11)$$

where p is the probability of the plane intersecting a sphere of diameter D_j so as to yield sections of size d_j . This equation is common to the various techniques for conversion to particle size distribution and coefficients are used to describe the probability term. These coefficients are obtained from the probabilities of a random plane intersecting a sphere to give the various sections. The final point of similarity derives from the use of a successive subtraction process. If a polydispersed system of spheres is intersected by a plane then allowance must be made for the fact that some of the sections derive from spheres of larger diameters. The number of these latter sections must be subtracted from the total number to obtain those sections due only to spheres of one size. Details of the Schwartz-Saltykov technique are given in Appendix A.1.

The particle-size distribution determination for loose powders is relatively simple and several different techniques are available [40]. In optical microscopy, special graticules are available allowing the sizing of particles to be done with reasonable speed. Alternatively, measurements can be made on micrographs provided a statistically reasonable number of measurements are made. Other techniques such as sedimentation and the Coulter counter are well documented in the literature. A comparison between mean particle size, surface area and volume fraction measured by quantitative microscopy and more conventional techniques has been made by Underwood [39] on a composite of convex Al_2O_3 particles dispersed in copper. The results are shown in Table 9. The agreement between the particle size determinations is reasonable even though the methods have different bases (weight, volume, number, etc.)

These differences can be resolved by intercomparison of the data using lognormal functions. The agreement between the surface area and volume fraction data is less consistent. For volume fraction determinations such discrepancies occur quite often and may be a result of the inaccuracies about location of the particle boundaries.

(ii) The Lognormal Distribution

The lognormal distribution may be defined as the distribution of a variate whose logarithm obeys the normal law of probability. Although the function is derived from 'normal' behaviour it can be still studied fundamentally since it arises from a theory of elementary errors by a multiplicative process. The same theory combined with addition rather than multiplication would give a normal distribution. Many examples of lognormal distributions exist in nature and it is frequently observed in the field of particle statistics. The size distribution of small particles in soils or rocks and mechanical processing of solids such as grinding, often give rise to skew distributions which obey the lognormal law. Distributions of grain-size or sieved particles are further areas where a lognormal distribution have been observed. In these situations, the lognormal distribution has the advantage that, if an elementary variate is lognormally distributed, so are any powers of the variate ("moments"). For example, from a lognormal weight distribution the size distribution can be derived. The history, mathematics and philosophy of the lognormal distribution has been discussed recently in a monograph by Aitchison and Brown [41] but more relevant and simpler approaches can be found in the general texts on particle statistics.

Mathematically, the lognormal distribution is:

$$y = \frac{1}{\log \sigma_g \sqrt{2\pi}} \exp \left[-\frac{(\log x - \log x_g)^2}{2 \log^2 \sigma_g} \right] \quad (1.12)$$

where x_g is the geometric mean and σ_g the standard deviation.

The moments of these distribution (i.e. $\sum n_i x_i^r$) are also distributed lognormally with the same standard deviation. The ratio of these moment averages is simply

$$x_r/x_{r-1} = \exp(0.5 \log^2 \sigma_g) \quad (1.13)$$

It should be noted here that this relation between the arithmetic and logarithmic parameters are reasonably reliable when $\log_{10} \sigma_g$ does not exceed 0.14 [42]. Important parameters are based on these moments such as a volume or surface distribution. The average of such a distribution will be based on the ratio of two moment distributions. An average based on a volume distribution is given by [42]

$$x_v = \frac{\sum n_i x_i^4}{\sum n_i x_i^3} \quad (1.14)$$

For a lognormal distribution we find from equation (1.13) that

$$\log x_v = \log x_g + 3.5 \log^2 \sigma_g \quad (1.15)$$

Finally, it can be shown that the arithmetic, geometric and harmonic means also follow similar relations. The lognormal distribution, therefore allows extensive mathematical flexibility. Graphical representation of lognormal distributions is accomplished with probability paper which has a logarithmic scale on the x-axis. Data plotted on such paper gives a straight line for a lognormal distribution. Tests are available to determine the degree of lognormality [41]. In some cases, mixtures of two or more distributions may be identified. In a bimodal distribution with sufficiently separated averages the distribution curve will show a double inflection [42].

1.4.4 Contiguity of Two-Phase Systems

In dispersed phase systems, there is a probability of interparticle contact. Such a phenomenon would change the size distributions of the original powders giving rise to "larger" particles determined by quantitative measurements on the fabricated material. The degree of contact or contiguity of a system may have a pronounced effect on its properties. For example, Gurland [43] has shown that the conductivity of a silver-bakelite mixture will suddenly decrease when the average number of contact points is ~ 1.5 . In relation to the fracture of brittle composites, the contiguity will influence the spacing distribution between particles and interparticle contacts could give rise to preferable sites for crack initiation. The fracture path in such systems could be influenced by the contiguity. In a recent article Gurland [43] has reviewed quantitative measurements for contiguity in such systems. These contiguity parameters can be determined on a plane of polish, based on the geometric probability relations of Smith & Guttman [44]. The average fraction of surface area shared by one grain of a phase with neighbouring grains of the same phase or contiguity ratio (C_t) is

$$C_t = \frac{2N_L}{N_{L\alpha\beta} + 2N_{L\alpha\alpha}} = \frac{S_{v\alpha\alpha}}{S_v} \quad (1.16)$$

where $N_{L\alpha\alpha}$ is the number of intersections of the interface between α particles with a random line of unit length, $N_{L\alpha\beta}$ is for interface intersections between α and β (the matrix) and S_v is the total area of contact. The ratio varies from 0 to 1 as the distribution changes from completely dispersed to fully agglomerated and makes no assumptions about particle size and shapes. Referring back to equation (1.7), contiguity tends

to increase the mean free path by reducing $N_{L(\alpha\beta)}$.

Parameters such as the average number of contacts can be derived but require assumptions about the size and shape of the contact areas. For spherical particles with a circular area of contact the average number of contacts (\bar{C}) is [45].

$$\bar{C} = \frac{2N_{V\alpha\alpha}}{N_{V\alpha}} = \frac{8}{\pi^2} \left(\frac{N_{A\alpha\alpha}}{N_{A\alpha}} \right)^2 \frac{N_{L\alpha\beta} + 2N_{L\alpha\alpha}}{N_{L\alpha\alpha}} \quad (1.17)$$

The state of aggregation of a constituent in a heterogeneous phase mixture is often termed the degree of dispersion and can be quantitatively related to three measurable parameters: These are the surface of separation, the fineness and the spatial distribution of particles within the matrix.[43]. In particular, the degree of separation (d_p) is

$$d_p = 1 - C_t \quad (1.18)$$

The condition for particle contact has been analysed by Forscher [46] for a random array of spheres dispersed in a continuous matrix: In his review, Gurland concludes by discussing the requirements for continuity within an aggregate in relation to the number of particle contacts.

1.4.5 Interparticle Spacing.

The properties of dispersed phase systems often depend on the size and spacing of the dispersed phase. These parameters rarely have absolute values since the particles are generally not uniform in size, shape or distribution. The interparticle spacing can be calculated on the basis of several definitions leading to different numerical values for a given structure. It is therefore, important to assess the

applicability and limitations of these different derivations and to indicate the difference in numerical values they produce.

The stereological parameters for random microstructures (section 1.4.2) can be simplified if the dispersion is assumed to be uniform spherical particles (radius R). The principal equations become [36, 37]

$$N_V = \frac{\pi N_A^2}{4N_L} = \frac{N_A}{2R} \quad (1.19)$$

$$R = \frac{2N_L}{\pi N_A} = \frac{3V_V}{4N_L} \quad (1.20)$$

$$N_A = \frac{3V_V}{2\pi R^2} \quad (1.21)$$

$$\bar{L}_3 = \frac{4}{3} R \quad (1.22)$$

and
$$\lambda = \frac{4}{3} R \left(\frac{1 - V_V}{V_V} \right) \quad (1.23)$$

In an average sense, these equations may still apply for a distribution of spherical particle sizes. The average particle radius, R , however, should be determined from observations of plane sections and not assumed from the original powder particle size distribution. Interparticle contact and aggregation could produce changes from the original size distribution.

The basic characteristics of a dispersed phase system can be described in terms of the volume fraction and average particle size. The interparticle spacing is a function of these two parameters. In

general, there are two concepts of interparticle spacing, i.e. the mean free path and the nearest-neighbour distance. It is important to understand the difference between these concepts since they can give rise to large numerical differences.

The mean free path was defined earlier and although this definition was in linear terms, the parameter is also correct in a three-dimensional sense. In physical terms, the mean free path is the average distance between particle surfaces along any straight random line. The nearest-neighbour distance (Δ) is defined as the average centre-to-centre distance. In this case the averaging occurs between particles in any direction and not in a straight line as for the mean free path.

The nearest-neighbour distance for a randomly distributed array of points has been given by Gurland [43] for two cases. The nearest-neighbour distance in a volume (Δ_3) is given by

$$\Delta_3^G = 0.554 N_V^{-1/3} \quad (1.24)$$

and on a plane (Δ_2) by

$$\Delta_2^G = 0.500 N_A^{-1/2} \quad (1.25)$$

For the case of spherical particles this last equation can be rewritten as:

$$\Delta_2^G = 0.500 \left\{ \frac{\pi R \lambda}{2(1-V_V)} \right\}^{1/2} \quad (1.26)$$

or

$$\Delta_2^G = 0.500 R \left\{ \frac{2\pi}{3V_V} \right\}^{1/2} \quad (1.27)$$

Analogous equations can be derived for differently shaped particles based on Underwood's formulae for mean intercept length as a function of particle geometry [36].

These equations have drawbacks since the centres of finite particles do not behave like a random array of infinitesimal points. Particles cannot be closer than a distance equal to the sum of their radii. The above equations are approximately valid, however, for dispersions of small particles at very low volume fractions.

Bansall and Ardell [47, 48] have attempted to overcome deficiencies in the above analysis by considering the volume occupied by the particles in a random array of monosized dispersed spheres. The nearest-neighbour distance in the volume (Δ_3^{BA}) and on a plane (Δ_2^{BA}) are given by:

$$\Delta_3^{BA} = R \left\{ 2 + \frac{e^{8V_V}}{3V_V^{1/3}} \cdot \Gamma(1/3, 8V_V) \right\} \quad (1.28)$$

and

$$\Delta_2^{BA} = R \left\{ \frac{\pi}{2} + \frac{1}{12V_V} \int_0^{6V_V} \frac{\Gamma(1/2, x) e^{-x} dx}{(6V_V - x)^{1/2}} \right\} \quad (1.29)$$

where the symbol $\Gamma(\)$ refers to the incomplete gamma function. It should be noted that Δ_2^{BA} refers to the distance between the centre of circles formed by the intersection of the spheres with the reference plane and not with the centre-to-centre distance. These equations, when applied to polydispersed particles with narrow distributions should be good but may lead to inaccuracies for non-spherical particles. The nearest-neighbour edge-to-edge distance (Z) may be found by subtracting the near particle diameters from the values per Δ since

$$Z_3 = \Delta_3 - 2R \quad (1.30)$$

$$\text{and } Z_2 = \Delta_2 - 2r \quad (1.31)$$

where r is the radius of the circle produced by intersection with a random plane ($r = \frac{\pi}{4}R$). The nearest-neighbour distances may also be

defined in terms of the average distance between first, second; third, etc. nearest neighbours.

For uniformly distributed particles the situation changes. The mean free path, for example, will depend on the direction of the test lines and planes. Quantitative measurements can be made only if the measurements of data is carried out on the basis of specifically oriented lines or planes within a single crystal or grain. In the case of cubically-arranged particles, attempts have been made to evaluate the nearest-neighbour distances. Brown and Ham [49] examined the planar analogues of a cubic array and have shown the centre-to-centre distance between particles arranged on a square lattice [SL] (Δ_2^{SL}) as

$$\Delta_2^{SL} = N_{A(SL)}^{-1/2} \quad (1.32)$$

The nearest-neighbour distance in a volume can be deduced from this equation since this distance will always be equal to the length of the edge of the distribution cube, i.e.

$$\Delta_3^{CL} = (N_A^{CF})^{-1/2} \quad (1.33)$$

where N_A^{CF} is the number of particles per unit area on a plane section lying specifically along the square faces of the cubic array. Tyson [50] has modified these equations to evaluate the corresponding edge-to-edge, nearest-neighbour distances. The equations based on cubically-arranged particles tend to be very specific and the derivations presuppose a combination of particle distribution and specimen sectioning which rarely occurs in practice and differs significantly from randomness. In a recent review Corti et al [51] have evaluated and compared these different approaches to interparticle spacing. Their data give valuable insight

into the different concepts and the difference in numerical values for interparticle spacing that can be obtained.

As mentioned earlier, the confusion surrounding interparticle spacing makes difficult comparison between models and properties. It also gives rise to a confusion between different workers and hinders the progress of understanding spacing-dependant properties. Obviously, care must be taken to use an evaluation of interparticle spacing that is relevant to the process being studied (e.g. a planar spacing is more realistic than a volumetric spacing when discussing cracks propagating between obstacles on a fracture surface.) Furthermore, the nature of microstructure itself must be taken into account (e.g., a uniformly distributed, theoretical evaluation is no good for a random microstructure). Finally, the method of evaluation and its reasoning should be clearly described.

This situation has been recognized for some time in the current theories of dispersion-strengthening of alloys. In these materials, the property-controlling spacing is the distance between the surfaces of the particles on the slip plane of the matrix since the strength is often controlled by the movement of dislocations between the particles. In this case, it would appear that the mean free path concept is not realistic since a dislocation line is not straight. The nearest-neighbour distance must also be in doubt since it is not possible for the dislocation to lie only between nearest-neighbours even when the dislocation line is pinned unless it is closest particles that control the process. The interparticle spacing needed to describe this situation must lie between these limits.

Kocks [52, 53] has suggested a contiguity approach which determines the critical obstacle spacing (Δ_2^K) required to pin a dislocation moving through a random array of strong point obstacles, on a plane under the influence of a stress. This critical spacing is given by

$$\Delta_2^K = 1.18 N_A^{-1/2} \quad (1.34)$$

which becomes

$$\Delta_2^K = 1.18R \left(\frac{2\pi}{3V_V} \right)^{1/2} \quad (1.35)$$

for randomly distributed spherical particles. Foreman and Makin [54] have also discussed a critical obstacle spacing and based on a computer analysis. Their result is very similar to Kock's except for the numerical constant.

$$\Delta_2^{FM} = 1.23 R \left(\frac{2\pi}{3V_V} \right)^{1/2} \quad (1.36)$$

for strong point obstacles. Several workers in this field have based their results on the cubic lattice evaluation discussed earlier using the edge-to-edge nearest neighbour distance. It would seem, however, that the last two derivations are more relevant since the particle distribution on a slip plane is not evidently based on a cubic lattice. The difference between these evaluations and that of a random array of points (Δ_2^G) is a numerical constant. Therefore, all these approaches obey the general form of the Orowan equation [55] used to describe dislocation-particle interactions.

This problem of obstacle spacing has not been recognized in theoretical and experimental studies of fracture in particulate composites. Most of the experimental data has been discussed in terms of the mean free path which for reasons similar to those outlined above

is incorrect. The problem is similar to that encountered in dispersion-strengthened alloys but the use of point obstacles must be in doubt (larger volume fractions).

To clarify the situation, a comparison has been made of the various formulations and is shown in Figure 10. The computer programme for evaluating Z_2^{BA} is given in Appendix A.2 though Bansal and Ardell supply tables of Z_2^{BA}/R and Z_3^{BA}/R on request. As a general comment, the statistical chance of preparing a section so that the single nearest-neighbour to any reference particle lies on that section decreases as the volume fraction decreases. For samples with volume fractions greater than ~ 0.10 , the difference between Δ_2^G and Δ_3^G tends to be small [51]. It can be seen in the figure that the random point array for nearest-neighbours does give rise to spacings less than the particle diameters for volume fractions greater than 0.13. The approach by Bansal and Ardell corrects for this but only gives rise to a slight increase in spacing. The formulations based on a square lattice or a contiguity criterion give rise to larger spacings still, as would be expected. The mean free path values are large and for volume fractions less than 0.06 the difference is, more than an order of magnitude.

For the fracture in particulate composites the approaches similar to Foreman and Makin [54] and Kocks [52, 53] would appear to be most relevant, though a correction for the finite size of the particles should be made. This correction, however, is probably small since the difference between Z_3^G and Z_2^{BA} is not large even at volume fractions up to 0.20. Kocks [53] suggests that these refinements can

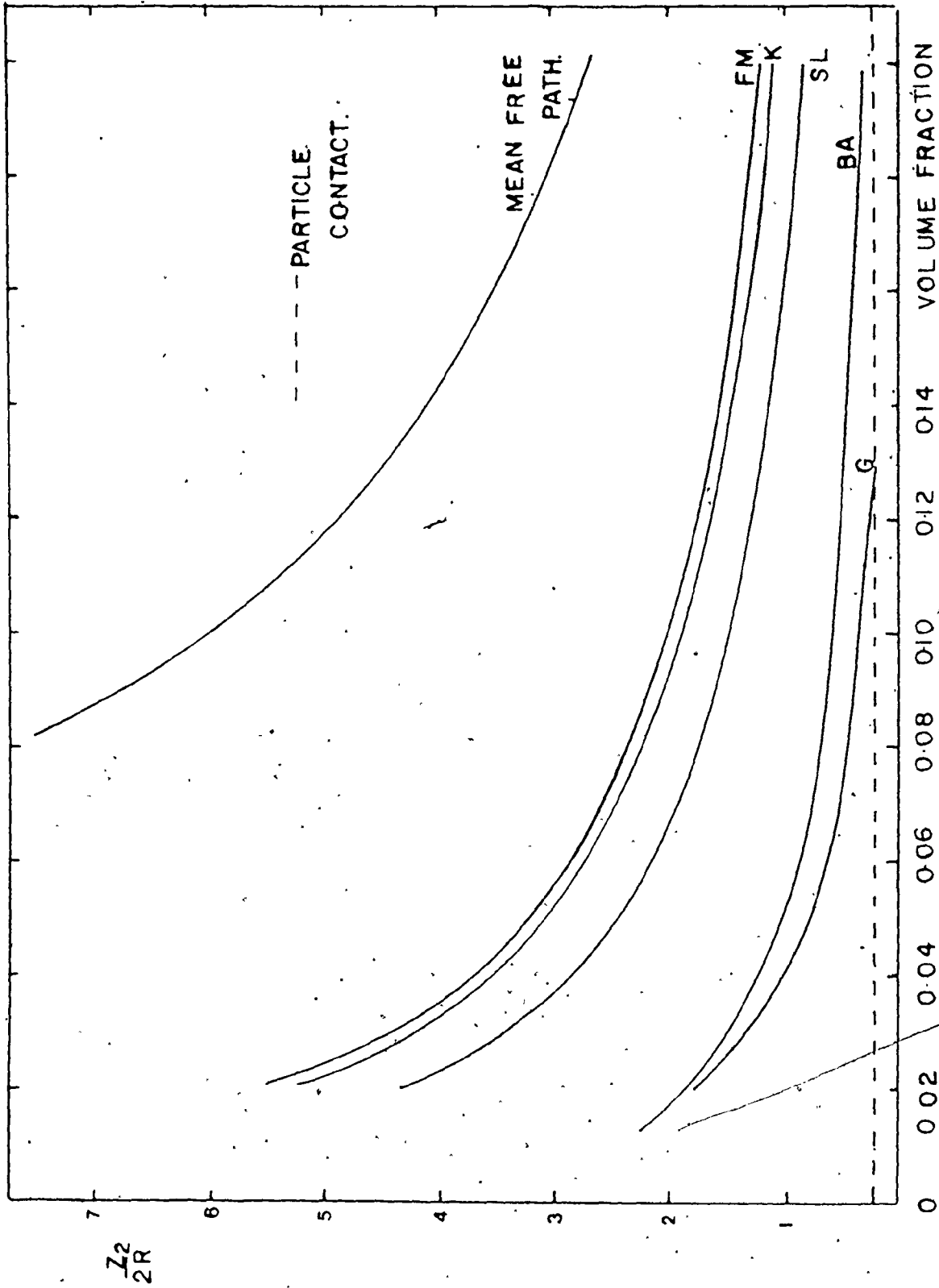


Figure 10. Various Formulations for Interparticle Spacing as a Function of Volume Fraction and Size of Second Phase Particles.

be made but that for most purposes use of equation (1.43) should be adequate to a first approximation. It also obeys the same functional relationship as Δ_2^{FM} and Δ_2^{K} . Therefore, this equation will be used for the description of interparticle spacing in this thesis. It is clear that the concept of interparticle spacing when relevant to a particular property should be carefully analyzed to ensure the approach is physically reasonable.

CHAPTER 2

ENERGY ABSORBING PROCESSES IN THE FRACTURE OF HIGHLY BRITTLE MATERIALS

2.1 Overview

In recent times, many new applications have been discerned for highly brittle materials since they possess many attractive properties such as hardness, chemical inertness, low thermal and electrical conductivities and high temperature stability. The serious drawback of these materials is their proneness to catastrophic failure especially under mechanical and thermal shocks. The resistance to fast fracture is not generally considered in conventional design procedures but an approach known as fracture mechanics has been developed to supplement conventional design criteria. This approach recognises the energetics involved in fracture and depends on an applied mechanics, continuum approach. The resistance of a material to fracture is generally referred to as its fracture toughness and will depend on the energy absorbing processes available in a material when it is subjected to a stress.

For the materials science approach to this problem, it is important to be able to relate this continuum approach to the microstructural and atomistics aspects of a material. In doing so, the material scientist will then possess the capability of designing a microstructure to fulfill more demanding performances such as increased fracture toughness.

For this thesis, the microstructural feature which has been selected is the interaction of a crack front with second phase particles in a

brittle material. For structural application, such brittle particulate composite systems appear to be of secondary importance but by choosing a model system where the microstructural parameters are well defined, it should be possible to study crack front interaction in a basic sense. The approach is, therefore, to measure the macroscopic fracture properties of the material and then relate these properties to the model particulate microstructure.

Fracture is generally considered as a competition between plastic and brittle processes but in this discussion the role of plasticity will be de-emphasized. It is hoped, thereby, to indicate that highly brittle failures are not simply the production of new surface area but that there is also a competition of brittle fracture processes.

There is an increasing demand for methods of increasing the toughness of brittle materials and fibre composite and multiphase composite systems appear to show great potential in this respect. This potential will only be fully realized when the energy absorbing processes in such materials are more completely understood. In this chapter, the fracture mechanics approach will be briefly reviewed and the emphasis will be on the discussion of the microstructural aspects of highly brittle failure especially with respect to particulate composites. A more complete discussion of the fracture of brittle materials is available in a recent book by Lawn and Willshaw [56] and of highly brittle materials by the present author [57].

2.2 The Continuum Approach to Fracture

There are several modes of failure that a structure may undergo and the skill of a structural engineer lies in the recognition of these

possibilities. These failure modes can be generally listed as failure
by

- (i) elastic instability (buckling)
- (ii) excessive elastic deformation (jamming)
- (iii) gross plastic deformation (yielding)
- (iv) tensile instability (necking)
- (v) fast fracture (cracking)
- (vi) slow crack growth (environmentally-assisted crack growth)

For highly brittle materials, it is the last two modes of failure which are of prime importance and for this work the emphasis is on fast fracture. If a material is to fail in a brittle manner (i.e. before general yield) or in a highly brittle manner (i.e. before yield), it must contain a stress concentrator which confines the cracking mechanism to a local region. The aim of fracture mechanics is to be able to relate the processes which occur in this region to the applied stress system. It should be noted here that fracture mechanics is not the only way to measure the resistance to fracture but that various sorts of fracture indices such as the transition temperature have been used. These latter procedures are useful for comparative purposes but for quantitative information, fracture mechanics provides a more exact approach to the problem.

2.2.1 Stress Concentrations and the Griffith Approach

The first fundamental problem of the mechanical strength of solids is to explain why they are so weak. Bond strengths are of the order 1 to 10 eV and act over distances of 3 to 10 Å. Refined estimates of the

bond strength or theoretical strength generally gives values of $E/7$ to $E/20$, where E is the Young's modulus. The approach to these fundamental strength calculations has been expertly reviewed by Kelly [58].

In practice, solids are much weaker than these theoretical strength values because stress concentration occurs near flaws. Thus, as dislocations lower the yield stress of a material so cracks lower the fracture strength of a material. This problem was clearly stated and immediately solved by A.A. Griffith in 1920 [59], when he considered the extension of an isolated crack in a solid subjected to an applied stress, in terms of the fundamental energy theorems of classical thermodynamics and mechanics. Retrospectively, his approach can be seen as a breakthrough in the understanding of fracture and it provided a basic framework for the scientific methodology for studying the fracture process.

Griffith recognized that stresses could be sufficiently concentrated by essentially geometrical factors on an atomic scale. For the case of a crack, stress cannot be transmitted across the crack surface so that the load that should be carried by these bonds must be carried elsewhere. In fact, it concentrates at the end of the crack, so that the crack can be seen to act as a "lever" concentrating the stress at its tip. The work of Griffith was dependant on an earlier elastic stress analysis; of an elliptical hole in a uniformly stressed plate, performed by Inglis [60]. He had shown that the maximum stress (σ_{\max}) occurred at the end of the major axis and is given by:

$$\sigma_{\max} = \sigma_A (1 + 2a/b) \quad (2.1)$$

where a and b are the major and minor axes respectively and σ_A is the applied stress. For the case of an elliptical crack, length c ($b \ll a$), equation (2.1) reduces to

$$\sigma_{\max} = \sigma_A (c/\rho)^{1/2} \quad (2.2)$$

where ρ is the radius of curvature of the crack tip. If the crack is atomically sharp, it need not be very long to amplify the stresses by several orders of magnitude. The variation in local stresses at the tip of an elliptical hole is shown in Figure 11. This example typifies the general behaviour of a stress concentration in that the perturbation of the stress field occurs only within a distance $\approx c$ from the boundary of the hole and the greatest stress gradients are confined to a smaller region of dimension $\approx \rho$ around the position of maximum stress. For very sharp cracks, the analysis will run into problems, as the elastic assumptions of small strains are violated. The highest principal stress occurs at the crack tip in the plane of the hole and one would expect an elliptical notch to crack or yield preferentially at its tip. For plane strain conditions (thick specimens) there will also be a transverse stress component σ_{33} . The subscripts for the stress components are based on a tensor notation, where the axes are shown in Figure 11. At distances away from the notch tip ($r > 0$), a triaxial or biaxial stress state exists and the maximum principal stress does not occur across the plane of the notch. This type of stress state tends to promote cleavage over yielding so that when one considers the heterogeneous nature of a material, fracture events may occur away from the crack tip. Inglis considered other geometric stress concentrators and found that the maximum stress concentration occurs in the region of highest curvature. Surface notches can be considered simply by

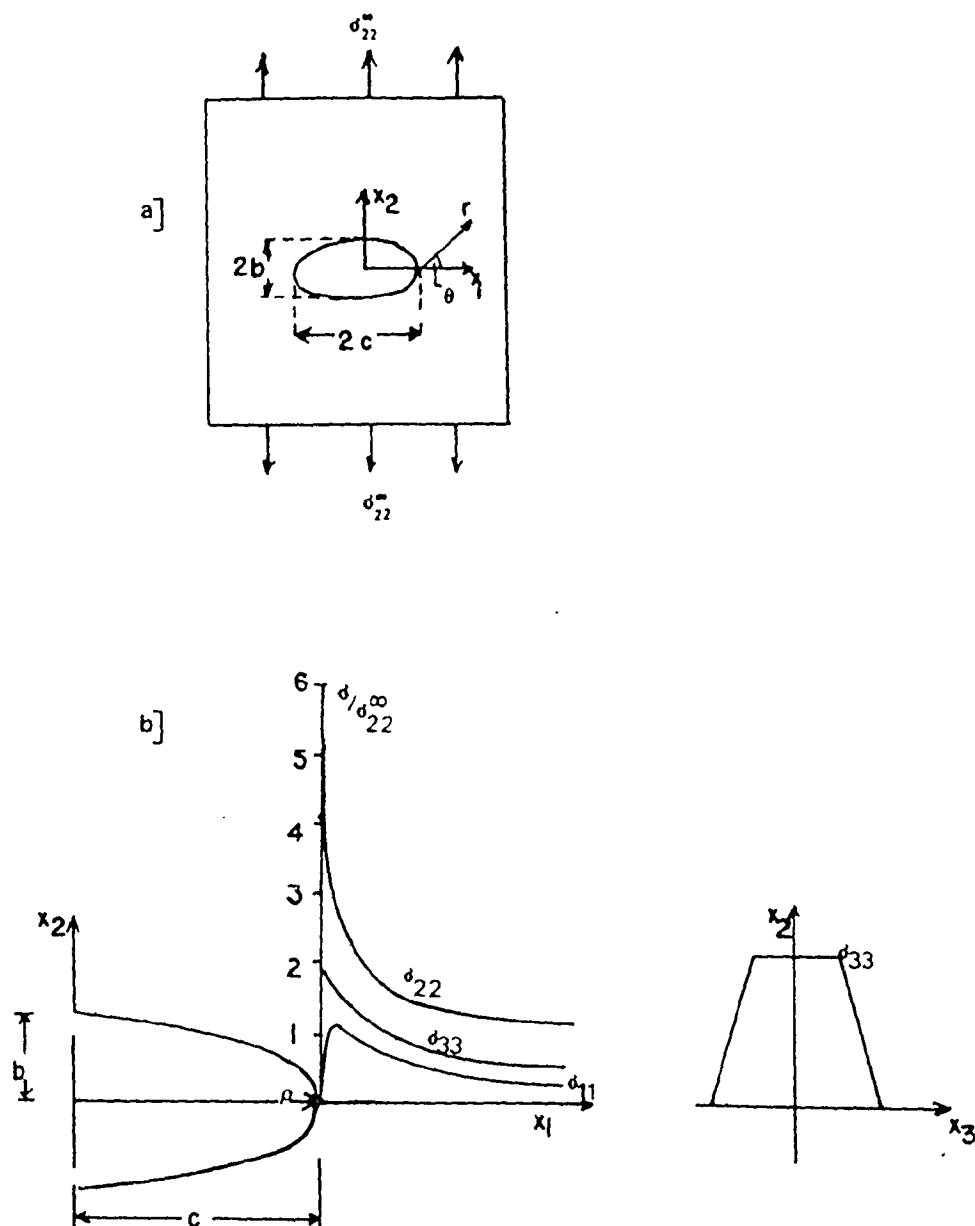


Figure 11. a) Co-ordinate System for Plate containing Elliptical Hole.

b) Stresses ahead of Elliptical Hole along $x_2 = 0$ ($c \sim 3b$)

assuming it can act in the same way except it is now a semi-elliptical hole in a semi-infinite plate.

Griffith recognized this stress concentration problem but realized that if a crack were to grow, such a process must be energetically favourable. Two factors govern this energy balance, i.e., the total elastic energy and the crack surface energy. The total potential energy of a system, consisting of a strained solid containing a crack of length $2c$, normal to the applied uniaxial tensile stress σ_A under plane stress, is

$$V = - (\pi \sigma_A^2 c^2 / E) + 4\gamma c \quad (2.3)$$

where γ is the surface energy. The configuration which minimizes the free energy of the system ($\partial V / \partial c = 0$) then gives a fracture criterion, i.e.,

$$\sigma_f = \sqrt{\frac{2E\gamma}{\pi c}} \quad (2.4)$$

In plane strain, E must be replaced by $E/(1 - \nu^2)$ in the above equation. Within these considerations, the crack should open or close depending on whether $(\partial V / \partial c)$ is negative or positive. This approach can only deal with a static crack situation. For a dynamic crack, a kinetic energy term must be added to equation (2.3). It is generally assumed that the Griffith criterion represents a threshold for instability but as pointed out by Glucklich [61] and amplified by the present author [57] this may not always be true. Indeed, crack stability is dependant on the material properties, the loading geometry and the notch sharpness.

Griffith [59] verified his theoretical predictions on glass as his model brittle material. His criterion for failure is also powerful

in the sense that it relates the macroscopic strength behaviour of a material to its microstructure. For example, if one returns to the Inglis equation (2.2) one can estimate the theoretical bond strength by assuming ρ is a constant and of atomic dimensions.

It should be recognized that the Griffith result is a statement of the necessary energy conservation. It may be necessary to supply additional forces to break the atomic bonds with part of the energy being dissipated as heat. Orowan [62] has given a qualitative argument to show that within an order of magnitude, the Griffith load should also be sufficient to debond the atoms. In this work, he estimated the theoretical cleavage strength to be

$$\sigma_{th} = \sqrt{\frac{E\gamma}{a_0}} \quad (2.5)$$

where a_0 is the lattice spacing. In conjunction with the Inglis equation (2.2) this yields a fracture criterion of

$$\sigma_f = \sqrt{\frac{E\gamma}{4c} \frac{\rho}{a_0}} \quad (2.6)$$

which for cracks with $\rho = a_0$ is approximately the same result as Griffith. It is clear though, that the Inglis equation must be in doubt and that the force laws of the atoms at the crack tip require subtle treatment. Indeed, the shape and sharpness of real cracks is also open to question. Furthermore, to explain the weakness of real solids, one must postulate the occurrence of inherent flaws in a material. The genesis and growth of these flaws into well-developed cracks is still not completely understood.

2.2.2 Linear Elastic Fracture Mechanics

The approach known as fracture mechanics was introduced by

G.R. Irwin and his associates circa 1950. The impetus for this development was the result of some serious engineering design failures especially in regard to the Liberty ships and tank disasters of World War II. The approach retains the thermodynamic approach of Griffith and is based on a continuum view of materials. The Griffith approach can be seen to be very specific as it only deals with reversible crack propagation for an ideal brittle solid in a specific loading geometry. It was necessary that the concept be placed in a more general framework, so that crack propagation could be described by a critical parameter (preferably a material constant) which characterizes the resistance to fracture for non-specific loading geometries and includes the irreversible nature of crack propagation in real materials.

This problem can be analysed in two ways and these are typified by the approaches on Inglis and Griffith. Following Inglis, the first approach would be to solve the stress and displacement fields for an arbitrarily loaded crack. The second approach concentrates on the energetics of the situation and calculates the mechanical energy associated with crack extension. For this initial discussion, the concepts will be generalized for ideally brittle, isotropic materials.

For the stress analysis approach, continuum mechanics distinguishes three basic failure modes. These three modes are illustrated in Figure 12. Although modes II and III are occasionally important in macroscopic applications, on an atomic scale the free surface of the crack is not truly free unless Mode I is present. Modes II and III are shearing modes and are analogous to the motion of edge and screw dislocations. Mode I typifies the concept of crack extension by progressive stretching and failure of cohesive bonds across the crack plane.

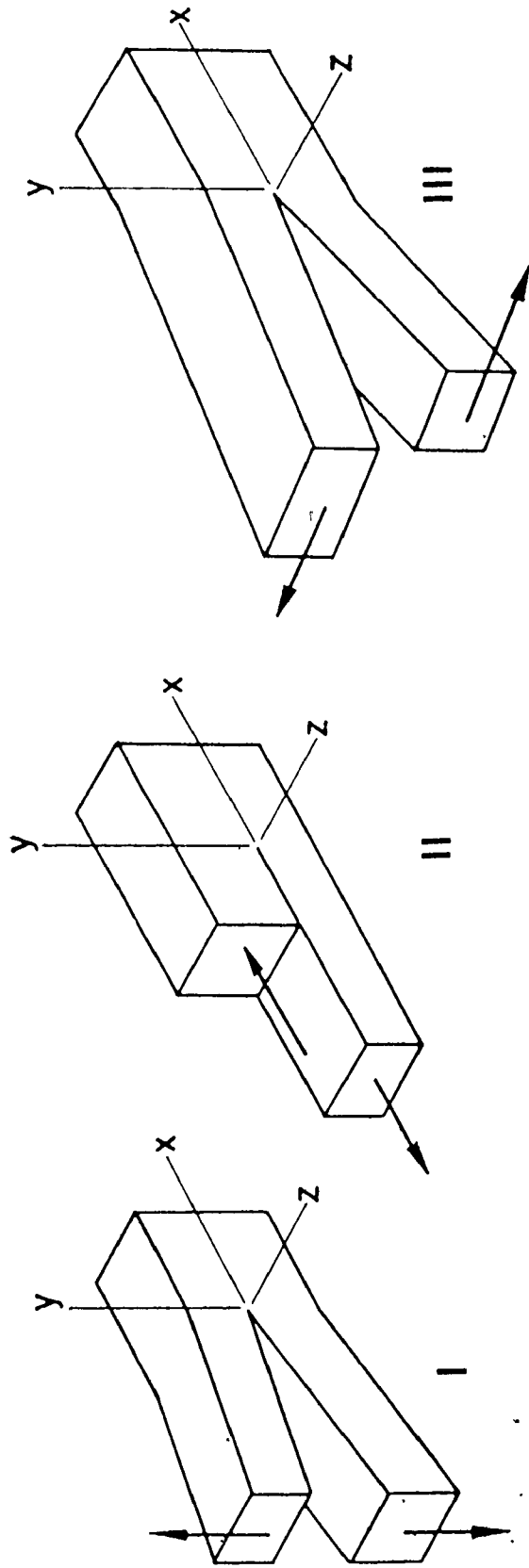


Figure 12. The Basic Modes of Crack Surface Displacement.

The elastic solution to the crack stress analysis problem is generally done by modelling the crack as an infinitely sharp slit in a continuum so that the crack remains sharp at all times and the crack walls remain free of any tractions. This approach gives rise to a series solution, of which the first term is dominant for distances close to the crack tip compared to the crack length. These first term stress components are then representative for the near-tip stress field. In terms of the co-ordinates shown in Figure 11, the solution for Mode I is

$$\left. \begin{array}{l} \sigma_{11} \\ \sigma_{22} \\ \sigma_{12} \end{array} \right\} = \frac{K_I}{(2\pi r)^{1/2}} \left\{ \begin{array}{l} \cos(\theta/2)[1 - \sin(\theta/2)\sin(3\theta/2)] \\ \cos(\theta/2)[1 + \sin(\theta/2)\sin(3\theta/2)] \\ \sin(\theta/2)\cos(\theta/2)\cos(3\theta/2) \end{array} \right.$$

$$\left. \begin{array}{l} \sigma_{rr} \\ \sigma_{\theta\theta} \\ \sigma_{r\theta} \end{array} \right\} = \frac{K_I}{(2\pi r)^{1/2}} \left\{ \begin{array}{l} \cos(\theta/2)[1 + \sin^2(\theta/2)] \\ \cos^3(\theta/2) \\ \sin(\theta/2)\cos^2(\theta/2) \end{array} \right.$$

$$\sigma_{33} = \nu^1(\sigma_{11} + \sigma_{22}) = \nu^1(\sigma_{rr} + \sigma_{\theta\theta})$$

$$\sigma_{13} = \sigma_{23} = \sigma_{rz} = \sigma_{\theta z} = 0$$

$$\left. \begin{array}{l} u_1 \\ u_2 \end{array} \right\} = \frac{K_I}{2E} \left(\frac{r}{2\pi}\right)^{1/2} \left\{ \begin{array}{l} (1+\nu)[(2\kappa-1)\cos(\theta/2) - \cos(3\theta/2)] \\ (1+\nu)[(2\kappa+1)\sin(\theta/2) - \sin(3\theta/2)] \end{array} \right.$$

$$\left. \begin{array}{l} u_r \\ u_\theta \end{array} \right\} = \frac{K_I}{2E} \left(\frac{r}{2\pi}\right)^{1/2} \left\{ \begin{array}{l} (1+\nu)[(2\kappa-1)\cos(\theta/2) - \cos(3\theta/2)] \\ (1+\nu)[-(2\kappa+1)\sin(\theta/2) - \sin(3\theta/2)] \end{array} \right.$$

$$\begin{aligned} u_{33} &= -(\nu^1 z/E)(\sigma_{11} + \sigma_{22}) \\ &= -(\nu^1 z/E)(\sigma_{rr} + \sigma_{\theta\theta}) \end{aligned} \quad (2.7)$$

where E is Young's modulus, ν is Poisson's ratio

and $\nu = (3 - \nu)/(1 + \nu)$, $\nu^I = 0$, $\nu^{II} = \nu$ plane stress
 or $\nu = (3 - 4\nu)$, $\nu^I = \nu$, $\nu^{II} = 0$ plane strain.

The term K_I is known as the stress intensity factor and is a result of the boundary conditions for the crack system. The solution for modes II and III are given elsewhere [56] but they all give stresses of the form

$$\sigma_{ij} = K(2\pi r)^{-1/2} f_{ij}(\theta) \quad (2.8)$$

and for the displacements

$$u_i = \left(\frac{K}{2E}\right) \left(\frac{r}{2\pi}\right)^{1/2} f_i(\theta) \quad (2.9)$$

The stress intensity factors depend only on the applied loading and crack geometry and they determine the intensity of the stress field. The radial and angular components determine the field distribution and depend on the inner boundary conditions. The stress intensity factors have the general form

$$K = Y\sigma_A(c)^{1/2} \quad (2.10)$$

where Y is a geometrically-dependant constant. In the case of the crack configuration studied by Griffith $Y = (\pi)^{1/2}$. The solution for the stress and displacement fields given in equation (2.7) lose their validity at large r because the other terms in the series solution become important. For example, at $r = a/2$ and $\theta=0$, the value of σ_{22} for a Griffith-type crack would be equal to σ_A . This condition is incorrect since $\sigma_{22} = \sigma_A$ is an outer boundary condition.

The mathematical devices of an infinitely sharp crack and the linear elastic continuum are analytical conveniences. Indeed, they

lead to a stress singularity at $r = 0$; a situation which is physically unreasonable. It is generally assumed that a crack has a finite tip radius so no infinities occur in the local stresses and strains. The errors involved in equations (2.7) for small and large r lead to uncertainties in describing the detailed nature of the stress-strain field in these regions. Fortunately, these uncertainties do not interfere with K , which defines the stress field intensity. For the intermediate region equation (2.7) should be reasonably correct and could be used to describe fracture mechanisms.

The stress components given in equation (2.7) are illustrated in Figure 13. The prediction of $\sigma_{11} = \sigma_{22}$ is not valid when one admits a finite crack tip radius. The σ_{33} component can vary substantially from zero at the free surfaces to a higher value in the median plane. Eventually, for thick plates it should reach a value $\nu(\sigma_{11} + \sigma_{22})$. Three dimensional photoelasticity [63] supports these general statements though the cubic dilation change from plane stress to plane strain conditions appears to be larger than predicted by fracture mechanics.

An important point about the near-tip stress field is the $r^{-1/2}$ dependence. This results in a longer range stress field than, for example, a dislocation (r^{-1}). Regarding the self energy of a crack, this near-tip form is divergent for an infinite crystal and it is clear that the boundary conditions play an essential role in determining the physical properties of cracks. The concept of line tension, which is frequently used in dislocation theory, cannot be applied to crack for this reason.

A final point about these fracture mechanics stress solutions is

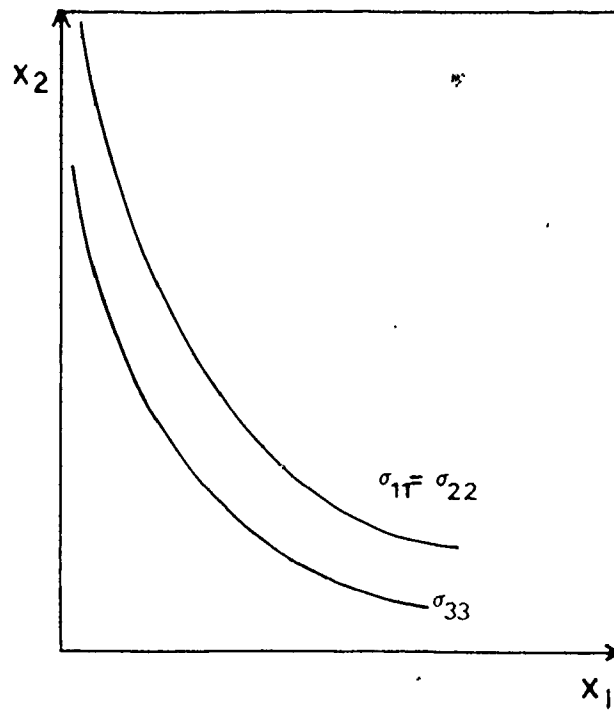


Figure 13. Stresses ahead of Infinitely Sharp Crack (Elastic Stress Analysis).

that their common form allows the principle of superposition to be applied. The stress intensity factors for a given mode are additive. This allows complex loading situations to be analyzed more readily.

Because the stress intensity factor describes the field intensity at a crack tip, one may expect that a critical value of K might describe the condition for crack extension. The derivation of K , however, does not rely on any fracture criterion.

The second approach to fracture is to consider the energetics of crack extension. One of the most important concepts in this respect is the elastic force exerted on a crack by an external stress. This concept may appear to have philosophical difficulties but mathematically one can define an effective force, the crack extension force G , which is the negative derivative of the total elastic energy with respect to crack length. From elasticity arguments [57], one can show that, for a two-dimensional crack,

$$G = - \frac{\partial V^1}{\partial c} = 1/2 P^2 \frac{d\psi}{dc} \quad (2.11)$$

where V^1 is the total elastic energy, P is the load and ψ is the compliance of the specimen. The crack extension force can be determined experimentally in a simple fashion.

One may also expect that a critical value of G , like K , may also describe a condition for crack extension. Indeed, it is reasonably straightforward to show that G and K are interrelated, i.e., for Mode I crack extension.

$$\begin{aligned} G_I &= K_I^2/E \quad \text{plane stress} \\ \text{or } G_I &= (1 - \nu^2)K_I^2/E \quad \text{plane strain} \end{aligned} \quad (2.12)$$

Both G and K can be determined experimentally by either compliance measurements or stress analysis solutions. Stress intensity factors have now been determined for many crack geometries particularly those used in fracture toughness testing. Table 10 lists the stress intensity expressions for many common testing geometries and some that are of relevance for this thesis. The interaction of two parallel, non-coplanar edge cracks to form fracture surface steps is discussed in Appendix A.3 from a stress intensity viewpoint. These surface steps are a feature of many particulate composite and are therefore of relevance to this thesis.

The Griffith criterion for crack equilibrium can be obtained from the fracture mechanics approach by setting the crack extension force (G), which opens the crack equal to the surface tension of the opening surfaces, which resists this opening, so that for plane stress

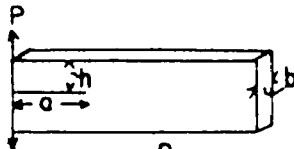
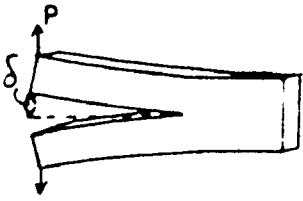
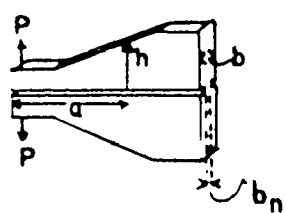
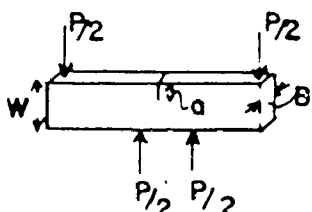
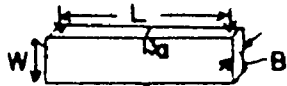
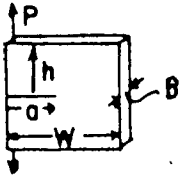
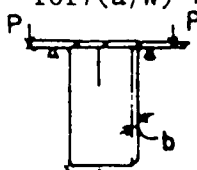
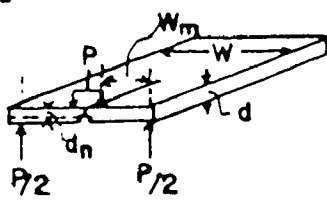
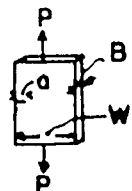
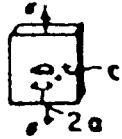
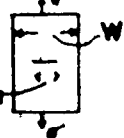
$$G_c = 2\gamma = K_{Ic}^2/E \quad (2.13)$$

For the Griffith crack configuration where $K_I = \sigma_A \sqrt{\pi c}$, this expression reduces to the original Griffith criterion (equation 2.4).

2.2.3 Crack Paths

In the fracture mechanics approach, the problem of crack paths is generally ignored. For most problems, the plane of the crack is generally taken as normal to the applied stress and one assumes the crack extends along its own plane. Common experience indicates that a crack will generally follow a curved path. The details of these trajectories are of great discussion in the current literature and may be of great practical importance.

TABLE 10. Stress Intensity Expressions for Several Common Testing Geometries.

<u>Double Cantilever Beam (DCB)</u>	$K_I = 3.45 \frac{Pa(1 + 0.7h/a)}{bh^{3/2}}$	
<u>Wedge-loaded DCB</u>	$K_I = \frac{\sqrt{3} E \delta h^{3/2}}{2 a^2 (1 + 0.64h/a)^2} = \left(\frac{3\sqrt{3} \delta P^2 E}{2 b^2 h^3} \right)^{1/2}$	
<u>Tapered DCB.</u>	$\left\{ \begin{aligned} K_I &= 2P \left(\frac{m}{b b_n} \right)^{3/2} \\ m &= 1/h + 3a^2/h^3 \end{aligned} \right.$	
<u>Four Point Bend</u>	$K_I = Y \cdot \frac{6Ma^{3/2}}{BW^2}$ $Y = 1.99 - 2.47(a/W) + 12.97(a/W)^2 - 23.17(a/W)^3 + 24.80(a/W)^4$	
<u>Three Point Bend</u>	$K_I = Y \cdot \frac{6Ma^{3/2}}{BW^2}$ $Y = 1.96 - 2.75(a/W) + 13.66(a/W)^2 - 23.98(a/W)^3 + 25.72(a/W)^4$ if $L/W=4$ $Y = 1.93 - 3.07(a/W) + 14.53(a/W)^2 - 25.11(a/W)^3 + 25.80(a/W)^4$ if $L/W=8$	
<u>Compact Tension</u>	$K_I = Y \cdot \frac{Pa^{3/2}}{BW}$ $Y = f(a/W)$ $Y = 29.6 - 185.8(a/W) + 655.7(a/W)^2 - 1017(a/W)^3 + 63.9(a/W)^4$	
<u>Constant Moment Arm DCB</u>	$K_I = \frac{M}{(Ib)^{3/2}}$	
<u>Double Torsion</u>	$K_I = PW_m \left(\frac{3(1+\nu)}{Wd^3 d_n} \right)^{1/2}$	
<u>Single Edge Notched (SEN)</u>	$K_I = Y \cdot \frac{Pa^{3/2}}{BW}$ $Y = 1.99 - 0.41(a/W) + 18.70(a/W)^2 - 38.48(a/W)^3 + 53.85(a/W)^4$	
<u>Semi-elliptical Surface Crack</u>	$K_I = 1.12 \frac{\sigma(\pi a)^{1/2}}{\Phi}$ Max. Value $\Phi \cong 3\pi/8 + \pi a^2/8c^2$ $\Phi =$ Complete Elliptical Integral of 2nd Kind	
<u>Centre Cracked Plate</u>	$K_I = \sigma(\pi a)^{1/2}$ Infinite Plate $K_I = \sigma \left[W \tan \left(\frac{\pi a}{W} \right) \right]^{1/2}$ Finite Plate	

Several suggestions have been made to imagine how a crack "chooses" the direction of its next incremental extension. For example, it has been suggested that the crack will follow the direction of the maximum normal or the maximum principle stress. A phenomenological theory has been put forward by Sih [64] in which he suggests the crack will follow a radial of minimum strain energy density. Finally, on thermodynamic grounds, it has been suggested that the orientation of the crack path should be such that it maximizes the decrease in total system energy. This suggestion corresponds to a maximization of the quantity $G - 2\gamma$. For an isotropic system this reduces to maximizing G . Unfortunately, once the crack extends out of its own plane, a complex geometric and mathematical problem arises. There are, however, some limiting cases which can be studied and give insight into this crack trajectory problem. For all these suggestions, the crack direction for the two dimensional case depends on the K_{II}/K_I ratio. In some experimental work [65, 66] it has been suggested that this ratio must reach a critical value before the crack changes direction.

The nucleation of a crack on a new misoriented plane has been treated by Gell and Smith [67] as a simple tensor transformation on the near-tip stresses. For the case of a tilt or twist rotation, the stresses acting on the new plane can be determined from equation (2.7). The variation of G for tilt (θ) and twist rotations (ϕ) is shown in Figure 14. For both cases, G is maximized when crack extension proceeds along the original plane. Planar extension is not always possible especially in polycrystalline materials. For example, during intergranular failure, the crack must tilt and twist, according to the topography of the grain

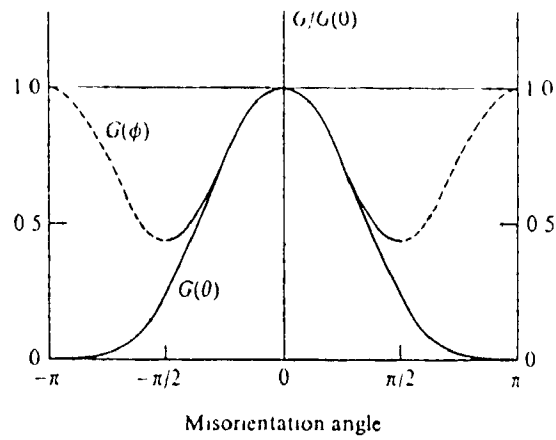


Figure 14. Normalised Crack Extension Force as a Function of Tilt(θ) and Twist (ϕ) Misorientation Angles for Mode I Loading.(Plane Strain). After Lawn & Willshaw (56).

boundaries. Such failures must involve more energy than require for planar extension.

The problem of mixed mode failures can also be considered using this maximum G approach. In this case, contributions to the stress components will arise from the mode II or III fields. For modes I plus II, the problem gives rise to a tilt-dependant function while for modes I plus III, it gives a twist dependant function. These are illustrated in Figure 15 for various K_{II}/K_I ratios. The crack extension functions now exhibit directional instability. The use of mode II shear waves to modulate the growth of a mode I crack, is a technique that is to be used in the experimental part of this thesis.

For the combined mode I and III situation, a twist rotation is predicted. Such a rotation cannot be carried out in a continuous fashion and the crack must segment into partial fronts separated by secondary fractures. This effect has been shown to produce fracture lances in glass [68] and fracture surface steps [56] as transgranular cracks cross grain boundaries. Fracture surface steps are also observed in particulate composites. The formation of these steps and the energy involved in the secondary fracture are of relevance to this work.

The problem of crack trajectories discussed here is very qualitative. Crack nucleation may occur away from the crack tip, the mathematical analysis of non-coplanar extension is complex and anisotropic effects such as preferred cleavage directions were not included.

2.2.4 Fracture Mechanics of Particulate Composites

Recently, a number of papers have been written about the influence

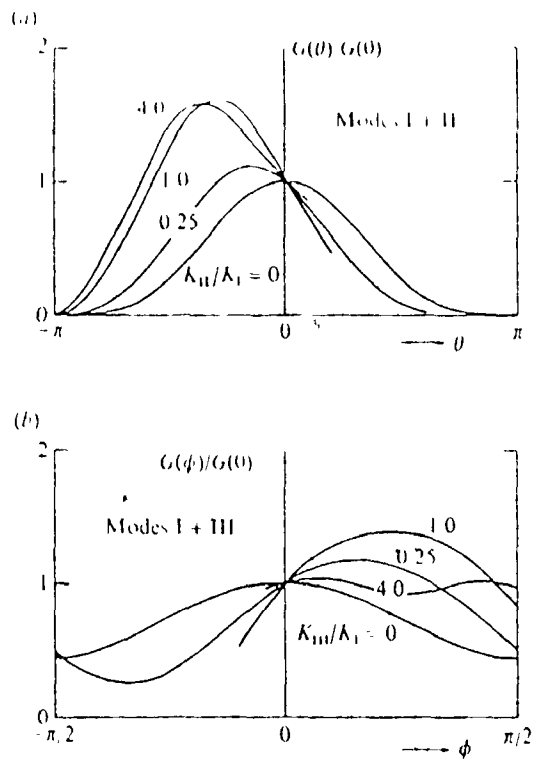


Figure 15. Normalised Crack Extension Force as a Function of Misorientation Angle for a) Superposed Modes I + II b) Superposed Modes I + III (Plane Strain Conditions) From Reference 56.

of inclusions on cracks from a fracture mechanical viewpoint. In general, these solutions consider a small crack in the vicinity of the inclusion and this crack is usually perpendicular to the applied stress on the equator of the inclusion. These approaches are usually concerned with fracture initiation in the vicinity of these particles.

The stress field associated with the difference in elastic properties between an inclusion and the matrix has been appreciated for some time. The simple case of a cylindrical inclusion subjected to a uniaxial tensile stress is discussed in Appendix A.4. In general, one finds that if the particle is harder than the matrix, there is a stress concentration above and below the particle. For a softer particle, the enhanced stresses occur around the equator of the particle. The situation is illustrated in Figure 16 along with a conception of what may happen to the crack path [69]. The terms, hard and soft are rather qualitative here but in general they depend on the ratio of the shear moduli and the Poisson's ratios.

Tamate [70] and Atkinson [71] have both considered the influence of the elastic stress field of the inclusion on a nearby crack, located on the equator of the inclusion. Atkinson [71] suggests that it is the internal stress field due to the inclusion which produces the major effect. The interaction of the crack stress field with the inclusion is assumed to be only of secondary importance. This suggestion has been substantiated recently by Tirosh and Tetelman [72], who corrected the basic solution with second and third order corrections but showed that the basic solution is the major term. These approaches appear to break

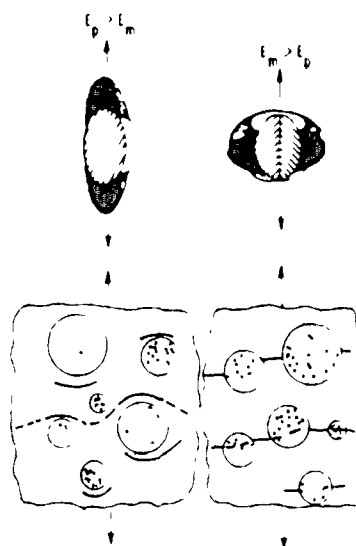


Figure 16. Schematic Representation of the Enhanced Tensile Stresses (shaded volume) around a Spherical Particle (Modulus E_p) in a Matrix (Modulus E_m). The Location of the Cracks and Possible Fracture Paths (broken lines) are also shown.

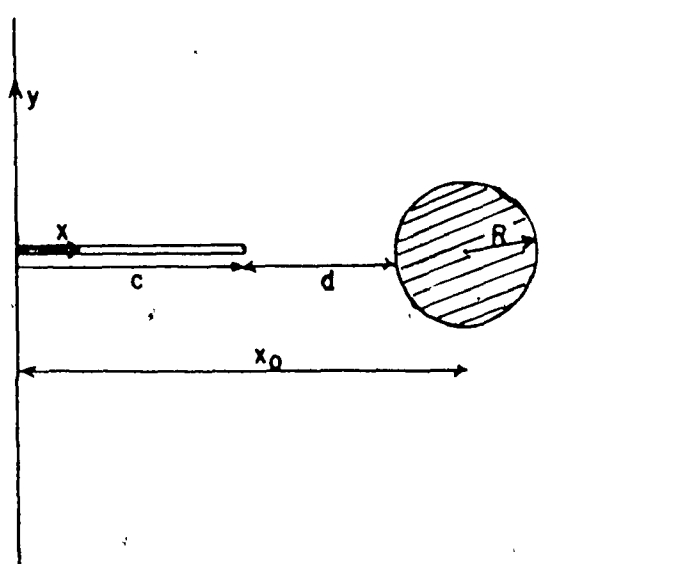


Figure 17. Crack Approaching a Cylindrical Hole along Its Equator (After Tirosh and Tetelman (72))

down when the crack length is much larger than the inclusion.

From these solutions, one finds that for the case of a hole there is an increase in the stress intensity factor at the crack tip (K_I) over the value for an unperturbed crack (K_I^0). For the configuration shown in Figure 17, Tirosh and Tetelman give a first order solution.

$$\frac{K_I}{K_I^0} = 1 + \frac{\gamma}{2} \left(\frac{R}{R+d}\right)^2 \left(\frac{R+d}{R+d+c}\right)^{1/2} - \frac{3\delta}{2} \left(\frac{R}{R+d}\right)^4 \left(1 - \frac{c}{2x_0} + \frac{c^2}{8x_0^2}\right) \left(\frac{R+d}{R+d+c}\right)^{1/2} \quad (2.14)$$

The values of γ and δ depend on the difference in the elastic properties between the matrix and the inclusion. For a rigid or a hard inclusion the stress intensity is generally decreased. Debonded particles behave like holes though the increase in stress intensity is not expected to be as great. The attraction of a crack to a hole is physically appealing since one expects to reduce the elastic energy locally by such a procedure. In the same sense, one can argue that hard particles will tend to 'repel' the crack.

Erdogan [73] has also looked at the first order solutions for arbitrarily located cracks. The effect on stress intensity is more complex and depends on the position of the crack front. Fortunately, the solutions can be understood in terms of the prior stress field. In this way, it can be seen that the mode II component will now be available and tends to change the crack path towards the positions of maximum stress concentration. In this way, one expects that for hard particles, the crack will tend to avoid the particles and stay within the matrix, while for holes or debonded inclusions, the crack will

be attracted to the particles. An exact solution to the crack path problem would be very complex. This suggestion, however, can be aided by experimental observations. For example, Stett and Fulrath [74] showed that by increasing the interfacial strength in a glass/nickel composite, the crack would remain in the matrix while for a non-bonded or poorly-bonded particle the crack 'prefers' to intersect the particles.

Hancock [75] observed the attraction of a crack front to voids in polystyrene while Wagoner and Hirth [66] have studied this void-trapping in a more sophisticated way.

It should also be pointed out that the interaction with a second phase inclusion also changes the stress singularity. For normal cracks, the stresses depend on r^{-n} , where $n = 1/2$. For a crack approaching an inclusion of lower modulus n will be greater than $1/2$ and vice versa for harder inclusions.

The approach of a crack to a second phase inclusion seems better understood but once the crack intersects the inclusion, exact stress analyses must become extremely complex.

2.2.5 The Non-Linear Crack Tip Field

In Irwin's generalization of the Griffith concept, the problem of the events in the vicinity of the crack tip have been ignored. The singularities in the linear elastic stress field were inconsistent with any local fracture criterion and it is clear that other dissipative events can occur during fracture e.g., plastic flow, heat and phonon generation, etc. The fracture of a single bond cannot even be

described by a linear elastic process.

Rather than dealing directly with non-linear systems, Irwin modified the approach by applying corrections to the linear model and confining the non-linear zone to a small well-defined region near the crack tip. For a small inner zone, the elastic stress field should not be greatly disturbed, as the $r^{-1/2}$ dependence of the stresses is relatively long-ranged (St. Venant's Principle). In this way, the inner non-linear zone should remain insensitive to the nature of the outer boundary conditions. In energetic terms, the mechanical energy variation is still specified exactly as in the linear case but the non-linear forces do work in creating new surfaces which includes the other dissipative processes. The equality $G = 2\gamma$ is no longer valid and we now define $(\partial U_S / \partial c) = 2\Gamma$, which at equilibrium gives

$$G_c = 2\Gamma \quad (2.15)$$

The fracture resistance term has been referred to by several names; e.g. fracture surface energy, fracture toughness and work of fracture. For real brittle materials $\Gamma > \gamma$ and for ductile materials $\Gamma \gg \gamma$. In this guise, the fracture process is viewed through macroscopic eyes and appears to remove the classical grandeur of the energy balance approach. Fracture resistance is no longer determined by the amount of fracture surface but by the behaviour of the material adjacent to the crack tip. The theoretical and experimental description of the non-linear zone for plastic materials has been reviewed recently [76].

The description of the non-linear zone has been improved by a mathematical device which involves the use of path independent integrals. When the path coincides with the boundary of the zone it becomes the J

integral. The inner zone must be described by a mechanistic approach. For example, if we confine the non-linear zone to an infinitesimally narrow slit-like region ahead of the nominal crack tip, the J integral gives

$$J = G = 2 \int_0^{u(c,0)} \sigma(u) du \quad (2.16)$$

This type of non-linear region was used by Barenblatt [77] and one can now include the details of the atomic force laws into the fracture mechanical framework for this 'cohesive zone'. This zone is a result of the removal of the stress singularity at the crack tip. For a brittle solid, it can be shown that

$$G_c = \frac{8\sigma_{th}^2 D_c}{\pi C} = \sigma_{th} u_c = 2\Gamma \quad (2.17)$$

where D_c is the length of the cohesive zone, σ_{th} is the theoretical cleavage strength and u_c is the crack opening displacement. In this way Γ is now defined in terms of material constants.

A similar approach was taken independantly by Dugdale [78] for plastic materials and his result can be written

$$G_c = 2\sigma_y^* u_c = 2\Gamma \quad (2.18)$$

where σ_y^* is the microscopic yield stress. This type of approach can also be couched in terms of continuous dislocation distributions which has evolved into the use of crack opening displacements for measuring fracture toughness even in cases where fracture follows extensive yielding.

The Barenblatt approach brings the two-dimensional theory of the continuum approximation of the brittle crack to its ultimate per-

fection. The crack tip must be sharp rather than elliptical and the width of the cohesive region depends on the details of the force laws. These models have extended the range of fracture mechanics but they also indicate the limitations of a continuum approach in that the actual fracture mechanisms can only be dealt with exactly, on the microstructural and atomistic levels.

2.3 Microstructural Aspects of Crack Propagation

For well-developed cracks in highly brittle materials, such as covalent and some ionic-covalent solids at ambient temperatures, fracture will occur by bond rupture at an atomically-sharp crack tip. The elastic stress field should describe the situation well though modifications should be applied to account for the microstructural interactions. Defects such as dislocations are expected to be immobile.

It is necessary to account for the energy expenditure in such systems in terms of the interaction of the crack-tip field and the microstructural features. Such an understanding allows the characteristic fracture parameters of a material to be determined but more importantly it may suggest techniques to control the toughness by microstructural design.

For highly brittle materials, the relation $\Gamma = \gamma$ should be a necessary and sufficient criterion for fracture. Fracture mechanical measurements on these materials generally give values of Γ which are greater than γ . This inequality could result from local plastic deformation but even in its absence, processes are available which apparently increase the fracture resistance of a highly brittle material. In the

following discussion, the emphasis will be on crack-tip interactions with internal interfaces and second phase particles. For these highly brittle materials, fracture mechanics should be applicable with the minimum of modification though anisotropic effects tend to be more pronounced when one starts looking at structural details and the non-linear zone tends to be interpreted slightly differently.

The only equilibrium fracture resistance process in highly brittle materials is the production of surface area. Therefore, if fracture occurs so that the surface area associated with the fracture is larger than the cross sectional area associated with planar extension, the fracture resistance will be greater. The production of decohesed zones at a crack tip or simply surface roughness as the crack deviates from its original path should therefore lead to increased fracture resistance. This type of behaviour may lead to a period of slow crack growth. It is not clear, however, that a fracture mechanics determination of say K_{IC} will reflect this increased surface area problem.

The other way that the microstructure may appear to increase the fracture resistance of a material is that all stored elastic energy may not be efficiently converted into fracture surface. For example, the interaction of a crack front with a void will locally blunt the crack. Provided the void is small compared to the crack length it does not alter the stored elastic energy in the system but it does change the stress distribution in the vicinity of the crack tip. In this case, the Griffith criterion is no longer necessary and sufficient for failure ($\rho \neq a_0$) and the stored energy may have to be increased before fracture occurs. The excess energy could be dissipated as kinetic energy or

internal friction but ultimately as vibrations and heat.

Hasselmann et al [79] have discussed this problem on the basis of global and local instability. On thermodynamic grounds they identify two values of critical fracture stress. The lower value corresponds to the Griffith criterion for reversible fracture and represents the minimum stress level for slow crack growth by a reversible thermally activated process i.e. the fatigue limit. The highest stress corresponds to the stress required for irreversible catastrophic failure. This latter mechanism requires a larger expenditure of energy in excess of the surface free energy. For the stress range intermediate between these two values, the material is prone to slow crack growth even in the absence of stress corrosion. Their discussion of local instability does not rely on surface roughness or microcrack zone mechanisms but obviously such mechanisms could help to extend this region. A similar discussion has also been put forward by Bartenev [80] and Plateau [81].

Some workers prefer to use 2γ as the fracture resistance term. In this way, the Griffith criterion is retained as a conservative but safer estimate of strength and the fracture resistance term retains its identity as a material constant. For 'irreversible' failure, ~~the~~ fracture surface energy corresponds to a higher stress and extends the stress range over which the material can be used. Unfortunately, it is not clear that this parameter is a material constant and the criterion may depend on the test conditions and the particular microstructure.

2.3.1 Surface Roughness

In many materials, crack propagation does not proceed in a planar fashion. For example, in polycrystalline materials the crack may have

to tilt or twist as it follows the cleavage planes for transgranular failures. In particulate composites, the stress field around the particles may alter the crack path and lead to surface roughness. In absolute terms the increase in fracture resistance should be related to the increase in surface area. Let us consider a hypothetical material which has a plane of weakness which is oriented at some angle θ to the main crack, (Figure 18). For this two-dimensional picture the crack should tilt along the weak surface to produce surface roughness. For this problem γ is no longer isotropic. A sharp peak should occur in the $G(\theta)$ curve (Fig. 14) and it is clear that the stress needed to nucleate such a crack will depend on θ . For increasing θ , a larger stress will be needed to nucleate such a crack. Once nucleated, the crack can only grow under a mixed mode loading and should undergo some slow crack growth till it reaches its critical length. Provided the slow crack growth occurs in a small region compared to the crack length, the process should not alter the stored energy in the system so from equation (2.7)

$$K_I = K_I^{\text{app}} \cos^3 \frac{\theta}{2} \quad (2.19)$$

and
$$K_{II} = K_I^{\text{app}} \cos^2 \frac{\theta}{2} \sin \frac{\theta}{2}$$

For instability, however, it may be necessary to increase K_I^{app} but it is not clear to what value it has to be increased. The main question is whether this increase will simply reflect the increase in fracture surface area.

In polycrystalline materials the grains are crystallographically misoriented with respect to one another. A crack intersecting the boundary between two grains may either traverse the boundary, and thereby continue the propagation through the second grain with relative

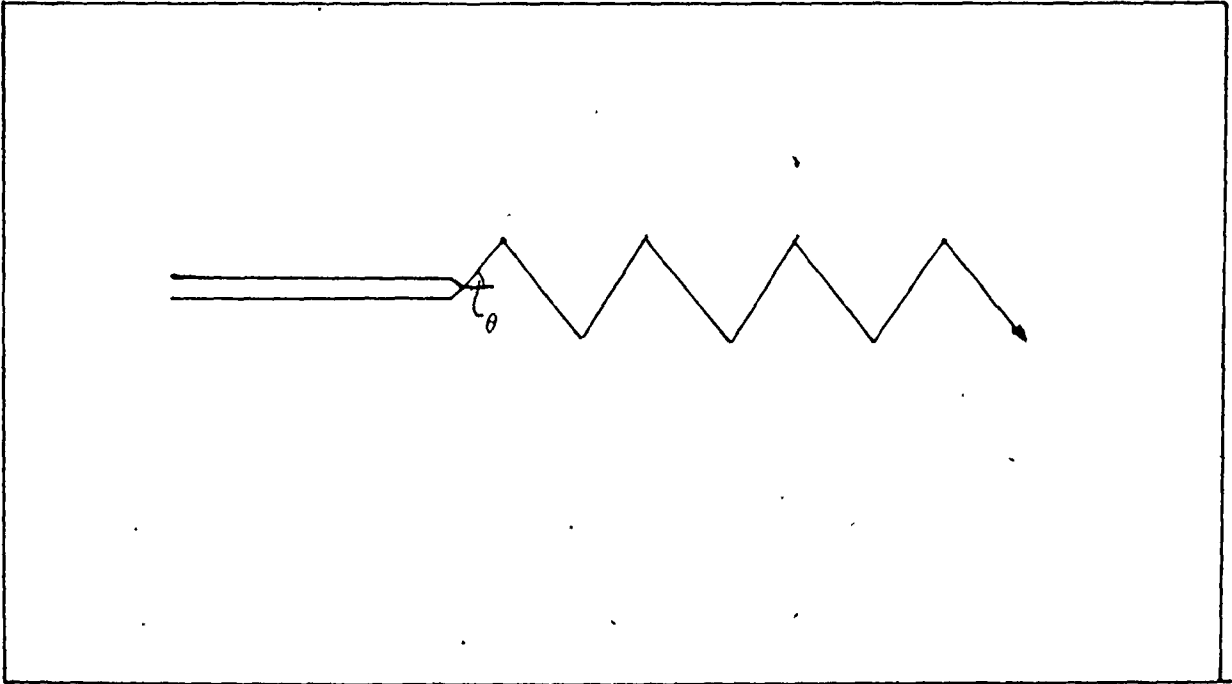


Figure 18. Hypothetical Material containing a Plane of Weakness that tilts at an angle (θ) to the Plane of the Crack.

minor adjustments to the crack plane, or follow the grain boundary itself. Two grain misorientations have an effect on the orientation of the cleavage plane, i.e., the tilt (θ) and twist (ψ) components. A tilt rotation can be accommodated by a continuous adjustment of the crack front while a twist rotation can not. In this latter case, the crack segments into partial fronts linked by cleavage steps as often observed. For transgranular failure, one can think of the process in a similar way to our hypothetical model and the process leads to an apparent increase in fracture surface energy. It is clear when referring to Figure 14 that a grain tilt misorientation of 60° is predicted to increase Γ effectively by a factor of two. A similar result would appear by just considering the increase in fracture surface area. Even this description of transgranular failure is somewhat idealized, mode II components may play a role and the geometry of a real polycrystal is more complicated. It is interesting to note that polycrystalline fracture surface energies are often an order of magnitude greater than the single crystal values. The effect of surface roughness does not explain this result.

Grain boundaries and other interfacial defects constitute locations of relative weakness in a crystal. This is particularly true in ceramic materials where the directionality and charge requirements of covalent-ionic bonds can lead to substantial reductions in the interfacial cohesion. Such interfacial weakness may be further emphasized by the presence of internal stresses due to elastic mismatch between phases, phase transformation or anisotropic thermal expansions. Cracks tend to propagate along these interfaces. In particulate composites there is a tendency for decohesion of the particles. Intergranular fracture is

often characterized by a tortuous crack path leading to greater variations in fracture energy than one would expect from transgranular failure.

For intergranular failure, the fracture energy may be written as

$$2\Gamma = 2\gamma - \gamma_i \quad (2.20)$$

where γ_i is the reversible interface energy. Note that two units of free surface are produced by the destruction of one internal interface. A series of experiments by Class and Machlin [82] on KCl bicrystals clearly demonstrated the weakening effect of grain boundaries.

Although the grain boundaries may be inherently weak in highly brittle materials, the abrupt changes in crack path at each grain will lead to a substantial reduction in the local mechanical energy release rate. In a similar way to our earlier discussion, the tortuous nature of the crack will apparently increase the fracture surface energy. This problem may be accentuated at larger grain sizes when a crack approaching an interface may lead to its decohesion. This problem has been discussed by Cook and Gordon [83] for the special case of an interface at right angles to a crack. Such a crack has been locally blunted and the local stress distribution will change. Further propagation of such a crack will require an increase in stored energy before a sufficient criterion for failure is reached. It is clear from the above discussion that the crack propagation in polycrystalline materials is a complex process involving a large number of microscopic events. The fragmented, discontinuous propagation of local segments of the crack front, secondary crack formation, the sensitivity of the interface energy to chemical effects or internal stress; the competition between intergranular and transgranular fracture at each grain; the production of surface steps; all these effects may play a role in what appears to be an intractable problem.

2.3.2 Microcrack Zones

The presence of weak interfaces has already been emphasized with respect to the microstructure of highly brittle materials. Such features may be present either in single phase (grain boundaries) or multiphase materials. From a theoretical strength viewpoint, the strength of these interfaces will be reduced by the lower surface energy of these boundaries or by the increase in 'effective bond length' across such interfaces. For some materials, these interfaces may be only partially coherent. If these interfaces are present in sufficient density, it is clear that the region ahead of a well-developed crack may consist of a decohesed zone, that will increase the fracture toughness of material if the fracture area associated with such a zone is large. Furthermore, it should lead to a period of slow crack growth as this zone develops. It is also possible that such a zone will tend to blunt the crack tip and a energetic criterion may no longer be a sufficient criterion for unstable fracture.

There has been evidence of such behaviour in many diverse materials. In polymers, the production of a crazed zone is a related mechanism. In concrete, the formation of discrete cracks ahead of the primary crack [84] has been observed. In a study of the fracture of rocks, Rosenfield et al [85] observed such behaviour and pointed out that the energy dissipated in the fracture of rocks is associated with the creation of a large amount of surface area. They also pointed out that such a microcrack zone allows one to rationalize the discrepancy between R and surface energy values, the discrepancy between measured and calculated unnotched

strength values, size effects, microstructural effects and the apparent insensitivity of R to notch root radius. In the field of ceramics, similar behaviour was observed on a calcia partially-stabilized zirconia [86, 87]. In this case, the weakness was proposed to occur at the grain boundaries as a result of the phase transformation of the pure ZrO_2 precipitated at these boundaries. Anisotropic thermal expansion in some ceramics has also been shown to lead to microcrack formation [88, 89].

More recently, Claussen et al [90, 91] have used this idea to design 'tougher' microstructures where effective use can be made of microcrack formation. The problem of decohesion has also been identified in composite materials as an important failure mechanism.

In general, evidence for microcrack zone formation is often indirect. For example, acoustic emission is often observed in highly brittle materials prior to failure. Microcracks also tend to lower the effective modulus of a material and is reflected as a non-linear compliance region in the deformation curve prior to failure [87]. Rosenfield et al [85] also shows that the permeability of rocks to epoxy resin is greater in the vicinity of the crack tip compared to the bulk material. In some cases, direct observations have been made of microcrack zones. In concrete, for example, the increased fracture surface has been shown to be 10-20 times that necessary for planar extension [84, 92].

The problem of the formation of microcrack zones is discussed more fully in Appendix A.5. The same concept can be applied to particulate

composites as the interface between the particles and the matrix may be a source of weakness. The size of the decohesed zone can be estimated if one assumes that the interface will fail when the stress normal to the interface exceeds a critical value. For the decohesion of spherical obstacles, there should always be part of the interface that is subject to the maximum normal stress so that all the particles within the zone should decohere to some extent. This approach assumes the particles are small compared to the zone size. It is possible to estimate the effect on fracture surface energy of such a zone. From a mechanistic viewpoint, the contribution to fracture surface energy for zone formation (Γ_m) would be:

$$\Gamma_m = \frac{1}{2} N_A A_{TC} (\sigma_T a_0) \quad (2.21)$$

for the two dimensional case, where A_{TC} is the area of the critical decohesed zone, N_A is the number of particles per unit area, σ_T is the stress needed to decohere the interface and a_0 is the interatomic distance. For a random distribution of uniform spheres (radius r) we have

$$N_A = \frac{3V_v}{2\pi r^2} \quad (2.22)$$

and from Appendix A.5 we have

$$A_{TC} = 1.12 \left(\frac{K_{IC}}{\sigma_T} \right)^4 \quad (2.23)$$

so that

$$\Gamma_m = 0.84 \frac{K_{IC}^4 a_0}{\pi \sigma_T^3} \left(\frac{V_v}{r^2} \right) \quad (2.24)$$

For a highly brittle composite where $K_{IC} = 1 \text{ MNm}^{-3/2}$, $\sigma_T = 10^2 \text{ MPa}$, $r = 10 \text{ } \mu\text{m}$, $a_0 = 10^{-9} \text{ m}$ and $V_v = 0.10$, the damage zone can be calculated

to be 10^{-9} m^2 . For this case, $\gamma_m = 0.3 \text{ Jm}^{-2}$, which is an order of magnitude smaller than γ for even highly brittle materials. The contribution for decohesed-zones could, however, be substantial for lower values of σ_T , i.e., a factor of 10 smaller value for σ_T leads to a 10^3 increase in γ_m in the last calculation. The value of σ_T is difficult to determine experimentally but the form of equation (2.24) is of importance, i.e.,

$$\gamma_m = M \left(\frac{V}{r^2} \right) \quad (2.25)$$

where M is a material constant. It should be noted that decohesed particles also reduce the matrix fracture surface area so that approximately

$$\gamma = \gamma_0 (1 - V_V) + M \left(\frac{V}{r^2} \right) \quad (2.26)$$

where γ_0 is the matrix fracture surface energy. Evidence for this decohesion has been put forward by Broutman and Sahu [93] for epoxy-glass particulate composites using a water absorption technique.

From this discussion, it is clear that the formation of a decohesed zone in brittle materials could be a useful way to increase the toughness of a material. It should be stressed that this does not imply an increase in strength, as weak interfaces are likely sites for crack nucleation. It is also possible that energy could be consumed by crack sliding and frictional effects and that the damage zone could lead to crack blunting as it relaxes the stresses at the crack tip.

2.3.3 Fracture Surface Steps

Fractographic observations often lead to vital information about a crack's history, in particular such observations may give visual

evidence of the microscopic energy absorption processes. The fracture surface step is one of the most prevalent features in brittle failures. Its occurrence is often linked to a local disturbance in the crack front which forces the crack to segment onto different planes. For example, it has already been noted that as a crack crosses a twist grain boundary that steps will form between the segmented crack front. Interactions with dislocations and other defects can also lead to step formation [94]. In particular, the interaction between a crack and a second phase particle or a void often leaves a fracture surface step at the rear of the particle. In this case, the crack segments in order to bypass the obstacle but during the interaction with the stress field of the obstacle the two secondary cracks adjust their plane so that when they reach the rear of the particle they are non-coplanar. The partial fronts merge after a short distance from the particle and the step is formed by a secondary fracture, leaving a fracture "tail" at the rear of the particle. A mode III shear disturbance can also lead to step formation (fracture lances). Other mechanisms of step formation are crack bifurcation, the coalescence of small cracks from non-coplanar source and stress wave interactions.

Once formed the individual steps can interact with their neighbours. The interactions can either reinforce or annihilate each other. The commonly observed 'river patterns' associated with cleavage fracture are a result of this interaction. For particulate composites the step often disappears shortly after leaving the particle but at high volume percent, interaction with another obstacle may occur before the annihilation can take place.

The mechanism of step separation is important too, as the local stresses will have to extra work near the vicinity of the step, if only to create additional surface area. The step is expected to locally retard the advance of the crack acting like an obstacle to crack propagation [94]. The link up of partial fronts will occur behind and transverse to the line of the crack front. In this way, the unbroken steps may act as ligaments behind the main crack front. Swain et al [95] considered the stress intensity between the opposing, adjacent cracks. Their theoretical considerations showed that there is considerable attraction between the two partial segments but in such a way that crack overlap is likely. [Appendix A.3]. This overlap produces a connecting sliver of material which can lead to step discontinuity if the base fracture is deflected from one side of the sliver to the other or in some cases the sliver may fracture at both ends leaving it as surface debris. The geometry of the step would be expected to be curved for non-crystalline material, where the crack path will be influenced by the shear stresses. For crystallographic materials the fracture surface steps appear more abrupt. In his study of fracture lances in glass Sommer [68] made a careful geometric profile of the step using interference microscopy. Figure 19 shows the cross-section profile of such a step. The formation of the steps has been discussed previously [95-97] and is in agreement with the overlap mechanism.

The increase in γ associated with step formation in a highly brittle solid will clearly depend on the additional surface area created. Ahlquist [98] has suggested that the increase in fracture surface energy in void-dispersed MgO compared to void-free MgO could be a result of the work done to create the fracture steps. The estimated work done

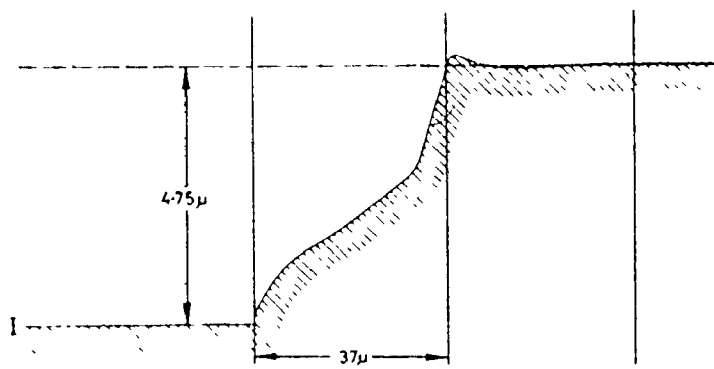


Figure 19. Cross-section Profile of a Lance Step as found by Optical Interference Measurements. (After Sommer (68))

(γ_s) is

$$\gamma_s = 1/2 \tau \left(\frac{h}{s}\right)h \quad (2.27)$$

where τ is the shear stress acting during step formation, h is the height of the step and s is the step spacing. Therefore the force per unit area of crack surface is $\tau(h/s)$ and he assumes the displacement is h . For a highly brittle material we expect τ to be the theoretical shear strength. On this basis and comparison with his experimental results Ahlquist believes the increase in toughness is related to the work done in step formation. It is not clear, however, that the displacement needed from the step should be h . In reality the displacement necessary for fracture is more like the interatomic spacing as illustrated in Figure 20. For example, substituting values into equation (2.27) of $\tau = 10^4$ MPa, $h = 20 \mu\text{m}$ and $s = 100 \mu\text{m}$ (typical values for a glass/particle composite) an unreasonable value of $\gamma_s = 200 \text{ Jm}^{-2}$ is obtained as it is a few orders of magnitude greater than γ_0 . On the other hand substitution of a value for the displacement (d_0) of the interatomic spacing would give

$$\gamma_s = 1/2 \tau \left(\frac{h}{s}\right) d_0 \quad (2.28)$$

With a value of $d_0 = 10^{-9} \text{ m}$ we now have $\gamma_s = 1 \text{ Jm}^{-2}$, which is now less than the fracture surface energy glass but is more consistent with the increase in fracture surface associated with such fracture steps. The production of fracture surface steps will increase a material's resistance to fracture but it is unlikely unless there is extensive undercutting that the variation will be greater than a factor of two.

2.3.4 Crack Blunting

As previously mentioned, a crack front will be blunted locally when

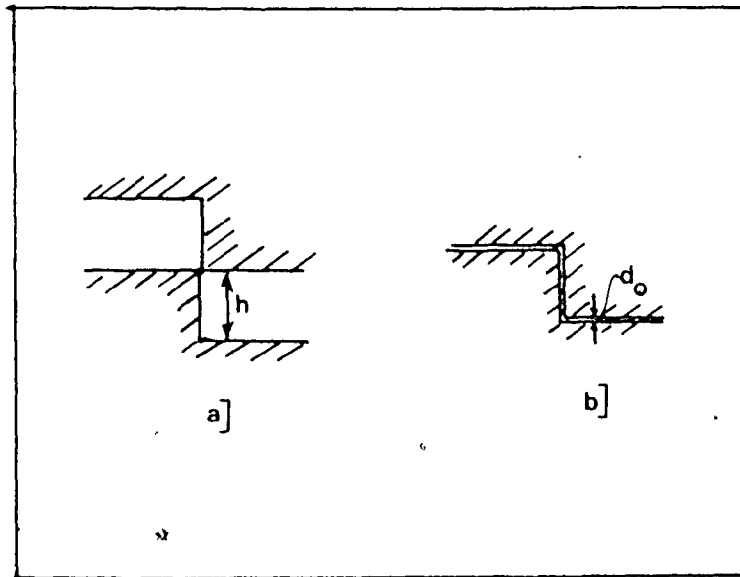


Figure 20. Displacement needed for Step Separation as suggested
a) by Ahlquist (98) b) in the Present Work.

it intersects a void. Such a process will alter the local stress distribution ahead of the void. Considering a through-the-thickness crack of length c (Figure 21a) which is blunted by drilling a hole, radius ρ at the crack tip, from the work of Inglis [60] it can be shown that if one approximates the crack configuration to an elliptical hole (tip radius ρ) the increase in elastic strain energy due to the hole is given by

$$\Delta U_E = \frac{\pi \sigma^2 A}{E} (a^2 + b^2) \quad (2.29)$$

For $\rho \ll a$ this approximates to

$$\Delta U_E \approx \frac{\pi \sigma^2 A}{E} (a^2 + a\rho) \approx \frac{\pi \sigma^2 A a^2}{E} \quad (2.30)$$

and there is no difference between this expression and the one used by Griffith i.e. the system is insensitive to the presence of the hole. Indeed, Berry [99] has shown that in terms of a energy criterion the value of the critical applied stress changes by only 1% over the range $b/a = 0 - 0.16$. In terms of a limiting stress concept, however, we have

$$\sigma_f = \sigma_g \left(\frac{\rho}{3a_0} \right)^{1/2} \quad (2.31)$$

This argument was used by Orowan [62] in an attempt to show the equivalence of the two approaches. Unfortunately as $\rho \rightarrow 3a_0$ the Inglis solution must become invalid. For this case, the solution may be reasonable and using a value $\rho = 3 \times 10^4 a_0$, $\sigma_f = 100 \sigma_g$ is obtained and the energy criterion is no longer sufficient. A much higher stress must be applied to the body so leading to a higher value of critical stress intensity. The drilling experiment was hypothetical. A more realistic process may be the interaction of a crack with a series of voids. (Figure 21b). In this

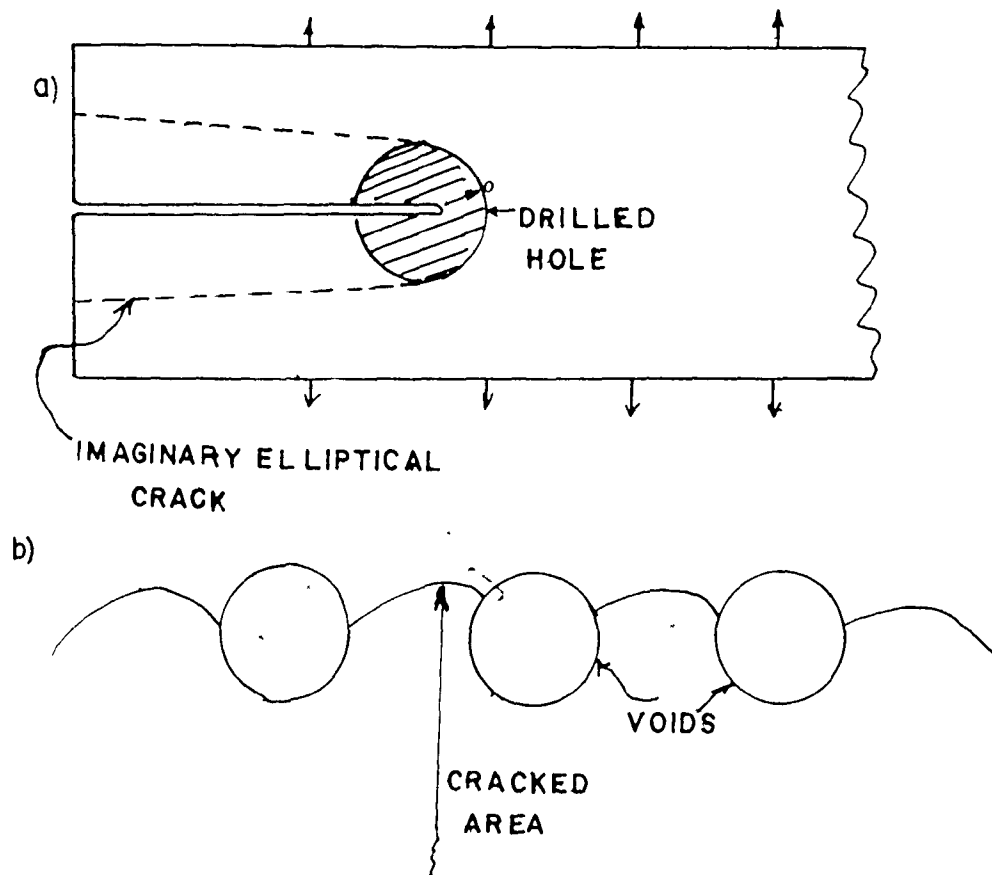


Figure 21. a) Blunting of a Sharp Crack by drilling a Hole, Radius ρ at Crack Tip. The Approximation of the Configuration to an Elliptical Hole is shown by the Broken Lines

b) Interaction of a Crack Front with a Series of Voids.

situation, it is less clear whether an energy criterion will be necessary and sufficient.

Neuber [100] found in his approach to sharp notches ($\rho \rightarrow 0$) the elastic stress concentration factor would tend to infinity as continuum theory is no longer valid. To resolve this problem, Neuber introduces the concept of a small but finite particle (dimension η) at the notch root. This particle is small enough to justify the assumption of constant stresses at its bounding surfaces. Since η must be assumed to be a material constant it follows that the elastic stress concentration even for a sharp crack remains finite. The elastic stress concentration factor for a typical Griffith crack is therefore given by

$$K_t = 1 + 2\left(\frac{c}{2\eta}\right)^{1/2} \quad (2.32)$$

Although this procedure is similar to arguments used for the plasticity correction, an interpretation of η as characteristic of a given materials capacity to resolve a stress gradient is more appropriate. In some recent work Pabst [101] has determined η to be $\approx 25\mu\text{m}$ for high alumina ceramics, so it appears that the finite structure of grains, grain boundaries, pores etc., there is a finite limit below which it is unrealistic to extrapolate the notch tip radius.

2.3.5 Brittle Particulate Composites

For a simple model system where particles are dispersed in a glass matrix it has been observed that the dispersion increases the fracture surface energy of the system. Several mechanisms could be involved with this increase in toughness.

First, plastic deformation may occur in the particles [102] or be enhanced by the stress concentration produced by the particle [103] in the matrix. The other mechanisms of surface roughness, step formation, decohesed zone and crack blunting (particle decohesion) are all relevant to such composite systems. Another mechanism, based on fractographic evidence, is that there is a tendency for the crack front to change its shape in the vicinity of a second phase particle. The shape change may be a result of an increase in the elastic strain energy of the body as the crack front circumvents the particle especially if the particles act to momentarily pin the crack front. This approach, as initially conceived by Lange [104] is analogous to the line tension concepts used in dislocation theory which has been used with great success to model the increase in yield strength observed in dispersion-strengthened alloys. The pinning of a dislocation by a particle is shown in Figure 22 as it is reflected by surface steps.

For crack-particle interactions, changes in crack shape have been generally deduced from the topography of fracture surfaces. Figures 23 and 24 show the interaction of a {100} cleavage crack in pressurized voids in single crystal MgO [105]. During cleavage fracture, steps often form on the fracture surface (see section 2.3.1) which coalesce to give the familiar 'river' patterns. These steps form perpendicular to the crack motion and the position of the crack front can therefore be traced as it interacts with the particles. This process was illustrated in Figure 23. It is worth noting that a change in crack shape would be expected during the formation of the fracture surface steps [97]. Figure 25 shows a similar behaviour around a void in single crystal NaCl.



Figure 22. An Avalanche of Dislocations stopped by an Inclusion
(Fraser, M. J., Caplan, D., and Burr, A. A., *Acta Met.*,
4 (1956) 194)



Figure 23. Cleavage Step Pattern on a $\{100\}$ MgO Fracture Surface when Crack interacts with a Void. Three positions of the Crack Front are illustrated by Broken Lines. (From Lange (104))

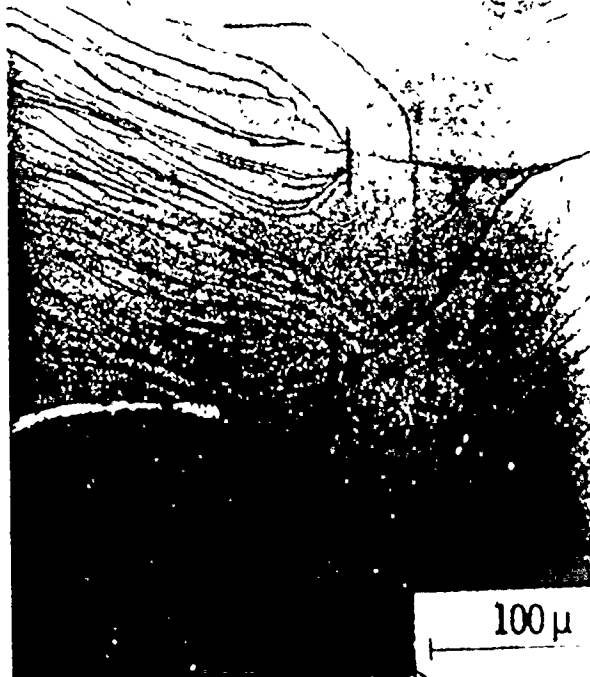


Figure 24. Cleavage Step Pattern formed between Two Voids on $\{100\}$ MgO Fracture Surface. Micrograph shows Crack Front changes Curvature as It moves between the Voids. The Crack moved to right

Ahluquist [98] has made similar observations for the interaction of {100} cleavage cracks in LiF and MgO single crystals containing hard and soft second phase particles.

In conchoidal fractures, the progressive motion of the crack is not so easily traced. Occasionally, however, as the crack interacts with the stress field of an inhomogeneity, the plane of the fracture changes and leaves a mark on the fracture surface. These features are known as 'gull-wings' and an example is shown in Figure 26 where a crack front in glass has passed through a void [106]. In all these figures a fracture surface step forms at the rear of the particle as discussed earlier. These steps indicate that the segmented cracks which bow between the particles change plane during the process and necessitate a secondary fracture to complete failure. These steps and the change in crack shape is generally taken as evidence of crack pinning. This may not always be the case, especially if the particle interface fails. In this case there may be a change in crack shape but the crack is not necessarily pinned at the front of the particle. This point tends to be overlooked but is quite clear in the experimental results of this thesis. Other observations of these fracture surface steps are shown in Figure 27 and 28 from a fracture surface of a $\text{Li}_2\text{O} - \text{CaO} - \text{TiO}_2 - \text{SiO}_2$ glass containing immiscible spheres [107]. The lines on Figure 28 were drawn to represent the successive crack front positions. Observations of crack bowing have also been made in fibre composites [108] and Figures 29 and 30 show these observations.

The most convincing evidence for the change a crack shape is shown in Figures 31 and 32 where the position of the crack front has been im-



Figure 25. Cleavage Step Pattern around Void In NaCl. (After Bethge)

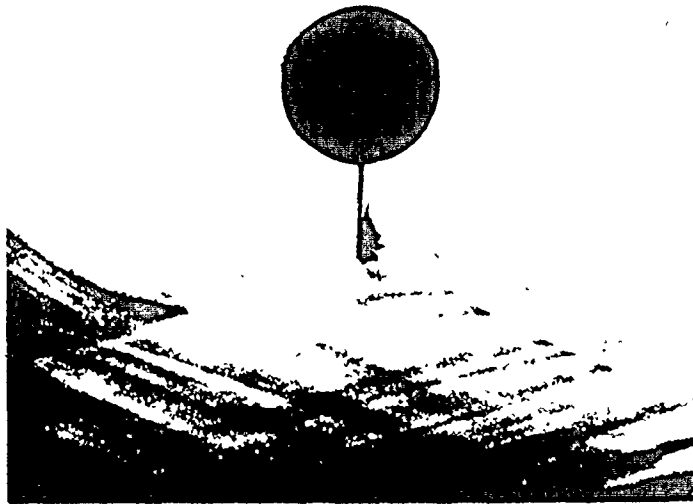


Figure 26. Intersection of a Bubble in Glass by Crack Front and generating a Fracture Surface Step and Full Gull Wings Fracture moved from Top down. (70x)



Figure 27. Interaction of a Matrix Crack with a Row of 0.8mm Fibres.
The Crack moved from Top down.

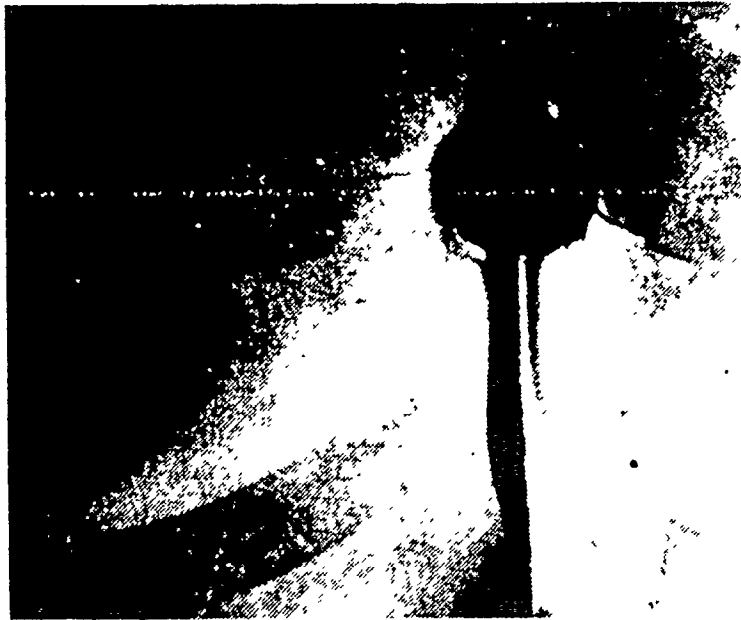


Figure 28. Fractograph showing Interaction of Slowly Propagating
Crack with an Isolated Fibre. The Crack moved from Top down.



Figure 29. Fracture Surface of $\text{Li}_2\text{O}-\text{CaO}-\text{TiO}_2-\text{SiO}_2$ Immiscible Glass showing Adhering Droplets, Complementary Holes and Split Droplets.

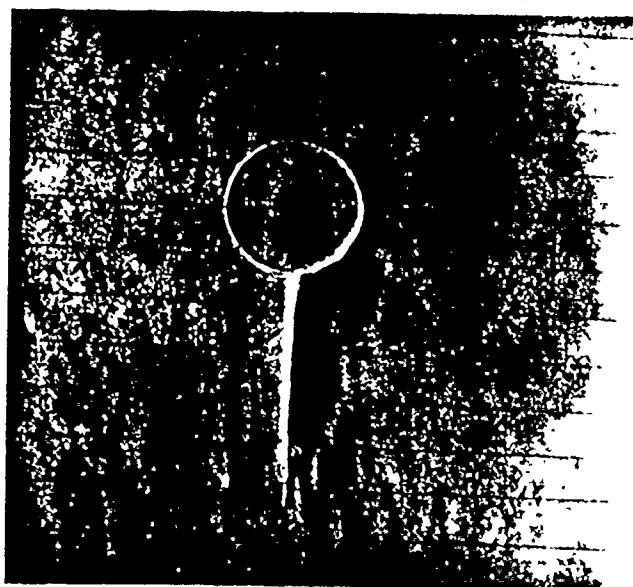


Figure 30. Model showing Crack Propagation Fronts around Immiscible Glass Droplet. Crack moved from Top down.

printed onto the fracture surface by an ultrasonic modulation technique. This technique has been used mainly to determine fracture velocities but it can also generate important evidence about crack shape. To the author's knowledge this technique has not been used expressively for determination of crack front shapes. Figure 31 shows the interaction of a crack front in glass with a capillary tube [109]. The motion of the crack is from top to bottom. It is clear that there is an attraction of the crack to the void in its approach. This attraction is a result of the interaction of the crack front with the stress field around the void which was discussed in section 2.2.4 and is basically a result of the decrease in local elastic strain energy associated with the void. The capillary is then seen to impede the crack motion so that the two segments bow as they bypass the void. Finally the crack breaks away at a high local velocity, leaving a step at the rear of the tube. It is clear in this figure that the crack front is not pinned by the obstacle but the tube does impede the local motion of the crack. Figure 32 shows a fracture surface in a glass containing a crystalline phase (CaF_2). The motion of the crack here is from bottom to top. The crack is repelled locally by the particle in its approach as a result of the presence of a 'hard' particle. The crack front here is pinned for a short time at the front of the particle but before the segmented cracks bow to circumvent the particle in a bypass mechanism, the particle fractures and the crack front is no longer pinned or impeded.

Crack-particle interactions will only take place if the crack path is intersected by a particle. The crack front is attracted or repelled by the stress field round an inclusion depending on whether

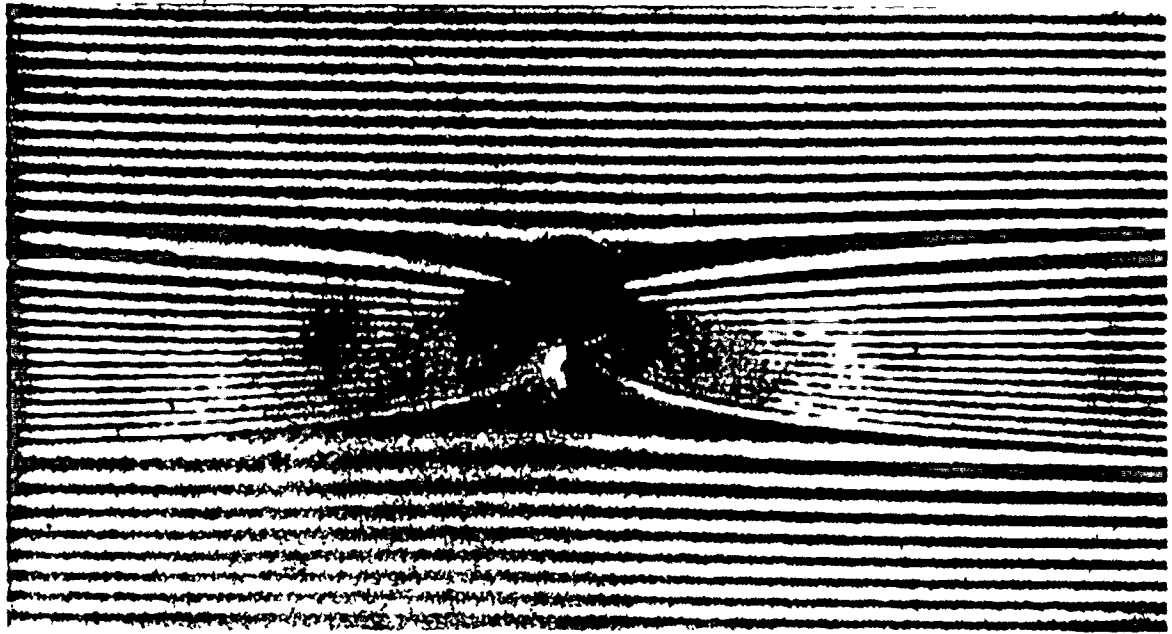


Figure 31. Ultrasonically-modulated Fracture Surface in the Neighbourhood of a Normal Capillary Tube (diameter 0.065mm). The Crack moved from Top to Bottom. The Average Crack Speed was 60 m/s. During the Interaction the Crack slows down to 20 m/s and then breaks away at 150 m/s.

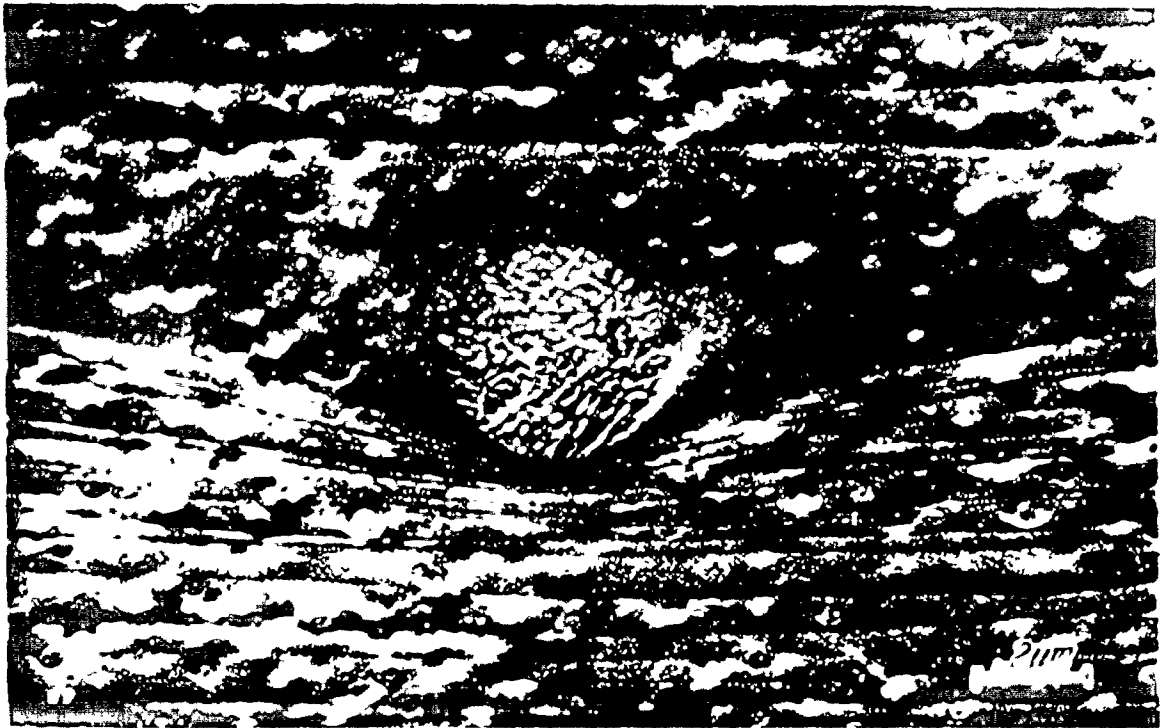


Figure 32. Electron Fractograph of Ultrasonically-modulated Fracture Surface in Neighbourhood of an Inclusion in Opal Glass. The Crack moved from the Bottom up. As the Crack approaches the Inclusion the crack slows from 0.7 m/s to 0.1 m/s and then breaks away at 5 m/s. (US frequency 1MHz)

the particle is softer or harder than the matrix. A similar effect can be found as a result of internal stress. In their work on glass/particle composites Davidge and Green [110] found that for composites with a thermal coefficient of expansion of the matrix less than that of the particle, the crack would avoid the particles while it would intersect particles (softer than matrix) when the expansion coefficients were the same. Presumably in a matrix where preferred cleavage planes exist, a crack may have difficulty in avoiding a hard particle.

(i) Lange's Model

With the fractographic evidence of crack shape changes and based on the assumption that a crack front has a line energy, Lange [111] developed a model that suggested that the increase in crack length as the crack changes its shape could contribute significantly to the fracture energy of brittle, dispersed-phase composites. The idea of line energy for cracks was originally advanced by Friedel [94] who was considering the brittle elastic crack as a piled-up group of climbing dislocations with particular reference to the formation of cleavage steps. Since that time, the concept of a crack as a dislocation pile-up has been developed extensively. Unfortunately, it is not clear that the concept of line energy can be so developed. Lange restates the Friedel approach by associating the increased strain energy due to the crack with just the crack periphery. This idea is reasonable for a dislocation with its $1/r$ dependant stress field. For a crack, however, the stress field depends on $(1/r)^{1/2}$ and it is no longer clear that one can integrate this to produce a unique line tension. In a recent review, Thomson [112] points this out and states that the tension depends critically on the crack shape. Therefore, although the line tension concept of

a dislocation has been successful in modelling the behaviour of dispersion-strengthened alloys, the analogous crack line tension needs more study before it should be applied to interpreting the fracture resistance of particulate composites.

Lange's model is shown in Figure 33, where a portion of a crack front is interacting with a linear array of equally spaced pinning positions. Prior to stressing the crack front is straight. As the applied stress increases, the crack front bows between the particles and increases its length. With the assumption of line energy, this increase in length can be related to the increase in elastic strain energy. The expression for fracture energy of this system should therefore contain two terms; one defining the energy needed to increase the crack length and the other defining the energy to form new fracture surface. The contribution of the second term depends on the amount of bowing that occurs between the pinning positions before the crack breaks away and the magnitude of the crack line tension T . Based on the assumption that the pinning positions were dimensionless points and the breakaway position occurs when the crack front is semicircular, Lange derived geometrically the following expression for the fracture surface energy of the composite,

$$\gamma = \gamma_0 + \left(\frac{T}{d}\right) \quad (2.33)$$

To determine the validity of his model Lange [9] investigated the fracture energy of a glass - Al_2O_3 composite system and his results are shown in Figure 34 for three different size dispersions. The inter-particle spacing is taken as the mean free path. The experimental results verify the $1/d$ relationship but unfortunately it appears that the increase

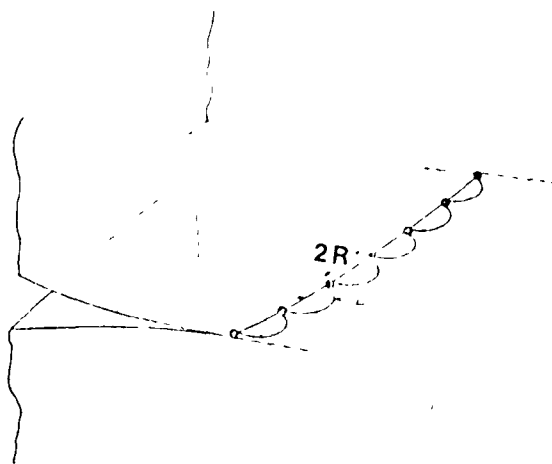


Figure 33. Model used by Lange to represent the Interaction of a Crack with a Linear Array of Dispersed, Dimensionless Inhomogeneities equally spaced by a Distance $2R$. The Straight Line illustrates the Crack Front prior to stressing. The Bowed Position shows the Situation just prior to Breakaway and Fracture.

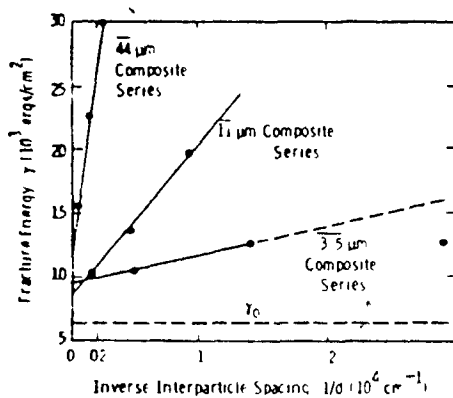


Figure 34. Fracture Surface Energy versus the Inverse of Mean Free Path for a Sodium Borosilicate Glass containing 3 Size Dispersions (3.5, 11, & 44 μm) of Al_2O_3 . γ_0 is the Fracture Surface Energy of the Glass without the Dispersed Phase.

in fracture surface energy also depends on the particle size. This effect is not predicted by Lange's model which we would expect a linear plot which is independent of particle size (slope T). To overcome this difficulty, Lange further postulated that the size of the particle may control its pinning ability. That is, for small particles, the overlapping stress field of two bowing segments will be greater and the change in crack shape will not be so great. This idea is appealing but crack interactions [113] also depend on the interparticle spacing such that the effect of decreasing the particle size at a given volume fraction is simply balanced by the increase in interparticle spacing. Lange estimated a value of the line tension of a semicircular crack by dividing the elastic strain energy associated with a semicircular crack by its crack length and obtained a value [111]

$$T = 2/3\gamma_0 d \quad (2.34)$$

A similar estimate was also put forward by Thomson [112] ($T = \gamma_0 d$). Many other investigators have found a similar $1/d$ relationship in their fracture surface energy results, though often the data tends to pass through a maximum. Lange [114] suggests that these maxima are caused by an ineffective interaction with the particles when they become closely spaced. The composite starts to appear as a continuum and the crack front no longer interacts with discrete particles. Broutman and Sahu [93] in using this idea for their polymer/glass composites suggested that decohesion of the particles may also be important and found that poor interfacial bonding led to higher fracture surface energies as a result of a decohesion zone around the crack tip. Lange [9] suggests that surface roughness also plays a role in the fracture of these composites. This effect will show up as an increase in the intercept value

of fracture energy when plotted against $1/d$. For his glass - Al_2O_3 composites, the surface roughness effect is observed to increase the fracture energy for the glass by a factor of 1.5 - 2.0.

Other criticism of Lange's model are

- (i) It is not clear that the breakaway crack shape should be semi-circular. At high volume fractures the bowing process may be incomplete before another particle is intersected.
- (ii) The interpretation of the interparticle spacing as a mean free path seems doubtful. Certainly for a linear array of particles, the mean free path may seem correct but for a real situation where the crack front is non-linear and, where the obstacles are not necessarily in a straight line, the interparticle spacing is often much less than the mean free path. In the same way the average distance between nearest-neighbours is also incorrect and underestimates the interparticle spacing. It is clear that the interpretation of interparticle spacing needs to be more carefully considered and probably an approach like Kocks [53] or Foreman & Makin [54] would be more reasonable. (section 1.4.5).

Another problem in relating a linear model to the microstructural parameters lies in the statistically variation of interparticle spacing. For example, if there is a tendency for interparticle contact in a system (agglomeration) this can lead to pronounced variations in the interparticle spacing and particle agglomerates may effectively increase the average particle size, leading to regions of much higher fracture resistance.

- (iii) The effect of the stress field of the particle is ignored and changes in the crack shape as a result of this interaction are not included in the Lange model, e.g., a crack also changes its shape as it approaches the particle (Figures 31 and 32).
- (iv) The particles themselves must make some contribution to the fracture resistance and mechanism of particle cleavage or interfacial decohesion should be included in an understanding of the fracture of such composites. The problem of particle decohesion is often overlooked and it may be that in many systems, the crack front is interacting with a void rather than a well-bonded second phase particle. It was emphasized earlier that in many brittle systems interfaces can be a source of inherent weakness.
- (v) The problem of crack path is not dealt with and as indicated earlier there is a tendency for a crack front to avoid "hard" well-bonded particles especially in a glass matrix system. For example, in Lange's glass - Al_2O_3 system the particles (Al_2O_3) have a higher elastic modulus than the glass and yet in his fractographic observations the crack front has interacted with the particles and not avoided them. These crack path considerations will be modified by the presence of a weakly-bonded interface, internal stresses and preferred cleavage planes.
- (vi) Finally, the fracture step at the rear of the particle may also make a contribution to the fracture resistance. It is not clear when these steps form; they could, for example, be left as ligaments behind the crack front. From an earlier discussion on fracture steps and decohesion zones it was indicated that these processes may also be dependant on the interparticle spacing.

A summary of fracture surface energy results is given in Appendix A.6 for several brittle particulate composites.

(ii) Evans's Model

Evans [113] has taken a fracture mechanical approach to the line tension problem. The approach considers a linear array of impenetrable obstacles and Evans computes the elastic stored energy associated with different crack shape configurations and in particular compares the stress to move secondary cracks between the obstacles (σ_A) with the stress to move the primary crack (σ_C). For a 'line tension' contribution to strength, the stress to move the secondary cracks must be greater than the stress to move the primary crack. The analysis does not depend on the line energy concept but it does show that the line tension can vary quite considerably. The model used by Evans is illustrated in Figure 35 and three situations are analyzed, where the secondary cracks are

- (i) Semi-circular and non-interacting
- (ii) Semi-elliptical and non-interacting
- (iii) Semi-elliptical and interacting

For his calculations, Evans states that the maximum stress position occurs as the secondary cracks break away from the obstacles ($x' = 2r_0$). There appears to be no justification for this idea and indeed may depend on obstacle shape, a problem which is glossed over by Evans except in his discussion about crack interactions. The work of Evans is extremely relevant here as he shows that an increase in fracture toughness can occur in systems where the crack is pinned ($x' = (\text{constant})r_0$) provided the primary crack length is much greater than C and is a function of

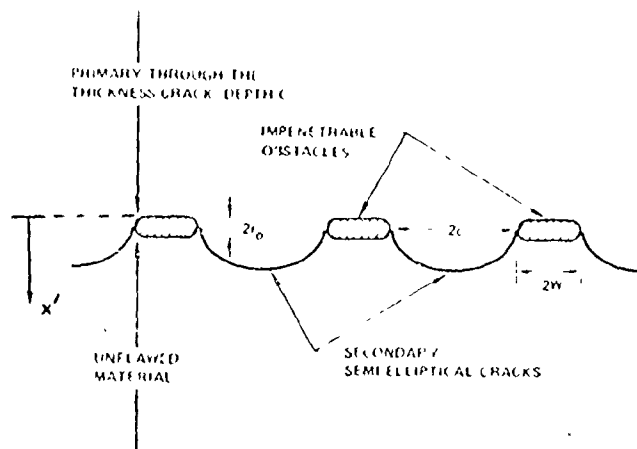


Figure 35. Model used by Evans to represent Interaction of Crack Front with a Linear Array of Impenetrable Obstacles by considering the Motion of Secondary Semi-elliptical Flaws in the Stress Field of the Primary Crack.

(r_0/C) . In his work, he also predicts the crack shape at breakaway as a function of (r_0/C) and indicates that the line tension (T) is not a constant. This has been re-analysed and is presented as Appendix A.7.

Some slightly different conclusions were reached by this author, i.e.,

- (i) The increase in toughness may be greater than that predicted by Evans but will be dependant on obstacle shape.
- (ii) The shape of the semi-elliptical cracks at breakaway are always less eccentric than semi-circular (i.e. $a < c$). In this sense, the semi-circular crack shape only occurs as the interparticle spacing $2C$ goes to zero. In his work, Evans shows that elliptical cracks with a major axis greater than half the interparticle spacing can occur. As an elliptical crack grows to be semi-circular under a uniform tensile stress, the stress intensity will be then approximately constant along its length [204] and further growth should occur with the crack remaining semi-circular. In the model, the stresses drop off more rapidly and even the semicircular condition will be unlikely.
- (iii) For non-interacting semi-elliptical cracks, Evans shows an asymptote for $C/r_0 \rightarrow \infty$ of $\sigma_A/\sigma_C = 1.21$ which does not agree with the limiting solution one would expect. In the appendix (A.5) a value of $\sigma_A/\sigma_C \approx 1.0$ is calculated and this appears more logical since for infinitely-spaced obstacles we would expect no increase in the fracture resistance.
- (iv) In the crack interaction discussion, Evans assumes the secondary cracks are coplanar as they break away whereas as we have discussed previously the segmented cracks are generally non-coplanar and must form a fracture step at the rear of the particle. For

this reason, the crack interaction term may not be as strong as Evans suggests.

There are other criticisms of the Evans' model and are similar to those discussed earlier with respect to the Lange model. For example, the effect of the obstacle's elastic stress field, the interpretations of and variations in the interparticle spacing, the obstacle failure mechanisms, the crack path problem and the role of the fracture steps are not discussed. In the interpretation of his model, Evans also uses the mean free path concept to describe his interparticle spacing and his comparison with previous experimental result is only fair. For a different interpretation of interparticle spacing, the agreement with experimental results is much worse and overestimates the observed increases in fracture surface energies. It is possible that this model may be more applicable to systems where the interfacial bond between the matrix and the particle is very strong, such as glass-ceramics. In a recent paper, Evans [205] has extended his ideas on crack shape for a discussion of slow crack growth and acoustic emission.

For a crack front interaction with an array of voids, the crack front can change its shape though not pinned by an obstacle. In terms of the Evans model pinning can be 'defined' by $x' > 0$. That is, if the primary crack front moves with the origin of the secondary crack, the crack front is not pinned. In the Appendix A.7 it is shown that as r_0/C goes to zero, the value of $\sigma_A/\sigma_C \approx 1.30$ for semi-circular non-interacting secondary cracks. In this sense, r_0 is a function of x' and is therefore an indication of the pinning. When one extends this to deal with semi-elliptical cracks one finds $\sigma_A/\sigma_C \approx 1.0$ for $r_0/C = 0$

and the crack front is predicted to remain straight. Therefore, the Evans' model predicts no increase in fracture surface energy for interaction of a crack front with a series of voids but it also predicts no shape change. This latter prediction would seem to be in disagreement with fractographic observations.

In this discussion, the work of Lange and Evans shows that a well-bonded array of second phase particles which are directly intersected (attractive field) by a crack front can lead to an increase in fracture surface energy provided the front is pinned by the particles. In favourable cases, a toughening of $\gamma = 10\gamma_0$ may be obtained, though it appears that the particles are often penetrated before these values are reached with the particle failing by decohesion or fracture. If crack shape is found to be an important parameter in the description of the fracture of brittle materials, it is clear that many situations, where the crack resistance force varies over a fracture surface, could depend on these crack shape considerations. Indeed, in Evans later paper [205] he considers the shape variation in a crystal cleavage process for a polycrystalline material undergoing slow crack growth. In metal-fibre composites, Antolovich et al [206] have postulated that crack shape may be important. Their model assumes decohesion of the fibres so the crack front is interacting with a series of cylindrical voids. Their expression for the increase in toughness is

$$\gamma = \gamma_0 \left(\frac{\pi C}{2d} \right) \quad (2.35)$$

From the microstructural considerations, it appears there are a variety of processes, that may occur in the fracture of highly brittle

materials. For particulate composites, processes such as surface roughness, obstacle decohesion, fracture surface step formation, crack blunting and changes in crack shape may all be of importance. The magnitude of the effects have been estimated either in this work or previously. A summary is shown in Table 11 for the case where the contribution to $\bar{\gamma}$ of the obstacles is ignored (e.g. voids).

The work of Evans [113] and Lange [9, 111, 114] are particularly relevant to this work but appear to be incomplete in many details. There is clearly a need for further theoretical and experimental work. In particular, the measurement of crack shape changes are necessary to clarify many of the ideas before the theoretical work can be extended.

TABLE 11. Energy Absorbing Mechanisms in Particulate Composites.
(Non-Bonded Particles or Voids)

MECHANISM	CONTRIBUTION	
Surface Roughness	$\Gamma_c = \Gamma_o \left(\frac{A_t}{A_o} \right)$	$\left\{ \begin{array}{l} A_t = \text{True Surface Area} \\ A_o = \text{Planar Surface Area} \end{array} \right.$
Fracture Surface Steps	$\Gamma_c = \Gamma_o(1 - V_v) + S \left(\frac{h}{d_c} \right)$	$\left\{ \begin{array}{l} S = \text{Constant} \\ h = \text{Step Height} \end{array} \right.$
Decohesion of Particles	$\Gamma_c = \Gamma_o(1 - V_v) + \frac{M}{(d_c)^2}$	$M = \text{Constant}$
Crack Shape a) Lange	$\Gamma_c = \Gamma_o + \frac{T}{d}$	$T = \text{Crack Line Tension}$
b) Evans	$\Gamma_c = F(r'/d)$	$\left\{ \begin{array}{l} F() \text{ is a Function} \\ r' \text{ is the amount of pinning} \end{array} \right.$

Note. d = interparticle spacing (edge-to-edge)
 d_c = interparticle spacing (centre-to-centre)
 Γ_c = fracture surface energy of the composite
 Γ_o = fracture surface energy of the matrix

CHAPTER 3

THEORETICAL ASPECTS OF THE EXPERIMENTAL PROCEDURE

In studies of the fracture of materials, a philosophical framework must be used in order to determine the strength-controlling parameters. For this work on a highly brittle material, the approach chosen was based on the original Griffith approach where strength (σ_f) is controlled by the fracture surface energy (γ), the Young's modulus (E) and the size of the flaw which produces the failure (see equation (2.4)). There is also a need to relate these parameters to the structure of the material being studied, i.e., a model glass-particulate composite. In this work, the emphasis is placed on understanding the structural relationships with regard to the fracture surface energy. For this approach, it is necessary to understand the energy absorbing mechanisms which are available to the composite. Information on these mechanisms is deduced from fractographic observations and, in particular, the technique of ultrasonic fractography. This technique has been used previously for crack velocity determinations by producing ripples on a fracture surface at a known frequency. It is clear that this technique also supplies information on the crack shape and therefore gives an indication of the amount of stored elastic energy needed to fracture a particulate composite and hence be related to the fracture surface energy. To the author's knowledge, this is the only technique for the precise study of crack shapes. As such, it could be used in situations where a crack front suffers variations in the crack resistance force which induces the change in crack shape.

In this chapter, the strength-controlling parameters and their measurements will be discussed together with an outline of the theoretical aspects associated with these parameters. This theory is compared with work on other brittle particulate composites. Finally, the technique of ultrasonic fractography is discussed.

3.1 Determination of Young's Modulus

Elastic constants appear in the expression for the strain energy release rate for an advancing crack and hence form part of a fracture criterion which is based on energy considerations. Elastic moduli were originally determined by static tests in which relatively large loads are applied to a sample and the resulting deflection measured. The static tests are less accurate than dynamic tests but are still of great engineering importance. The dynamic tests are of two types: the measurement of the wave propagation velocity and the measurement of the resonant frequency.

3.1.1 Measurement Techniques

(i) Wave Propagation Velocity

This technique has been highly refined over the last thirty years as the result of good MHz oscilloscopes and other associated electronic apparatus. A piezoelectric generator is attached onto a flat face of the specimen to excite sound waves and the transit time to a flat and parallel opposite face is measured. The transit time may be either the time to reach the opposite face where a receiver crystal is placed or the time for a reflected pulse to return to the original surface. The

Ultrasonic pulse is generally high frequency (~2MHz) to reduce attenuation of the elastic wave by scattering and non-linear effects. The velocity of longitudinal waves (v_l) in an isotropic medium is given by [115]

$$v_l = \sqrt{\frac{E}{\rho}} \quad \text{for thin rods} \quad (3.1)$$

and

$$v_l = \sqrt{\frac{E(1-\nu)}{\rho(1+\nu)(1-2\nu)}} \quad \text{for large samples} \quad (3.2)$$

The transition between these two values is not continuous and involves surface waves. The former equation is correct when the wavelength of the pulse is large compared to the diameter of the rod (or other suitable dimension). Modern high precision methods are capable of velocity determination within 0.3%. There is often a discrepancy between static and dynamic determinations of E which could be the result of the different stress levels or the different effects of defects such as cracks or pores for each method.

(ii) Resonance Methods

These methods could in principle be applied to a variety of shapes but practical application has been limited primarily to thin plates, slender cylinders or slender rectangular prisms and spheres, for which exact or reasonably accurate frequency equations exist. These methods are generally capable of an accuracy of $\leq 0.1\%$. In this technique, the sample is vibrated at a certain resonant frequency to produce a steady-state harmonic standing wave pattern after which the frequency and the mode number are measured to determine the elastic constants. A review of elastic constant determinations was presented recently by Wachtman [116].

3.1.2 Elastic Moduli of Particulate Composites

The elastic modulus has been the most widely studied mechanical property of particulate composites [117-119]. Correlations between theoretical models and experimental data can be made with fair accuracy, knowing the elastic properties of the matrix (m), and the particulate phase (p), and the volume fraction of the particulate dispersion (V_V). In general, the elastic modulus of a composite should be lower or higher than that of matrix depending on whether the particle modulus (E_p) is lower or higher than that of the matrix (E_m).

Rigorous theoretical models have been put forward which show that the elastic modulus of the composite should lie between maximum and minimum bounding conditions. For example, Paul has shown, using strain energy theories that the range is given by [120]

$$\frac{E_p E_m}{[(1-V_V)E_m + V_p E_p]} \leq E_C \leq (1-V_V)E_m + V_V E_p \quad (3.3)$$

These bounding conditions are for situations where both the matrix and particulate phases are equally stressed (lower bound) or equally strained (upper bound). This latter condition only applies where the Poisson's ratio of both phases are equal. Hashin and Shtrikman [121] have also calculated bounds in terms of the shear and bulk moduli. For modular ratios ($m = E_p/E_m$) which are small ($0.5 < m < 3$), the separation of the bounds is small and allows estimation of the composite modulus within 10%.

For composites of high modular ratio, the bounding solutions are too wide to estimate E_C . For these materials, approximate solutions are

available [114]. For example Ishai's relation is [122]

$$E_c = E_m \left[1 + \frac{V_v}{m/(m-1) + V_v^{1/3}} \right] \quad (3.4)$$

This solution is almost coincident to Hashin and Shtrikman's lower-bound. In recent times, finite elements techniques have been used to predict composite moduli. Figures 36 and 37 show experimentally determined moduli in comparison with these theories. Such results are representative of other experimental investigations. Particle size appears to have no effect on E_c , except that residual stresses are more likely to allow crack formation at bigger particles [114] which lowers the elastic modulus. Particle shape has a negligible effect unless the shape is susceptible to orientation during fabrication.

The use of these theoretical solutions in composites breaks down when voids or cracks are present. This may result from fabrication or differences in properties between the matrix and the particle. For example, cracks may form either within or around particles which have thermal expansion mismatch with the matrix. These cracks may only form during stressing, at higher stress levels than those used to measure the elastic modulus. These cracks are similar to voids as they do not transfer stress and make the material more compliant. The presence of these voids or cracks is usually first detected by an anomalously low elastic modulus [123]. Cohen and Ishai [124] have found the following relation useful for predicting the modulus of a two-phase composite which also contains voids.

$$E_c = E_m (1 - V_p^{2/3}) \left[1 + \frac{V_v}{[m/(m + V_p^{2/3} - 1) - V_v^{1/3}]} \right] \quad (3.5)$$

where V_p is the volume fraction of pores.

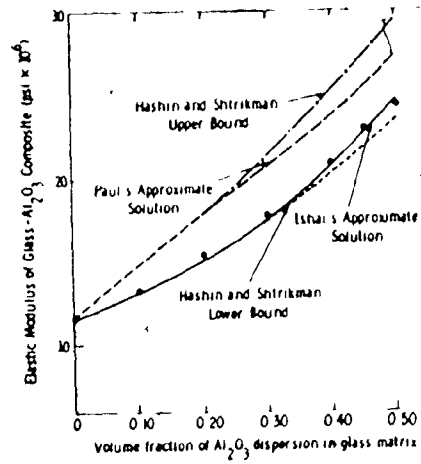


Figure 36. Elastic Modulus as a Function of Volume Fraction for an Al₂O₃ Dispersion in a Sodium Borosilicate Glass. (From Ref. 114)

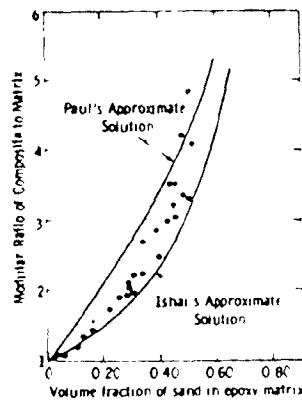


Figure 37. Modular Ratio of the Composite to Matrix Values as a Function of Volume Fraction of Sand dispersed in an Epoxy Matrix. (Ref 114)

The debonding of particles under a tensile stress leads to the formation of 'pseudovoids'. This terminology is used because the particles are not true voids but can still constrain the Poisson contraction of the matrix phase in its contact area. (see Figure 38). Evidence of such behaviour has been given by Sahu and Broutman [125] in a glass/polymer composite. A finite element, fracture mechanical approach has been taken by Sundström [126] for the initiation of interfacial microcracks at inclusions. This work indicates that above a critical tensile stress an interfacial crack may form. Such a crack may arrest as it enters the contact zone, and the particle wall therefore not immediately delaminate. Under triaxial stresses, complete delamination will be more likely.

The elastic modulus of a composite containing completely debonded particles has been estimated and is given by [127]

$$\left. \begin{aligned}
 E_c &\cong E_0 \left\{ 1 + \left[\frac{y^2}{2} (1-y) \right] (1-d) - \left[\frac{y^2 d}{(1-y)y^3} \right] \right\} \\
 \text{where } V_v &= y^3 \\
 \text{and } d &= \frac{(y^3/3)(1+y - y^2)}{(1-y+y^2)}
 \end{aligned} \right\} \quad (3.6)$$

There has also been much work to estimate the effect of porosity on the elastic modulus and the results usually given as

$$E = E_0 f(P) \quad (3.7)$$

where E_0 is the elastic modulus of a dense sample and $f(P)$ is some empirical function of the average porosity. Examples of these empirical functions are

$$\begin{aligned}
 f_1(P) &= (1 - bP) \\
 f_2(P) &= \exp(-bP) \\
 f_3(P) &= \left[1 - \frac{bP}{1+(b-1)P} \right]
 \end{aligned} \quad (3.8)$$

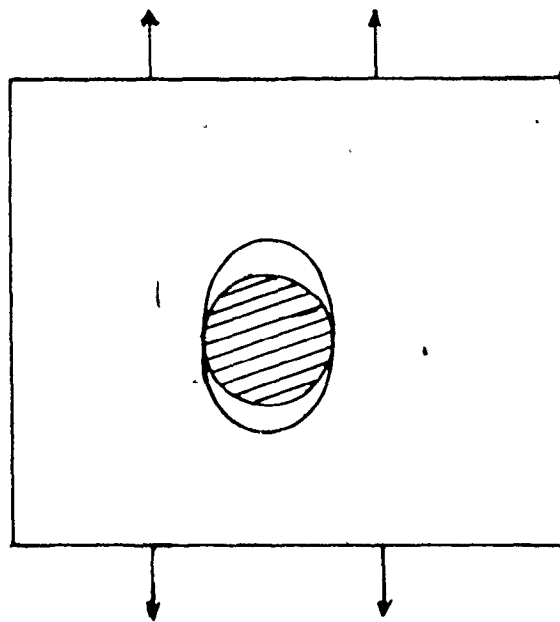


Figure 38. Formation of Pseudovoids around Non-bonded or Weakly-bonded Second Phase Particles in a Body under Tension.

- Rice [128] has recently argued against the use of average porosity, as inhomogeneous pore distributions and pore shape may influence the porosity dependence.

3.2 Fracture Surface Energy Determination: Double Cantilever Beam (DCB) Test

It has already been indicated that fracture mechanics parameters are useful in many aspects of engineering design and also as a tool for understanding the relationships between strength and the microstructure of a material. In fracture mechanics testing, a crack of known length is introduced into a sample and from a knowledge of the applied load at failure, the values of K_{IC} or G_{IC} can be determined. It has already been shown that

$$K_I = \sigma_A Y a^{1/2} \quad (3.9)$$

where Y depends on the specimen geometry. For geometries where Y has been determined by some stress analysis technique, the determination of K_{IC} is straightforward. As indicated in the last chapter, G_{IC} (or K_{IC}) can be determined by a compliance technique but the other method is relatively simple and more frequently used.

For brittle materials, it is reasonable to consider that fracture occurs when the normal stress at some location in the vicinity of the crack reaches the critical value for bond rupture. There will be a critical value of K_{IC} corresponding to this condition which should be a material parameter. The measurement of stress intensity for fast fracture (K_{IC}) has indeed shown this to be true when fracture occurs exclusively by mode I opening and when plane strain conditions occur at the crack tip. For very brittle materials, the lateral constraint along the crack front,

except near to the surface, generally ensures these plane strain conditions. In less brittle materials, plastic flow can relax this constraint, producing larger plane stress regions. In order to ensure plane strain conditions, the sample thickness is generally chosen to be greater than $2.5 (K_{IC}/\sigma_y)^2$. For specimens which do not satisfy this condition, a plane stress value of K is measured, which is larger than K_{IC} primarily because of the larger plastic zone.

Crack propagation can frequently occur for $K_I < K_{IC}$. This stage is generally characterized by K_I - crack velocity diagrams and this can be caused by inelastic processes occurring near the crack tip or kinetic fracture processes.

In terms of an energy criterion, the fracture is sometimes given as a fracture surface energy (Γ) which is an empirical parameter containing contributions from processes such as surface energy (γ_0), plastic work (γ_p) etc., but it is not known whether energy is also dissipated as heat, acoustic energy etc., which should be included in the total energy balance. It has already been shown that

$$2E\Gamma = \sigma_f^2 Y^2 a \quad (3.10)$$

Fracture surface energies have often been used for brittle materials in the hope of relating this parameter to the individual energy absorption processes. Stress intensity factors are now preferred by many workers as they are more convenient for failure prediction and other design purposes.

The choice of specimen geometry used for measurement of the fracture mechanics parameters is generally determined by the type of measurement

required. Evans [129] has suggested recently, the types of geometry suitable for different situations.

The thickness constraint is often satisfied for highly brittle materials though the sample should be thick enough to be microstructurally representative. Limited plasticity generally allows fracture mechanics to be used in an ideal way. It is generally adequate to measure the crack propagation load to evaluate K_{IC} . These measurements should be made from pre-cracked samples and techniques [129] are available for pre-cracking brittle samples.

The specimen geometry chosen for this work was the double cantilever beam (Figure 39), this has found great use in fracture toughness testing especially for highly brittle materials and was developed by Gilman. A stress intensity calibration was performed by Wiederhorn et al [130] and gives

$$K_I = 3.45 \frac{Pa}{bh^{3/2}} \left[1 + 0.66 \frac{h}{a} \right] \quad (3.11)$$

This analysis does put some constraints on the specimen geometry. For example, Wiederhorn et al [130] suggest that $\frac{a}{h} \geq 1.5$, based on experimental results and physical arguments. Swanson and Gross [131] also suggest the solution loses validity for long crack lengths so that an additional constraint of $(L - a)/t \geq 1.5$ must also be met. Because the stress analysis approach is for a semi-infinite body, it is also suggested that $L/h > 5$. A boundary collocation stress analysis was also performed by Gross & Srawley [132] with essentially the same result, i.e.,

$$K_I = 3.46 \frac{Pa}{bh^{3/2}} \left[1 + 0.70 \frac{h}{a} \right] \quad (3.12)$$

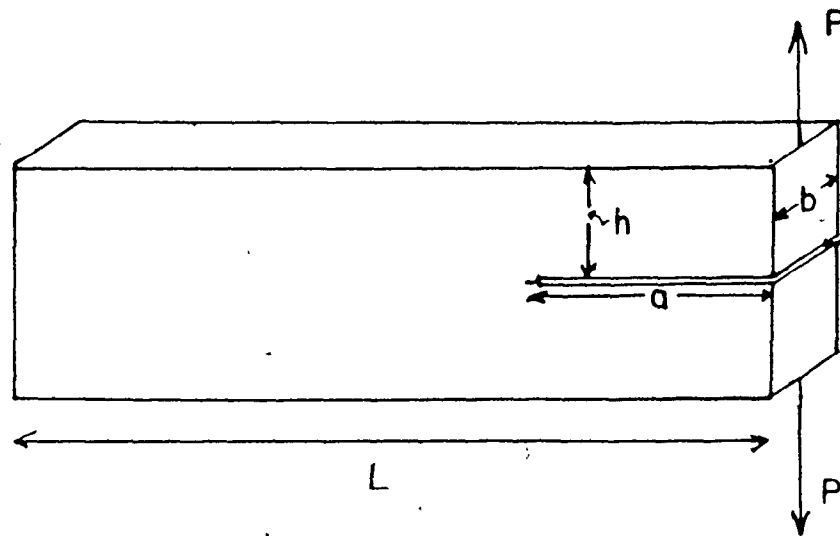


Figure 39. Specimen Geometry for Double Cantilever Beam Fracture Toughness Testing.

In his review, Evans [129] does not suggest the use of the DCB test for opaque samples because crack length and slow crack growth velocity measurements are often difficult. For such materials, he suggests the use of constant K_I samples which provide expressions for stress intensity which are independent of crack length. In particular, Evans has made great use of the double-torsion testing configuration. In recent articles, Gordon and Virkar [133] have now shown that this technique may present problem as a result of the crack front curvature especially in slow crack growth experiments. They have shown that measurements of load and beam displacement can be used instead of load-crack length measurements in DCB tests and that crack velocities can be calculated from load relaxation tests. This result is to be expected since load, deflection and crack length are inter-related.

It has been shown that G values can be obtained by compliance measurements. Therefore, if an analytical expression can be derived for this compliance, it should be possible to relate it to the stress intensity relation for a particular geometry using

$$G_I = \frac{K_I^2}{E} = \frac{P^2}{2} \frac{d\psi}{dA} \quad (3.13)$$

or
$$\psi = \int_0^A \frac{2}{P^2} G_I dA$$

Using this type of formalism, the deflection (δ) can be incorporated into fracture mechanics testing since $\psi = \delta/P$.

For example, in a DCB test, using elementary beam theory, and considering the bending moment of a cantilever beam rigidly attached at one end, it can be shown that [134]

$$\delta = \frac{2Pa^3}{3EI} \quad (3.14)$$

where δ is the total deflection of both beams in this case.

Therefore from equation (3.13),

$$G_I = \frac{Pa^2}{EIb}$$

or

$$K_I = \frac{2\sqrt{3} Pa}{b(h^{3/2})} \quad (3.15)$$

This expression is not satisfactory because it does not account for the shear deformation in the beams. To correct for this an additional term is needed [135], which for $\nu = 1/3$, is given by

$$\delta = \frac{2Pa^3}{3EI} \left(1 + \frac{h^2}{a^2}\right) \quad (3.16)$$

so that

$$K_I = \frac{2\sqrt{3} Pa}{bh^{3/2}} \left(1 + \frac{h^2}{3a^2}\right)^{1/2} \quad (3.17)$$

There is also a need for another correction term because the ends of the beams are not rigidly fixed but are attached to the rest of the sample. There has been considerable discussion about these correction terms [130, 136-138] but recently a sophisticated beam-on-elastic foundation approach has been used by Kanninen [139] that gives

$$\begin{aligned} \delta &= \frac{2P}{EI} (0.33 a^3 + 0.66a^2h + 0.61h^2a + 0.39h^3) \\ &= \frac{2P}{3EI} (1 + 0.64 h/a)^3 \end{aligned} \quad (3.18)$$

so that

$$K_I = \frac{2\sqrt{3} Pa}{bh^{3/2}} (1 + 0.64 h/a) \quad (3.19)$$

This final equation is in excellent agreement with the stress analysis results (equation 3.11 and 3.12) and confirms the approach. It is clear that by use of these equations, load-deflection measurements can be used to determine K_I . For example, equations (3.18) and (3.19) can be rearranged to give

$$K_I = \left(\frac{3\sqrt{3} P^2 \delta E}{b^2 h^{3/2}} \right)^{1/3} \quad (3.20)$$

Another useful approach to determine the compliance relationship is by an inverse procedure from the stress analysis results. In this way, the correction terms can be found. This has been done by Srawley & Gross [132] and Gordon and Virkar [133], their results using equations 3.11, 3.12 and 3.13 are:

$$\delta = \frac{2P}{EI} \cdot \left(\frac{a^3}{3} + 0.7a^2h + 0.5 ah^2 \right) \quad (3.21)$$

and

$$\delta = \frac{2P}{EI} \left(\frac{a^3}{3} + 0.66a^2h + 0.542 ah^2 \right) \quad (3.22)$$

respectively and these equations agree well with the Kanninen equation (3.18).

For crack velocity measurements in slow crack growth experiments, recent workers generally use constant K geometries with a load-relaxation technique. It is clear that load-relaxation technique could also be used for the DCB geometry and has been suggested by Gordon and Virkar [133]. It has also been suggested that crack velocities could also be determined from deflection-relaxation techniques in a constant load test.

In this way, the use of the DCB test can be extended beyond the limits suggested by Evans [129] and with a simple crack front geometry. The DCB test is limited for high temperature testing as the DCB rig must contain tensile components that are often metallic.

In DCB testing, there is a tendency for an unconstrained crack to turn from the desired plane of extension and break off one beam of the test specimen [140]. To promote planar extension, it is common practice to introduce side grooves in the specimen which guide the crack path. These side-grooves require two corrections to the earlier expressions for G_{IC} or K_{IC} i.e.,

- a) A width correction must be applied to account for the reduced fracture surface area.
- b) A moment of inertia correction to account for the reduction in strain energy stored in the specimen beams.

The first correction was originally proposed by Freed and Krafft [141] and is generally made. The second correction has been discussed by Hoagland [142] and will depend on the side-groove geometry. This second correction is not often applied and in many cases is small. In terms of the crack extension force, the corrections are simply given by

$$G_{sg} = G_p \left(\frac{b}{B}\right) \left(\frac{I_p}{I_{sg}}\right)^{1/3} \quad (3.23)$$

where the subscripts p and sg refer to plain and side-grooved samples respectively and B is the fracture web width.

A complete understanding of the crack directional instability in a DCB test depends on an accurate analysis of the stresses perpendicular and parallel to the crack plane. Even if this information were available, there would still be problems because crack trajectory problems are not completely understood. It has been suggested [140, 143] that the problem can be discussed qualitatively from a simple beam theory approach. In this engineering approach, the maximum bending stress is calculated in

the ligament (σ_L) and arm (σ_a) of the specimen. That is

$$\begin{aligned}\sigma_a &= \frac{6 Pa}{bh^2} \\ \sigma_L &= \frac{3 P(L + a)}{b(L - a)^3}\end{aligned}\tag{3.24}$$

This comparison has been made by Cotterell [140] for the compact tension sample and he shows there is a much greater tendency for directional instability when $\sigma_L/\sigma_a < 1$. This criterion is generally met for DCB samples. In a similar approach, Mostovoy et al [143] show that the introduction of side grooves will tend to reduce these bending stresses. It is clear that specimen anisotropy will play a role in the crack path problem. This beam theory approach is useful for understanding the problem but it can only be used as a guide and the problem of maintaining the crack in the desired plane must be solved experimentally. Usually, one increases the side groove depth until the crack runs straight.

In the DCB testing of brittle materials, care must be taken in design of the loading fixture because of the low loads required to fracture brittle materials. Proper alignment is critical and the loading fixture should be designed to minimize mode II and III stress intensity components. The load is generally applied via pins which are placed through holes in the sample. These holes are generally introduced by ultrasonic or diamond-core drilling. Recently, Hoagland et al [144] have used steel loading tabs glued to the specimen arms. This procedure removes the drilling problem which can be difficult for a brittle material but involves a correction to the crack length or displacement measurements [144].

Another important question in fracture testing is concerned with the behaviour of the crack, once it starts to propagate and the question

of crack stability. The DCB test has proved useful in three ways. Firstly, it often allows multiple pop-in and crack arrest to be studied in rate-sensitive materials. This process is illustrated in Figure 40 for fixed displacement conditions. Secondly, for rate-insensitive materials the DCB test often leads to crack stability and quasi-static cracking. For this case, the crack resistance force can be monitored in a continuous fashion as a static analysis should still be applicable to describe the crack system. In tests where crack instability occurs, the fracture resistance is essentially only measured at the instant of crack propagation. At any time after, the crack has acquired kinetic energy and the system cannot be described by the simple fracture mechanical approach. For quasi-static cracking, the fracture resistance force is often denoted as R ($R = 2\sigma$).

An early attempt to study the dynamic aspects of the DCB test was made by Berry [145]. In this work he introduced a useful concept which describes the locus of the Griffith condition. Using a simple beam approach (equation (3.14)), the locus of the Griffith condition can be described by

$$\delta_g = \frac{(2\sigma_B)^{3/2} (4EI)^{1/2}}{3P_g^2} \quad (3.25)$$

The form of this curve is shown in Figure 41 and it provides a useful graphical interpretation of the crack stability. The slope of the locus is negative for all values of P_g so that for constant deflection conditions, the system should be stable unless the Griffith condition is exceeded. For constant load tests, the system will be unstable. The concept of exceeding P_g was found to be necessary by Berry in order to

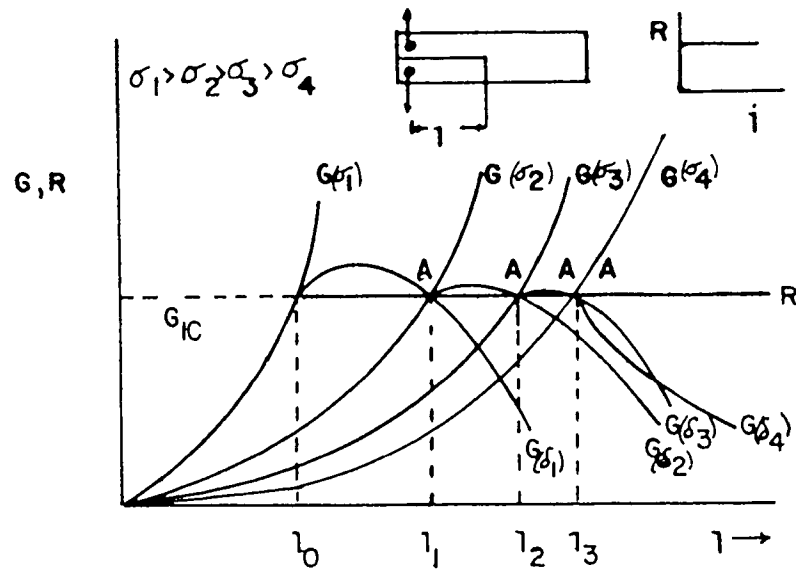


Figure 40. Crack Extension and Crack Resistance Forces for a Rate-insensitive Material in a DCB Fracture Test.

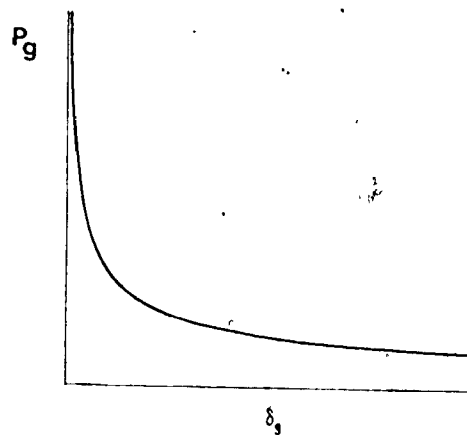


Figure 41. The Locus of the Griffith Condition (After Berry)

determine crack velocity relationships. For a DCB test, the nature of the slope is such that the discrepancy between the observed critical force and that predicted by Griffith [145] should be not as great as that found in a tension test. Furthermore, this discrepancy should decrease for longer crack lengths. In terms of crack stability, the crack behaviour depends on the rate-sensitivity of the material, the amount of overstressing and the crack length. For a rate-insensitive material under fixed displacement conditions, crack stability is expected and as pointed out by Hoagland [144], the load-displacement record should be a smooth hyperbolic curve with a negative slope and positive curvature (c.f. the Griffith locus). Various testing geometries have been analyzed by Clausen [146] and similar conclusions were reached about the DCB test. There is another variable however, and that is the stiffness of the testing machine. For a soft machine, the energy stored in the machine can lead to crack instability because the machine will not unload as rapidly as the sample. In this sense, a very soft-machine acts more like a constant-load test and leads to unstable growth in a DCB test. This problem has been discussed by Jaeger and Cook [147] with respect to compression testing of rocks. Mai [148] has reached similar conclusions to those of Clausen [146]. In the former work the effect of the side grooves was included and it was shown that they promote stable cracking in a hard testing machine. This result was confirmed with a test on polycarbonate which is rate-sensitive and leads to unstable cracking in ungrooved specimens. For grooved polycarbonate samples, cracking was shown to be stable. Dynamic aspects of DCB testing have also been treated by Kanninen [139, 149] and extensive use has been made of a wedge-loaded DCB test for dynamic studies of unstable crack growth and arrest at Battelle-Columbus.

Fracture toughness testing appears to offer great potential in materials development and failure prediction. For this work, the emphasis is on materials development and the understanding of the interaction of a crack front with second phase obstacles. In general, it has been stated that these obstacles often increase the fracture surface energy of a material and experimental results are given in Appendix A.6.

3.3 Fracture Stress Determination: Four-Point Bend Test

3.3.1 Strength Testing of Brittle Materials

Conventional strength testing of brittle materials is used to obtain fracture stress values under well-defined stress states. For advanced applications of ceramic materials, the tensile strength is generally considered most important. Strength measurements are generally used for two purposes; to compare the relative merits of different materials and to provide data for the adequate design of complex engineering structures. With respect to this latter purpose, a probabilistic design procedure requires a knowledge of the mean failure strength of a specific surface area of material under uniaxial stress conditions, together with a measure of the inherent material variability. For design purposes, strength tests for brittle materials must therefore have as small a testing variance as possible and allow strength parameters to be derived which are independent of the test method.

The strength testing of brittle materials can be a difficult process as imperfections in test apparatus and specimens, that might be alleviated if testing a ductile material, can become sources of parasitic stresses in brittle materials and give rise to erroneous strength results and misleading interpretations.

The direct, uniaxial tension test would appear to be the simplest technique for strength testing but eccentricity and gripping problems make the experimental details very difficult. For this reason, some indirect tension tests have been developed but these tests often entail difficulties in machining the test specimens. These difficulties have led to the use of non-uniform, uniaxial tensile tests. The analytical simplicity of a uniform stress field is traded for experimental simplicity. In this respect, bend tests are often used to obtain strength data because elementary theory shows that the outermost fibres of bend specimen experience uniaxial tensile stresses.

Bend testing is prone to parasitic stresses and care must be taken so that the specimen shape and dimensions and the test rig design are chosen to minimize errors, by ensuring that the deviations from simple beam theory are small. In this sense, it can be seen that all of the general limitations of the stress analysis used, also apply to the testing.

Stress analyses are based on certain assumptions and idealizations relating to material characteristics, loading conditions and specimen geometry. Deviations from these assumed conditions will be sources of error and recognition of these assumptions is essential in selecting and conducting tests, as well as interpretation of results. Some important factors affecting the accuracy of the stress analysis are:

- (i) distinction between statically determinate and indeterminate stress distributions
- (ii) deviations from assumed material characteristics
- (iii) imperfect loading conditions and specimen geometry
- (iv) test hardness.

The bend test is a statically indeterminate test in that the force-stress relationship is dependent on the material properties. The assumption is made that the strains are distributed linearly from a maximum tension at one surface to a maximum compression at the opposite surface. The resulting stress distribution depends on the stress-strain curve so that, for a linear elastic material, the stress distribution will also be linear. In this way, the assumed strain distribution and static equilibrium is not sufficient to determine the stress distribution and the system is termed statically indeterminate. Most brittle materials are linear elastic so that the problem disappears. For some brittle systems, however, there can be non-linear stress-strain curves and fracture stress values must be modified to account for this behaviour.

In strength testing, distinction should also be made between actual and nominal stresses. If the material is isotropic and homogeneous, the distinction is not important but real ceramics contain imperfections that cause the local stress to deviate from the nominal applied stress. If the imperfections are numerous and random, then it might be assumed that they are an inherent characteristic of the material. For more occasional flaws, serious distortions appear in the stress distributions and in the computed strength. Identification of these flaws can help in clarifying such ambiguities in test data. Systematic variations in properties can also be accounted for, provided the experimenter is aware of these possibilities. Non-destructive testing and careful fractography can be extremely useful in detection of these problems.

It has been proposed also that test hardness may be a factor in descriptions of strength dependence and scatter. Test hardness is related

to the amount of energy stored in the sample for a particular test geometry. For example, a comparison between a bend and direct tension test shows that less energy is stored in the system for a bend test, than for a direct tension test. The bend test is then termed a harder test than the tension test.

Finally, one must also be concerned with the assumed loading conditions and specimen geometry. For example, there will be a re-distribution of stresses near load contact points. According to St. Venant's principle, the effect will die away with distance from the load application point until the simplest, statically equivalent stress distribution is achieved. Distortions in the stress distribution can also appear from effects such as friction, imperfect specimen geometry, notches, eccentric loading and twisting.

The bend test has proved relatively simple to use and was chosen for the work in this thesis. In particular, the four-point bend test was chosen because it has the advantage of providing a maximum moment over a substantial length of specimen. The idealized moment and loading distributions are shown in Figure 42. Failures generally occur between the inner load points while failures occurring outside this region are generally discounted. It is generally assumed that the material is homogeneous and linear-elastic. This allows the use of simple beam theory where the longitudinal stress is given by

$$\sigma_{11} = \frac{M y}{I} \quad (3.26)$$

which can be shown to give a maximum outer-fibre stress in four-point bending of

$$\sigma_{\max} = \frac{PaW}{4I} \quad (3.27)$$

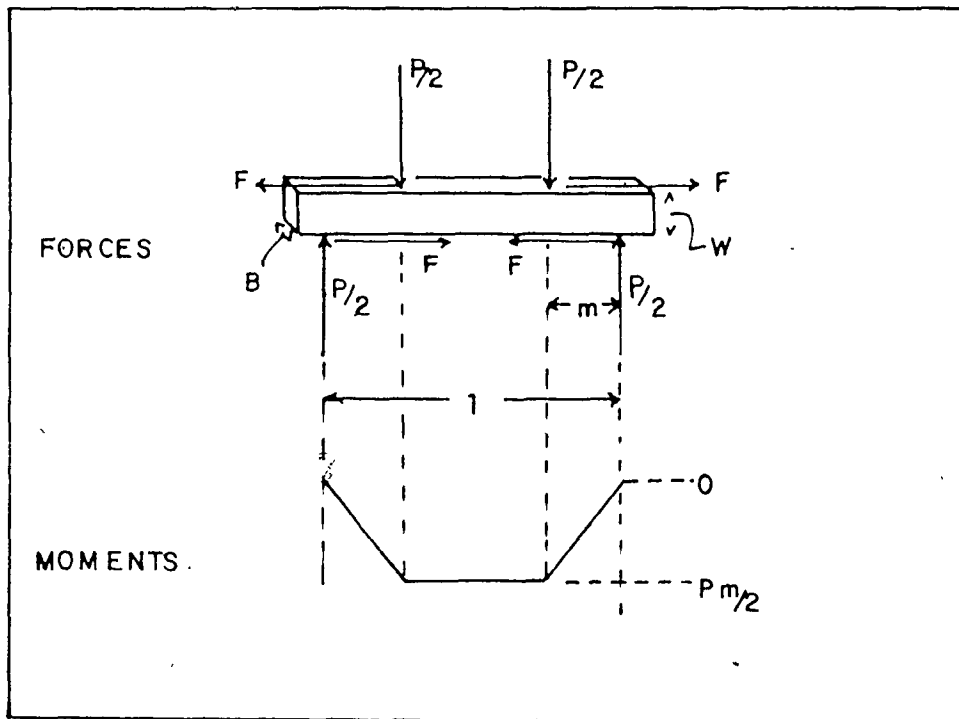


Figure 42. Specimen Configuration and Idealized Moment and Loading Distribution for a Four Point Bend Fracture Test.

This derivation is available in many elementary strength of materials textbooks and by Newnham [150] and the present author [151].

To summarize the assumptions of this simple theory;

1. the material is linearly elastic to the point of fracture with identical values of Young's modulus in tension or compression.
2. shear stress in the central portion of the beam is negligible.
3. the material is not constrained in the thickness direction, i.e. along x_3 so that no through-thickness stresses are developed.
4. the support members and load points are frictionless.
5. there are no local stress perturbations due to contact forces.

The major sources of first order errors in these assumptions are considered to be, in approximate order of significance,

- (1) friction forces developed at load points.
- (2) incorrect spacing of load points and unequal distribution of loads.
- (3) twisting
- (4) wedging.

These errors will be discussed briefly.

(i) Location of Loading Points

This can be a serious problem in four-point bend tests. Hoagland et al [152] have discussed the errors associated with four-point bend tests and their results are summarized in Table 12. The moment error $\Delta M/M$ will depend on the inner span length to moment arm ratio, so it is advantageous to design a bending fixture where this ratio is small.

Increasing the moment arm, also reduces the applied loads so that crushing and wedging effects are also reduced. In practice, it is generally useful to fix the outer and inner spans while still allowing for changes in the moment arm length.

TABLE 12. Sources of Error in Bend Testing. (After Hoagland et al)

Source.	Result. *
Unequal Moments	$\frac{\sigma_t}{\sigma_o} = 1 + \frac{\Delta M}{M}$
Twisting	$\frac{\sigma_t}{\sigma_o} = \frac{1}{2} + \frac{1}{k_2} \left[\frac{b^2}{l^2} + 9k_2^2 \right]^{\frac{1}{2}}$
Wedging	$\frac{\sigma_t}{\sigma_o} = 1 + 0.0579 \frac{c}{l}$ #
Friction	$\frac{\sigma_t}{\sigma_o} = 1 - \frac{2\mu c}{l}$

* in terms of maximum tensile stress to nominal bending stress

This is maximum effect on tensile side of beam at a distance
 $x = * c/2$ from the loading line

b = beam breadth, l = moment arm, k_2 is a function of b/c
 c = half beam depth, μ = coefficient of friction.

(ii) Friction Effects

These effects generally arise from friction between the loading points and the specimen and are caused by the longitudinal surface strains induced during bending. Any restraining force that prevents this movement will produce a counter moment in the specimen through friction at the load-specimen contact point. The net effect of friction is a reduction in the total stress at the specimen surface and an increase in the apparent strength of the test material unless this effect is accounted for, or removed. The magnitude of the frictional effect can be significant, especially for specimens with large length to depth ratios.

The frictional effects can often be minimized by using freely-rotating rollers for load application. Polishing of the specimen surface could also improve the reduction in friction. Any inelastic processes along the contact line will contribute to the rolling friction so, for test materials with high surface hardness, the use of hard loading pins is recommended. Some workers have attempted to apply the loads at the neutral axis but this could introduce additional errors and certainly complicate the specimen design. The magnitude of the friction as a source of error tends to be rather unpredictable and generally it is best to check the performance of a fixture after it has been constructed. For example, load-unload tests will tend to show hysteresis in a load-displacement record or high values of Young's modulus could be obtained if frictional effects are significant.

(iii) Twisting

A non-uniform load distribution might subject the specimen to a net torque. This effect could arise if the loading contact lines are not

parallel or if the specimen is skewed over its length from inaccurate machining. Hoagland et al [152] in their calculations indicate the error can be very significant. Torsional problems can be minimized by allowing rotation of the contact points about an axis which is parallel to the specimen axis and by careful machining of the samples.

iv) Wedging

The line contact points which result from the loading in a bend test produces a singularity in stress in terms of an unbounded compression immediately below the contact point. This effect is analogous to attempting to force a sharp wedge into the material. The resulting high stresses can lead to local crushing and in some cases, shear failure. These effects can lead to perturbations in the stress distribution around the contact lines. This stress distortion decays rapidly with axial distance from the loading points and the wedging effect can be reduced by decreasing the beam depth to moment arm ratio [153]. Wedging errors tend to be less than 3% for most specimens geometries. Wedging effects are generally of more concern in three-point bending because the maximum stress predicted by beam theory will never be reached. In general, it is worth noting that all these errors decrease as the moment arm is increased relative to the other specimen dimensions. With these problems in mind, Hoagland et al [152] have designed a bend fixture to minimize these errors and they showed that their fixture had effectively reduced errors to the order of 1%.

The assumption of negligible shear stresses is very good for four-point bend tests as no shear stresses are present between the inner loading points. The ratio of maximum shear stress to maximum

tensile stress is given by $W/4n$ so that decreasing this ratio can suppress the possibility of shear failures. Newnham [150] has shown that the through-thickness stresses tend to be very small for most bend specimens of practical dimensions and deformation occurs in a plane stress mode. Reduced loads in the rig can be obtained by using specimens with large n/W ratios.

Finally, Newnham compares the use of rectangular and circular cross-section beams because in square-section beams, there is a possibility of edge dominated failures, which may not be representative of the material. With a probabilistic approach, he shows that edge-dominated failures were unlikely on the strength testing of silicon nitride. His discussion was not supported, however, by fractographic evidence.

To summarize this discussion, it is useful to list the requirements needed for precise four-point bend strength testing.

- 1) The fixture should be designed with tiltable pins, adjustable span position and free-rolling, low friction loading pins.
- 2) Specimen with high ℓ/W ratios and large moment arms reduce friction effects and the magnitude of the shear forces and minimize stresses in the test rig. Generally values of ℓ/W less than 8 - 10 are not recommended and ℓ/m is generally not less than 4. Within these limits the moment arm should be as large as possible ($m \geq 2W$).

3.3.2 Strength of Particulate Composites

(i) Particle Size and Volume Fraction

The strength of several composite systems have been studied as a function of particle size and volume fraction. The other variables in

these systems such as modular ratio, interfacial bonding and thermal expansion stresses were fixed by the properties of the two phases and the fabrication conditions.

A glass- Al_2O_3 composite system has been studied by Lange [9] and Hasselman and Fulrath [154]. For their particular system, the thermal expansion coefficients were matched and the modular ratio (m) = 5. Their strength data is illustrated in Figure 43 and it appears that a significant increase in strength can be obtained. Hasselman and Fulrath obtained modulus data for this composite and Lange measured the fracture surface energy. The product (\sqrt{E}) can be shown to increase with both particle size and volume fraction. From the Griffith approach the fracture stress is proportional to $(\sqrt{E}/c)^{1/2}$ and it is evident that the strength data can be rationalized by stating that larger particle size dispersions lead to larger flaws. In this way larger particles are better crack precursors than smaller particles. For the two smallest particle dispersions (3.5 and 11 μm), there is some discrepancy and unexpectedly the 11 μm series has a greater strength.

A second system studied by Lange [114] was the Si_3N_4 - SiC composite which can contain large residual thermal expansion mismatch stresses. For this system (\sqrt{E}) is approximate constant, while the strengths remain constant or decrease with increase volume fraction. The strength decrease is accentuated by larger particle size and again it can be deduced that larger particles are better crack precursors. This effect was also found to increase with volume fraction. This concept is consistent with the work of Davidge and Green [110] and again it is found that smaller size dispersions are required to

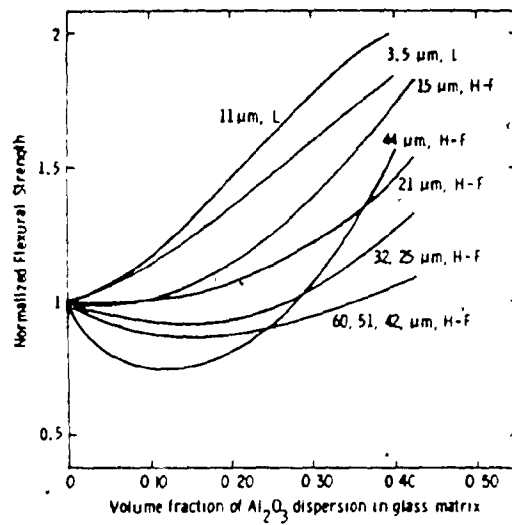


Figure 43. Strength as a Function of Different Particle-size Al₂O₃ Dispersions in a Sodium Borosilicate Glass (Ref 114)

achieve optimum strength.

In a third system $\text{Al}_2\text{O}_3 \cdot 3\text{H}_2\text{O}$ - epoxy, studied by Radford [155] and Lange & Radford [156], the behaviour is more complex. This is probably a result of the maximum observed in the fracture surface energy data which is reflected in the value of (σE). The strength values of all composites are less than that of the matrix and Lange [114] concludes that the large difference in elastic properties and expansion coefficients of the two phases can result in substantial stress concentrations. Moreover, the $\text{Al}_2\text{O}_3 \cdot 3\text{H}_2\text{O}$ is prone to cracking. It was still found that smaller size dispersions help to optimize strength. This general idea leads to a compromise in composite design since fracture surface energy values are generally greater for large size dispersions. In general, design often fixes the volume fraction so that strength can best be controlled by changing the particle size.

(ii) Interfacial Bonding

The effect of interfacial bonding has been most studied in polymeric particulate composites, where the degree of bonding is controlled by pretreating the particulate phase with parting or coupling agents. Sahu and Broutman [157] have made a detailed study of an epoxy-glass sphere system. The strength of these systems decreases with increasing volume fraction with the decrease greater for the poorly-bonded systems. It has already noted that in poorly-bonded systems there is the opportunity for decohesion and the formation of pseudovoids. For these systems, there is a drastic decrease in modular ratio. The particles can still constrain the Poisson contraction but the strength behaviour is often very similar to porosity behaviour.

Hasselmann and Fulrath [154] have studied a glass-nickel system in which the nickel spheres with a higher expansion coefficient than the glass contract from the matrix to leave a porous system. They observed a precipitous decrease in strength for uniaxial and biaxial tensile strengths with a zero porosity intercept that is considerably less than that of the matrix. This is to be expected as the first pore will lead to a stress concentration of two or three under conditions of biaxial and uniaxial conditions. In their discussions of these effects, Hasselmann and Fulrath postulated that the pore to flaw size will determine the strength-porosity behaviour. For situations where the flaw size in the dense material is less than the pore size, the flaw will be located entirely or almost entirely in material subjected to the maximum stress concentration. On introduction of the first pore the tensile strength will be reduced by this maximum stress concentration value. As the flaw size to pore size decreases, the decrease in strength should be less drastic because the critical flaw has less chance to be found with the volume subjected to the maximum stress concentration. This work was extended by Berlotti and Fulrath [158] and the results are in agreement with Hasselmann and Fulrath's hypothesis. This argument though qualitatively pleasing, is rather simplistic in its view of the different variables and ignores the fact that the porosity itself will tend to produce the critical flaw and play a critical role in determining its size.

To return to the problem of interfacial bonding, work on polymer composites has also been performed by Kenyon [159]. Stett and Fulrath [74] have investigated glass-nickel sphere systems, one of which is being

utilized in this thesis. By oxidizing the nickel, it is possible to form a good bond with the nickel spheres and this improves the strength of the composite quite drastically. They also reported that the optimum strength and thus the optimum bond depends on the thickness of the oxide layer. For these systems poor bonding is often reflected in a larger increase in τ but that the lower modulus and increased flaw size tends to lead to a decrease in strength. In this way, strength can best be improved by obtaining a well-bonded interface between the two phases.

(iii) Residual Thermal Stresses

These effects have been studied by several workers [74, 110, 160]. In general, it is seen that large differences in thermal expansion can significantly affect the strength behaviour especially with large particle size dispersions where cracks often form during fabrication. Interparticle cracks ($\alpha_m > \alpha_p$) were found to be more drastic than the hemi-spherical cracks produced when $\alpha_m < \alpha_p$. For small particle size dispersions, these fabrication cracks did not appear and increased strengths could be obtained. Again it is seen that smaller particle size dispersions can help to optimize the strengths of these particulate composites.

3.4 Determination of the Critical Flaw Size

The concept of a critical flaw which produces failure is derived from the Griffith approach to fracture. The nucleation of these flaws is rarely well understood and can depend on subtle microstructural, atomistic and kinetic effects. There is generally no suitable technique for detection of these flaws and their existence as a well-developed

microcrack is usually for a very short time. Direct detection is therefore not often available but with the parameters already discussed, it is possible to calculate the critical flaw size. A rearrangement of the Griffith equation gives

$$a_c = Y^2 E / \sigma^2 \quad (3.28)$$

Use of this equation depends on three conditions being satisfied. First, the value of fracture surface energy, measured on specimens containing relatively large cracks, must be assumed for the much smaller cracks that initiate fracture. The calculated crack size for particulate composites is usually much larger than the materials microstructure which controls its fracture surface energy so this condition is usually satisfied. Secondly, the value of the Youngs modulus must represent the response of the material at the fracture stress. Thirdly, the geometry and location of the crack must be assumed in order to choose a value of Y . For semi-circular cracks or interior circular cracks a value of $Y^2 = 4/\pi$ is generally suitable. The calculated crack size can only be an estimate, because, as we have seen the critical flaw size is often the most dominant parameter in determining the fracture stress. In relative terms, however, it can be a useful procedure to determine the effect of the particulate phase on failure. The larger particle sizes are more effective as crack precursors in these particulate composites. Hasselman and Fulrath [154] suggested that it is the mean free path limits the critical flaw size. Crack size data by Lange [9] and others show no supporting evidence for this idea.

The observation that large particles are better crack precursors has been studied by Davidge & Green [110]. For this work, each particle

is considered as a flaw and is thus a precursor to a crack. This statement is based on the observation of fabrication cracks around large inhomogeneities and theoretically it is known that second phase particles give rise to stress concentration as a result of differences in thermal expansion and elastic properties. Stresses around second phase particles are generally independent of particle size so this cannot explain the observations. Davidge and Green [110], therefore, suggested that there must also be a sufficient amount of stored elastic energy available in addition to the development of residual stresses. This total stored elastic energy will depend on the volume of material under the influence of these stress concentrations, which in turn depends on particle size. By invoking a Griffith concept of minimum free energy, they postulated that a crack only forms when the stored strain energy associated with the particle is equal to or greater than the energy to form a new crack surface areas. For a system which forms hemi-spherical cracks as a result of thermal expansion mismatch, Davidge and Green found in their calculation that there was a critical particle size (D_c) above which failure will occur. For this case D_c is given by

$$D_c = \frac{4^{\nu} \mu_m [E_p(1 + \nu_m) + 2 E_m(1 - 2\nu_p)]}{(\Delta \alpha \Delta T)^2 E_p E_m} \quad (3.29)$$

where μ is the shear modulus, $\Delta\alpha$ is the expansion coefficient mismatch and ΔT is the temperature difference. This concept does not explain the nucleation and growth process but it is consistent with theoretical and experimental observations and the fracture mechanics approach. The comparison of D_c with observed composites showed that calculated values were smaller by a factor of 0.5. It is clear, though, that reduced particle size should lead to reduced cracking. In real composites

account should be taken of strain-energy field overlap especially in composites where agglomeration is possible or at high volume fractions.

Stress concentrations will also arise from the differences in the elastic properties of the two phases. A similar concept to Davidge and Green should also be applicable to this situation. Lange [161] has extended the work of Davidge and Green [110] by using a more general analysis and has taken into account the size of the cracks. Davidge and Green's concept could predict that smaller cracks could be produced around the smaller particles. Evans [162] has also studied this problem and has calculated the stress intensity factors at interface cracks due to thermal expansion or elastic property mismatch. It was shown that conservative failure prediction based on an equivalence between inclusion size and crack size is usually acceptable for inclusions where the shear modulus or the expansion coefficient is larger than the matrix values. For the reverse situation, extensive cracking can develop at the inclusions and may lead to premature failure. For this case, effective methods for failure prediction are techniques that give directly the maximum K_{IC} i.e. proof testing and/or acoustic emission. The effect of the elastic property differences was discussed previously in Chapter 2. The stress concentration due to elastic mismatch can be estimated to be

$$K_M = K_0 [1 + 2A + 6B - 3(A + 6B)c/a] \quad (3.30)$$

for $\mu_m > \mu_p$, where K_M is the stress intensity factor due to the elastic stress concentration, c is the crack size and A , B and a are defined in the elastic stress solution (Appendix A.4). For the case of a void, $K_M = K$ when $c = 0.2a$ so that the flaws have to be quite large to cause fracture.

Finally, it is worth re-iterating the discussion on crack location and fracture path. This will depend on the stress distribution and fracture energy of each phase. This information can generally easily be deduced from fractographic observations. The effect of residual stresses is shown in Fig. 44. For $\alpha_p > \alpha_m$ either hemispherical cracks will form around the particles or the particles will crack. For the case where $\alpha_m > \alpha_p$, radial cracks develop and form a network of inter-particle cracks. The crack paths are indicated by broken lines. Poor interfacial bonding can lead to decohesion in either case but more readily for $\alpha_p > \alpha_m$. Observations of this behaviour has been given by Binns [160] and Davidge and Green [110]. Stett and Fulrath [74] and Kenyon [159] have shown that for poor interfacial bonding the particles decohere and the crack path links the particles. Figure 45 shows the situation for the elastic property mismatch problem. Unless the thermal expansion coefficients are equal these complex stress distributions must be superimposed on the uniform residual thermal stress distributions to obtain crack locations and fracture modes. In this figure, there is agreement with our earlier discussion of crack path, i.e. the cracks tend to move towards the position of maximum stress concentration. For hard particles in a soft matrix, the tendency is for the cracks to avoid the particles and to stay within the matrix. This is also in agreement with the observations of Stett and Fulrath [74].

It is useful to summarize at this point the important parameters which influence the mechanical properties of these particulate composites;

- 1) size and volume fraction of particles
- 2) shape of particles
- 3) difference in elastic properties of the two phases

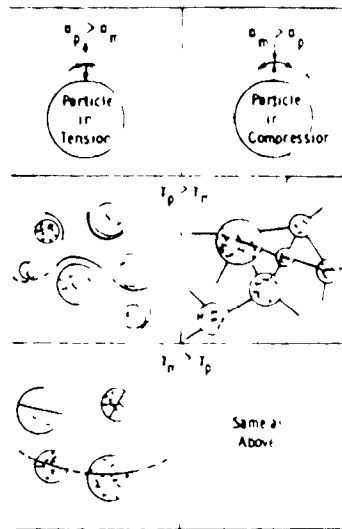


Figure 44. Nature of Residual Thermal Stresses, Crack Locations and Fracture Paths (broken lines) in a Particulate Composite. (α is thermal expansion coefficient, γ is the fracture surface energy and m and p refer to the matrix and particle respectively)

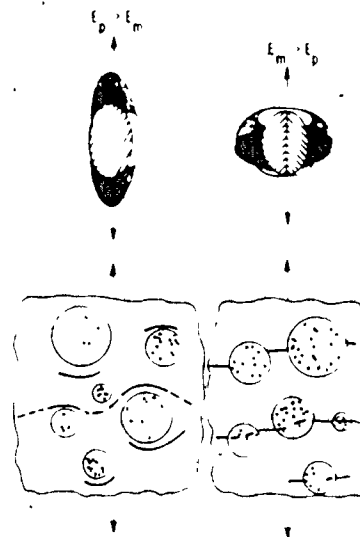


Figure 45. Schematic Representation of Enhanced Tensile Stresses around a Spherical Particle of Modulus E_p in a Matrix of Modulus E_m . The Location of the Cracks and Fracture Paths (broken lines) are also shown.

- 4) differences in thermal expansion coefficients of the two phases
- 5) interfacial bonding
- 6) mechanical behaviour and structure of two phases e.g. ductility, crystalline vs. amorphous, etc.
- 7) relative values of ν for the two phases.

3.5 Fractology

The fracture topography is a permanent record of the fracture process that can provide valuable information on crack propagation and failure mechanisms. In particular, it is often possible to identify the fracture origins. In this way, fractography should complement any strength or fracture surface energy - microstructure study. The fracture surface can also record such subtle influences as sonic waves, material inhomogeneity, local stress gradients and velocity interactions. The ability to detect these subtleties is not always straightforward so that in many ways it can remain a craft. Fractography of ceramics has been reviewed recently by Rice [163, 164] and Fréchet [165].

The fracture topography can be observed with the unaided eye, hand lens, scanning electron microscopy (SEM) and the transmission electron microscope (TEM). The unaided eye is useful for studying gross features such as crack branching and such viewing is rapid, versatile, allows large areas to be examined and prevents details from obscuring the overall pattern. The hand lens extends this capability. The optical microscope is a very versatile and cost effective tool. Bright field reflected illumination is normally used, though contrast techniques such as Nomarski interference can be very useful. Objectives below 8x

usually intercept insufficient illumination while objectives of 20x to 40x are generally an upper limit. In conjunction with the unaided eye, optical microscopy can be very effective. Fréchet [165] in his review describes a set-up for use in optical microscopy that he has found most convenient. The light is obtained from a well-defined source that is incident on the sample such that slight local undulations on the fracture surface are sufficient to spoil the reflection and hence give contrast. Silvering of the fracture surface can help to eliminate subsurface details in transparent materials and to enhance the brightness of the surface reflections. In this way, it is often possible to view many fine details on the fracture surface and as pointed out by Rice [163] it can often delineate fine topographical features that are missed in the more sophisticated SEM.

The SEM is a major advance in fractology but should be used in conjunction with optical microscopy. In all fractology it is good practice to view both fracture halves and in the SEM the depth of field also generally makes it possible to view both the fracture surface and the tensile surface simultaneously. For SEM work, it is necessary to coat ceramic samples with a thin (200\AA) conducting film to prevent charge build-up. The structure of very fine features is generally done by TEM replication, but the difficulty in locating specific areas with this technique normally limits its use to generalizations.

To discuss the use of fractology in detail would be a large task, so for this discussion, the general features will be noted briefly. In polycrystalline ceramics, the degree of intergranular or transgranular fracture can be determined. This information is often useful

as it may correlate with strength and cause of failure. Observations are often made of fracture interactions with twins, domains and slip-bands. The interaction of a crack with pores, inclusions and other cracks often results in the formation of a fracture surface step (fracture tail) at the rear of the obstacle. Fracture in glasses at relatively low stresses often produces very smooth fracture surfaces. Fine details such as rib marks, striations and Wallner lines can be sometimes discerned in this mirror region. Holloway [166] has discussed the formation of these features. In particular, Wallner lines are small undulations in the crack plane and are a result of a stress wave generated by the crack front as it passes an irregularity on the surface of the specimen. Pronounced Wallner lines can often be produced by lightly grinding the glass surface before breaking it. These lines can be used to determine crack velocities [166] though the process can be time-consuming and depends on chance events.

For cracks expanding under high stress, the energy release rate increases as the crack progresses and rougher fracture surfaces are produced. Indeed, at high crack velocities, macroscopic crack branching occurs. The increasing roughness generally allows three zones to be delineated on brittle fracture surfaces; a smooth inner zone called the mirror region which surrounds the fracture origin, an arc of rougher, stippled surface called the mist region and a very rough, striated zone which is called the hackle region. It has been found that the radius of the two inner zones (r_m) is an important parameter such that for a given material, $\sigma_f(r_m)^{1/2}$ is a constant. No completely convincing explanation has been made of this relation. Single crystals can also exhibit these regions though with some modification because of aniso-

tropic effects [164]. Mirror formation is generally not detected in weaker bodies.

The fractographic identification of the failure origin is a very important part of fractology. In materials where mirrors are formed the general location of the critical flaw can be identified. Fracture surface or cleavage steps can also be useful in this respect because they form perpendicular to the crack front. With such techniques, fracture origins can be determined in a majority of glass, single crystal and dense polycrystalline bodies.

In glasses, fracture originates from features whose appearance and dimensions are approximately those of a 'Griffith flaw'. Origins may come from a single or several overlapping flaws. The exact nature of the flaw is not so definable. In $MgAl_2O_4$ and Al_2O_3 , sources are often consistent with dislocation crack nucleation mechanisms. Polycrystalline fractures originate from 1) pre-existing flaws 2) cracks nucleated by microplastic flow mechanisms or 3) microplastic flow assisting the growth of sub-critical flaws.

Flaw origins are generally microstructural extremes such as large voids, large grains, clusters of grains and voids or machining cracks. The relation of microplasticity to these features is not always clear and microcrack mechanisms may also play an important role in the growth of sub-critical flaws.

3.5.1 Ultrasonic Fractography

There are several techniques that have been used to determine crack velocity in fracture tests. For brittle failures, these velocities

can reach values of ~ 1600 m/s so that a crack can pass through a sample in a few microseconds. Techniques to measure these speeds must be quite sophisticated and high speed photography and electrical methods have been used successfully [167, 168]. Information can also be obtained from the fracture surface but this is generally not very systematic. For example, Wallner lines are produced on glass fracture surfaces when a distortional stress wave interacts with the crack front. These lines can then be used to determine the crack velocity [166].

Kerkhof and his co-workers at the Ernst Mach Institute in Freiburg have developed an elegant technique that produces artificial Wallner lines on the fracture surface in a more systematic way than the unpredictable natural lines. These artificial lines are produced by sending a beam of transverse ultrasonic waves through the sample at the time of fracture so that the fracture path is modulated and leaves a permanent 'ripple' marking on the fracture surface. Crack velocities can then be obtained easily from the spacing of the ripples and the frequency of the imposed shear wave.

The early experiments using this technique were concentrated on glasses but more recently several plastics and single crystals have been studied [168]. The ultrasonic method has advantages over high speed photography as it gives a permanent record for the whole of the fracture surface and is potentially useful for opaque solids. It also has no synchronization problems and could be modified for use in temperature or environmental studies.

Another aspect of the ultrasonic technique is that it also leaves a record of the shape of the crack front. This aspect has not been exploited before and for particulate composites, where crack shape has been identified as an important parameter, the use of ultrasonic fractography could be a most useful tool in studying crack front interactions in more detail.

(i) Theoretical Aspects

The formation of the ultrasonic lines can be explained by a working hypothesis, according to which the crack will always spread orthogonally to the maximum principal tensile stress present at any given moment (normal stress law). In this way, the crack will be guided by this principal stress and the elastic processes are 'imaged' onto the fracture surface. The mechanical wave processes are thus documented on the fracture surface and at high crack velocities, do so with very good resolution.

On the other hand, the interaction of fracture and elastic events can be used to investigate crack propagation, if the elastic waves which guide the crack are sufficiently known.

Using the normal stress law, Kerkhof [169] has outlined a theoretical treatment of these problems for the two-dimensional case, i.e., for the effect of elastic stress components in a plane perpendicular to the crack front. Mode III loading will also affect the crack path (section 2.2.3) but to simplify his treatment, Kerkhof assumes that these transverse stress components are small. In this way, the crack direction is altered only in the plane perpendicular to the crack front.

Initially, Kerkhof [169] considers ideal shock loading situations in a tensile test, where the maximum principal stress (σ_1) that was originally in the direction of the applied stress (σ_A) is altered. The superposition of these two stresses changes the magnitude of the principal tensile stress and it will now act at a different angle (γ). The change in crack direction will also be defined by the same angle. Kerkhof [169] calculates σ_1 and γ for pure compression, tension and shearing shocks. In this treatment, it is assumed that the stress intensity factor of the growing crack is the same for the quasi-static applied stress as it is for the shock front.

The direction of the shock wave is defined by the positive x' direction of the right-angled co-ordinate system (x', y') shown in Figure 46. This system is rotated against the body-fixed system (x, y) depending on the incidence of the wave. The angle between the wave normal (x' direction) and the positive x axis is α for a longitudinal wave and β for a transverse wave. The applied stress acts in the y direction so that the original crack direction coincides with the x axis for the assumed law of normal stresses. After the action of a modulated stress, the fracture surface forms an angle γ with the original direction.

For a shear shock in the x' direction, the stress components in the (x', y') stress tensor are

$$\begin{pmatrix} 0 & -\tau \\ -\tau & 0 \end{pmatrix} \quad (3.31)$$

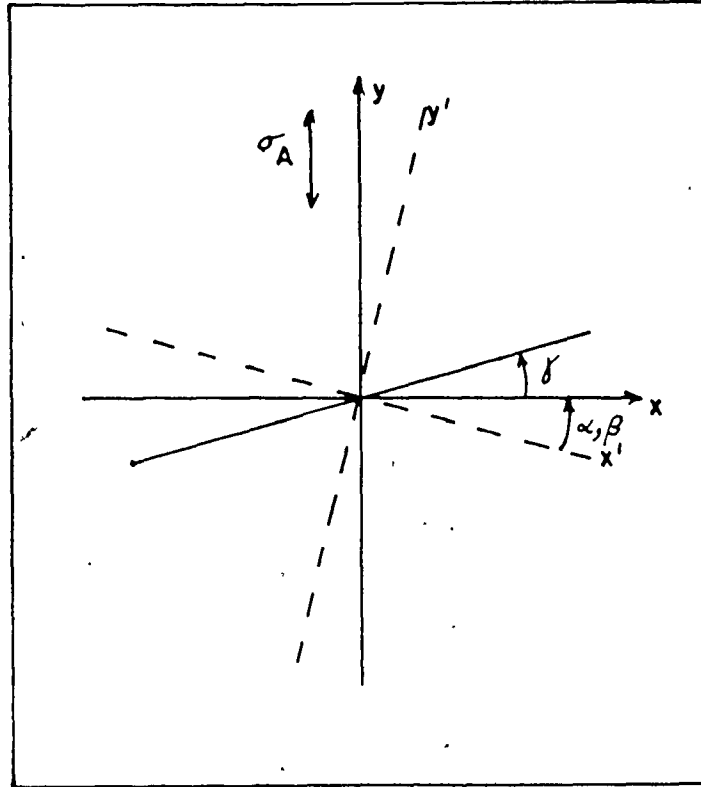


Figure 46. Co-ordinate System for the Theoretical Discussion of Interaction of Elastic Waves with a Crack Front. σ_A denotes the Quasi-static Applied Tensile Stress in the y Direction. The Normal of the Modulating Wave is in the x' Direction. The Change in Crack Direction is denoted by the Angle γ .

which transforms to the (x,y) system as

$$\begin{pmatrix} -\tau \sin 2\beta & -\tau \cos 2\beta \\ -\tau \cos 2\beta & \sigma_A + \tau \sin 2\beta \end{pmatrix} \quad (3.32)$$

The quasi-static stress σ_A is simply superimposed on the transformed σ_{yy} component. The principal stress axis is given by

$$\tan 2\gamma = \frac{2\tau \cos 2\beta}{\sigma_A + 2\tau \sin 2\beta} \quad (3.33)$$

For weak shocks this becomes

$$\gamma = \frac{\tau}{\sigma_A} \cos 2\beta \quad (3.34)$$

so that the change in crack direction depends on the ratio of the stress (τ/σ_A) and the angle of incidence of the shear shock. For weak shocks, the crack should adjust transverse to the shock direction ($\gamma > 0$) for $0^\circ < \beta < 45^\circ$ or in the direction of the shock ($\gamma < 0$) for $45^\circ < \beta < 90^\circ$. The maximum principal stress is given by

$$\sigma_1 = \frac{\sigma_A}{2} + \sqrt{\frac{\sigma_A^2}{4} + \tau^2 + p\tau \sin 2\beta} \quad (3.35)$$

It can be seen from equation (3.34) that for weak transversal waves there is no modulation for $\beta = \pm \pi/4$ and optimum modulation for $\beta = 0$ or $\pm \pi/2$.

(ii). Fracture Markings by Continuous Ultrasonic Waves.

The change in crack direction produced by pulse or shock waves can be studied from the fracture markings. This is not possible using ultrasonic waves but in this case it is possible to determine the crack

velocity instead.

An experimental set-up for this velocity determination is shown in Figure 47. A rod or plate with a cross-section of a few 10^2mm^2 and length ca. 200 mm is ruptured by a quasi-static tensile stress (σ_A). The fracture originates at the notch and the rod is exposed in the direction of tension by a transverse (shear) ultrasonic wave with its plane of polarization in the fracture plane. The maximum principal stress alters both in time and space according to the ultrasonic (US) frequency and the ratio of the sound amplitude to tensile stress. From the distance λ_b of the ultrasonic markings on the fracture surface and the frequency ν ; the crack velocity (v_b) for this experimental set-up is simply

$$v_b = \lambda_b \nu. \quad (3.36)$$

This expression can be derived by the transformation procedures used in the discussion of shearing shocks. For transverse waves, wavelength (λ_b), propagating in the x' direction with the wave number $k_t = 2\pi/\lambda_b$ and the displacement

$$f_{y'} = A \cos(k_t x' - \omega t) \quad (3.37)$$

the plane stress tensor has only shear components in the (x', y') system, i.e.,

$$\tau_{x'y'} = \tau_0 \sin(k_t x' - \omega t) \quad (3.38)$$

where $\tau_0 = AGk_t$ and G is the shear modulus.

For small amplitude waves, this gives

$$\gamma_t = \frac{\tau_0}{\sigma_A} \cos 2\beta \sin(k_t x - \omega t) \quad (3.39)$$

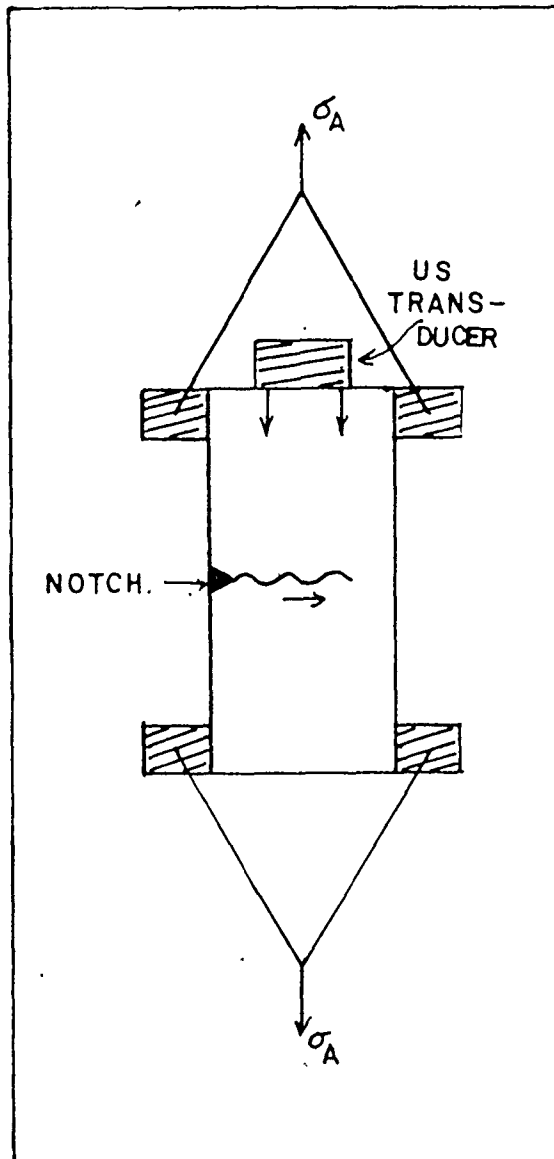


Figure 47. Experimental Set-up for the Ultrasonic Modulation of Fracture Surfaces (after Kerkhof)

This assumes that k is the same for the quasi-static stress as it is for the modulated stress. If the crack velocity is not affected by the US wave and is almost identical to its x component one obtains

$$x = v_b t \quad (3.40)$$

so that from equation (3.39) and a tensor transformation, the differential equation for a transverse wave is

$$\frac{dy}{dx} = \frac{\tau_0}{\sigma_A} \cos 2\beta \sin[(k_t \cos\beta - k_b)x - k_t \sin\beta y] \quad (3.41)$$

This is the formation law for the fracture markings under the influence of a transverse US wave where ($k_b = w/v_b$). The value of y can be assumed small ($\leq 1\mu\text{m}$) as realized in practice, and the solution of equation (3.41) can then be shown to be [170]

$$y_t = \frac{\tau_0}{\sigma_A} \frac{\cos 2\beta}{k_b - k_t \cos\beta} \cos(k_b - k_t \cos\beta)x \quad (3.42)$$

The velocity of the crack is

$$v_b = \frac{1}{\frac{1}{v\lambda_b} + \frac{1}{v_t} \cos\beta} \quad (3.43)$$

For ultrasonic waves perpendicular to the crack front, the simple expression of equation (3.36) is obtained. A similar expression is obtained for longitudinal waves but in this case the amplitude tends to zero for waves perpendicular to the front. For this reason, transverse ultrasonic waves are generally used in these modulation experiments. It has been shown by Kerkhof [171] that transverse waves parallel to the nominal fracture surface are preferable and that in this case equation [3.42] is the exact solution of equation [3.41].

In general, the US wave will also be reflected from the opposite side of the sample so that there are waves travelling in both directions with standing waves as a consequence. For $\beta = 0$ the profile curve is

$$y_1 = \frac{\tau_0}{\sigma_A} \frac{\cos(k_b - k_t)x}{k_b - k_t} \quad (3.44)$$

and for $\beta = \pi/2$

$$y_2 = \frac{\tau_0}{\sigma_A} \frac{\cos(k_b + k_t)x}{k_b + k_t} \quad (3.45)$$

The nodes of these profiles are different and the determination of crack velocity is complicated. For the resultant standing wave, the profile curves of equations (3.44) and (3.45) must be superimposed. For crack speeds which are much less than the wave velocity ($k_b \gg k_t$), the amplified profile curve becomes

$$y_A = \frac{2\tau_0}{\sigma_A k_b} \cos k_t x \cdot \cos k_b x \quad (3.46)$$

For this situation, there are two sets of superimposed US fracture marking with spacings given by

$$\left. \begin{aligned} \lambda_t &= v_t/v \\ \lambda_b &= v_b/v \end{aligned} \right\} \quad (3.47)$$

For this experimental set-up, it is therefore also possible to calculate v_t and elastic constant data from the US interference fields. It is usually very difficult to conduct experiments under the requirements of this two-dimensional theory. Kerkhof [169] has extended his discussion to situations where the crack direction involves the third dimension. The situation is more complicated since the fracture markings do not

coincide with the true crack front positions. If $\lambda_t \gg \lambda_b$, however, coincidence will return as the crack front can be considered stationary relative to the wave velocity.

For transverse waves at right angles to the crack, waves will also travel in both directions. The two wave profile will have a phase constant involved which depends on the geometry of the test. Provided the phase difference of the two waves is approximately the same at the fracture surface, the simple expression of equation (3.36) is obtained [169]. Klüppers [172] has shown that the limiting crack velocity is not affected by the US waves for this testing geometry.

(iii) Experimental Details

Kerkhof and his co-workers generally use the experimental set-up previously shown in Figure 47. For this set-up, the expression $v_b = \lambda_b \nu$ can be used and to determine crack velocity, a good photographic reproduction of the fracture markings and the US frequency is needed. The error in the frequency measurement is generally <1% for commercial devices so it is generally the measurements of λ_b which are important.

The most suitable method for photographing the fracture surface is the incident light-shadow method based on a defocussed image of the fracture surface and is illustrated in Figure 48. The ripple markings are very shallow but they can act as parabolic cylindrical mirrors to focus the light on the reference planes R_o and R_u as line foci. The magnification may be error by this technique since the surface (O_b) does not coincide with R_u or R_b . Interference microscopy is also very useful

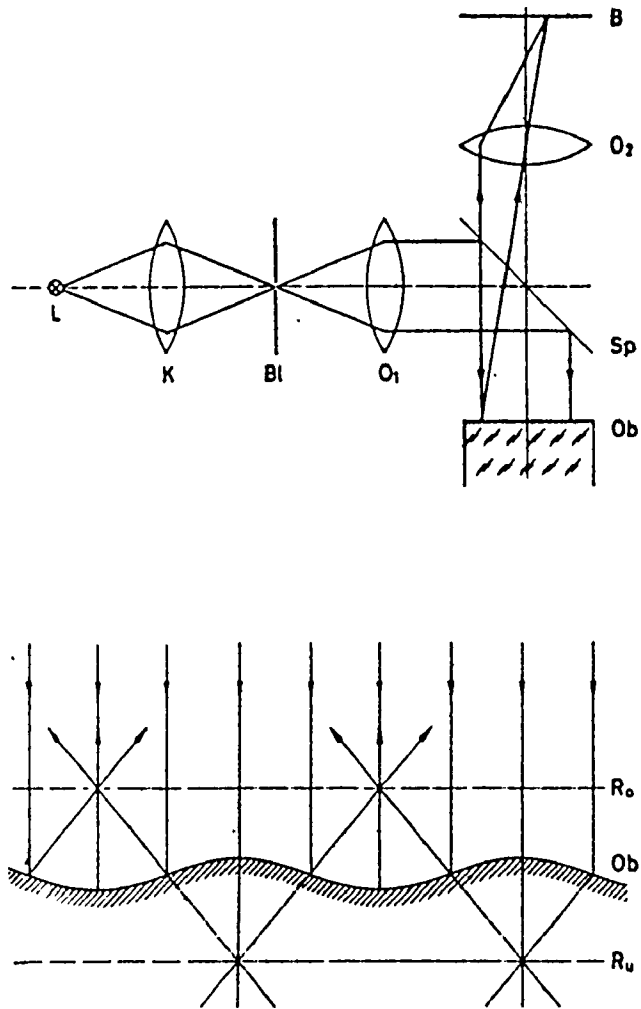


Figure 48. Principle of Viewing the Ultrasonic Lines using a Defocused Optical Image.

in studying the surface topography. For electron microscopy, larger surface deflections may be needed to obtain acceptable image contrast. Figure 49 shows the modulated fracture surface from a glass plate broken in tension. The ripple markings are visible to the naked eye but are fine enough to evaluate the crack velocity.

In order to drive the US transducer, a transmitter of 100 - 1000W has to be used. For glass samples, an intensity of $\sim 0.1 \text{ W/mm}^2$ should give acceptable results, though in detail, this depends on the material's properties, e.g., the elastic constants, strength, ultrasonic attenuation, the fracture velocity and frequency. In some materials, plastic deformation may result from heat production and dislocation processes [173].

The transducer has to be water-cooled and cemented to the sample. It is important to get as much power as possible from the transmitter into the transducer and from the transducer into the sample.

The method of ultrasonic fractography is only applicable to fractures that give smooth fracture surfaces and for materials with low attenuation coefficients. Greenwood [174] suggests that the specimen dimensions must be large in comparison with λ_t . Shorter wavelengths, or higher frequencies yield more information, but these factors also tend to reduce the wave intensity and are therefore less capable of deflecting the crack.

Ultrasonic fractography has been used extensively in Germany and most references appear in the German literature. Kerkhof [169] has reviewed these developments in his book. In the English literature,

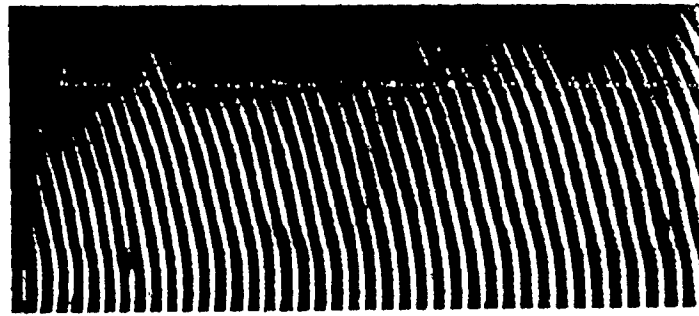
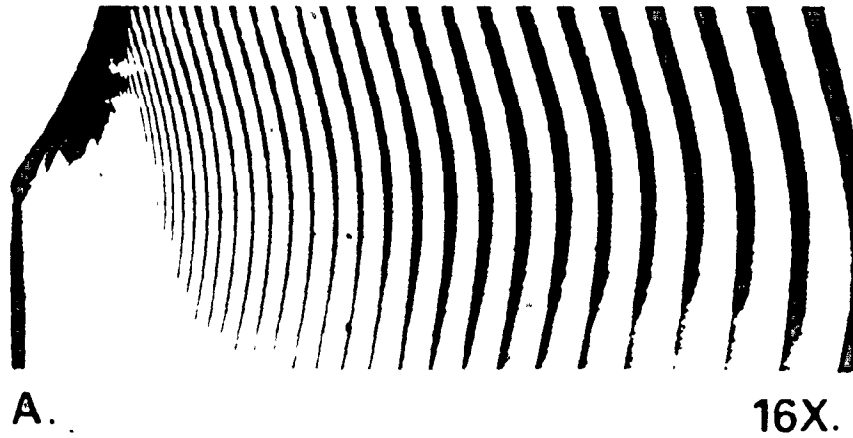


Figure 49. Ultrasonically-modulated Fracture Surfaces for Two Samples broken under Tension. Specimen a) courtesy of Dr. F. Kerkhof, Freiburg, b) courtesy of Dr. J. E. Field, Cambridge.

the technique has been discussed by Field [168], Erdogan [175], Schardin [176] and Kerkhof [177, 178] and has been used to determine fracture speeds in silicon and germanium [174], glass [179, 180], perspex [181], tungsten [182] and magnesium oxide [183].

CHAPTER 4

EXPERIMENTAL PROCEDURE

4.1 Materials

4.1.1 S Glass

The glass/nickel composite system is a model composite where control of interfacial strength, expansion coefficient mismatch and particle size is easily attained, [74]. For this work, one system was chosen - the S glass/nickel system. In this composite, no interfacial bonding exists as it has been shown [184] that unoxidized nickel is not wetted by the glass. Furthermore, no internal stresses should exist because the thermal expansion coefficients of the glass and the nickel are the same. The relevant properties of the S glass and the nickel are presented as Table 13. From the $\text{SiO}_2 - \text{Al}_2\text{O}_3 - \text{Na}_2\text{O}$ phase diagram (Fig. 2) we see that the S glass composition has a liquidus temperature of 940°C in the nepheline phase field. It is located near the ternary eutectic (760°C) in the Alkemade triangle, nepheline - sodium silicate - sodium disilicate.

The S glass was formulated from silica, sodium carbonate and alumina.* These raw materials were dry-mixed in a tumbling mill and then melted and fired in a fireclay crucible at $\sim 1450^\circ\text{C}$ in an electric glo-bar furnace. During the heating, the powders were calcined at 700°C for 4 hours before the temperature was raised to 1450°C . This calcination as

* Neutral Alumina (80-200mesh)
Anhydrous sodium carbonate
Silica (Floated power 240 mesh)

TABLE 13. Material Properties.

Material.	Composition. (wt %)	Expansion Coefficient (in/in °C x 10 ⁶)	Young's Modulus. (psi x10 ⁻⁶)	Poisson's Ratio.
Nickel		13.9	30.0	0.42
S Glass	55SiO ₂ 15Al ₂ O ₃ 30Na ₂ O	13.8	9.8	0.20

suggested by Lange [9] reduces excessive water and gas absorption during melting, which subsequently influences the hot pressing behaviour of the powder. The melt was allowed to fine for 6 hours and was then cast into cold graphite molds. The cast blocks invariably suffered thermal fracture but because the glass was to be ground, this was advantageous.

Initially, grinding was carried out in an alumina-lined ball mill with alumina balls. There proved to be problems of gas evolution in the hot-pressing of such powders so it was decided to keep the grinding process completely dry. The grinding was carried out by passing the coarse glass through a jaw crusher and then through a pulverizer.* The powders were magnetically separated after grinding. The final powder was coarser than that produced by ball-milling (generally <325 μm) and this aids in reducing the gas evolution problem. Even after such elaborate precautions, the powder still gave rise to bubbling during the hot-pressing. The powders were therefore given a further heat treatment by remelting in a vacuum furnace at 1100°C. The melt was then re-ground. Although the glass powder preparation was elaborate and time-consuming, it gave powders which were more amenable to vacuum hot pressing. The glass powder was characterized by density measurements (Appendix A.8) and chemical analysis.

P

4.1.2 Nickel

The nickel was purchased as smooth spherical particle powders from Sheritt-Gordon Ltd.** The particle size distribution of the

* BICA type UA pulverizer

** OSI 100 x 150 grade powder

particles was determined by projected diameter measurements from SEM micrographs. Chemical analysis and density measurements were also made on these powders.

4.1.3 Other Materials

Pyrex* and window glass plate was purchased for standardization of the fracture toughness testing arrangement.

4.2 Fabrication and Machining

4.2.1 Hot Pressing

Appropriate fractions of the S glass and nickel were thoroughly mixed in a plastic bottle containing teflon balls for 16 hours. These mixtures were placed in a graphite die and plunger arrangement and vacuum hot-pressed to form composite discs. Figure 50 shows the hot pressing arrangement. The die was positioned centrally between the plungers in the vacuum chamber. A Pt - Pt/10% Rh thermocouple inserted in the die body, was used to measure the temperature and the system was evacuated to less than 0,2 Pa. Induction heating was employed using a 6.2 mm copper coil attached to a Tocco RF generator. A linear differential transformer attached to the upper plunger was used to measure the sample's compaction. The temperature was raised slowly to 400°C and then a small pressure of 0.28 MPa was applied to the powder. It was found that this procedure helped to suppress the evolution of absorbed gases, the major problem in

* Corning Code 7740. Composition (wt%) 81 SiO₂, 2Al₂O₃, 4 Na₂O, 0.5 K₂O, 13 B₂O₃

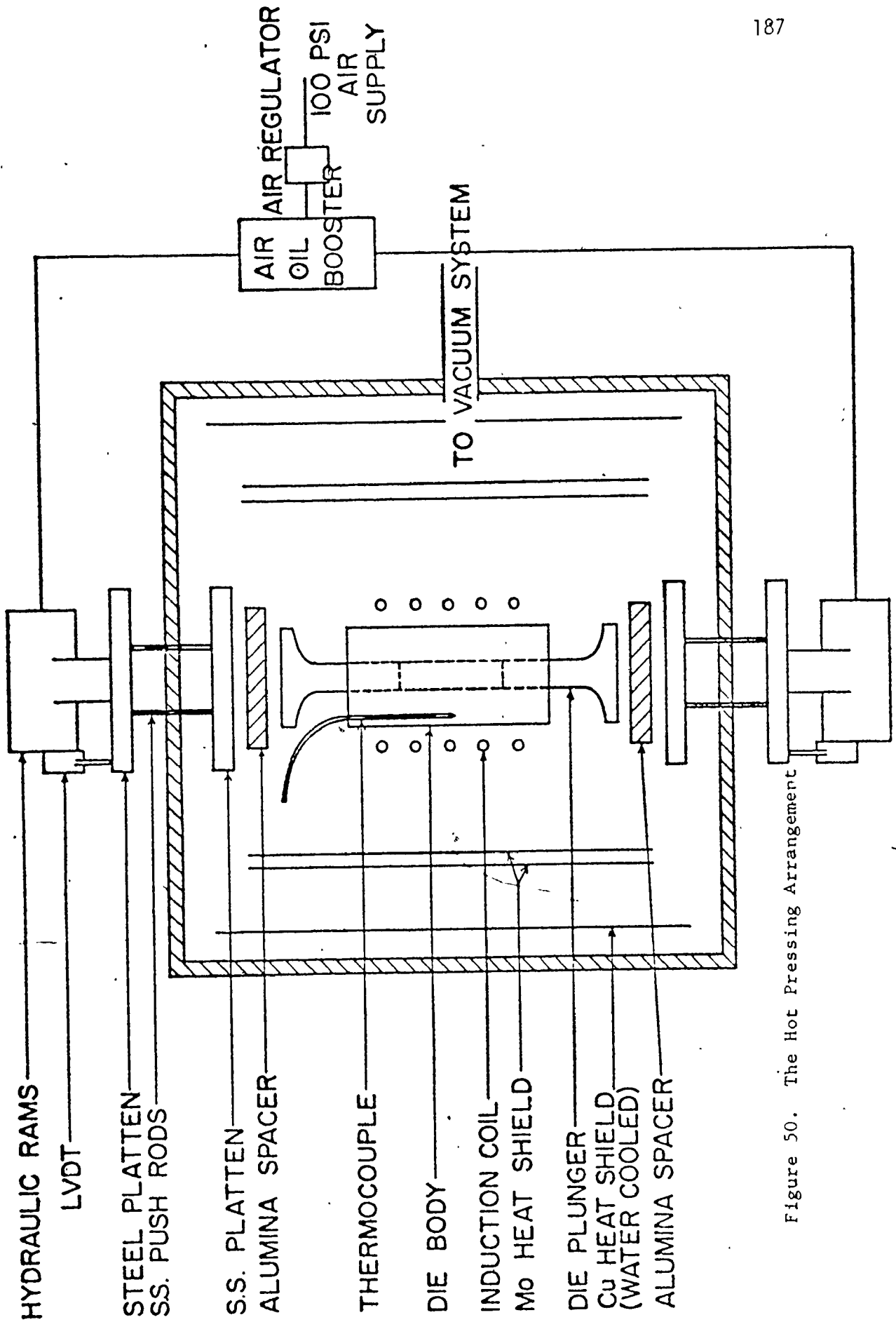


Figure 50. The Hot Pressing Arrangement

the hot pressing of glass powders. The temperature was then raised slowly to 680°C when densification under the small load ceases. At this point, a pressure of 7 MPa is applied for 15 minutes. After pressing, the temperature was cooled slowly at 500°C for a 15 minute anneal. The furnace was then turned off, allowing the sample to cool with the free rate of cooling of the furnace (~17°C/s). Several attempts were made to design a graphite mold which reduced the difficulty in removing the hot-pressed disc from the die and minimize the possibility of sample fracture. Eventually, a cylindrical die with a slight inside taper to a position just above the sample was found to reduce the sample damage. Polished graphite spacers were placed between the plungers and the sample. Polishing of the inside of the die body also increased the ease of sample removal.

The hot-pressed samples were annealed at 500°C for 2 hours to remove any residual stresses produced by fabrication. The composite disc appeared black after hot pressing because some of the graphite contaminates the surface of the disc. After polishing the discs remain very dark but it could be seen that small sections of the glass were transparent but with a blue/green tint. This coloration is probably due to iron contamination picked up during the melting and grinding stages.

It was found that the vacuum hot pressing of such composites can be very difficult unless precautions are taken. Absorbed gases tend to be evolved during the hot pressing especially under vacuum conditions giving rise to a very porous glass. Figure 51 shows polished sections of two glasses that were produced with and without the heat



Figure 51. Polished Sections of S Glass i) Without Heat Treatment (below)
ii) With Heat Treatment.

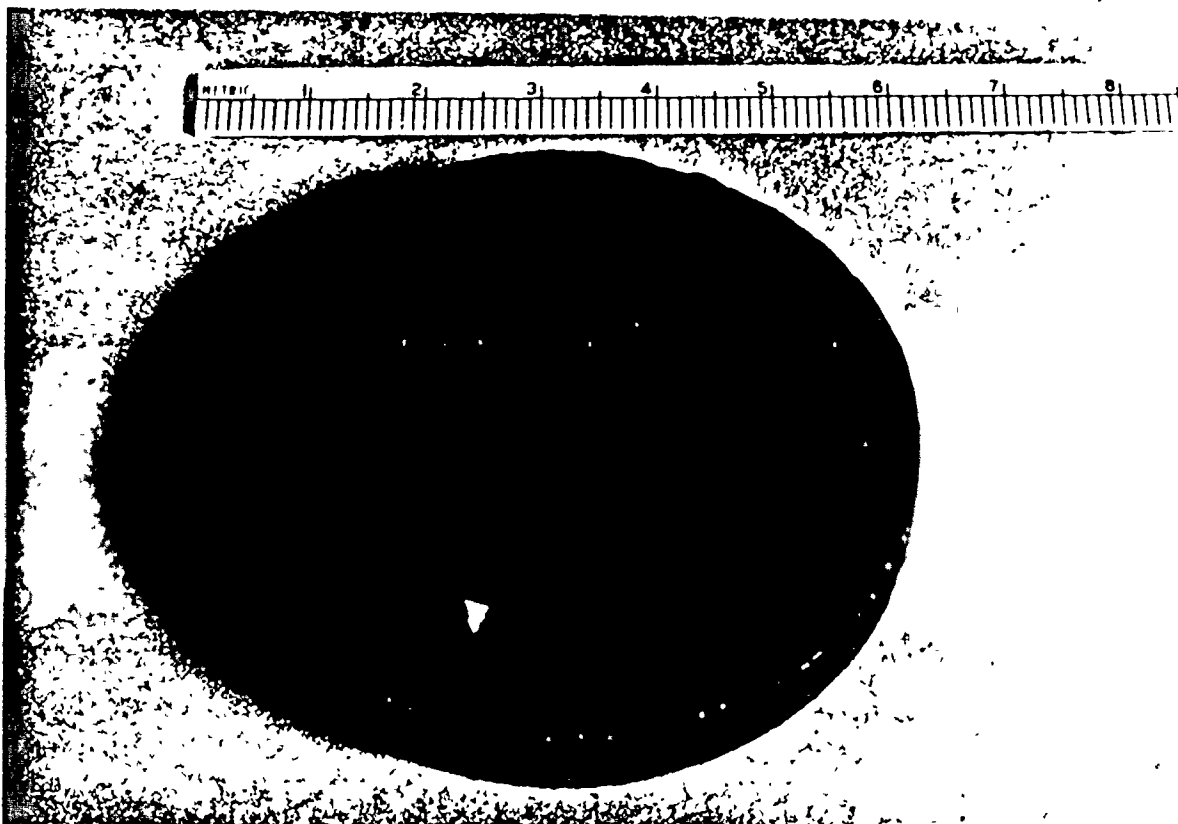


Figure 52. Example of Hot Pressed Glass Disc with Established Procedure.

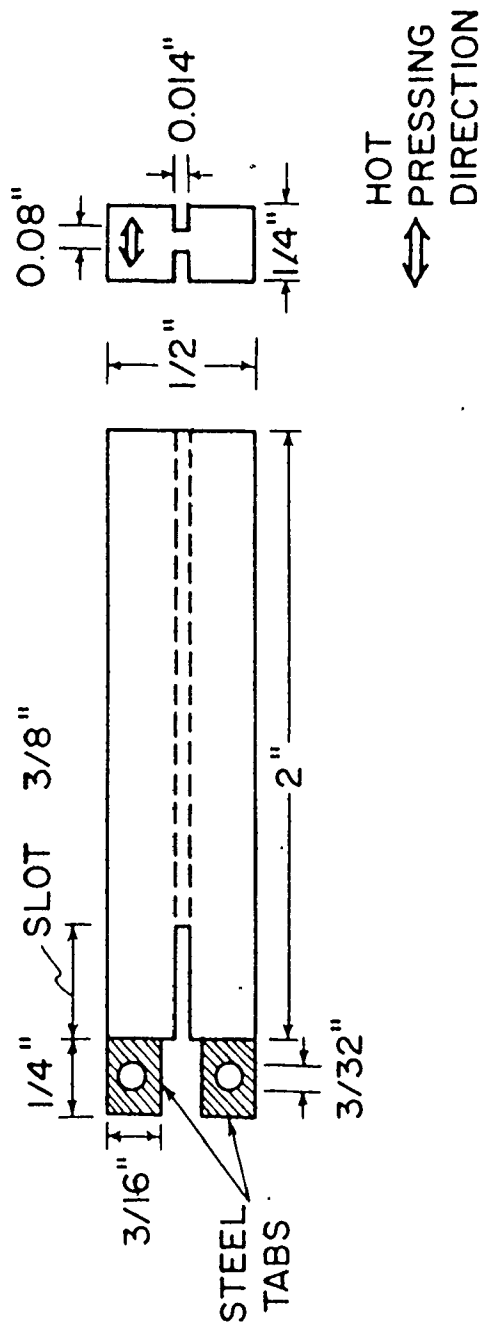
treatment. Figure 52 shows an as-pressed sample produced with the described precautions.

4.2.2 Machining

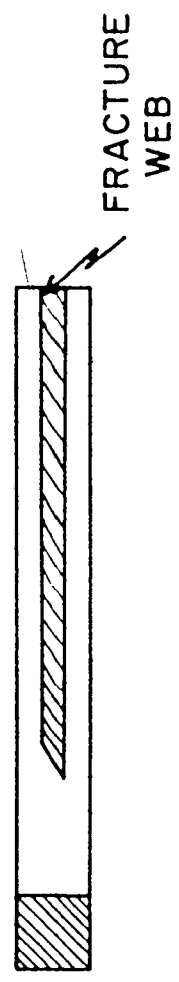
The composites were diamond-machined* into samples suitable for fracture testing. (Figure 53). The samples were side-grooved because in the double cantilever testing technique (DCB), there is a tendency for the crack not to run down the sample but to veer off to the edges. The special semi-swallow tail notch configuration aids in the pre-cracking of the notched sample. Because it is quite difficult to drill glass samples, it was decided that drilled steel tabs could be glued to the sample (5 minute epoxy). This complicates the elastic response of the sample slightly but decreases the machining problems. A typical machined sample is shown in Figure 54. The geometry of the side groove tip produced by diamond machining is shown in Figure 55. Fracture samples were also machined from the pyrex and window glass plate.

Samples for fracture toughness testing were pre-cracked, as is necessary for a valid K_{IC} determination. A special wedge-loading jig was designed and made for this purpose and is shown in Figure 56. The side screws and plates allow a small compressive load to be placed on the sample which aids the subsequent arrest of the pre-crack. For transparent glasses, the pre-crack is easily visible as it grows. For the glass/nickel composites this procedure was not possible but it was discovered that as the pre-crack forms or as the crack moves there is

* Micromatic Precision Wafering Machine



(a) DCB SPECIMEN SIZE



(b) NOTCH CONFIGURATION (SEMI-SWALLOW TAIL)

Figure 53. Machining Details for Fracture Samples.

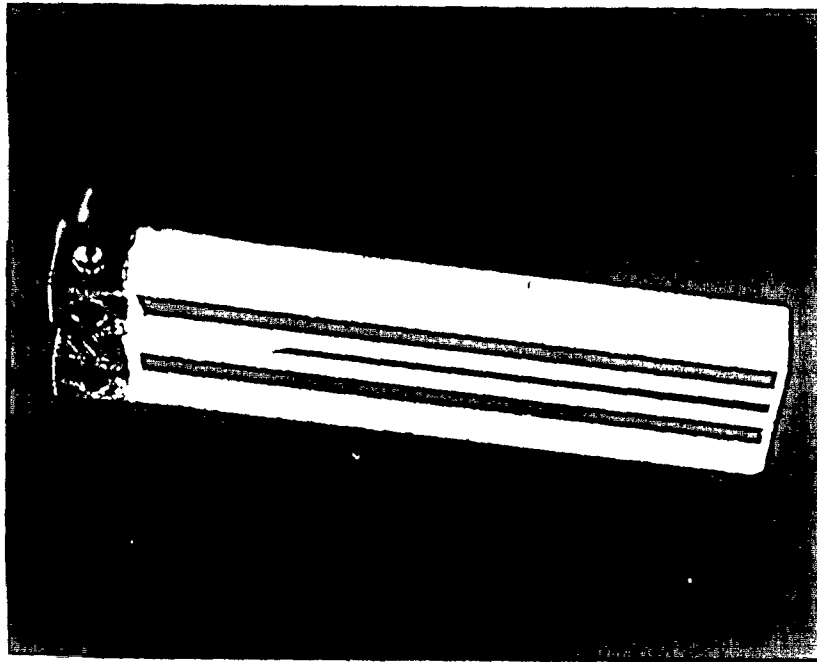


Figure 54. Machined Pyrex Sample with Steel Loading Tabs.

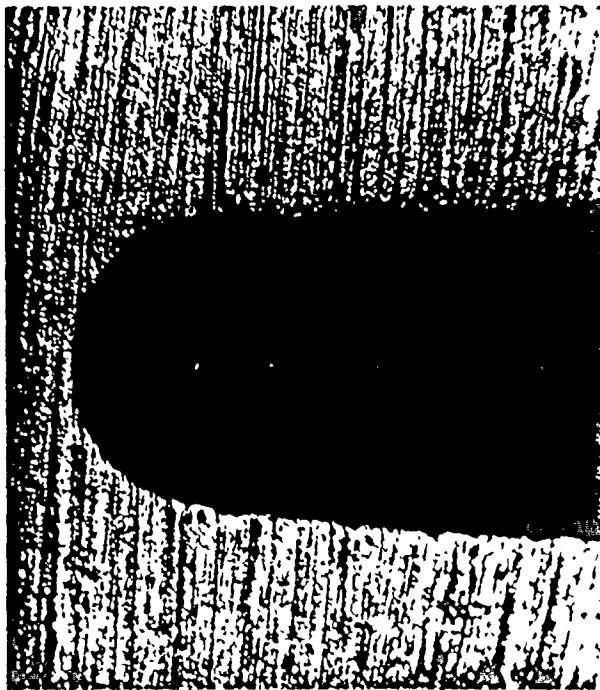


Figure 55. Tip of Machined Side Groove (Magnification 50x)

there is an audible click, allowing the production of a pre-crack to be determined. Figure 57 shows the device used for accurate attachment of the steel tabs. After machining, the samples were annealed again (450°C) to remove any stresses produced in this process. Lange [9] suggested that this anneal reduces the scatter in the fracture energy determination.

The density of the hot-pressed samples were measured by the Archimedes water-displacement technique (see Appendix A.8). A thin section of a high volume fraction composite was analyzed in a polarizing microscope with a sensitive tint plate to determine if any internal stresses were present in the as-fabricated materials. Polished sections were also made from each hot-pressed sample using emery papers and diamond-impregnated cloths. These sections were then analyzed on a Quantimet microscope to make a quantitative determination of the microstructural stereological parameters. It was found unnecessary to etch the samples for this purpose since there was high contrast between the glass and the nickel. A few samples were etched, however, to show the internal structure of the nickel spheres. The etching solution is given in Table 14 and is a slight modification of the one suggested by Greaves and Wrighton [185].

4.3 Determination of Young's Modulus

The Young's modulus of the composite samples was determined from measurements of the longitudinal sound velocity in the material. (see Section 3.1.1). The precision of these measurements is generally

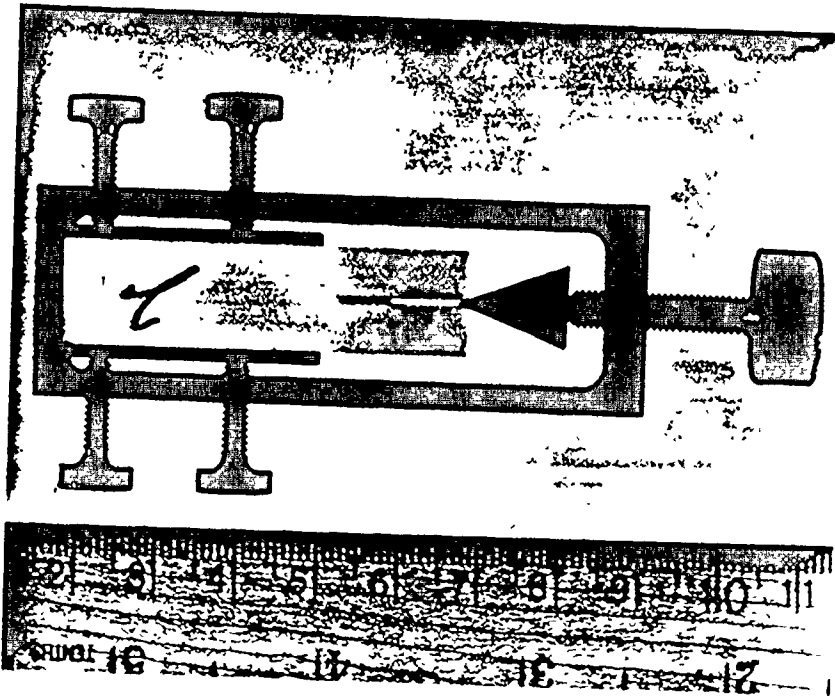


Figure 56. Wedge Loading Jig for Pre-cracking Fracture Samples.

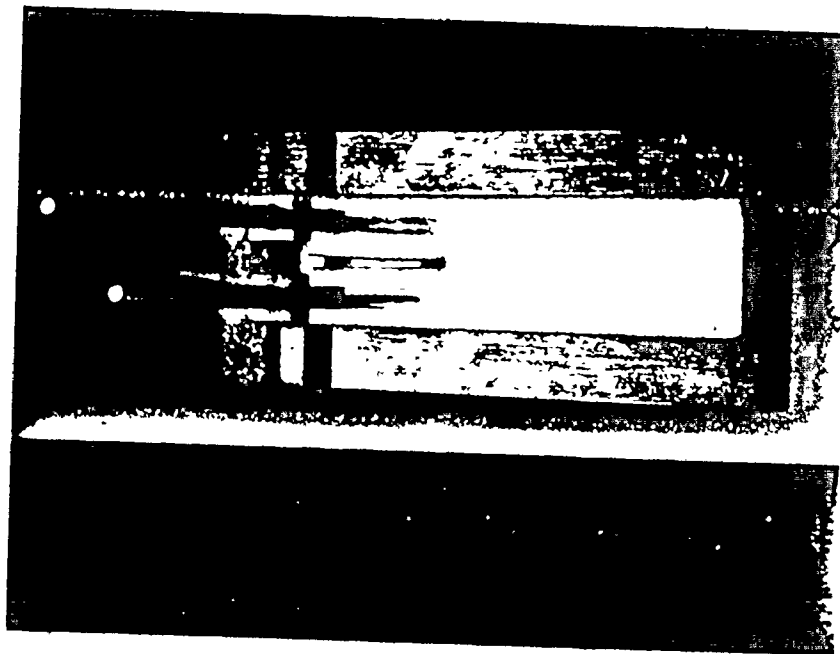


Figure 57. Jig for Accurate Attachment of Metal Loading Tabs.

TABLE 14. Etching Soution for Nickel

50 cc Nitric Acid (spec. gravity 1.42)
25 cc Glacial Acetic Acid.*
35 cc Distilled Water.

* The acetic acid must be added slowly to the diluted
nitric acid.

within 5%. The transmitter/receiver were 6mm SC_J crystals with frequencies of 2 1/4 and 5 MHz. The transmitted and reflected pulses were monitored on a Sperry UM775 Reflectoscope which had been calibrated with a Tektronic 549 oscilloscope. The accuracy of these measurements was determined using a pyrex standard for comparison with the literature values. The value of the Young's modulus is necessary for fracture energy determinations but for the analysis used, both the fracture energy and K_{IC} determinations are only weak functions of Young's modulus. The above-discussed accuracy was sufficient for the required determinations. Approximate values were also obtained from the flexure strength tests.

4.4 Determination of Room Temperature Fracture Energy

The fracture toughness parameters K_{IC} and γ were determined on the pre-cracked diamond machined samples. The loading rig was the double cantilever beam (DCB) which has been used extensively in fracture studies of ceramic materials (see Section 3.2). The loads encountered in the testing of brittle materials are often very low (less than 4.5 kg), so adequate precautions must be taken to reduce friction and the alignment load. Furthermore, the loading should be mode I, if other modes are present the fracture parameters determined will be in error. With these factors in mind, a rig was designed similar to that used by Hoagland et al [144] and is shown in Figure 58. A counter balance minimizes the effect of the sample weight and a hinged lower grip ensures vertical alignment. The top and bottom grips were aligned prior to

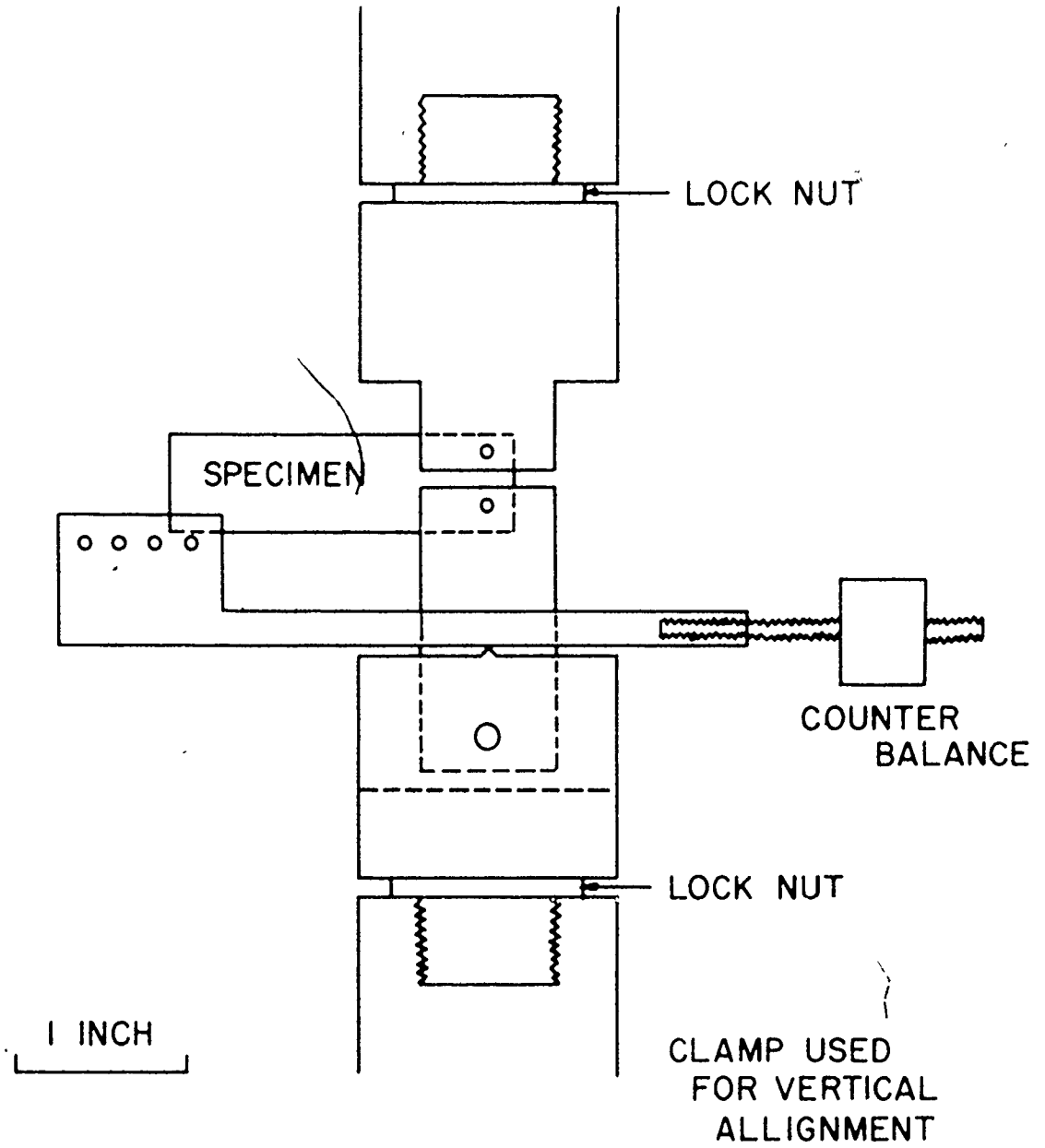


Figure 58. Design for DCB Loading Fixture.

testing with a template. The aligned rig and clamp is shown in Figure 59.

For glass/metal composites the restrictions on specimen size are minimal as there are no plastic zone complications. The ratio of crack or ligament length(L) to beam depth (t) however, should be greater than 1.5 for a valid determination.

The fracture toughness parameters can be determined from load and crack length or load and deflection measurements taken at the point when the loading becomes critical. For the pyrex and window glass samples, all three parameters were monitored but for the composite, where crack length measurements were difficult, the fracture toughness was determined from load and deflection measurements. The testing was carried out on an Instron Universal Testing machine* using an extensometer** to monitor the sample deflection at the loading points and load cell*** to measure the applied loads. The extensometer arrangement is shown in Figure 60. Special extensions were made to allow the use of the extensometer with the rig design. The extensometer complicated the analysis slightly as it is spring-loaded and applies a small compressive load to the sample. This problem was overcome because in most tests the extensometer was still attached to the sample for a short time after failure and the compressive load can be measured on the recorder. It was found to be approximately constant with a load of 0.52 kg. Crack length measurements were made using a

* Instron Corp. Canton, Mass. Floor model testing machine (TT-C)

** Instron strain gauge extensometer type G57-11

*** Instron Load cell (type CT) max range 200 lb

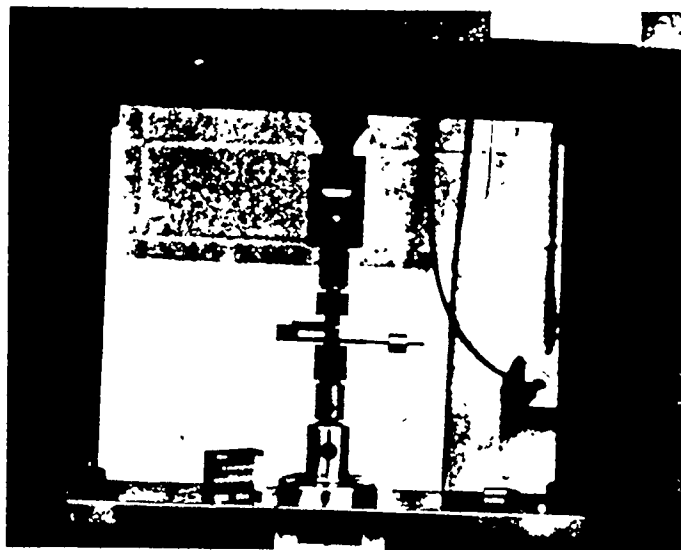


Figure 59. DCB Loading Fixture after Alignment on Instron Testing Machine,

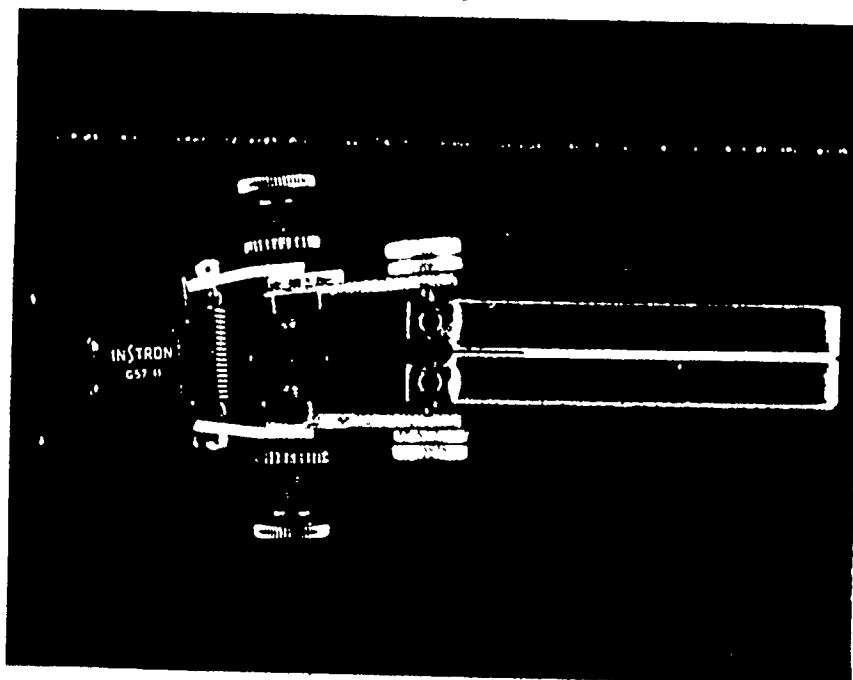


Figure 60. Extensometer Arrangement for Measurement of Sample Deflection during Fracture Testing.

travelling microscope to view the crack arrest lines visible on the fracture surface of the broken samples. The fracture toughness parameters can be determined using equations (3.11) and (3.20).

Many preliminary tests were made on the pyrex and window glass samples, to determine the precision and accuracy of the testing technique. The effect of cross-head speed and environment (toluene) in particular, were studied as glasses are often suspected to slow crack growth and its associated errors. Immersion in toluene reduces the effect of slow crack growth to a very small amount [186]. The results on pyrex could then be compared to values previously obtained in the literature and the accuracy assessed.

For the DCB test with a stiff loading system, the crack propagation should be stable (see section 3.2) and should allow more than one value of the fracture toughness parameters to be determined per sample. Alternatively, the crack resistance force (R) can be monitored in a continuous fashion for such a system. In pure S glass it was found that crack arrest was difficult unless the cross head was reversed immediately after the critical load. Presumably, either the machine stiffness was too low or the occurrence of slow crack growth just below the critical loads led to this behaviour. It was possible however, to monitor the crack resistance in a continuous fashion so presumably the instability was only transient. For the composite materials, crack arrest was more easily attained.

The fracture toughness parameters were determined for the S glass/nickel system up to 20 volume percent nickel at a crosshead speed of $0.8 \mu\text{m/s}$.

4.5 Strength Measurements

Four point flexural strength was measured at room temperature on samples polished from the broken DCB samples. The rig and specimen size was designed to reduce errors due to such problems as alignment, friction and incorrect stress analysis (see Section 3.3.1). The inner and outer load points were 25 and 38 mm respectively. These points was 8 $\mu\text{m/s}$ tool steel rods located in grooves. The cross head speed utilized was 0.02 in/min. The loading fixture is shown in Figure 61. The hemi-spherical ball and cavity was included to insure proper alignment of the fixture.

The strength was measured to determine the relationship between fracture energy, Youngs modulus strength and microstructure and for comparison with strength data for the S glass/nickel system of Stett and Fulrath [74]. At least six samples were broken for each volume fraction of nickel.

4.6 Ultrasonic Modulation of Fracture Surfaces

This technique of ultrasonic modulation of fracture surfaces has been used extensively in measurements of crack velocity (see section 3.5.1). In this approach, a transverse ultrasonic wave of known frequency is transmitted through the sample during fracture. The US wave imposes an additional oscillating tension on the crack front and causes the crack trajectory to modulate in response, producing ripple markings on the surface. In this way, a permanent imprint is made of the crack front and the spacing at the ripples record the crack velocity. More importantly for this work it also records the crack shape. As pointed out by Lange [111] and Evans [113], crack shape may be of great

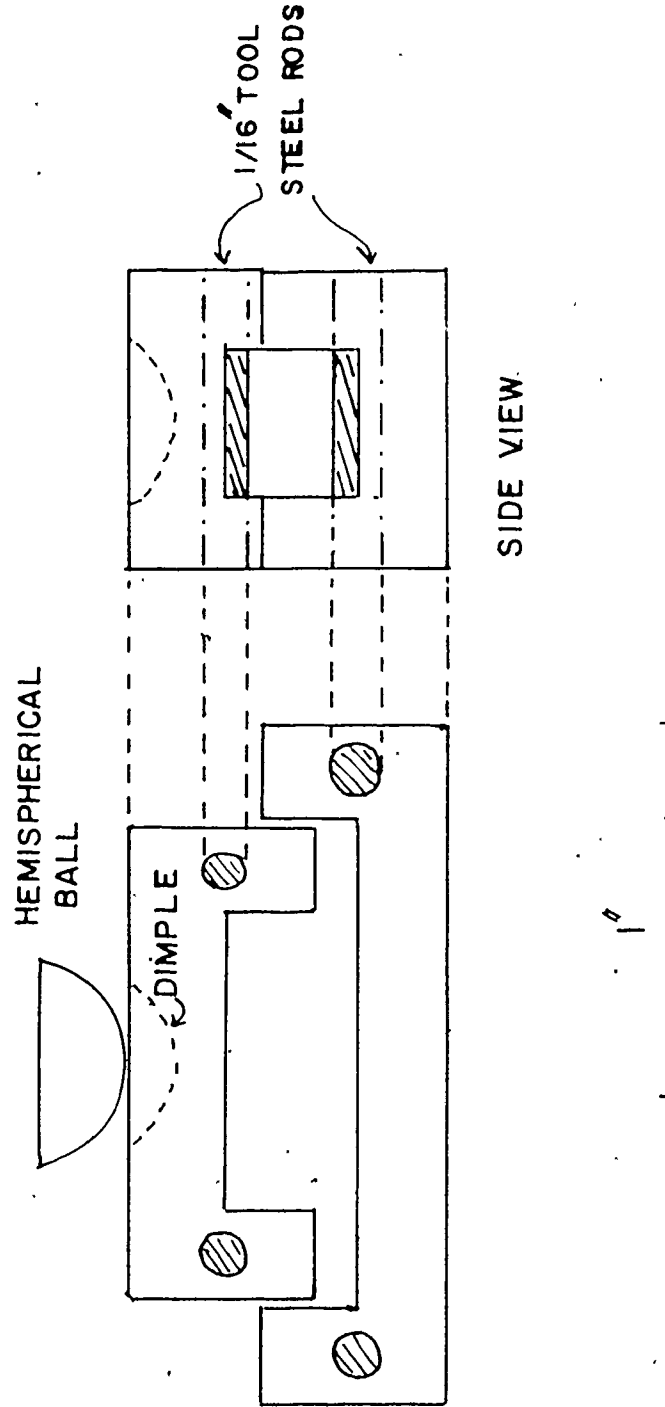


Figure 61. Design for Four Point Bend Strength Testing Rig.

great importance in the fracture resistance of brittle materials especially particulate composites and the technique of ultrasonic modulation provides a detailed insight into this aspect of crack propagation.

The technique does, however, provide experimental difficulties because the ultrasonic waves have to be reasonably strong to modulate a growing fracture. Typical power supplies need output power in the range 500-1000 watts and the transducer must be designed to reduce the possibility of dielectric breakdown and overheating while allowing as much of the power as possible to enter the sample ($\sim 0.1 \text{ W/mm}^2$). The design of the transducer and the power supply were based on the designs suggested by Kerkhof and Schinker [187] with slight modifications for components which were not readily available.

The design for the piezoelectric transducer is shown in Figure 62. The piezoelectric was 19 mm diameter, Y-cut quartz crystal* with a basic frequency of 1 MHz. The crystal was sealed with epoxy to the water cooled ground terminal with the direction of shear such that it would be parallel to the direction of crack propagation. A thin disc of teflon foil was used as insulation between the terminals. It was suggested that the distance between the quartz crystal and the surface of the aluminium plate should correspond to an integral number of half wavelengths of the US wave velocity in aluminium. In this way, the electrode should resonate allowing more power to enter the sample. For transverse US waves, the sample must be glued to the transducer to

* Valpey Fisher, Molliston Mass

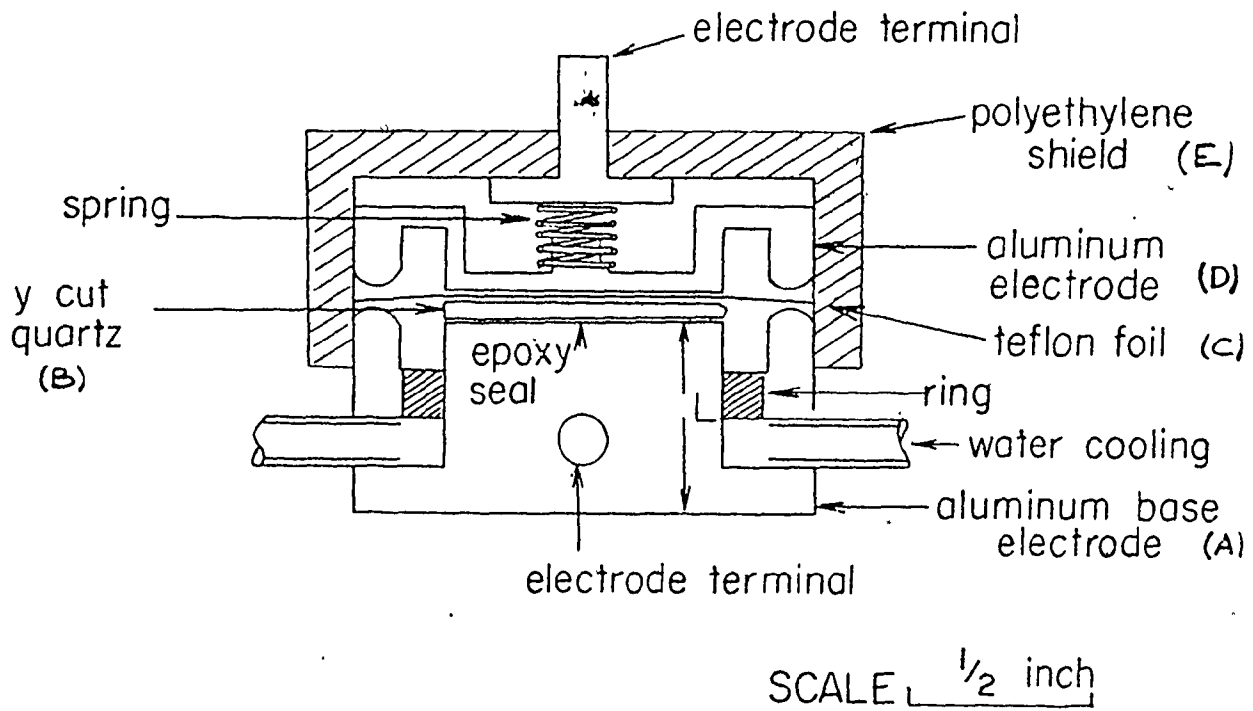


Figure 62. Design for Ultrasonic Transducer.

allow the waves to cross the interface. An exploded view of the transducer is shown as Figure 63.

The circuit design for the power supply is shown in Figure 64. The main modification to the design provided by Kerkhof and Schinker [187] was the introduction of a silicon diode rectification bridge compared to their valve rectification. The major component of the installation was the hand-wound silver-plated copper wire coil. The alumina body was purchased from Norton* and the copper wire was plated at McMaster. The plating solution was found from the literature [188] and the technique of application was based on a suggestion by J. Fairhurst [189]. Extreme caution was used in the plating procedure particularly to ensure the solution was alkaline because HCN can be evolved from acidic solutions, and to avoid any contact between the solution and one's skin.

The electronics of the finished power supply is shown in Figure 65. The high voltage supply is in the lower rack with the resonating circuit is shown in Figure 66.

For the fracture testing, the transducer is mounted with epoxy to the DCB sample. The water was circulated through the transducer with a vibrostatic pump.** The loading rig with the transducer attached is shown in Fig. 67. Initially, the transducer was mounted on top of the sample but it was found that this imposed constraint on the flexure

* Norton, Worcester, Mass. Dial-a-core Alundum tubes (for furnace windings)

** Lab Apparatus Co., Cleveland, Ohio, Vibrostatic Pump (8255603)

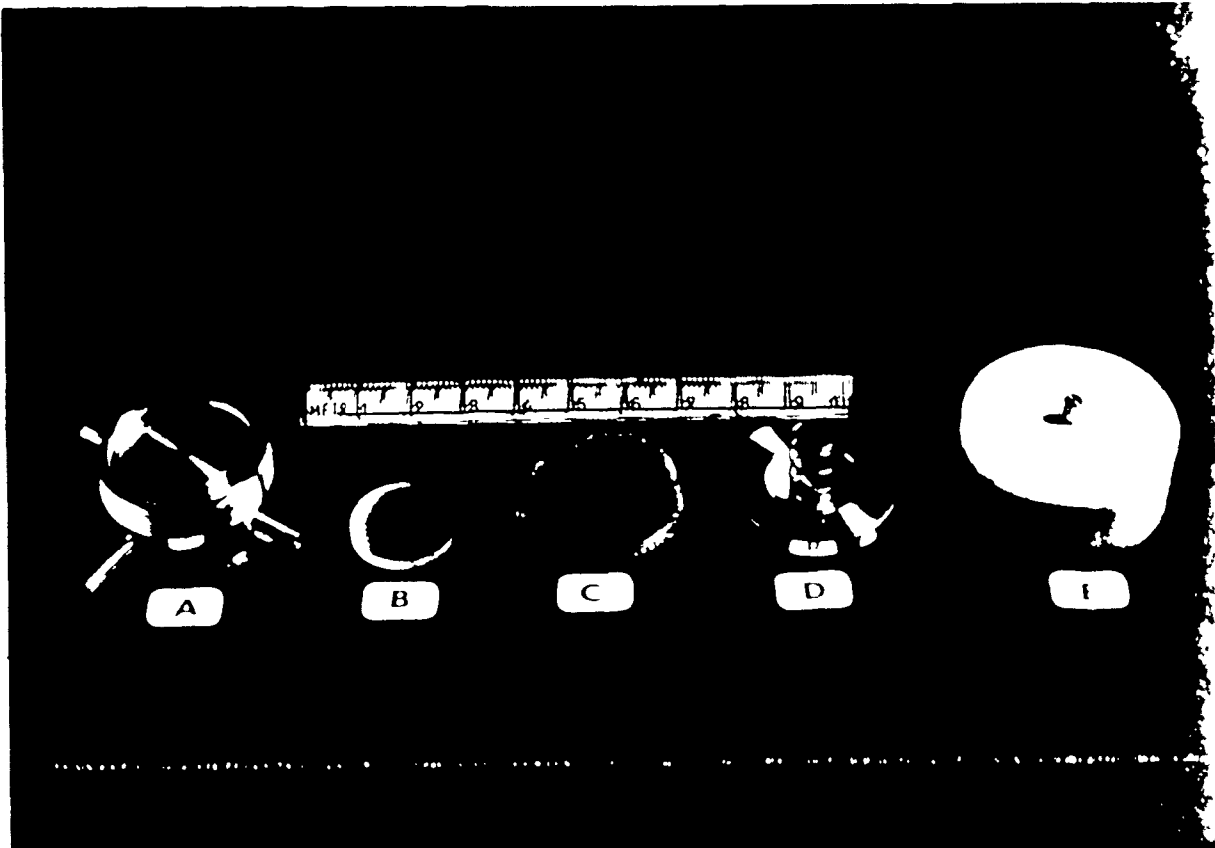


Figure 63. Exploded View of Finished Transducer.

CIRCUIT COMPONENTS.

L 60 turns of silver-plated 80 AWG copper on an alumina body: Diameter $4\frac{1}{2}$ in. Length $13\frac{1}{3}$ in.

207

$C_1 C_2$ - 6.8 nF / 3.3 kV

C_8 - 6.8 nF / 7 kV

C_3 - 20 nF / 6 kV

$C_9 C_{10}$ - 1.5 μ F / 6.3 kV

$C_4 C_5$ 500 pF / 15 kV

R_1 - 12 k Ω / 120 W

$C_6 C_7$ var. cap. 42-150 pF / 20 kV

$R_2 R_3$ - 25 Ω / 50 W

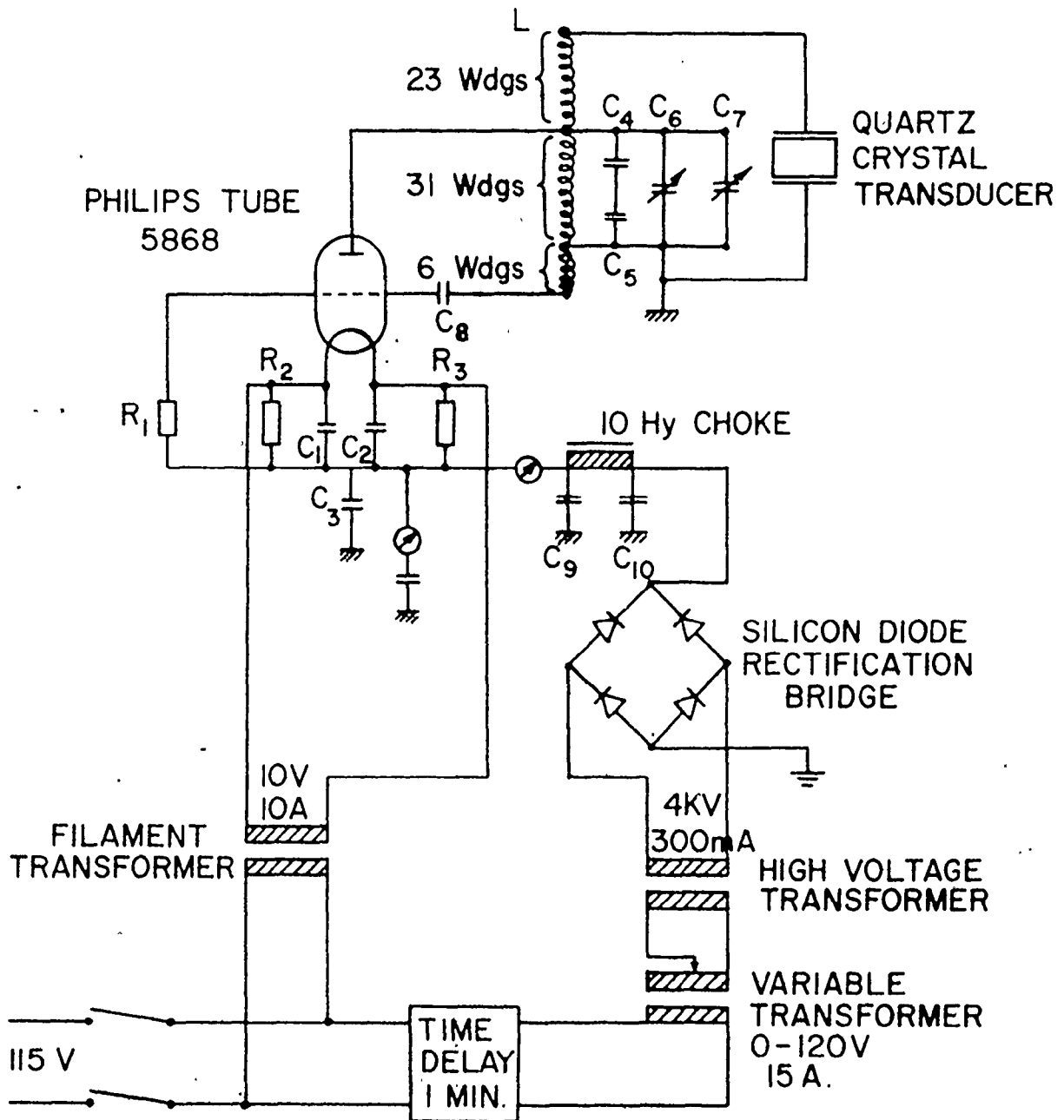


Figure 64. Circuit Design for Power Transmitter (adapted from Kerkhof & Schinker)



Figure 65. Arrangement of Electronics in Power Transmitter.

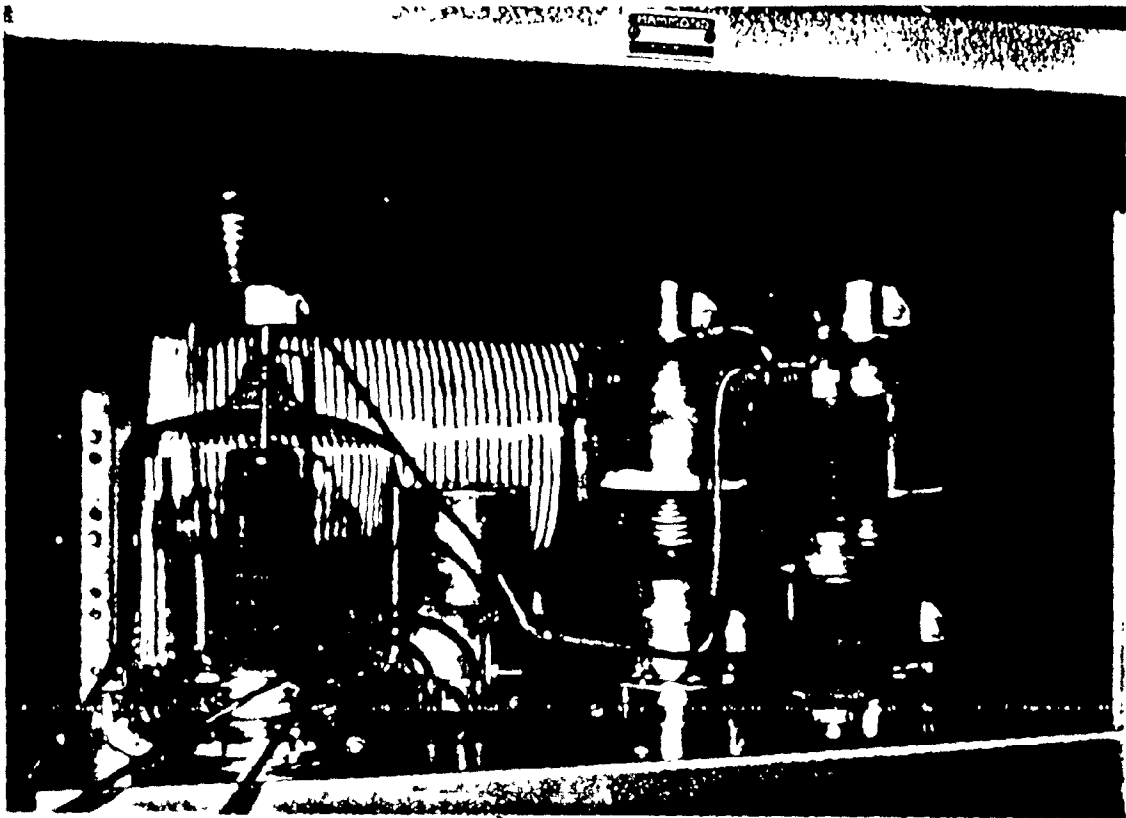


Figure 66. View of Resonating Circuit in Power Transmitter.

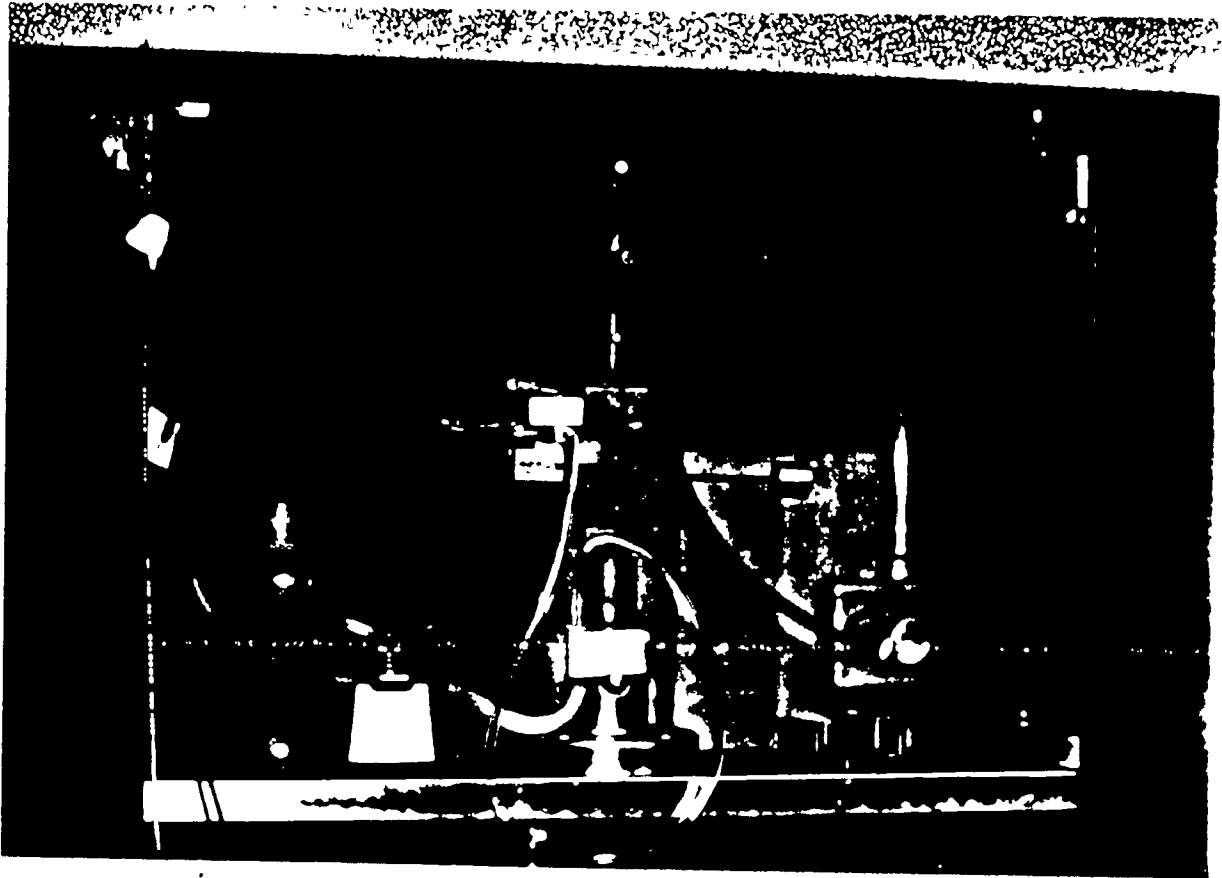


Figure 67: DCB Loading Rig with Attached Transducer and Water Cooling System.

of the top cantilever beam and caused the crack to diverge to the lower side of the sample. The geometry generally used by Kerkhof and his co-workers in Freiburg (section 3.5.1) cannot be used for the DCB testing geometry.

It was found more successful to mount the transducer on the end of the sample at right angles to the fracture path. In this position, the crack and the US wave are moving in opposite directions and should give rise to a frequency shift (Doppler effect). Fortunately the crack speed in the DCB test was typically less than 50 m/s which compared to the speed of the US wave in the glass composites (~2000 m/s) gives rise to only a negligible shift in frequency.

Before testing, the variable capacitors were changed till the quartz crystal resonated. The frequency was determined using a Philips frequency counter* and the water-cooled transducer was attached to the sample. The power supply was increased to voltages between 2 and 3kV since it was found that these gave rise to observable ripple marking for the S glass/nickel composites. The resonant frequency for the majority of tests was 1.02 MHz. The entire mechanical testing rig for the ultrasonic tests is shown in Figure 68.

4.7 Fractography

The fracture surfaces of the composite samples were studied on the SEM to obtain information on the fractographic features. The samples were coated with a thin film of aluminium. Some samples were viewed in the optical microscope for evidence of fracture mirrors and other

* Philips Electronics Industries Ltd., Toronto
Frequency Counter PN 6607/01

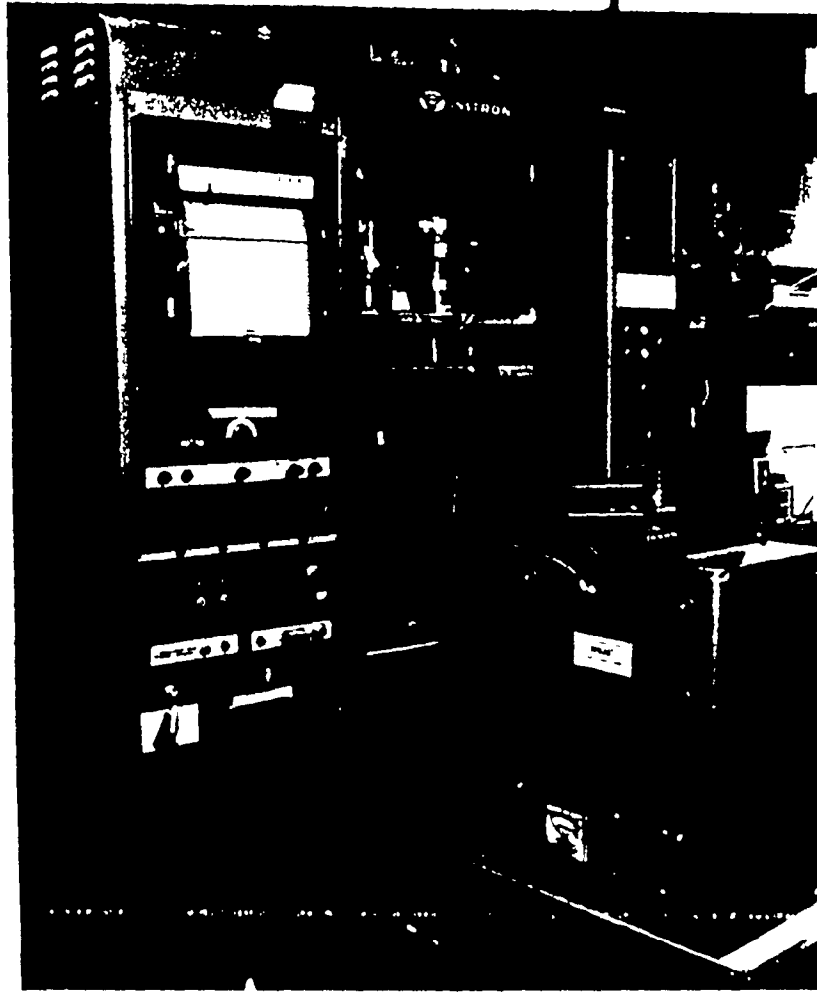


Figure 68. Complete Experimental Arrangement for the Ultrasonic Modulation of Fracture Surfaces.

features. The roughness of the fracture surface made these observations difficult except at low magnifications and here there were no distinct features except those observable in the SEM.

The ultrasonically modulated samples pose more of a problem as the ripples are generally less than $1 \mu\text{m}$ in height. For planar fractures with relatively large ripple spacings observations can be readily made on the optical microscope at low magnifications because the topography of the surface tends to provide its own contrast. For the composite system where surfaces are rougher, such observations are difficult especially in resolving detailed information about the crack shape in the vicinity of the particle. Interference microscopy also provides useful information for relatively plane surfaces but rough surfaces tend to make interpretation difficult. The interference microscope was used, however, for S glass and the partially-fined S glass. Improved resolution was obtained using the Nomarski interference technique and a detailed study was made on the S glass/Ni samples at all volume fractions and the partially-fined S glass. The samples used in the interference microscopy were coated with gold to improve the reflectivity of the surfaces.

The modulated samples were also viewed on the SEM. It was found that observation of the ripples was difficult since the height of the ripples ($< 1 \mu\text{m}$) are close to the limit of resolution for the SEM. It was found that coating the samples with carbon at right angles followed by shadowing at 5° in the direction of crack propagation led to improved resolution especially when the sample was tilted at angles greater than 30° relative to the electron beam. The amount of gold (M grams)

needed to produce a 20 nm layer at a shadow angle θ is given by:

$$M = \frac{32\pi \rho r^2}{3 \sin \theta 10^6} \quad (4.1)$$

where ρ is the density of gold and r is the distance between the source and sample.

It was felt that this shadowing technique would allow the gold to be deposited on only one side of the ripples allowing contrast to be obtained between the carbon and the gold.

CHAPTER 5

RESULTS AND DISCUSSION

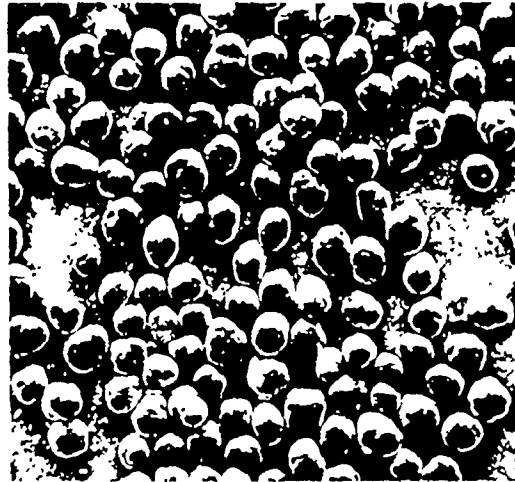
5.1 Starting Materials

The starting materials were characterized by density, particle size, chemical analysis and microscopy.

5.1.1 Nickel Powder

The as-received nickel powder was seen, from SEM observations, to consist of approximately spherical particles (Figures 69 and 70). There was some indication that the particles were agglomerated during fabrication. The particle surfaces showed sub-micron surface irregularities (Figure 71). The agglomeration and surface roughness is presumably a consequence of the manufacturing process, in which the particles are grown by a precipitation reaction. The powder has few visible pores and the size distribution was relatively narrow. An occasional particle had a rough, pebbly surface (Figure 72). In these cases, the manufacturers control of particle shape had presumably broken down and the particle appears more like the regular grades of nickel powder.

The SEM micrographs were used to determine the particle size distribution of the nickel powder from the projected particle diameter. The distribution is shown in Figure 73 and is approximately normal with a slight positive skew. The data were re-plotted on log-normal probability paper (Figure 74) and a good correlation to a lognormal distribution was observed. This behaviour is often observed in powder particle size



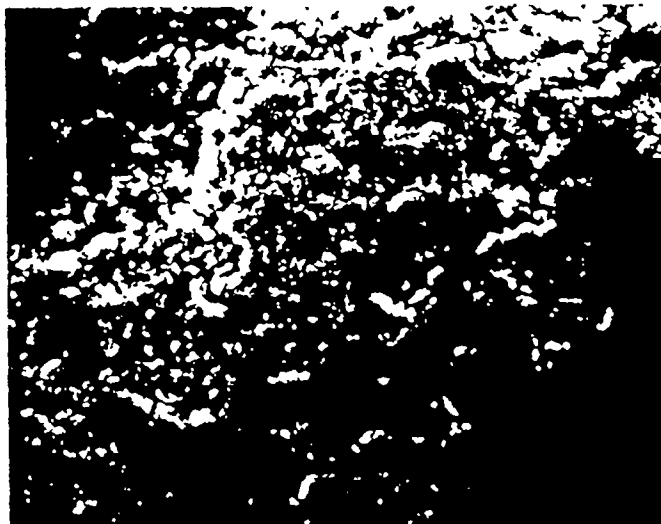
300

Figure 69. SEM Micrograph of As-received Nickel Powder.



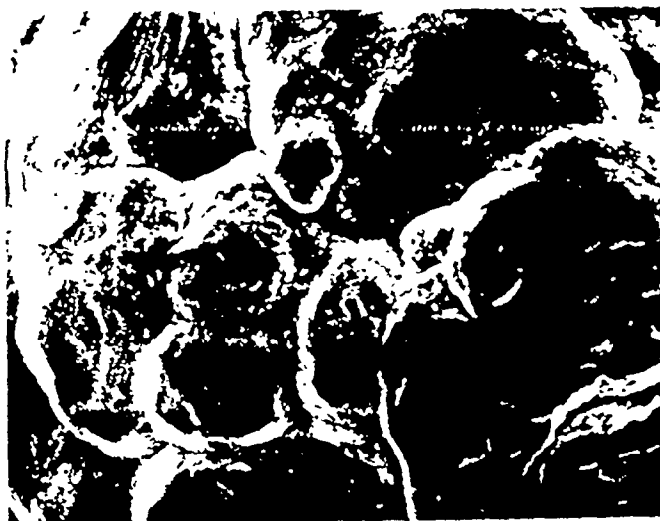
38

Figure 70. SEM Micrograph of As-received Nickel Powder.



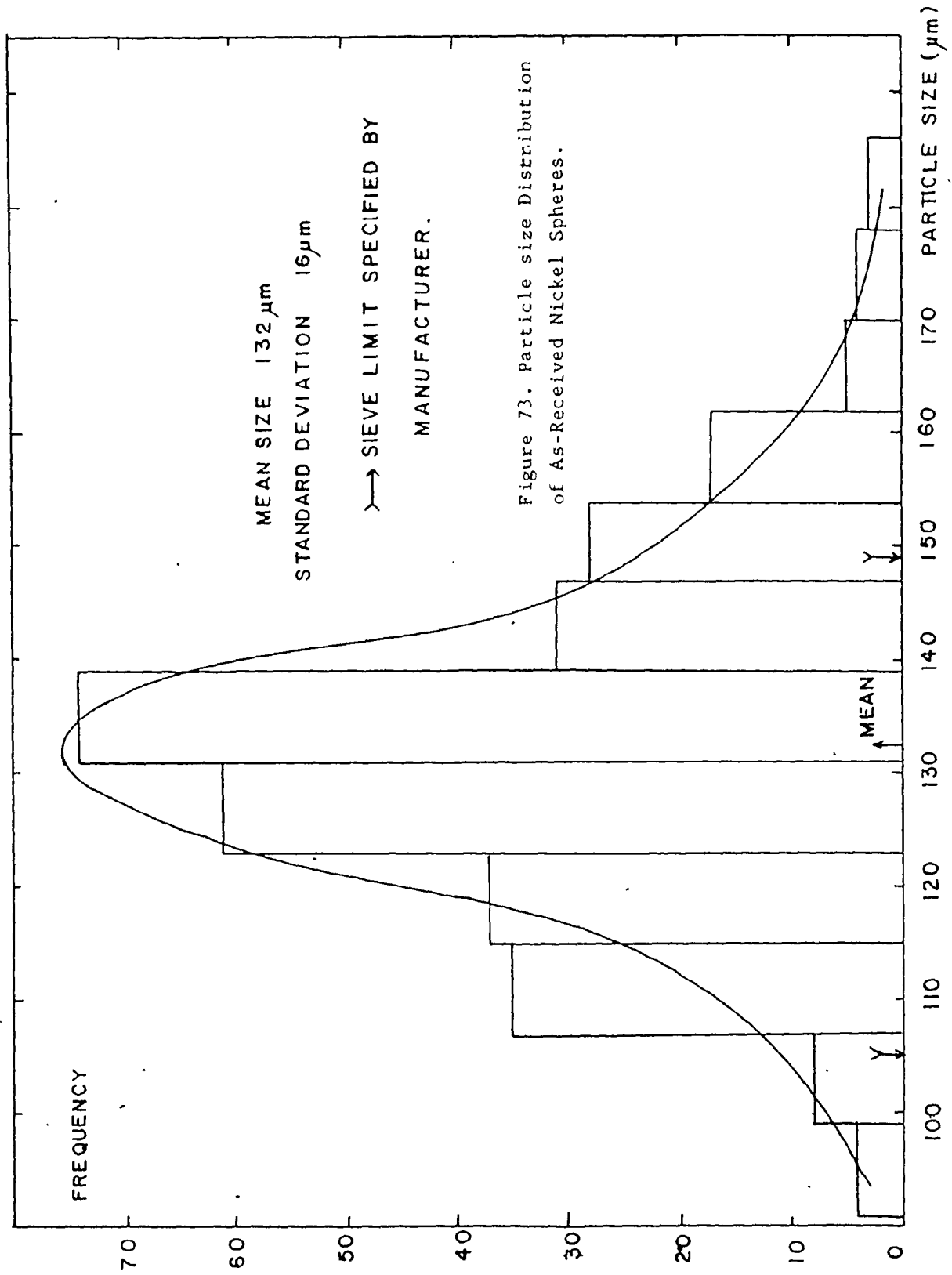
4.0

Figure 71. SEM Micrograph showing Surface of Nickel Sphere at High Magnification.



8.0

Figure 72. Non-spherical Nickel Particle (Surface).



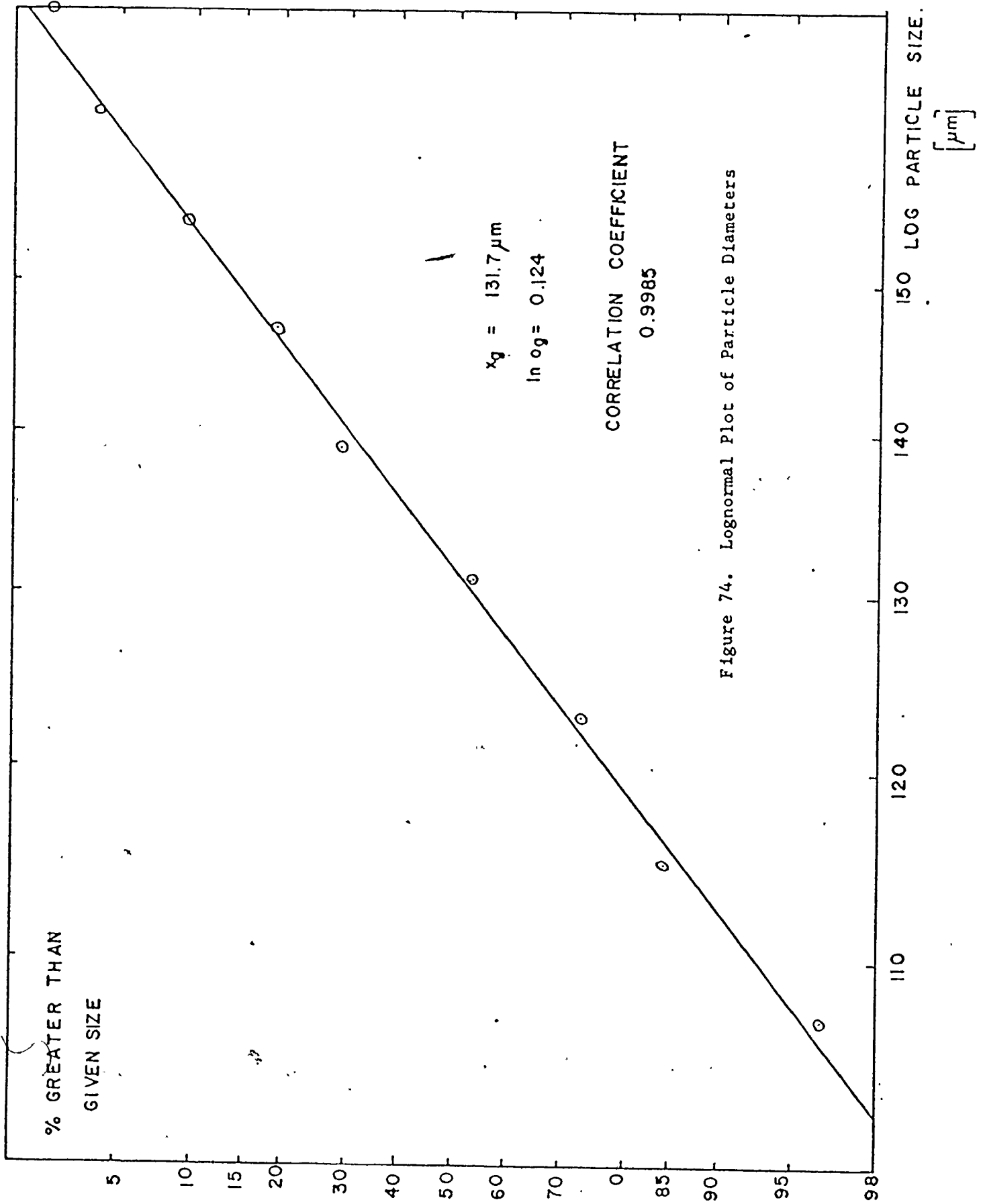


Figure 74. Lognormal Plot of Particle Diameters

analysis (section 1.4.3). In particular, it should be noted that once the geometric mean and standard deviation have been determined for a lognormal distribution, the other moment and weight averages can be easily calculated (equation 1.13). Table 15 lists the values of these averages for the nickel powder.

Chemical and sieve analyses were performed by the manufacturer and their results are shown in Table 16. The sieve analysis shows good agreement with the particle distribution of Figure 73 with the majority of particles having diameters between the 100 and 150 Tyler sieves. The results of the chemical analysis determined at McMaster are shown in Table 17 and are in good agreement with the manufacturer's specifications.

The density of the nickel powder was determined by the Archimedes water displacement technique and a value of $8.87 \times 10^3 \text{ kg/m}^3$ was obtained. This value is close to the theoretical density of nickel ($8.90 \times 10^3 \text{ kg/m}^3$).

5.1.2 S Glass Powder

The S glass powder was produced by a series of melting, grinding and heat treatment stages and had a greyish appearance. This coloration is probably due to impurities picked up in one or more of the fabrication stages. For example, melting in fireclay crucibles will probably lead to iron contamination, while the vacuum heat treatment using graphite crucibles will lead to carbon impurities. The presence of these impurities were confirmed by chemical analysis (Table 18) though the impurity levels were much less than 1 wt %. At these levels, the impurities should not greatly affect the mechanical properties of the glass composites unless

TABLE 15. Moment and Weight Averages for Nickel Powder.

AVERAGE	VALUE (μm)
Geometric x_g	131.7
Arithmetic x_{av}	132.7
Surface x_s	133.7
Volume x_v	134.8
Volume/Surface x_{vs}	136.9
Geometric Weight x_w	137.9
Arithmetic Weight x_w	139.0

TABLE 16. Manufacturer's Specifications on As-received Nickel Powder.

Chemical Analysis (wt %)

<u>Ni*</u>	<u>Co</u>	<u>Cu</u>	<u>Fe</u>	<u>S</u>	<u>C</u>
Bal.	0.27	0.0062	0.0034	0.0125	0.1

<u>Screen Analysis</u>			
	+100 mesh	6.0%	> 0.147mm
	-100 +150	89.2%	< 0.147 > 0.104mm
	-150	4.8%	< 0.104mm

Apparent Density $5.12 \times 10^3 \text{ kg/m}^3$

TABLE 17. Chemical Analysis of the Nickel Powder.

ELEMENT	AMOUNT(wt. %)
Co	0.457
Cu	0.0066
Fe	0.0045
C	0.104
S	0.018

TABLE 18. Chemical Analysis of S Glass Powder.

ELEMENT	AMOUNT (wt. %)
Fe	0.173
C	0.094

they are present as large inclusions. No evidence of such inclusions were observed and it is more likely that these elements were incorporated into the glass network.

The theoretical density of the S glass was determined to be 2.51×10^3 kg/m³ a value which is slightly higher than the value quoted by Stett and Fulrath [74] of 2.47×10^3 kg/m³.

5.2 Microstructural Characterization of the Fabricated Composites

The bulk density of each hot-pressed billet was determined by the Archimedes water-displacement technique and the results are summarized in Table 19. The fabrication method gave consistent densities with the majority of billets having a density greater than 99% of theoretical. The densities of cast S glass, the partially-fined S glass and pyrex are also included in this table.

The glass phase in the hot-pressed composites appeared dark but when a chip of the composite was viewed in transmitted light, it was observed to have a bluish-green tint and slight opacity. The coloration was probably due to the presence of ferrous ions, introduced during the melting stage from the fireclay crucibles. There was no evidence of nickel, or cobalt ions in the glass as these are all strong colorants.

5.2.1 Detection of internal stress

Although the S glass-nickel system was chosen so that the thermal expansion coefficients of the two phases were approximately the same,

TABLE 19. Density Measurements.

Volume % Nickel	Average Density(%)	Number of Pressings
0	>99	6
2	>99	4
4	>99	2
6	>99	4
10	98	3
15	99	3
20	>99	3
0 (cast)	2.50×10^3 kg/m ³	
0 (part-fined)	2.49×10^3 kg/m ³	
Pyrex	2.23×10^3 kg/m ³	

there is the possibility that the fabrication procedure could still lead to internal stresses. For example, the physical properties of the glass could be influenced by impurities or improper annealing could lead to internal stress within the glass network.

A chip of the composite (thickness ~2mm) was viewed in transmitted polarized light and no destructive interference was observed. The sensitivity limit of this technique can be calculated from equation (1.4). For soda-lime-silica glass, the stress optical coefficient is rather small (Table 5), so that for a plate 2 mm thick, a difference in principal stresses of 120 MPa would be required to reach the first order fringe in white light ($r = 600 \text{ nm}$). With a mica sensitive-tint plate a relative retardation of ~ 50nm can be detected (Table 4), which for this case corresponds to a principal stress difference of 10MPa (1500 psi).

It is also worth considering what magnitude of internal stress could be generated by a thermal expansion coefficient mismatch ($\Delta\alpha = \alpha_m - \alpha_p$). For a 5% mismatch, using the formula of Selsing [190] the stress at the particle interface (P) can be calculated, i.e.,

$$P = \frac{\Delta\alpha \cdot \Delta T (E_p E_m)}{E_p (1 + \nu_m) + (1 - 2\nu_p) E_m} \quad (5.1)$$

where ΔT is the temperature difference. Because all composites were annealed at 450°C , $\Delta T = 425^\circ\text{C}$ and substituting the values from Table 13, a value of $P = 17 \text{ MPa}$ (2500 psi) is obtained. This is the maximum stress at the interface and these stresses decay rapidly with distance into the matrix [190]. The maximum difference in principal stresses for

this situation is approximately given by $2P$ or ~ 34 MPa. This magnitude of internal stress should easily be detected in the polarizing microscope. Only when the expansion mismatch is less than about 2%, will there be difficulty in detection. Other techniques such as shift of X-ray diffraction peaks would also not be able to detect stresses lower than 10 MPa. It was therefore concluded, that a small amount of internal stress may be present in these composites but of a magnitude that is small enough to neglect.

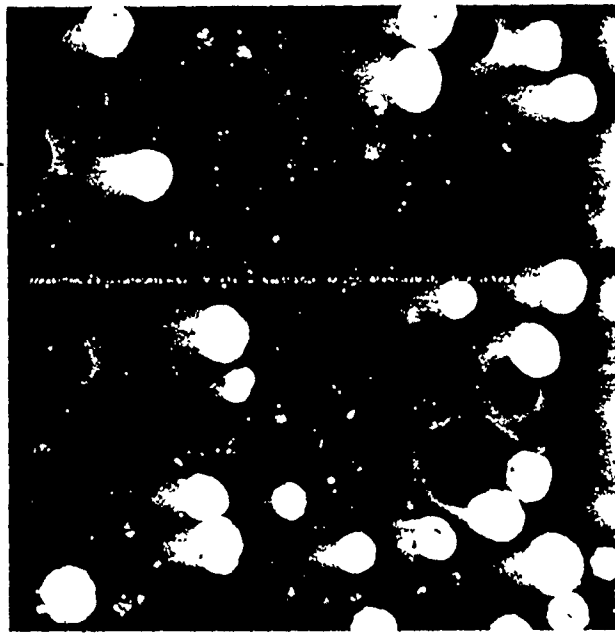
5.2.2 Quantitative Microscopy

Typical polished sections of the hot-pressed composites are shown in the optical micrographs (Figures 75-76). There is an increased tendency for nickel interparticle contacts with increasing volume fraction, leading in some case to sintering of the nickel particles. These polished sections were etched to reveal the structure of the nickel particles (Figure 77). The structure of the nickel has a 'sawn-timber' concentric ring appearance which is related to the precipitation plating procedure utilized by the manufacturer. The grain structure within the bands consists of equiaxed platelets of grain size $\sim 8\mu\text{m}$. There was no evidence of interfacial cracks between the glass and the nickel. An etched section as observed in the SEM is shown in Figure 78.

Quantitative measurements were made on the polished sections by measuring the particle intercept diameters, the fraction of test points intercepted by the nickel spheres and the number of particles observed in the test area. The results (Table 20) show a summary of the stereological parameters obtained (section 1.4). The measured volume fraction



200



200

Figure 75. Optical Micrograph from a Polished Section of an S Glass-Nickel Composite a) 6 vol.% b) 10 vol. %.

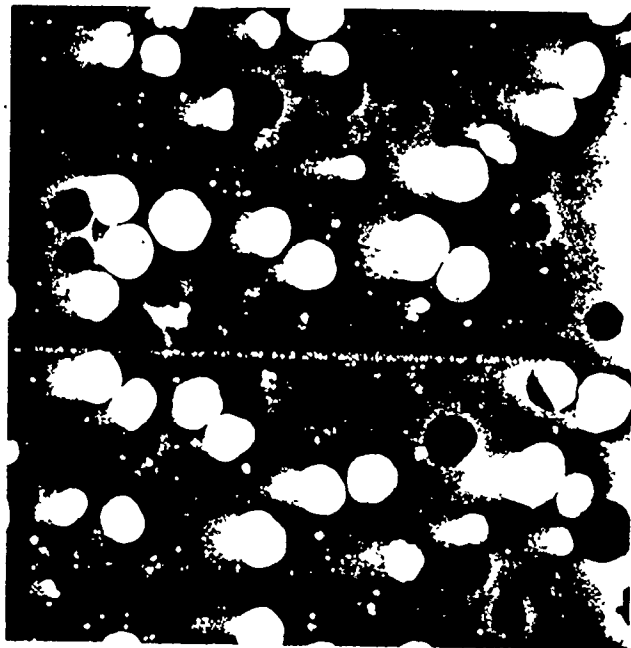
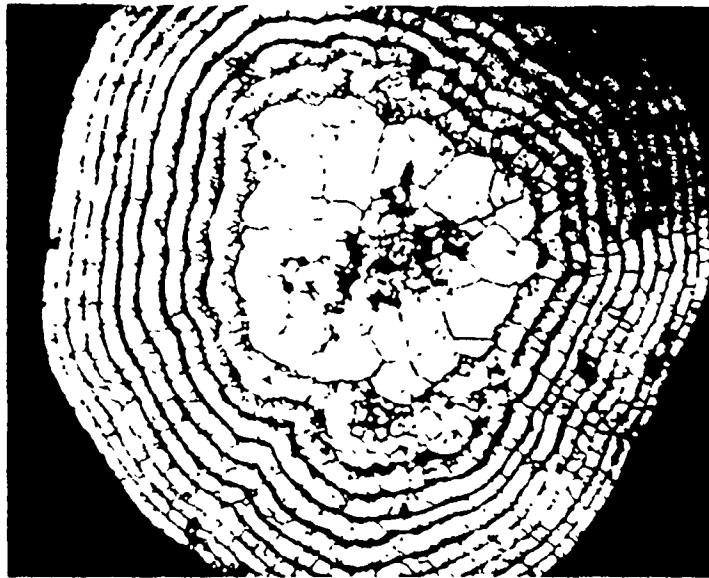


Figure 76. Optical Micrographs from Polished Sections of S Glass-Nickel Composites, a) 15 vol% b) 20 vol%:



17

Figure 77. Optical Micrograph of Etched Microstructure of a Sectioned Nickel Sphere.

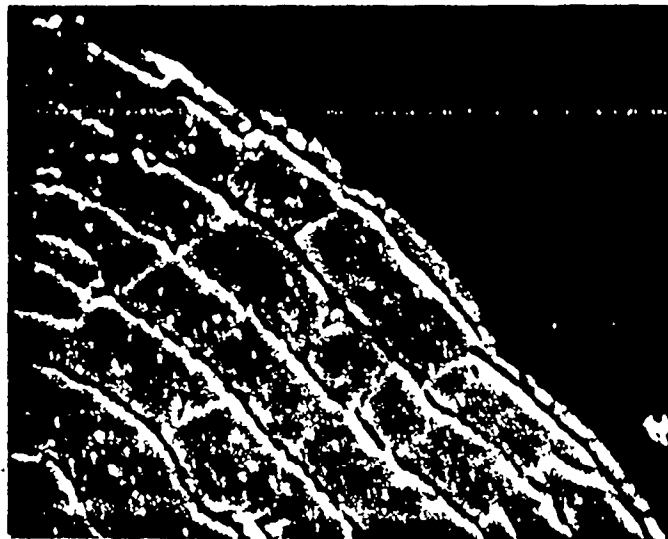


Figure 78. SEM Micrograph of Nickel/S Glass Interface.

TABLE 20. Quantimet Stereological Measurements.

$V_V(\text{nominal})$	V_V	\bar{d} (μm)	\bar{A} (mm^2)	\bar{L}_3 (μm)	λ (μm)	P_L (mm^{-1})	PA (mm^{-2})
0.06	0.07 (± 0.01)	117 (± 13)	0.0121	34.2 (± 2.8)	1430 (± 300)	1.35 ($\pm .26$)	11.6 (± 2.1)
0.10	0.12 (± 0.02)	118 (± 15)	0.0126	34.8 (± 2.5)	805 (± 180)	2.25 ($\pm .38$)	19.3 (± 4.2)
0.15	0.17 (± 0.02)	109 (± 10)	0.0121	36.2 (± 4.7)	536 (± 88)	3.12 ($\pm .44$)	32.7 (± 3.3)
0.20	0.25 (± 0.05)	111 (± 8)	0.0124	35.6 (± 3.2)	336 (± 64)	4.13 ($\pm .64$)	40.7 (± 5.4)

Brackets indicate standard deviation in results

TEST POINTS 600 x 500
TEST AREA 2.8 mm^2

TABLE 21. Comparison of Particle Parameters Before and After Fabrication.

V_V	\bar{D}_0 (μm)	\bar{D} (μm) **	λ (μm) **	λ (μm) #	d (μm) **	d (μm) #
0.06	132(± 16)	157(± 13)	1380	1430	286	291
0.10	"	160(± 10)	790	805	198	196
0.15	"	165(± 21)	500	536	118	118
0.20	"	167(± 13)	350	336	110	90.6

\bar{D}_0 is average particle diameter as measured on nickel powder
* assumed distribution of mono-sized spheres
from quantimet results
** calculated from \bar{D}_0 assuming a random distribution of mono-sized spheres

(V_V) is slightly higher than the values expected from the initial mixing (V_V^0). This effect is common in quantitative microscopy and is generally associated with counting problems at the particle edges especially if there is any relief polishing. In these composites, this problem may be accentuated by the reflectance of spheres from below the sectioning plane. Included in Table 20 is the values obtained for the mean free path.

If the assumption is made that the particle distribution consists of equi-sized spheres, many of the stereological parameters can be calculated from the particle size distribution before fabrication. This comparison is given in Table 21. The calculated average particle size is larger than the value obtained earlier. This is consistent with the problems encountered in measuring volume fraction but it is also shown that the average particle size increases with increasing volume fraction. This increase is probably associated with the increasing interparticle contact at higher volume fractions, which is to be discussed later.

There is good agreement between the measured and calculated mean free paths. This parameter has been used by Lange [9] as the measure of the average interparticle spacing in his model which describes the interaction between a crack front and second phase particles. As pointed out in section (1.4.5), the mean free path must be incorrect because a crack front will sample more obstacles than indicated by these considerations. Figure 79 illustrates the interparticle spacing problem. Following the suggestion by Kocks [53], a better approximation to the mean centre-to-centre distance (Δ) for this type of process is given by

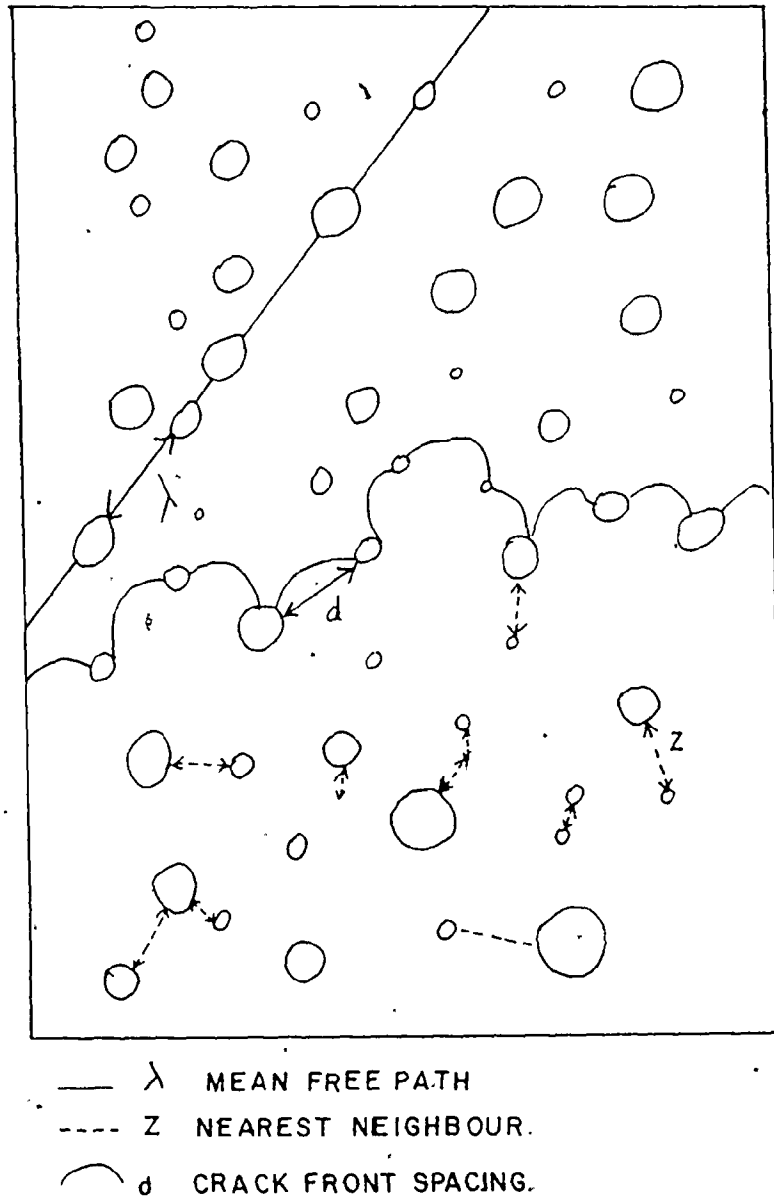


Figure 79. Different Concepts of Interparticle Spacing.

$$\Delta = N_A^{-1/2} \quad (5.2)$$

For a random array of spherical particles, this leads to an interparticle spacing (d) which is given by

$$d = r \left[\frac{2\pi}{3V_v} \right]^{1/2} - \frac{\pi r}{2} \quad (5.3)$$

$$d = \Delta - \pi r/2 \quad (5.4)$$

The second term accounts for the finite size of the particles. This expression will be used to describe the interparticle spacing for the process of crack interactions with a second phase particle in this thesis. For a statistical distribution of particles, it is also necessary to indicate what spacing controls the process. For this work, it was postulated that the crack interaction process is controlled by the average interparticle spacing and average particle size. It is clear from equations (5.3) and (5.4) that d can be calculated from the initial particle size distribution or from the quantitative microscopic measurements. This comparison is also included in Table 21 and there is good agreement between the calculated and measured values.

Particle Size Distributions

Theoretical approaches to crack-particle interactions [9, 113] have suggested that the size and spacing of the particles control the fracture properties. It is important, therefore, to characterize these parameters carefully. In particular, if there is a tendency for agglomeration (enhanced interparticle contact) in a composite system, this should be accounted for, as this will tend to change the distribution parameters. In the last section, the values of \bar{D} and d were compared before and after fabrication (assumed mono-sized). It is also possible to compare the particle size distributions before and after fabrication.

The distribution of particle intercept diameters was measured and the results are shown in Figures 80-83, plotted as relative and cumulative frequencies. In these figures, the initial peak, which implies an abundance of very small intercept areas could be an indication of the spheres reflecting from below the sectioning plane or possibly the presence of reflective impurities. The former factor is in agreement with the previous discussion about the measured volume fraction and particle diameter. As the volume fraction increases, the distribution widens and at 20 vol. % small peaks appear at approximately two and three times the average intercept diameter. This is indicative of the increased amount of two and three particle contact at higher volume fractions.

From the data on intercept diameters, the particle size distributions can be calculated provided assumptions are made about the particle shape. For example, it can be assumed that for the glass-nickel system, the nickel exists as a random dispersion of poly-sized spheres. The particle size distribution was calculated with this assumption using the Schwartz-Saltykov method (Appendix A.1). The results are shown in Figure 84. The average particle is still slightly higher than those calculated from the original distribution (Table 21). The evidence for the effect of interparticle contacts is clearer but there may still be the edge counting problems. There is a slight increase in the average particle size with increasing volume fraction, reflecting the increase in interparticle contact. For the 20 vol. % samples, the bimodal nature of the distribution is apparent. These distributions can be plotted on lognormal probability paper (Figures 85 and 86). These plots

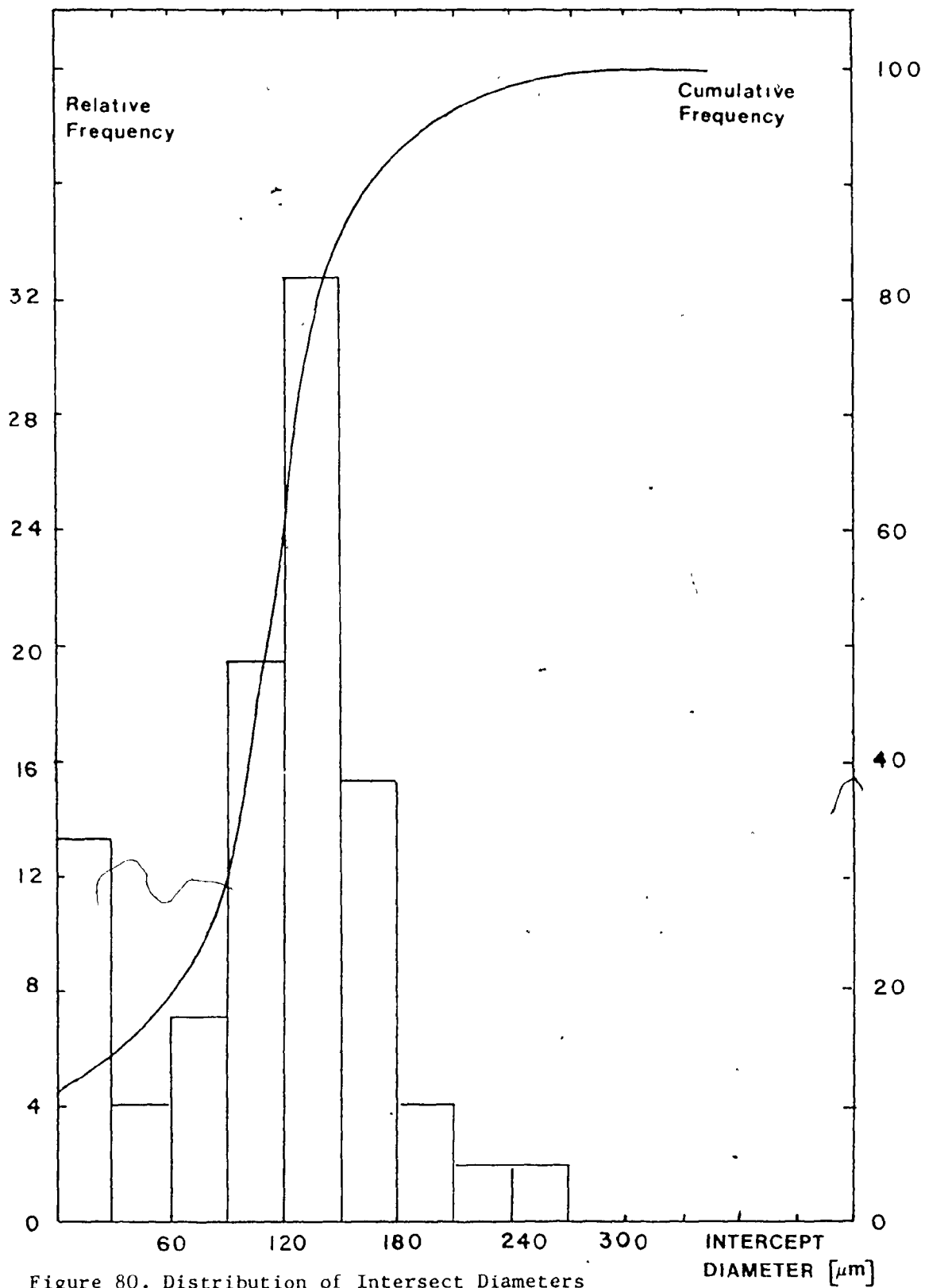


Figure 80. Distribution of Intercept Diameters
-6 vol.%

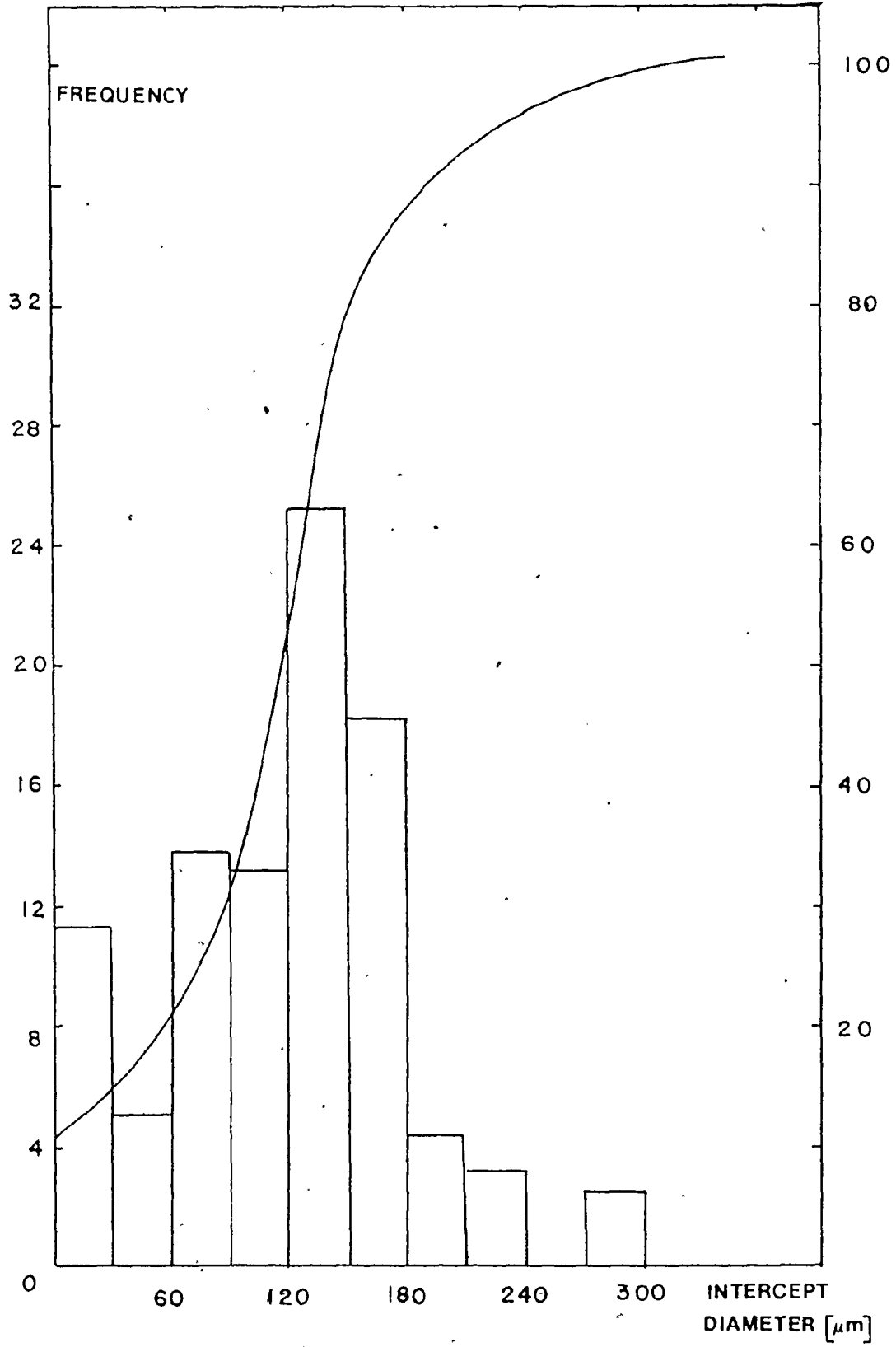


Figure 81. Distribution of Intercept Diameters-10 vol.%

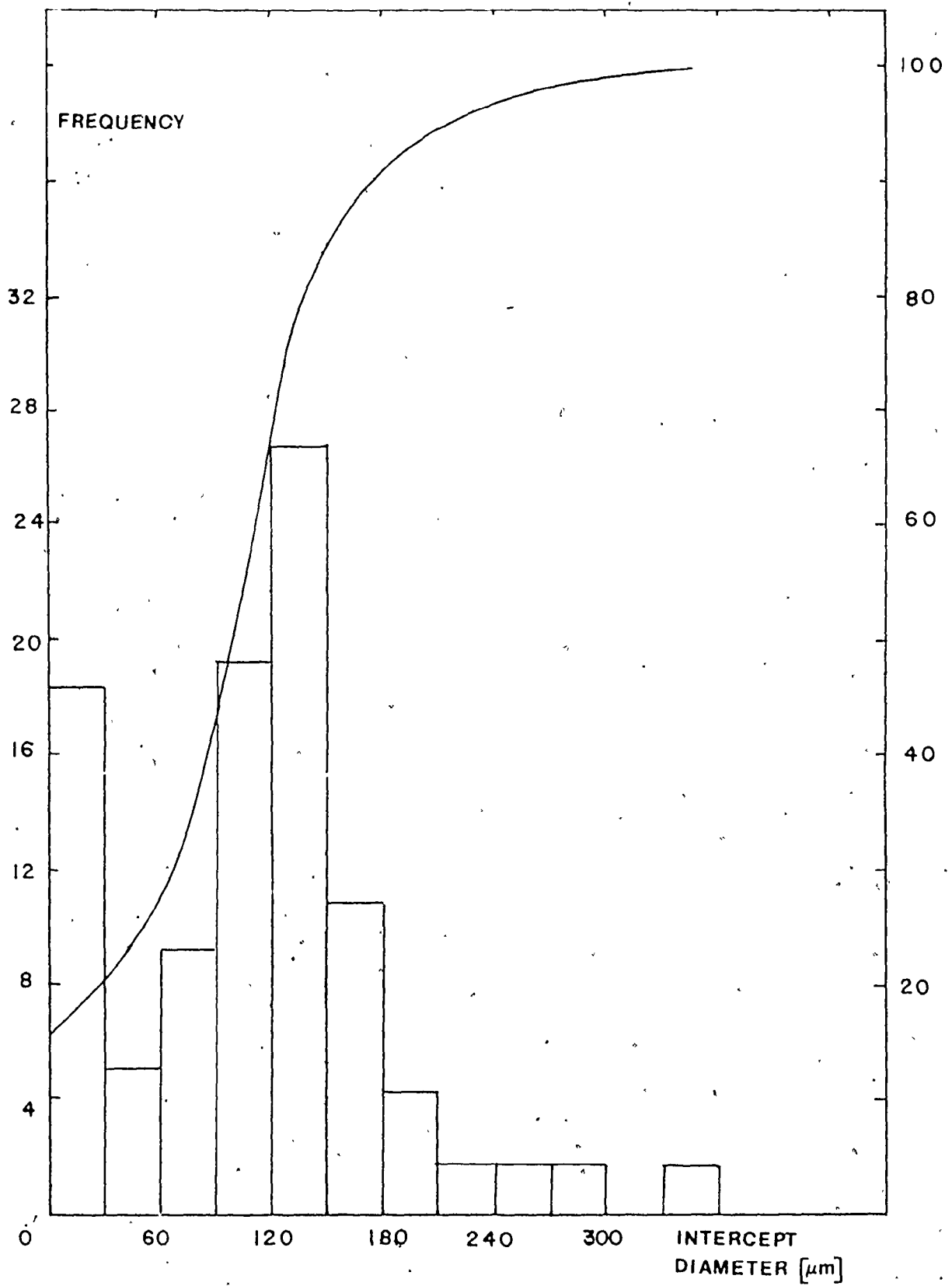


Figure 82. Distribution of Intercept Diameters-15 vol.%

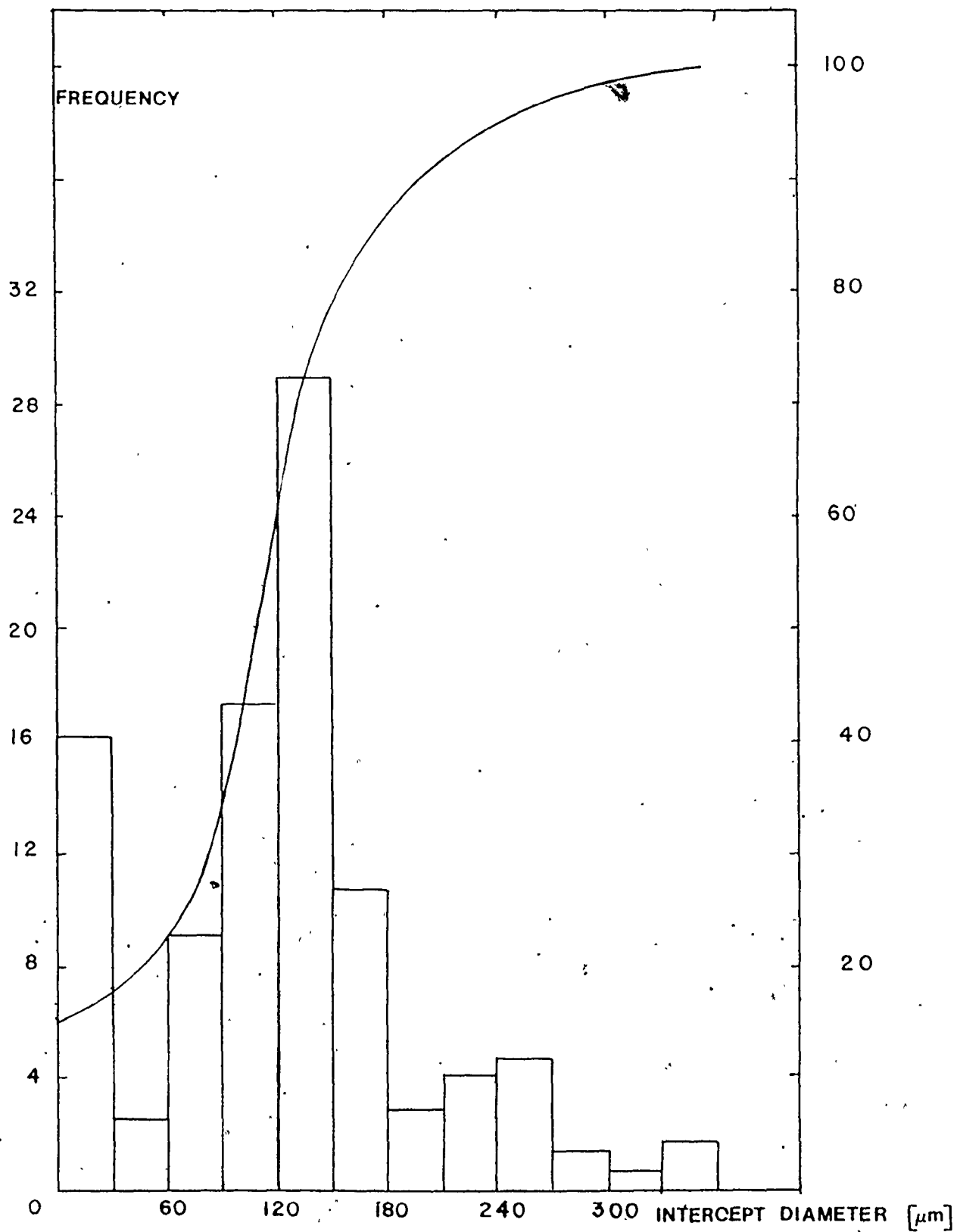


Figure 83. Distribution of Intercept Diameters - 20 vol. %.

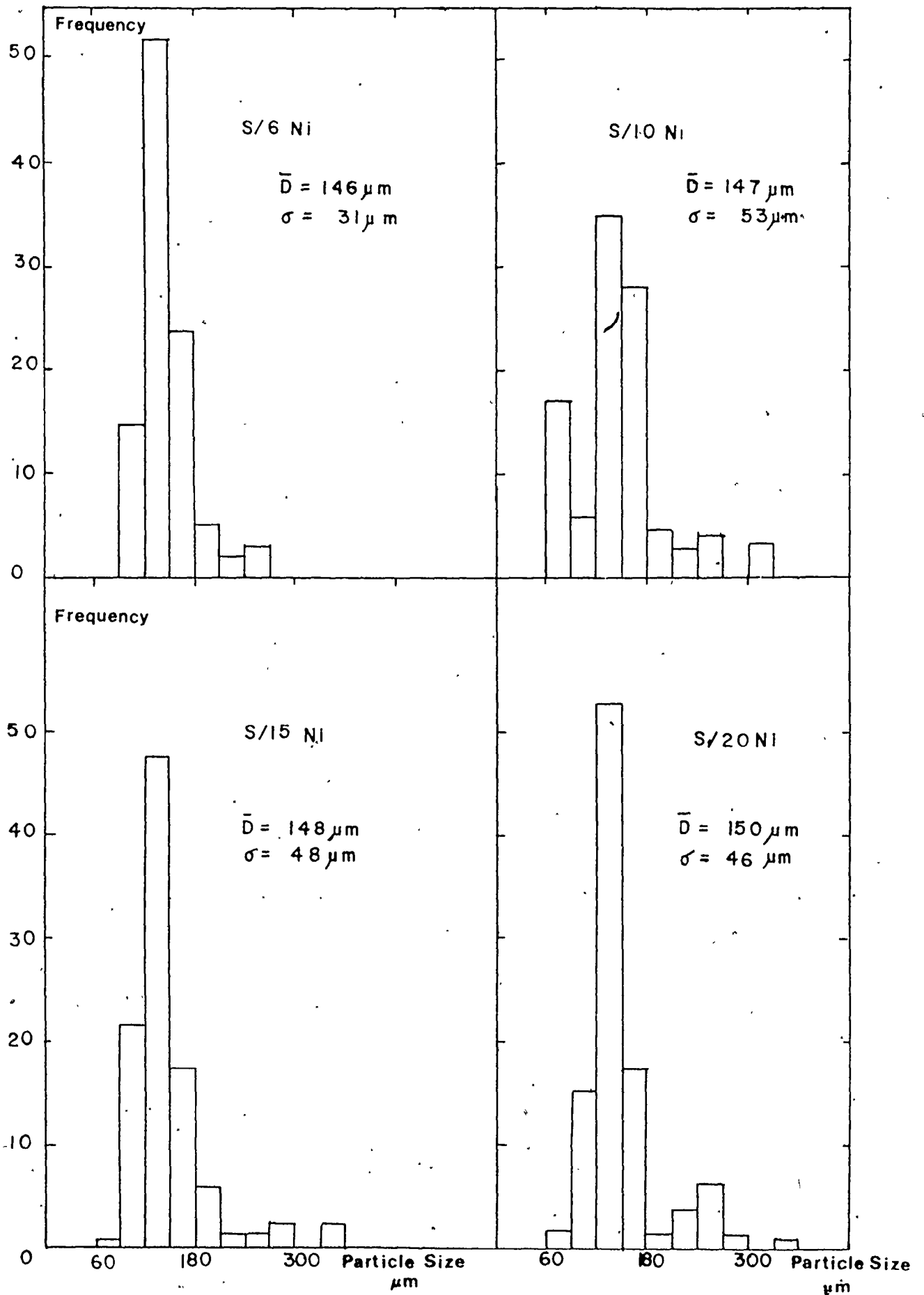
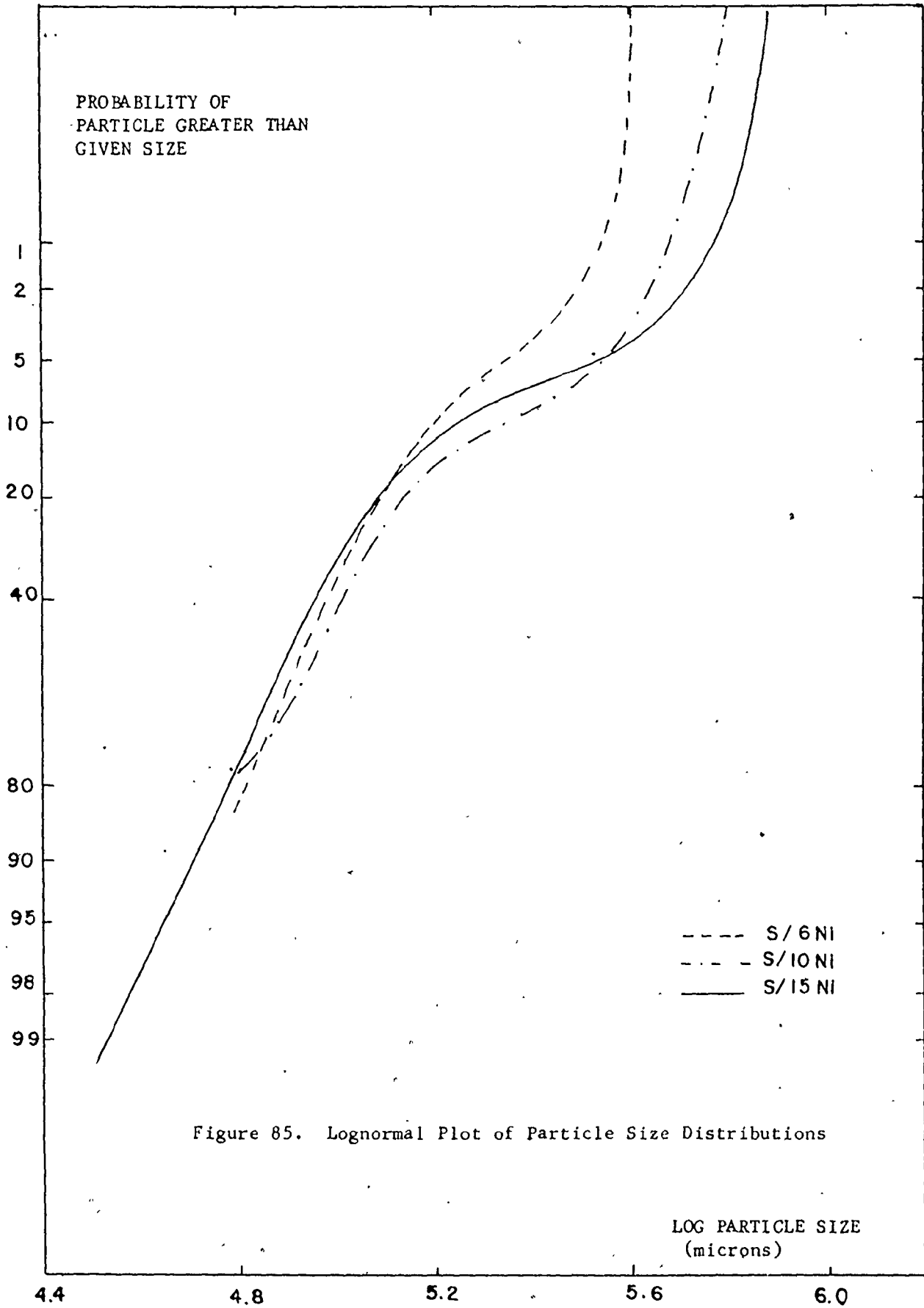
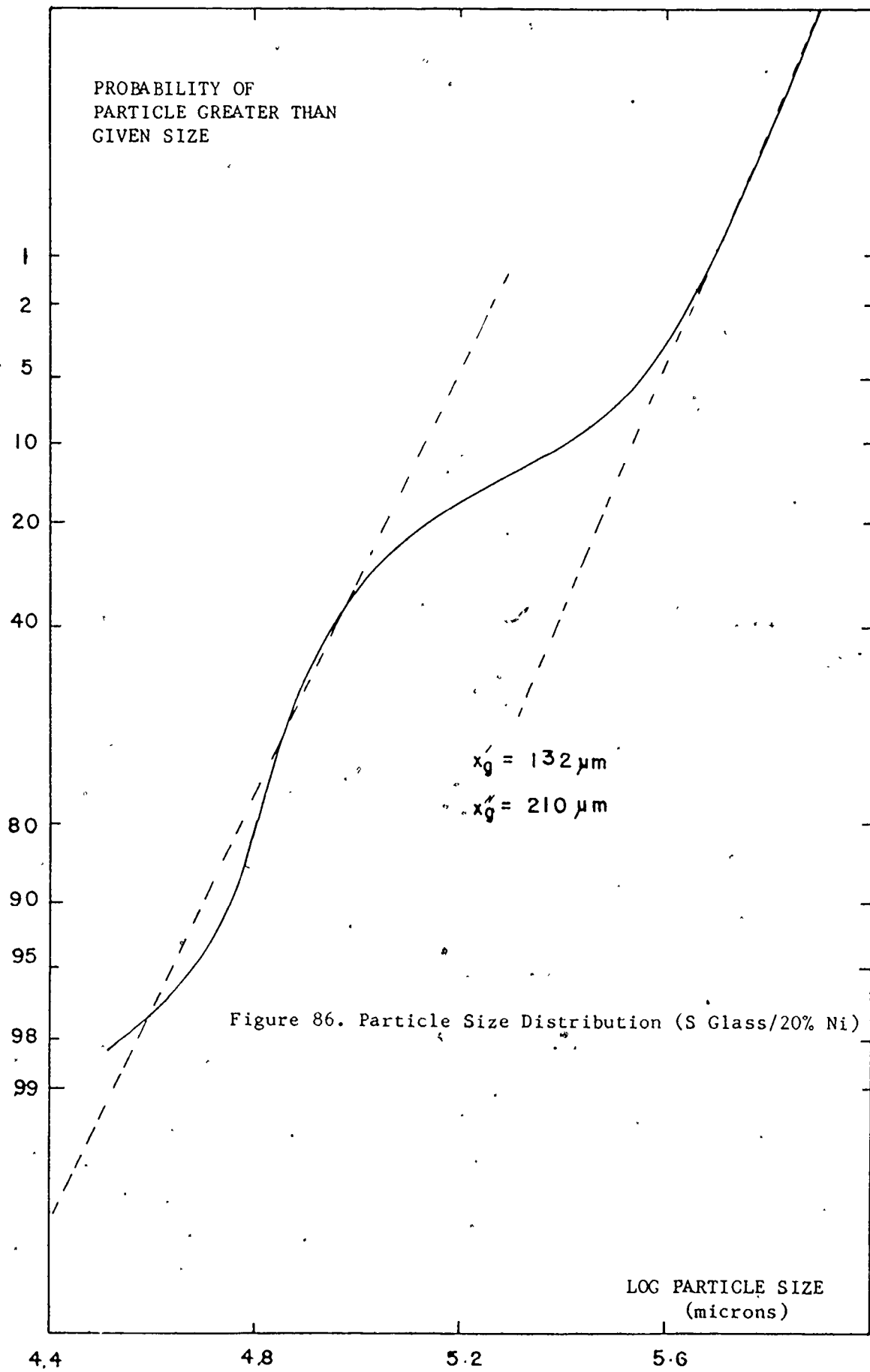


Figure 84. Particle Size Distributions from Polished Sections of the Composites.





show the characteristic nature of bimodal distributions and for Figure 86, the mean particle size for the two distributions are approximately 136 μm and 210 μm . The former value agrees very well with the average particle size observed in the original distribution (Figure 73) so it appears that edge counting problems are minimal.

It can be concluded that for this system, there is a tendency for interparticle contact, which increases with volume fraction. The behaviour affects the measured values of the average particle size and interparticle spacing. The measured values of \bar{D} and d are given in Table 22, recalculated from the data of Figure 84. These are again compared with the value of \bar{D} and d calculated from the original distribution. It can be seen that the measured values are slightly larger than the calculated values. Therefore, although there is a tendency for interparticle contact in this system, the values of \bar{D} and d are not greatly affected. If there was a tendency for agglomeration, the values of \bar{D} and d would be affected more strongly. Conversely, the assumption that the particles are well-dispersed, would not greatly affect the values of the average particle size and average interparticle spacing.

The degree of separation or inversely, the contiguity ratio (C_t) of a two phase system can be quantitatively expressed using equations (1.16) and (1.18). Table 23 shows the approximate variation of (C_t) with volume fraction. This data, as expected, show there is an increased tendency for interparticle contact as the volume fraction increases.

TABLE 22. Comparison of Interparticle Spacing and Average Particle Size Before and After Fabrication:

V_V	\bar{D}_o (μm)	d_o (μm)	\bar{D}_f (μm)	d_f (μm)
0.06	132(+16)	286	146(+31)	300.
0.10	"	198	147(+53)	206.
0.15	"	118	148(+48)	131.
0.20	"	110	150(+46)	104.

Subscript o refers to before fabrication and f to after fabrication

TABLE 23. Contiguity Parameters for Glass-Nickel Composites.

V_V	N_{BB} (cm) ⁻¹	N_{AB} (cm) ⁻¹	c_t
0.06	6.8	0.4	0.11
0.10	11.2	1.2	0.18
0.15	15.6	3.3	0.30
0.20	22.6	4.1	0.27

5.3 Fracture Surface Energy Standardization Tests

Fracture energy tests were carried out to establish the reproducibility of the testing technique. The specimen dimensions and test geometry of these standard tests were identical to those chosen for the hot-pressed material. Two materials were tested: a commercially available window glass (soda-lime-silica) and pyrex glass (Corning Code 7740). The majority of the tests were performed on the pyrex because there has been previous results published in the literature on the fracture toughness of this material. Moreover, this glass seems particularly sensitive to slow crack growth and any experimental difficulties involving this phenomenon should be reflected in the results. The source and composition of the window glass was unknown and therefore only preliminary tests were made on this glass.

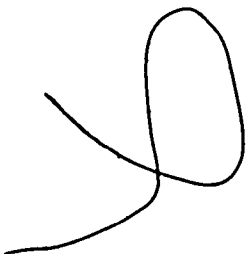
As previously discussed (section 3.2), fracture toughness data can be established by load and crack length data or load-deflection measurements. The latter method is particularly useful for opaque materials where accurate crack length measurements are difficult. In these standard tests, a comparison of both approaches was made.

5.3.1 Stress Analysis Approach


The initial tests were made on window glass to test the experimental procedure and rig design. The critical stress intensity factor (K_{IC}) was determined from equation (3.11) and the results are shown in Table 24 compared with the results of Wiederhorn [191] for a soda-lime-silica glass. There is doubt about the crack length measurements in these results as metal tabs were used in loading the samples. For these

TABLE 24.

Preliminary Fracture Toughness Results



Material and Test Conditions	K_{IC} (MNm ^{-3/2})
Window Glass (Air 296°K)	0.740(± 0.017)
Soda-Lime-Silica Glass (Dry N ₂ , 300°K) Reference 191.	0.754(± 0.012)



tests, however, the crack length was simply taken as the distance between the loading points and the crack tip. The comparison of the results on window glass is reasonable.

A typical load-deflection curve for pyrex tested in air is shown in Figure 87. More than one measurement of K_{IC} can be determined for each sample, by reversing the cross-head after the critical load. The ability to arrest the crack this way does, however, decrease with increasing deflection-rate. As discussed previously (Section 3.2), two corrections are often made to the experimental data. The first correction accounts for the decrease in fracture area afforded by the use of side grooves. The second correction accounts for the decrease in the moment of inertia of the cantilever beams produced by the side grooves. For these tests, the first correction was made but the second correction was neglected because the moment of inertia was only slightly reduced by the particular geometry of side grooves used in these tests. Two further corrections are relevant to these standard tests. First, there is some doubt about how the crack length should be measured. If the loading tabs are considered to be perfectly rigid then the crack length should be measured from the edge of the sample. Fracture toughness values calculated this way were found to be ~ 10% less than published data. A correction should be made for the compliance of the loading tabs. An approximate approach to this problem can be found if the length of steel between the edge of the sample and the loading points (e) is assumed to behave like a cantilever beam. An equivalent length in glass (l_g) can then be found using a simple strength of materials approach

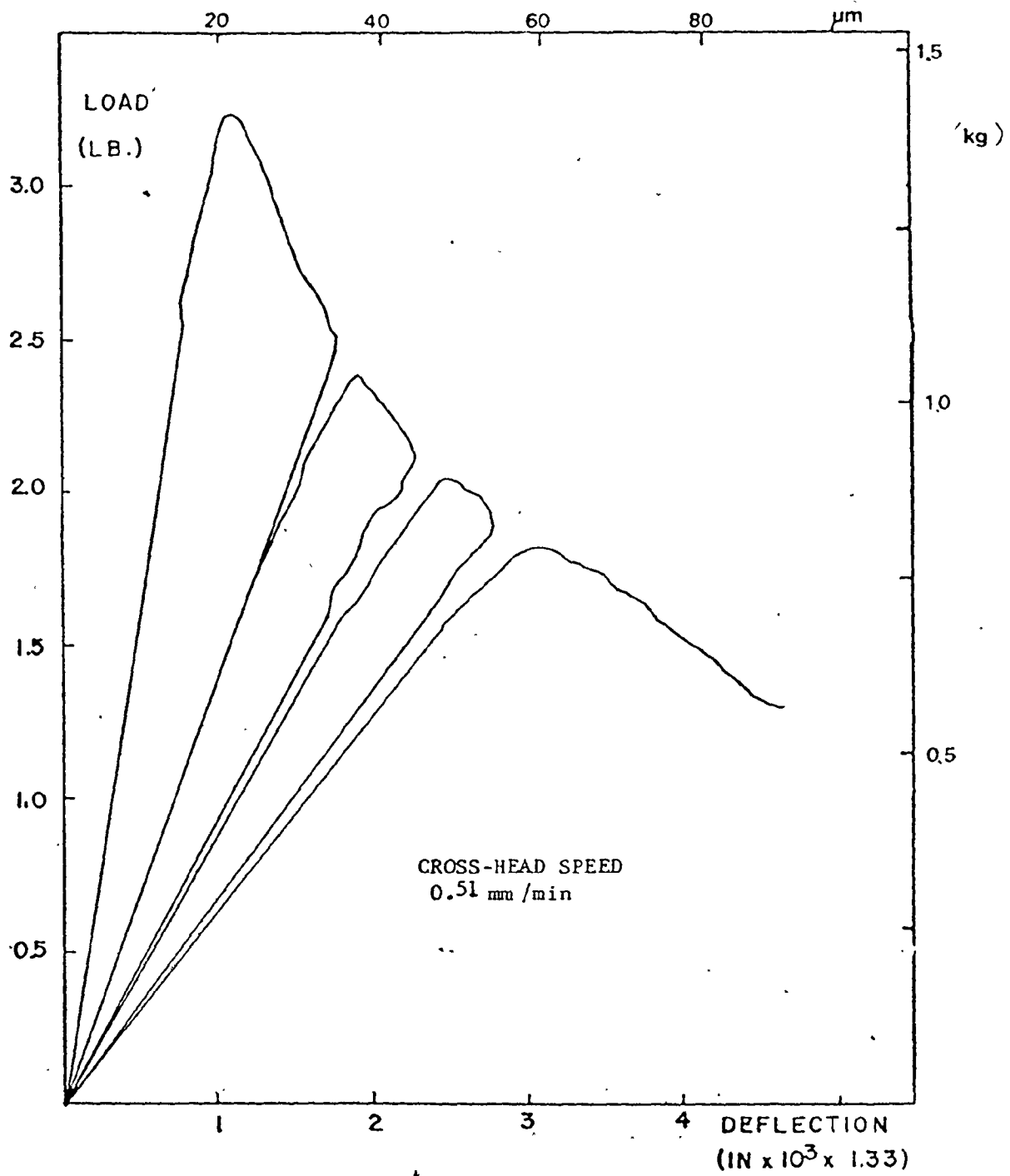


Figure 87. Load-Deflection Curve for Pyrex Glass (Start/Stop)

[192] as

$$\frac{(e)^3}{E_s I_s} = \frac{(lg)^3}{E_g I_g} \quad (5.5)$$

where E_s and E_g are the Young's modulus of steel and glass respectively and I_s and I_g the respective moments of inertia. It was found that $lg = 0.91e$; therefore, it was decided that no compliance correction need be made but the crack length should be measured from the loading points to the crack tip. This assumption will overestimate the critical stress intensity values obtained but by less than 1%. The values obtained for pyrex with this assumption are reported as K_{IC} in Table 25 as a function of loading-rate.

The second correction made to the data, attempted to account for any slow crack growth, which would reduce the accuracy of the crack length measurements. It will be seen in the next section, that the load-deflection data allow a value of crack length to be calculated. Therefore, by subtracting the crack length calculated from the critical load and displacement data from the crack length calculated from the initial compliance of the sample, the amount of slow crack growth may be calculated. The values of critical stress intensity (K_{IC}) based on the corrected crack length is also shown in Table 25. The data in Table 25 are shown as a function of loading rate. It was hoped initially, that increasing the loading rate would decrease the influence of slow crack growth. It can be seen, however, that the data are not affected in any consistent fashion by loading rate changes over the range of rates used in the present study.

TABLE 25. Fracture Surface Energy of Pyrex - Stress Analysis

Cross-Head Speed (mm/min)	Test Conditions	K_{IC}' (MNm ^{-3/2})	K_{IC}'' (MNm ^{-3/2})
0.51 {7	Air (23°C)	0.754(+ .011)	0.772(+ .016)
1.27 {6	"	0.721(+ .012)	0.741(+ .017)
2.54 {13	"	0.733(+ .022)	0.759(+ .017)
0.51 {8	Toluene (23°C)	0.748(+ .010)	
OVERALL {26	Air (23°C)	0.736(+ .021)	0.758(+ .020)

{ Brackets indicate number of Measurements

TABLE 26. Fracture Surface Energy of Pyrex - Compliance Analysis

Cross-Head Speed (/min)	Test Conditions	K_{IC} (MNm ^{-3/2})
0.51 {7	Air (23°C)	0.835 (+ .012)
1.27 {7	"	0.816 (+ .034)
2.54 {11	"	0.838 (+ .013)
Overall {25	"	0.831 (+ .022)

5.3.2 Compliance Analysis

Initially, an attempt was made to measure the deflection of the DCB sample from the cross-head motion. To do this, the compliance of the machine must be measured and then theoretically the compliance of the sample can be deduced from the load-time output for a given cross-head speed. It was found that the load-time output was only approximately linear which made measurement of machine compliance difficult. An approximate value of machine stiffness in the load-range used was calculated as $\sim 10^2$ kg/mm. It was observed later that the stiffness of the DCB sample is of the same order as the machine stiffness and this technique proved to be too insensitive to the sample deflection to be of any use. Indeed, when an extensometer was used to measure the opening deflection the resulting curve was completely different for the load-time data. The load-displacement curve now clearly indicated a non-linear region before maximum load indicative of the subcritical crack growth process which was absent in the load-time data.

The growth of the crack was observed to be stable with no sudden drop in load. The crack however, could not be easily arrested except at long crack lengths or if the cross-head was reversed. This behaviour is probably due to some transient instability and could be related to the machine stiffness (section 3.2).

The values obtained for the critical stress intensity using equation (3.20) are shown in Table 26. The initial crack length can be calculated from the load-deflection data (equation 3.18) but these calculated values proved to be $\sim 15\%$ higher than those measured. Hoagland

[142] observed similar behaviour in his experiments. This behaviour is probably a reflection of a fundamental difference between the compliance and stress analyses approaches.

The compliance approach also allows the fracture resistance of a material to be determined in a continuous fashion in stable fracture tests. Such behaviour is observed for the pyrex samples and a typical load-displacement record is shown in Figure 88. This data can then be translated into load-crack length and fracture resistance (R) - crack length curves (Figure 89). From this figure it can be seen that R is approximately constant as the crack grows (rate-insensitive material).

5.3.3 Comparison Between Two Approaches and Literature Values of K_{IC} For Pyrex

The fracture toughness of pyrex has been evaluated previously. The results of these studies are shown in Table 27. Most of the values are in good agreement with the data obtained on pyrex from the stress analysis approach. One value, however, shows better agreement with the compliance approach.

The difference between the two approaches is somewhat puzzling and it would seem that the literature data do support the stress analysis approach. For the glass/metal composites, however, the compliance approach does possess several advantages. Firstly, the side-grooved opaque samples make accurate crack length measurements difficult especially as there are no visible crack arrest steps on the fracture surface as was exploited in the pyrex tests. Secondly, the tests can

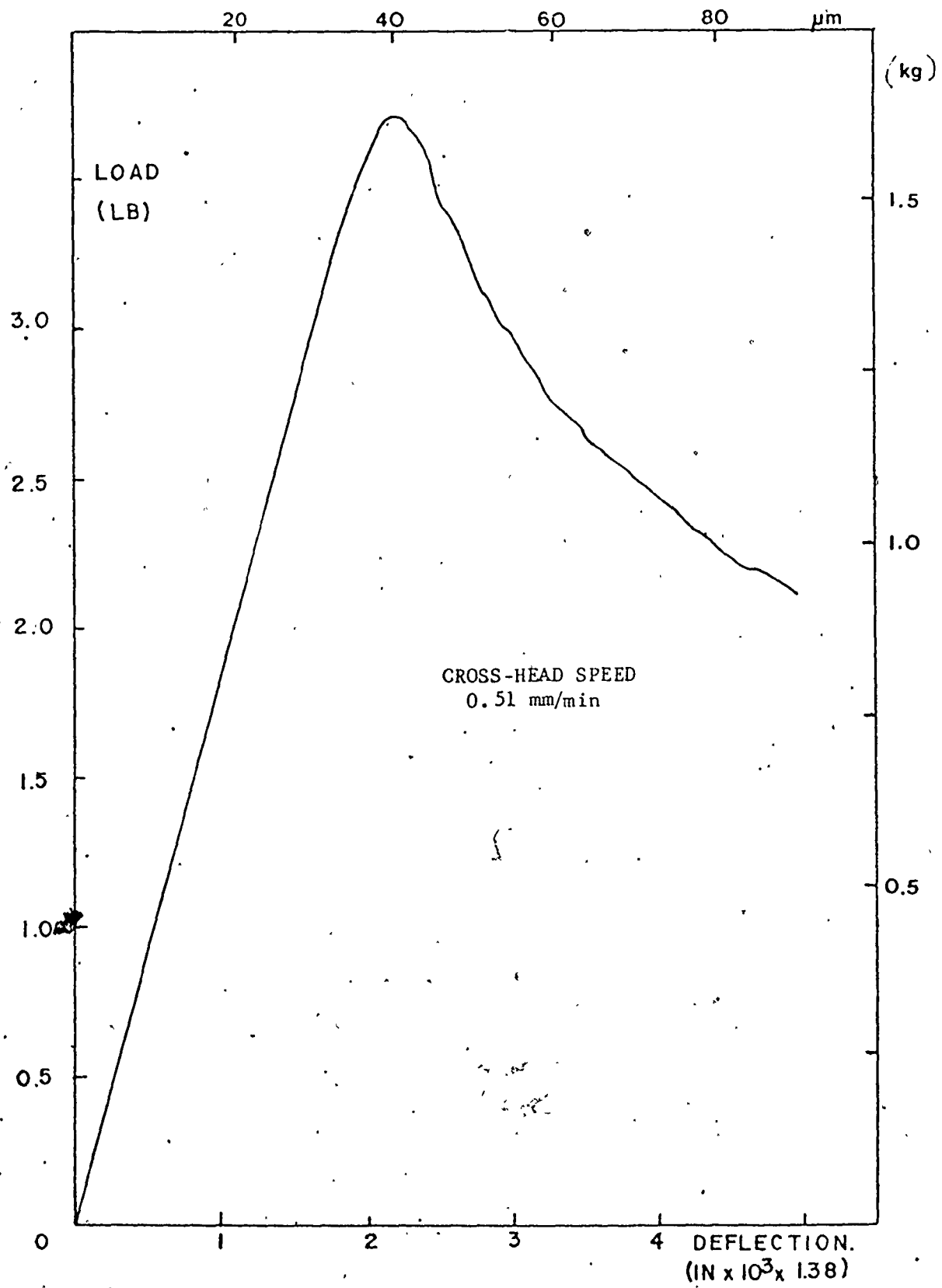


Figure 88. Load-Deflection Curve for Pyrex Glass (Continuous)

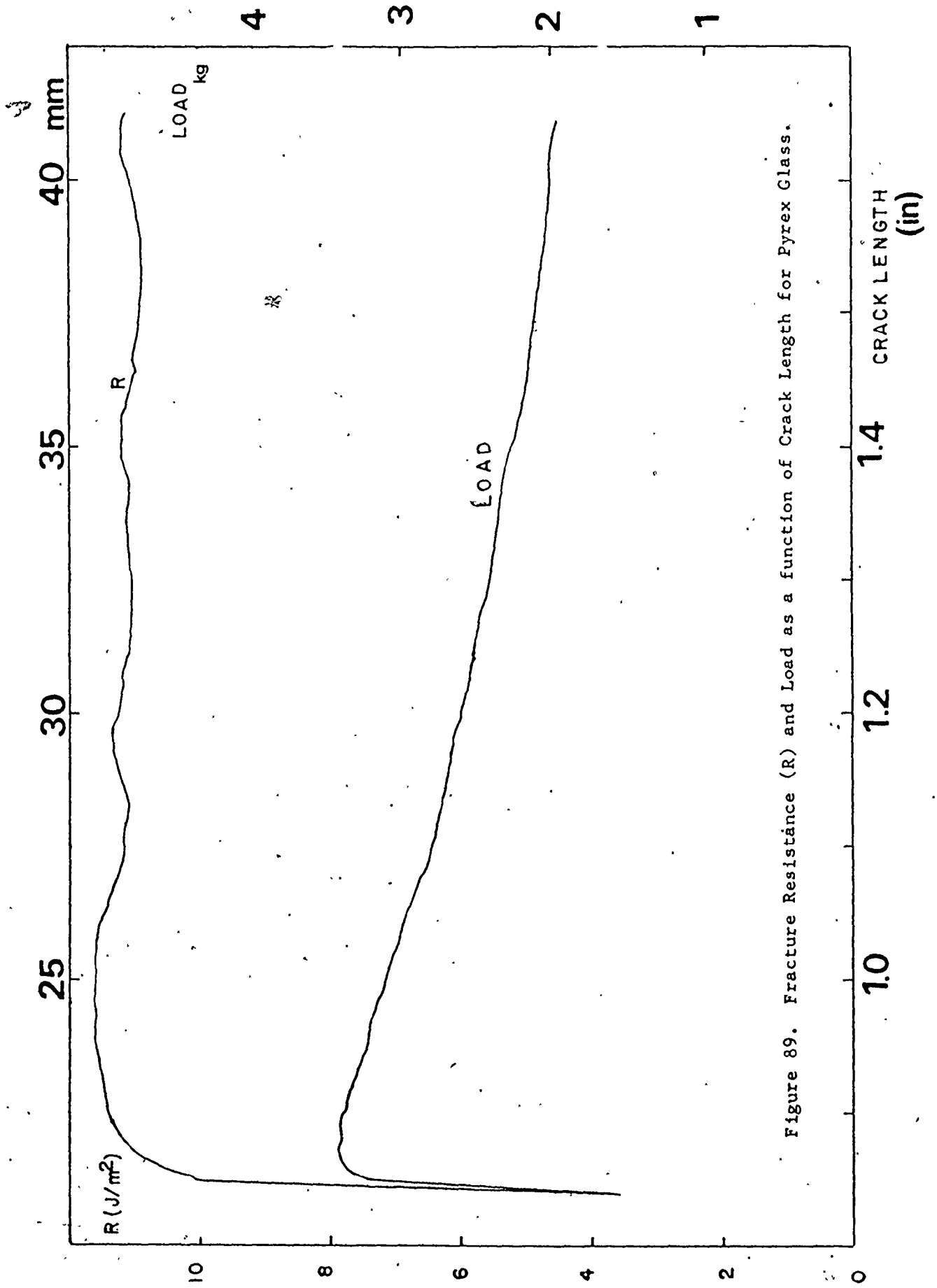


Figure 89. Fracture Resistance (R) and Load as a function of Crack Length for Pyrex Glass.

TABLE 27. Literature Values of Fracture Surface Energy of Pyrex at Room Temperature.

Atmosphere	Test Geometry	K_{IC} (MNm ^{-3/2})	Reference
Dry Nitrogen (0.02RH)	DCB (Stress Analysis)	0.764 (\pm .008)	193
Vacuum	DCB (Stress Anal)	0.760 (\pm .007)	193
Vacuum (Pre-Treat)	DCB (Stress Anal)	0.770 (\pm .012)	193
Vacuum	Three-Point Bend (Stress Anal)	0.777 (\pm .032)	193
Air (0.20 RH)	DCB (Compliance)	0.78 *	194
Vacuum	DCB (Compliance)	0.88 *	194

* Young's Modulus Assumed to be 62 GPa

be performed without the experimental difficulties encountered when attempting to avoid subcritical crack growth. Thirdly, the tests can be performed at lower loading rates which allows more measurements to be made on each sample and which also ensures that any misalignment in the pre-cracking operation will be reflected in only the first experimental result per sample. Testing at lower loading-rates also reduces the possibility of dynamic factors affecting the results. Fourthly, the compliance approach also allows the fracture resistance to be studied in a continuous fashion (R curve analysis) without monitoring the changing crack length. It was decided to use the compliance approach for the glass/nickel composites although this throws some doubt of the absolute values of the fracture toughness measurements. The relative variations in fracture toughness, however, should still allow an accurate study of the fracture behaviour of these composites. The difference observed between the two experimental approaches seems real and must point to some basic conceptual, theoretical or experimental problem in their formulation.

5.4 Determination of Young's Modulus

The Young's modulus of the glass/nickel composites were measured in two ways. Approximate values were obtained from the four point bend flexure tests and more accurate ultrasonic measurements were made of the longitudinal sound velocity.

5.4.1 Four Point Flexure Data

A value of Young's modulus can be determined from the four point

bend strength tests using the relationship [151]

$$E = \frac{7P}{32\delta bw^3} \quad (5.6)$$

for the test geometry used. This was considered only an approximate approach and the deflection (δ) was deduced from the load-time data after correcting for machine stiffness. The load-time response was non-linear but showed a slight increase of slope with increasing load. The machine stiffness was calculated in two ways. Firstly, by placing a large piece of aluminium (50 mm x 9 mm x 6 mm) in the apparatus which would be approximately rigid under the applied load. Any deflection would then be a result of the machine and the test rig. Secondly, the machine stiffness can be deduced by using a bend sample of known modulus and thereby standardizing the test procedure. It was thought that the second technique would give rise to more accurate results. The results of this determination using a pyrex standard are shown in Table 28. The scatter in the data is quite large but there seems to be a decrease in modulus with increasing volume fraction of nickel.

5.4.2 Ultrasonic Measurements

The longitudinal sound velocity was determined at Westinghouse (Atomic Power Division) and the results are shown in Table 29 with the calculated value of Young's modulus. Included in this table is Young's modulus data for pyrex from the ultrasonic testing and a comparison with previous literature values. All results in Table 29 were calculated from equation (3.1), which gives a better correlation with the literature than equation (3.2). These results appear to be more accurate than the

TABLE 28. Determination of Young's Modulus from Four-Point Bend Tests
(Pyrex Standard)

Material	Young's Modulus (psi x 10 ⁻⁶)	E (GPa)	No. of Samples
S Glass	8.4 (+ 1.6)	58 (<u>+11</u>)	11
S/6% Nickel	6.7 (+ 0.7)	46 (<u>+ 5</u>)	6
S/10% Nickel	7.8 (+ 1.8)	53 (<u>+12</u>)	5
S/15% Nickel	7.0 (+ 1.3)	48 (<u>+ 9</u>)	6
S/20% Nickel	7.0 (+ 0.9)	48 (<u>+ 6</u>)	6

TABLE 29. Determination of Young's Modulus from Ultrasonic Data

Material	Longitudinal Sound Velocity (km/s)	Density (kg/m ³ x10 ⁻³)	E (psi x 10 ⁻⁶)	E (GPa)
S Glass	5.3	2.50	10.4	72
S/2% Nickel	5.1	2.63	10.2	70
S/4% Nickel	4.8	2.77	9.3	64
S/6% Nickel	4.4	2.89	8.0	55
S/10% Nickel	4.4	3.09	8.5	59
S/15% Nickel	4.2	3.47	9.0	62
S/20% Nickel	4.0	3.78	9.0	62
Pyrex	5.3	2.23	9.1	63
Pyrex (Ref. 193)			9.1	63
Pyrex (Ref. 191)			9.24	63.7
Pyrex (Ref. 194)			8.8	61
	(+ 2%)		(+ 4%)	(+4%)

values calculated from the bend data but show the same variation with volume fraction. There is a difference, however, in the absolute value of modulus determined by these two approaches. Differences in the static and dynamic values of Young's modulus has been observed by many authors especially in the study of rocks where the presence of microcracks seems to accentuate this difference [195]. A similar effect may be present in these composites where there is, by experimental design, no bonding between the glass and the metal which will lead to pronounced scattering of the sound waves. It should be noted that the compliance approach^{*} used in the fracture toughness measurements, exhibits only a weak dependence on Young's Modulus. Both G_{IC} and K_{IC} are functions of the cube root of modulus (equation (3.20)), therefore, inaccuracies in the modulus determinations will give rise to only small errors in the determination of these parameters.

For a well-bonded composite, it is expected that for the S glass-nickel system, the Young's modulus should increase with increasing volume fraction of nickel (Section 3.1). The S glass-nickel system was chosen so that there should be no interfacial bond. The variation in Young's modulus for this non-bonded situation has been predicted by Sato and Furakawa [127]. Figure 90 shows the comparison between their prediction (equation 3.6) and the calculated values. The correlation is not very good though both functions give rise to a similar decrease in E. Included in Figure 90 is the variation in E predicted theoretically [127] for a well-bonded S glass-nickel system and by Hasselman and Fulrath [196] for spherical pores in glass ($\nu_m = 0.20$). Hasselman and Fulrath [196] confirmed their prediction experimentally.

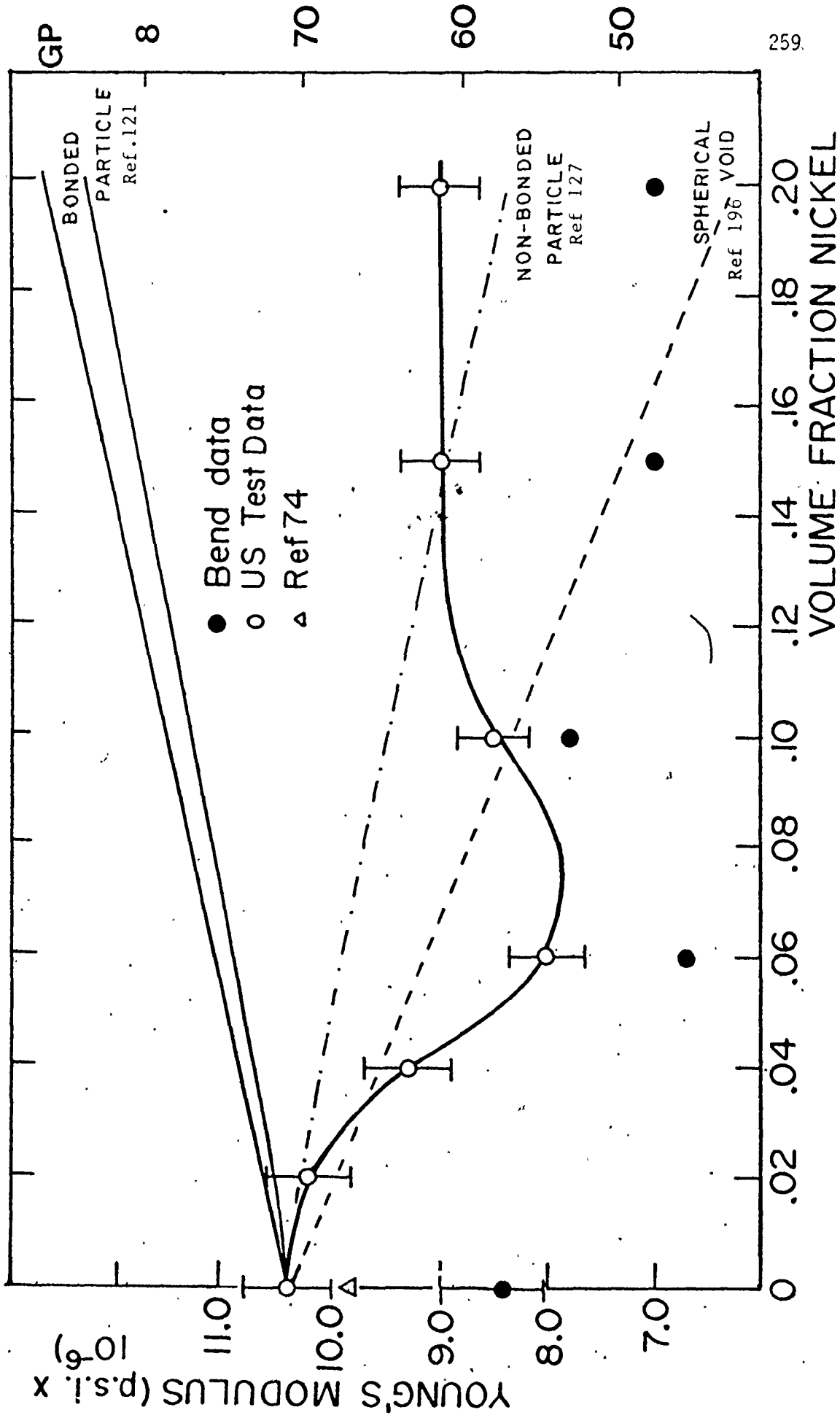


Figure 90. Young's Modulus as a Function of Volume Fraction Nickel - Experimental Results and Theoretical Predictions

The Young's modulus data is consistent with a non-bonded interface in this system so that the particles may be considered as 'pseudoporosity' (section 3.1). The detailed variation of E is not predicted exactly by any of the theoretical approaches but it is more consistent with the theoretical variations for non-bonded particles or spherical pores than for well-bonded particles.

5.5 Fracture Toughness of S Glass-Nickel Composites

The fracture surface energy of the glass nickel composites was measured from the DCB load-deflection data. The results are plotted in Figure 91 and show a substantial increase in γ with increasing volume fraction of nickel. The various mechanisms that could be involved in the fracture of particulate composites were discussed in Chapter 2. It is important to identify which of these mechanisms are important.

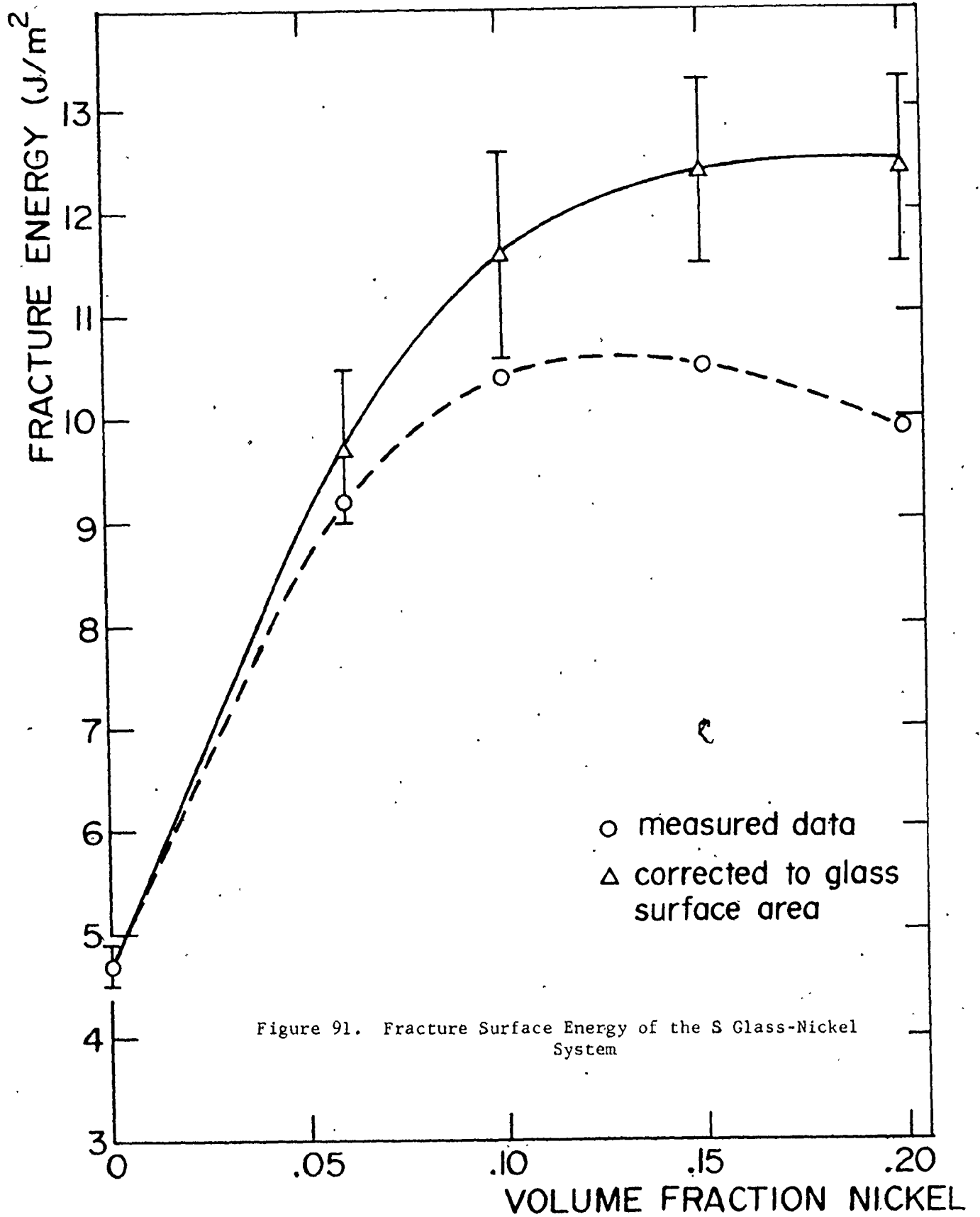
5.5.1 Areal Contribution

If the approach is taken that the fracture toughness of highly brittle materials is simply related to the amount of fracture surface produced, then it is relatively simple to compare the actual fracture surface area and the projected (planar) fracture surface area.

First, let us consider a planar fracture in a particulate composite. The fracture surface energy of the composite (γ_c) could be approximately given by

$$\gamma_c = (1 - V_v) \gamma_m + V_v \gamma_p \quad (5.7)$$

where m and p refer to the matrix and particle respectively. For a non-bonded interface, $\gamma_p = 0$, so that the particles give no contribution to the fracture surface and



$$\gamma_m = \frac{\gamma_c}{(1 - \nu_y)} \quad (5.8)$$

The data in Figure 91 were corrected using this last equation and it can be seen that the increase in fracture surface energy is further emphasized* and does not remain constant. This approach assumed no bonding and a planar fracture surface but as discussed later neither of these factors are sufficient to explain the observed variation in fracture toughness. The areal contribution approach does not explain the results but first the various energy-absorbing mechanisms will be discussed in more detail, i.e.,

- (i) Plastic deformation of the nickel spheres
- (ii) Surface roughness
- (iii) The formation of the fracture surface steps
- (iv) Decohesion of the particles
- (v) Change in crack shape or crack pinning due to the interaction with the second phase particles.

5.5.2 Plastic Deformation

It is feasible that the high stresses in the vicinity of a crack tip could induce plastic flow in nickel particles close to the crack tip. Under conditions of plain strain, the size of the plastic zone (r_y) is approximately given by [19]

$$r_y \cong \frac{1}{6\pi} \left(\frac{K_{IC}}{\sigma_y} \right)^2 \quad (5.9)$$

Assuming reasonable values of $\sigma_y = 170$ MPa (25 ksi) and $K_{IC} = 1$ MNm^{-3/2} (750 in lb/in²), a plastic zone size of $r_y \cong 2.0$ μ m is obtained.

For non-bonded particles, however, no stresses can be transmitted to the particles as the stress field near the crack tip is triaxial. For the S glass-nickel system, plastic flow cannot make any contribution to the fracture toughness. Even if a weak bond were present, the particles would probably decohere before the crack reaches the particle.

5.5.3 Surface Roughness

Returning to the areal contribution approach, it is clear that surface roughness would tend to increase the measured values of \bar{v} . In bonded particulate composites where the fracture follows the particle-matrix interface, the particles themselves will increase the surface roughness. A model has been analyzed for this process [198] but it only gives rise to a small roughness factor, i.e., 1.08 for 30 vol. % spheres.

There is also a tendency for a crack to change its path in the vicinity of a particle. For the glass-nickel system, this will be reflected in surface roughness of the glass matrix. The roughness was observed to be primarily associated with ledges and steps in the vicinity of the particles. A general undulation of the fracture surface was observed as well. Figures 92-93 show side views of the fracture surface of these composites. An estimate of the surface undulation was made and gave a roughness factor of 1.04 - 1.08 with a maximum tilt angle of $\sim 10^\circ$. This is also consistent with the approach shown in Figure 14 for $G(\theta)$.

It is concluded that the observed surface undulations are insufficient to explain the observed variation in \bar{v} .

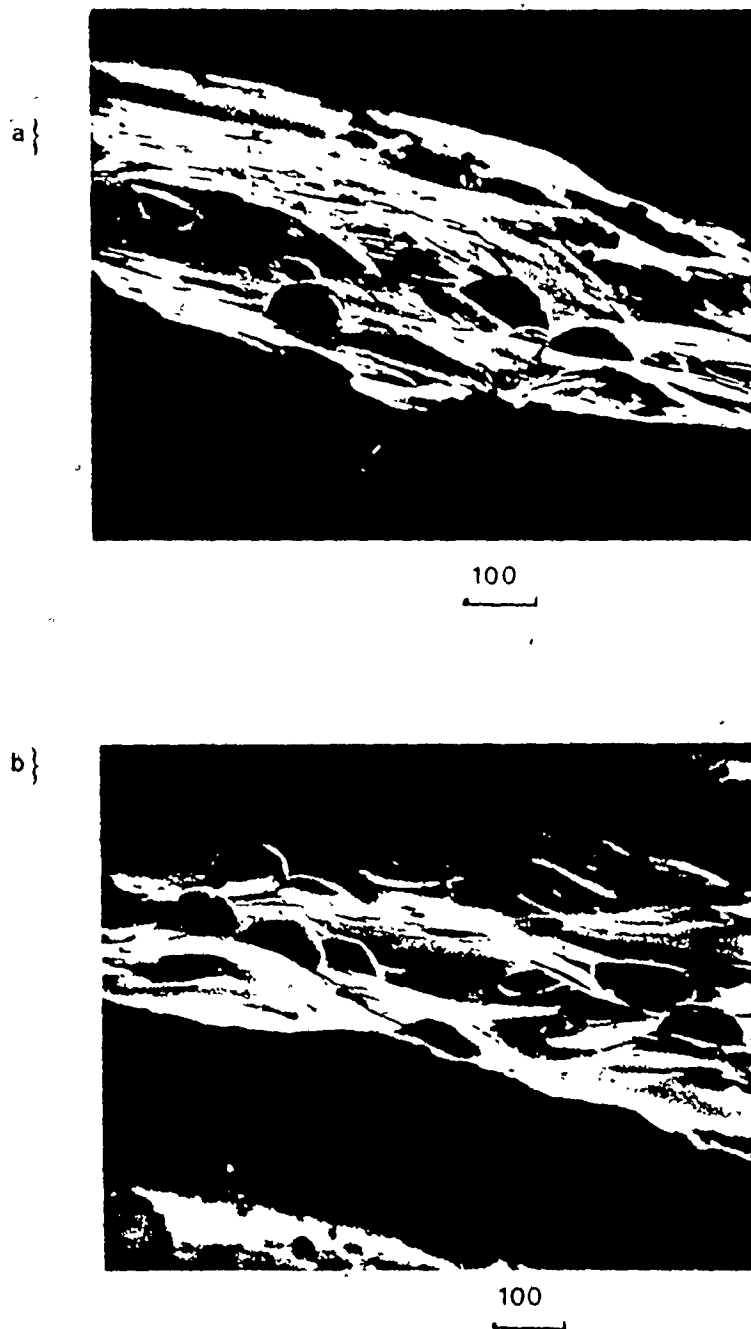
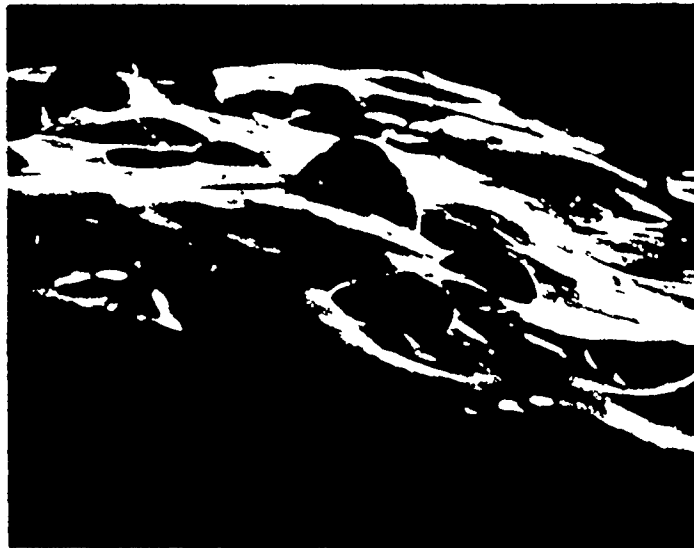


Figure 92. Side View of Fracture Surfaces in S Glass-Nickel Composites,
a) 6 vol.% b) 10 vol.%



100



100

Figure 93. Side View of Fracture Surfaces in S Glass-Nickel Composites,
a) 15 vol.% b) 20 vol.%

5.5.4 Fracture Surface Steps

The interaction of a crack front with inclusions often results in the production of a surface step or 'tail' at the rear of the particle. During this interaction, the local stress field must influence the trajectory of the segmented cracks such that when they reach the rear of the particles they are non-coplanar. To recombine, they must form a secondary fracture at the rear of the particle.

These fracture surface steps were readily observed in the glass-nickel composites. Figure 94 show a typical fracture surface step at the rear of a nickel particle. Another feature in this figure is a ledge at the front of the particle. This ledge is probably a result of a sudden change in crack direction as the crack enters the stress field around the inclusion. The fracture steps and ledges will require extra fracture energy for their formation because they constitute an increase in fracture surface area.

From fractographic observations, the ledges are less predominant than the fracture tails and become less distinct at higher volume fractions. The fracture tails increase in density with increasing volume fraction till a saturation occurs at higher volume fractions when they connect particles and are not eliminated by coalescence.

The additional surface area associated with these tails was estimated to be 6% for a 20 vol. % sample. It has been suggested that undercutting of steps is common so that for complete undercutting a factor of two would be involved. This is the last feature associated with surface roughness and the increased area is still not sufficient to



Figure 94. Fractographic Features around Nickel Particles in S Glass.

explain the γ results. The maximum roughness factor for the surface undulations and fracture surface steps is ~ 1.20 .

It has been suggested [98] that the crack extension force in step formation might be increased as the secondary fracture does not occur under mode I loading.

This problem was discussed in section 2.3.3 and using equation (2.28), a value of the contribution to γ of the fracture surface steps can be estimated. For the situation where the height of the steps is $\sim r_0$ (the particle radius) as is approximately observed and $s = 2(d+r_0)$ equation (2.28) can be rewritten as

$$\begin{aligned}\gamma_s &= 1/2 \tau d_0 \left(\frac{r_0}{2(d+r_0)} \right) \\ &= 1/2 \tau d_0 \left(\frac{r_0/d}{2(1+r_0/d)} \right)\end{aligned}\quad (5.10)$$

For highly brittle solids, $\tau = 1/2 \sigma_{th}$ so that finally

$$\gamma_s = \frac{1}{2} \gamma_0 \left(\frac{r_0/d}{2(1+r_0/d)} \right) \quad (5.11)$$

For a 20 vol. % sample, r_0/d can be found from Figure 10 to be ~ 0.4 so that $\gamma_s = \gamma_0/14$. This value is in good agreement with the observed increase in fracture surface area contribution (6%) due to the steps.

It appears that from either of the two approaches, the formation of the fracture surface steps will only give a small contribution to the value of γ . It is, however, possible that the fracture surface steps are fractured after the primary crack front has passed

the particles. In this case, the unbroken steps will be left as ligaments behind the primary crack and could give rise to an increase in γ . Equation (5.11) should still give a reasonable estimate of this contribution though the density of steps will be increased as more steps are now resisting the crack opening.

5.5.5 Decohesion Zone

There is a possibility, that there is a weak interfacial bond between the glass and the nickel. It can be seen from equation (5.7) that if $\gamma_p = 1/10\gamma_m$, then this would only make a small contribution to γ_c . There is, however, the possibility that decohesion will also occur above and below the fracture surface and form a decohesion zone near the crack tip. This problem was discussed in section 2.3.2, and the contribution to γ can be calculated from equation (2.24). This equation is only valid if the radius of the decohesed zone (r_m) is much smaller than the crack length, i.e.:

$$r_m = 0.7 \left(\frac{(K_{IC})^2}{\sigma_T} \right) \ll 25 \text{ nm} \quad (5.12)$$

This criterion implies that $\sigma_T \geq 10^7 \text{ Nm}^{-2}$ for equation (2.24) to be valid. For values of σ_T less than this, the decohesed zone would be large and would give rise to non-linear elastic behaviour in the load-deflection data. Such non-linear behaviour was not observed in the strength testing. Substituting reasonable values into equation (2.24) of $\sigma_T = 10 \text{ MPa}$, ($1.5 \times 10^3 \text{ psi}$), $a_0 = 1 \text{ nm}$, $V_V = 0.20$ and $r = 66 \text{ }\mu\text{m}$, a value of $\gamma_m = 14 \text{ Jm}^{-2}$ is obtained. On comparison with the fracture surface energy of glass (4.8 Jm^{-2}), it is seen that such a decohesion zone could give rise to values of composite fracture surface energy

data, that is consistent with the measured values. For values of $\sigma_T > 10 \text{ MPa}$, the value of γ_m decreases very rapidly.

The Young's modulus data for the glass-nickel system reflects the non-bonded nature of the interface and yet an interfacial strength of 10^7 Nm^{-2} implies that the interface is reasonably strong. In the modulus determination, small amplitude ultrasonic waves were used and for such interfacial strengths, the particles should behave as if they are well-bonded. This is not reflected in the modulus data. Therefore, although a decohesion zone could explain the fracture surface energy variation, the evidence is that for the S glass-nickel system, the particles should be considered non-bonded.

5.5.6 Crack Shape

It has been proposed by Lange [111] that a change in crack shape could contribute significantly to the fracture resistance of brittle particulate composites (Section 2.3.5). For this type of approach, the energy absorbing processes need not be discussed, it is enough to calculate the increase in elastic strain energy of the system for different crack shape configurations:

Using a line tension postulate Lange derived equation (2.35) which gives a linear function of γ when plotted against $(1/d)$. For the interparticle spacing, Lange used the value of the mean free path, which is incorrect. Figure 95 shows a similar plot for the S glass-nickel system where d is now defined by equation (5.3). The fracture surface energy - reciprocal mean free path data is included in the

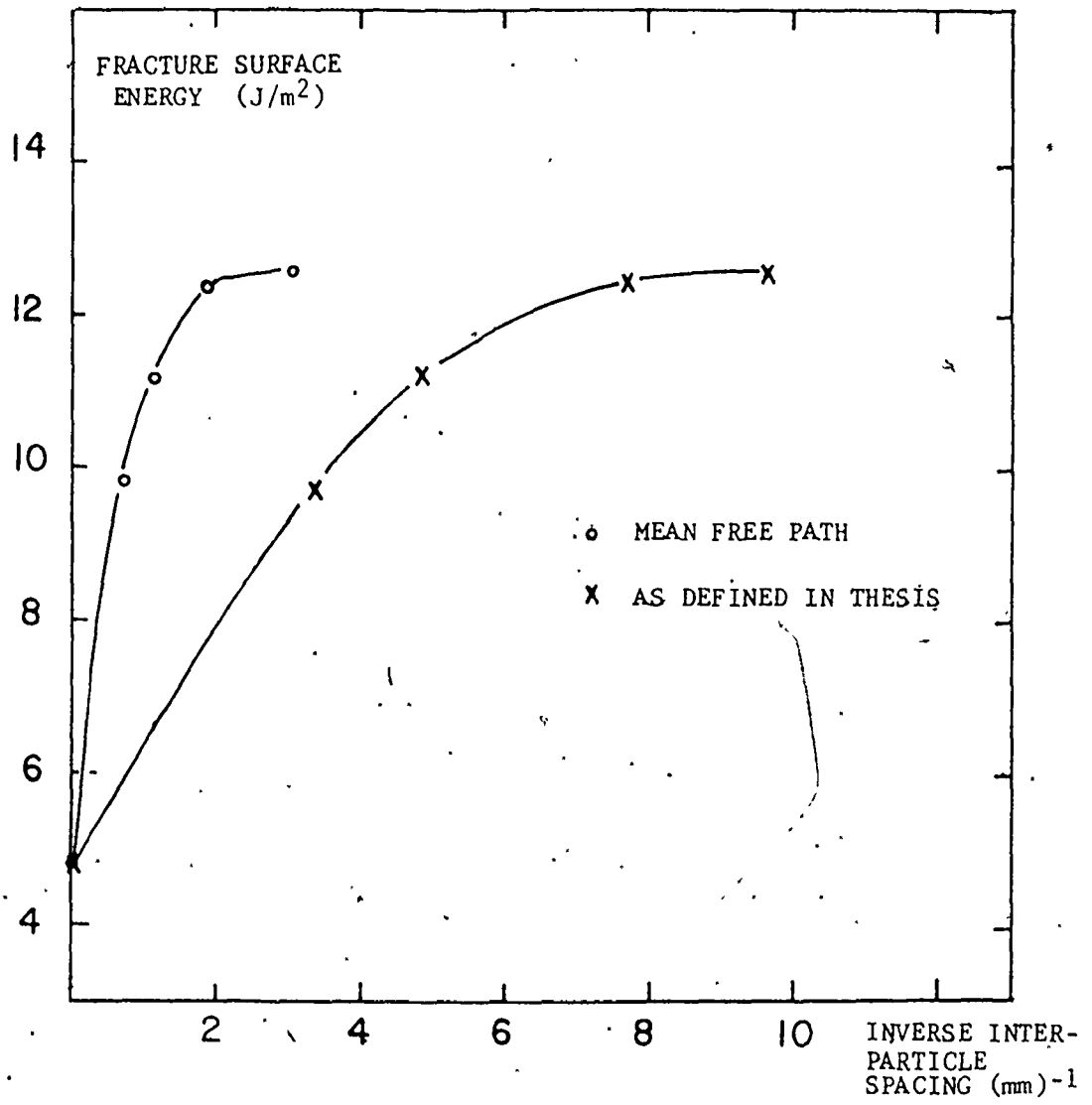


Figure 95. Fracture Surface Energy as a Function of Inverse Interparticle Spacing.

figure for comparison. Neither approach gives rise to lineal function and both show a similar variation. The major difference is the slopes of the curves and a value of T can be calculated for the initial portion of the curves which are approximately linear.

For the γ versus $1/d$ function $T = 1.3 \text{ mJ/m}$ (130 ergs/cm) 0.13 Jm^{-1} . Lange [111] derived a theoretical expression for T which is given in equation (2.34) though he defines d as the crack length rather than the interparticle spacing. For the glass - Al_2O_3 system, Lange [9] obtains an approximate theoretical value of T as 0.15 to 0.60 mJ/m. Unfortunately, the concept of line tension for a crack front is rather tenuous (section 2.3.5).

Evans [113] extended the idea of Lange without using the line tension postulate although he demonstrated that even if such a concept were valid, the value of T is not constant. In this approach, the crack front must be pinned by the obstacle. For a void or non-bonded particle, this type of pinning is not available. As shown in Appendix A.7, for the case of no pinning, the Evan's model predicts that the crack front will remain straight with no increase in fracture surface energy. This is contrary to most fractographic observations of cracks interacting with voids so it appears that the model of Evans is incomplete.

The change in crack shape was studied experimentally for the S glass-nickel system and the ideas of Lange and Evans will be extended in a later section.

5.5.7 Crack Blunting

As a crack front intersects a void or non-bonded particle, the crack front will be locally blunted and the stress distribution ahead of the crack will be altered. Although such a process does not affect the energy criterion, it may be that the stress in the vicinity of the void is no longer sufficient for bond failure (section 2.3.4). It is experimentally observed that increasing the crack tip radius, can increase the apparent value of K_{IC} [199], so attention is forced on the small region ahead of the crack. Figure 96 shows the effect of ρ on the local stresses for a sharp fracture mechanical crack and finite radius cracks calculated from a Neuber analysis. Weiss et al [200] have shown that a useful expression to describe the reduced stresses ahead of the crack is given by

$$\sigma_{22} = \sigma_A \sqrt{\frac{4c}{\rho + 4r}} \quad (5.13)$$

This expression reduces to the sharp crack expression when $\rho = 4r$.

For a crack interacting with a series of voids or non-bonded particles, the value of σ_{22} will be locally reduced and this will give rise to a local variation in the fracture resistance. This process should be reflected by a change in crack shape. It remains to be shown that the combination of the crack blunting and crack shape ideas are sufficient to explain the measured variation in σ . This problem will be discussed in a later section. The other energy absorbing mechanisms discussed in sections 5.5.1 to 5.5.5 appear to give either a small or negligible contribution to the fracture surface energy in the S glass-nickel system.

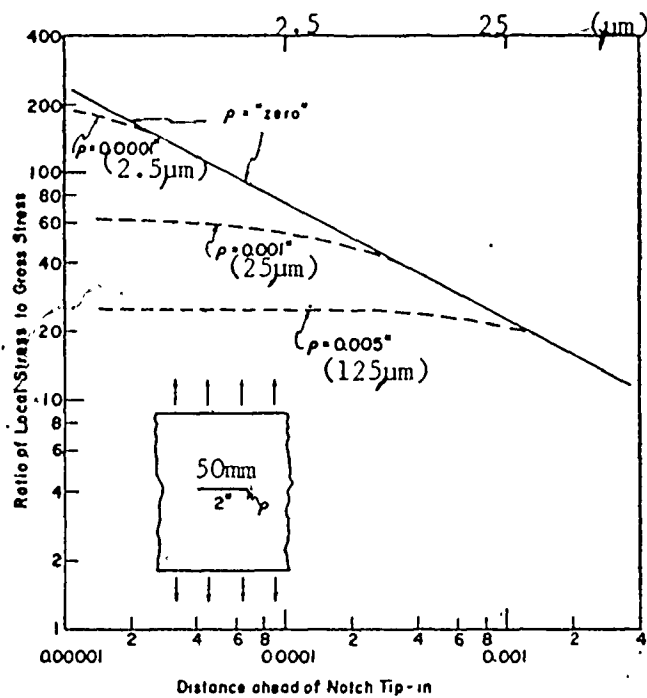


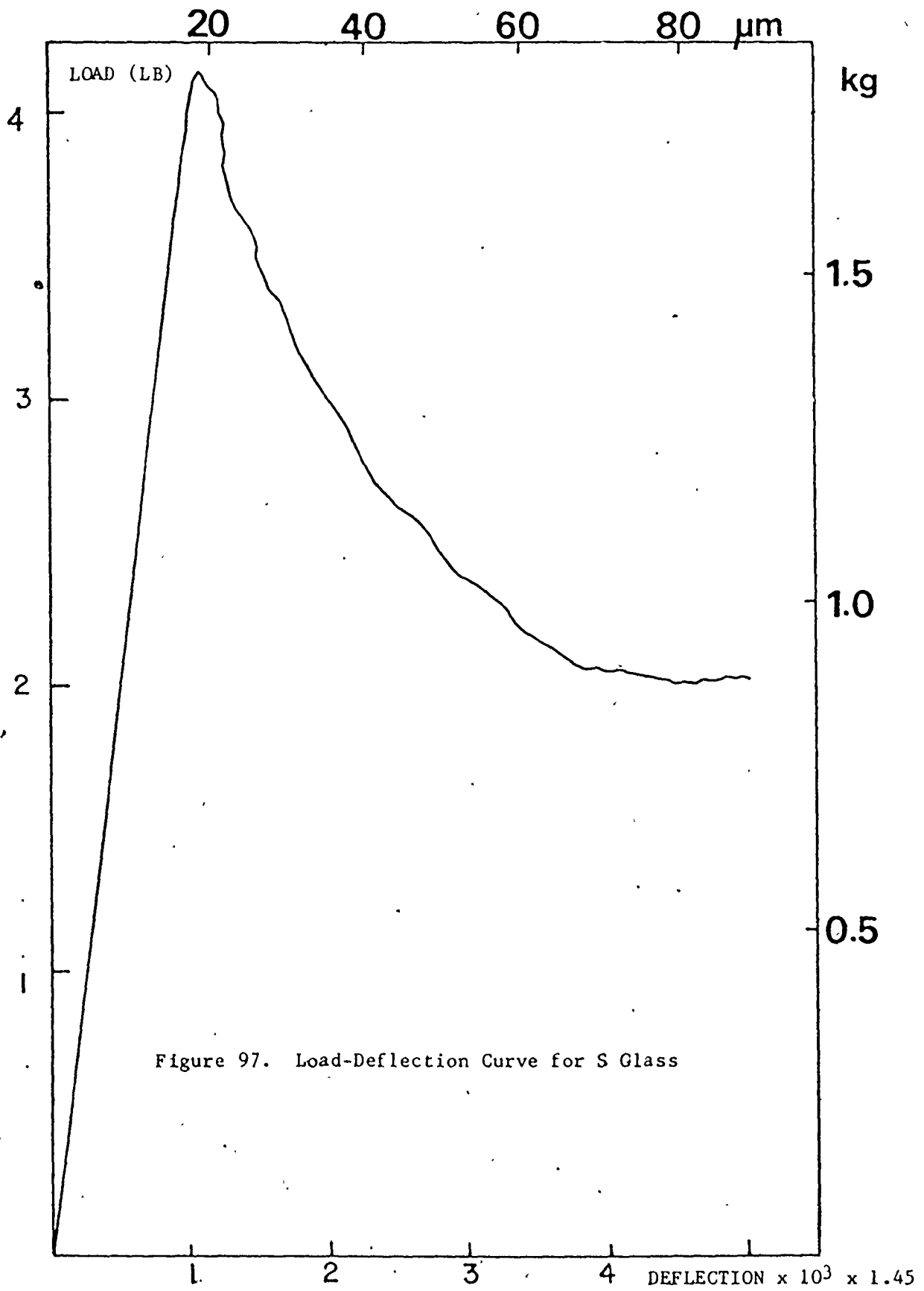
Figure 96. Comparison of Local Stresses in the Vicinity of the Notch Tip.

The fracture resistance of these composites was also measured in a continuous fashion as stable fracture occurred. The data are presented in Figures 97-102 as load-deflection curves and the derived fracture resistance - crack length plots. For the pure S glass, R is essentially constant as would be expected for a homogeneous, rate-insensitive material. The behaviour is similar to that observed in the pyrex glass (Figure 89). As the volume fraction of nickel increases, oscillations appear in the R curves and is a reflection of the heterogeneous nature of the material. In certain areas of the samples, the particles must offer a greater resistance to fracture and R increases. Then as the crack breaks away from the regions, R decreases. Table 30 gives the values of R expressed as ranges, which reflects the variation in fracture resistance better than a single value.

5.6 Strength of the S Glass-Nickel Composites

The strength of the composites was determined in four point bending and the results are shown in Figure 103. Included in this figure are some of the data of Stett and Fulrath [74]. The fracture strength of these composites decreases with increasing volume fraction nickel.

The size of the critical flaw that controls the fracture strength can be estimated from equation (3.28) provide the value of σ_c measured on samples containing relatively large cracks, is also valid for the much smaller cracks that initiate fracture. With this assumption, the size of the critical flaw was calculated (penny-shaped flaw) and the results are shown in Table 31. It can be seen that the values



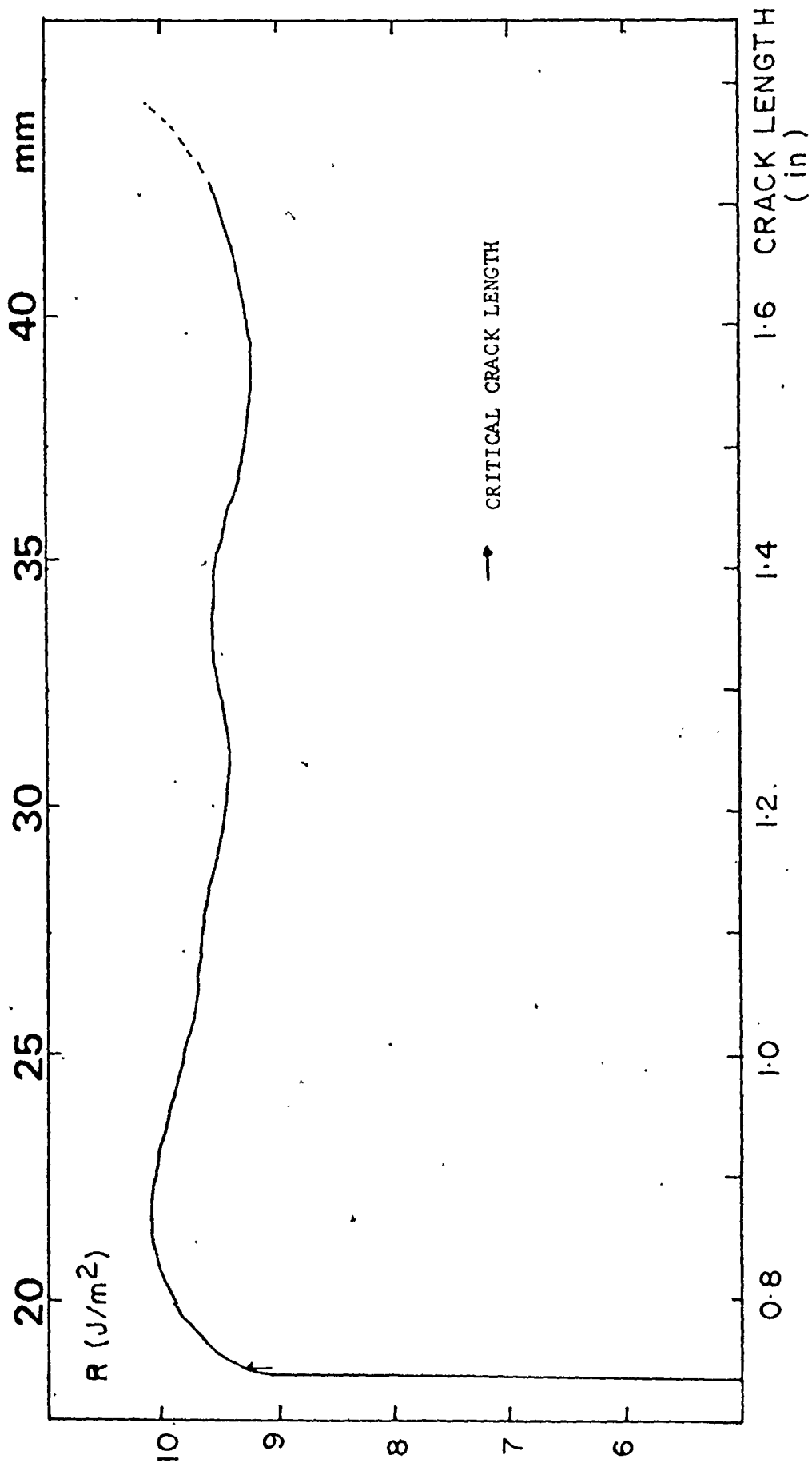


Figure 98. Fracture Resistance Curve - S Glass

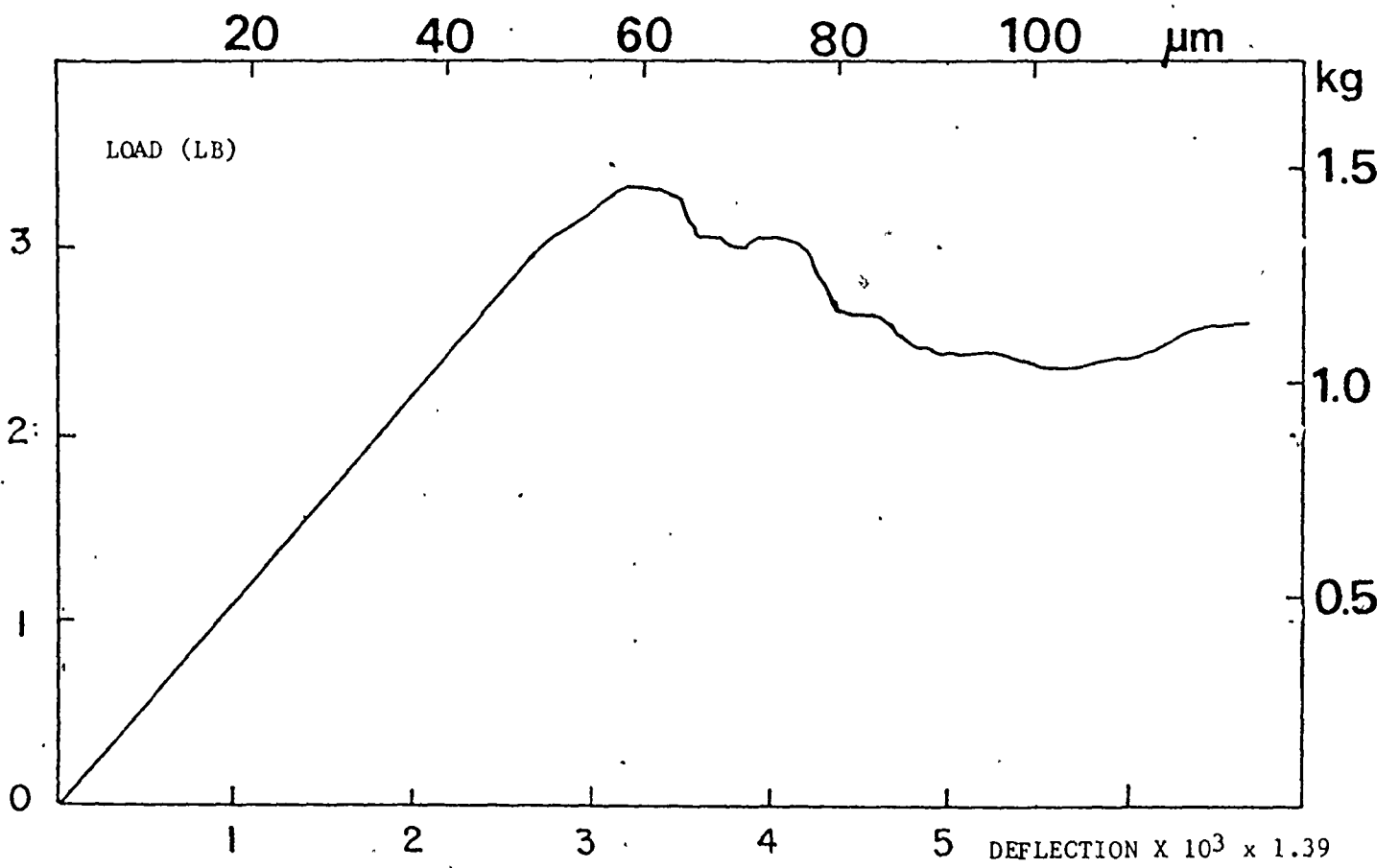


Figure 99. Load-Deflection Curve for S Glass-10% Nickel

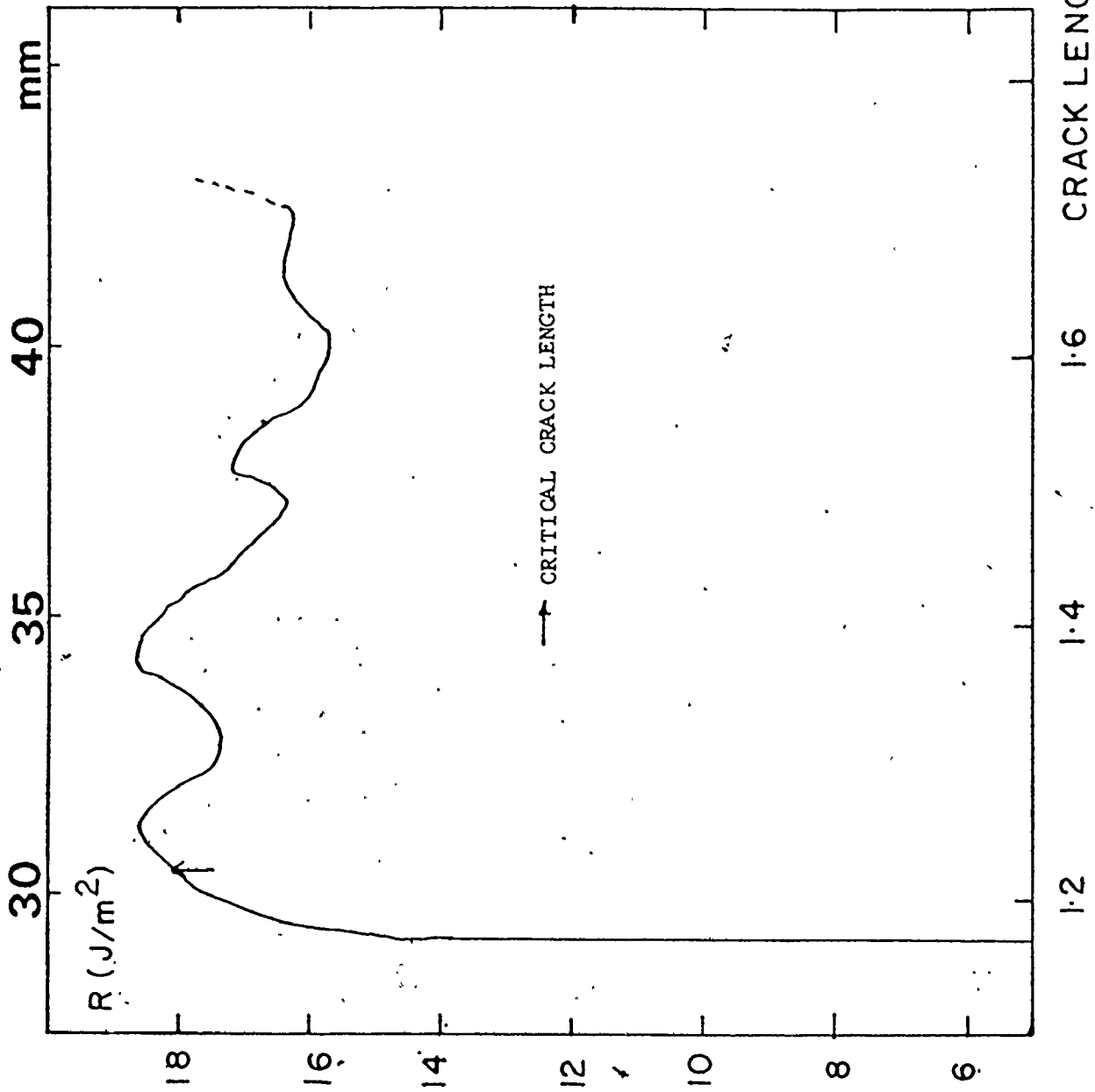


Figure 100. Fracture Resistance Curve- S Glass/10% Nickel. (in)

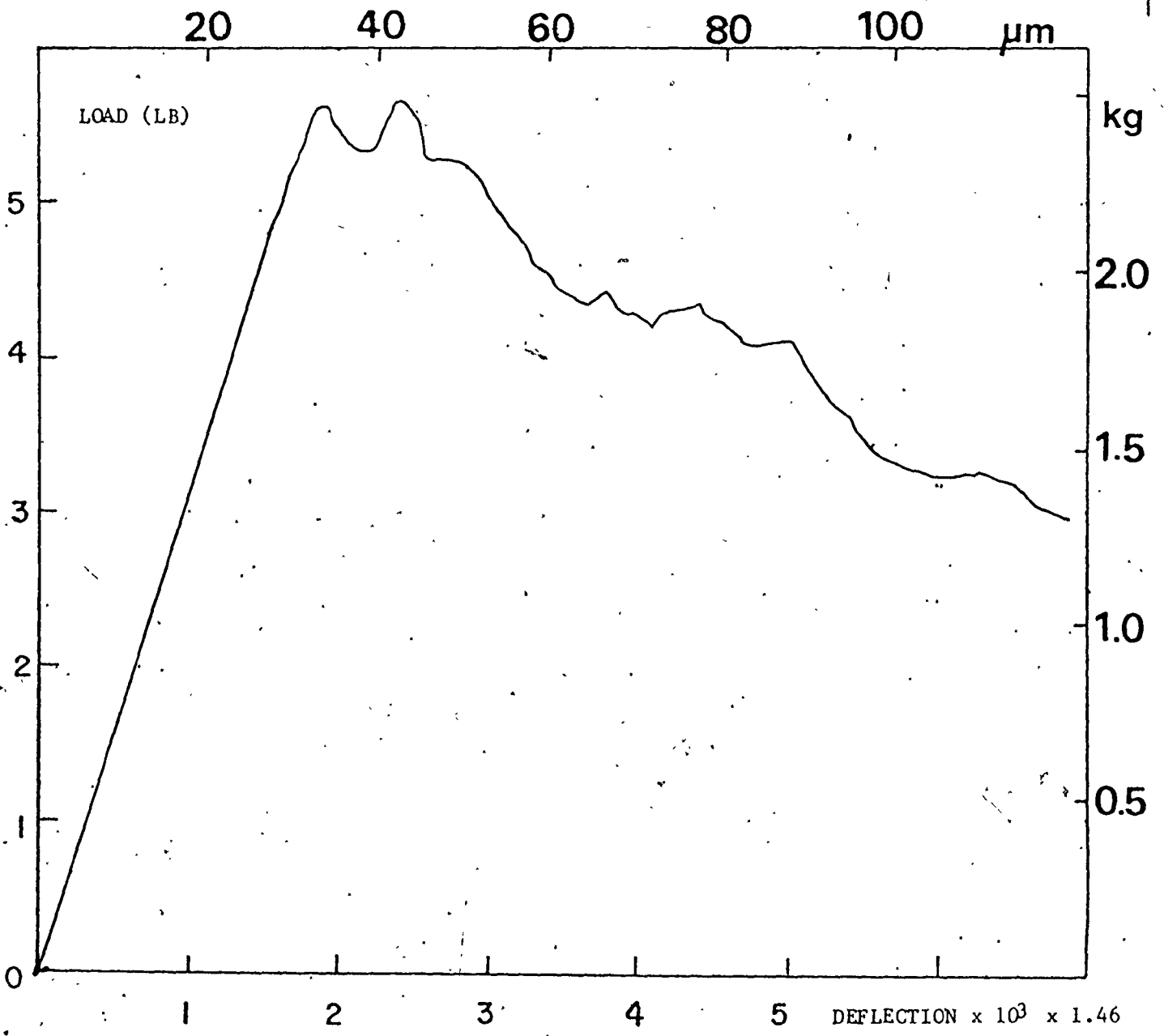


Figure 101. Load-Deflection Curve for S Glass/15% Nickel.

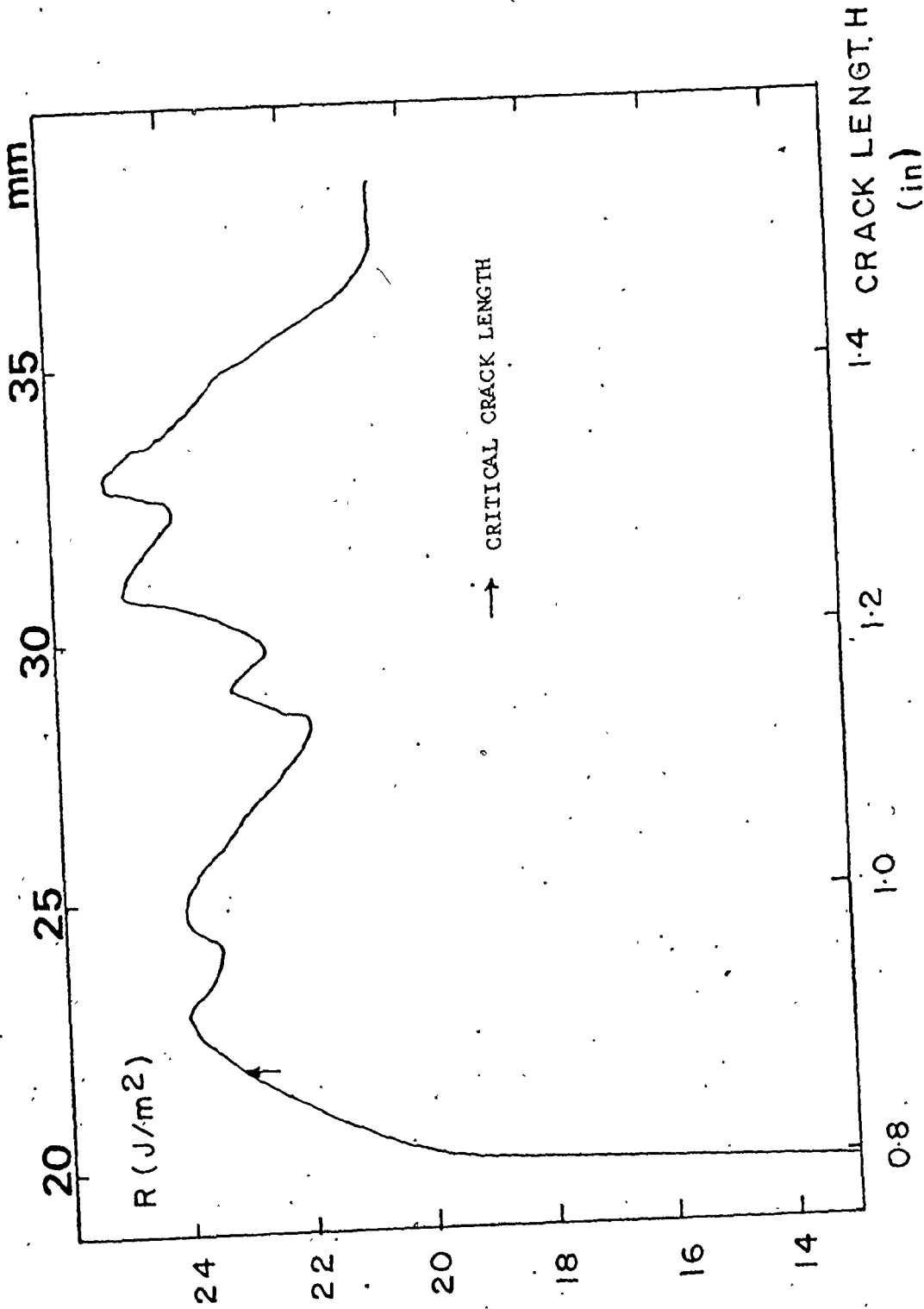


Figure 102. Fracture Resistance Curve- S Glass/15% Nickel.

TABLE 31. Calculated Critical Flaw Sizes

Material	Critical Flaw Size (mm)	λ (mm)
S Glass	0.19	
S/6% Nickel	0.58	1.38
S/10% Nickel	0.62	0.79
S/15% Nickel	1.01	0.50
S/20% Nickel	0.85	0.35

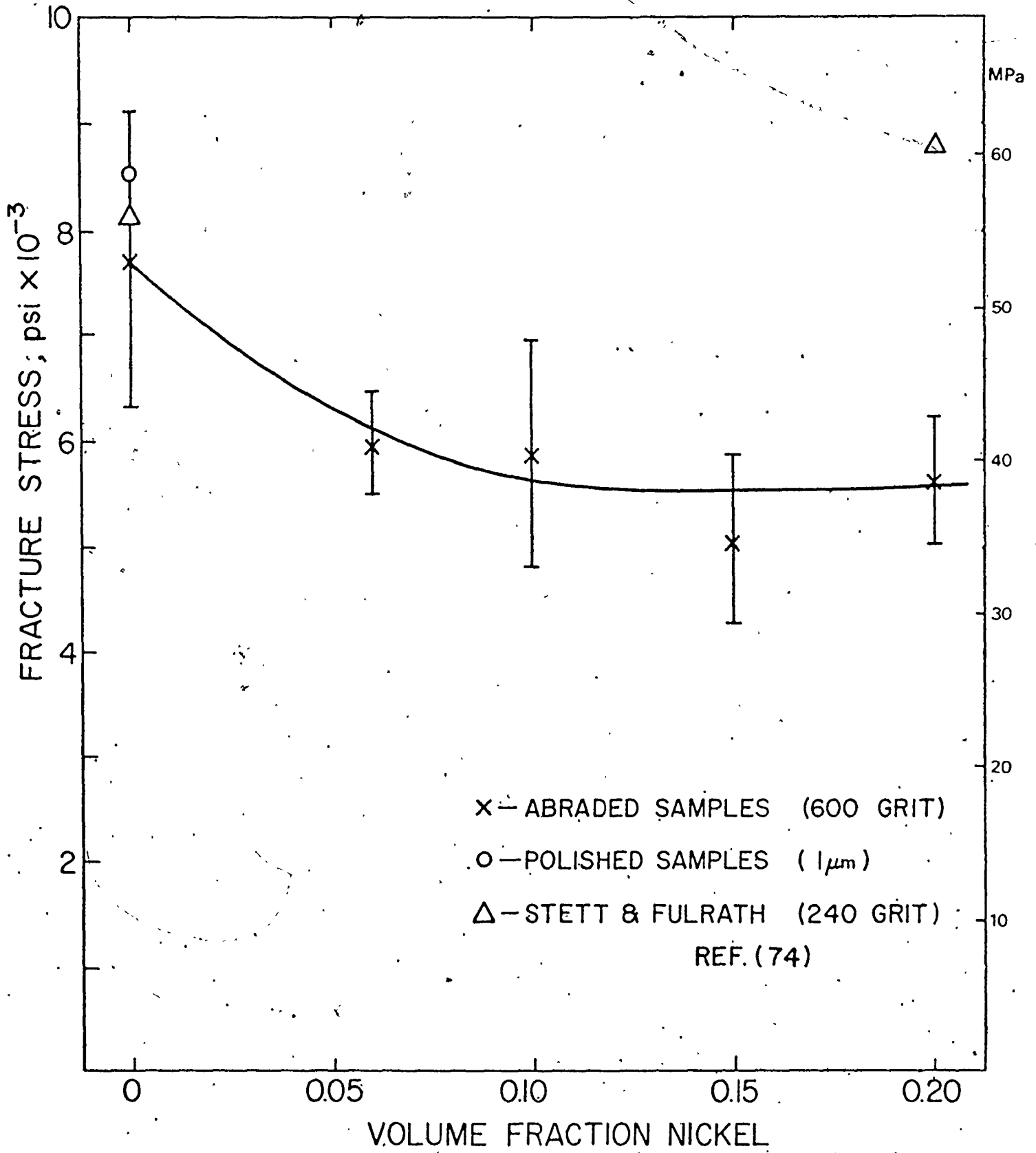


Figure.103. Fracture Stress of S Glass-Nickel Composites.

of a_{cr} increase substantially with increase in volume fraction of nickel. In this way, it can be seen that the strength of these materials is greatly affected by these flaw-sizes. It appears that the particles themselves can act as sites for crack nucleation, and calculated flaw sizes are much larger than the particle size (0.13 μ m). Included in Table 3l are the data for mean free path because Hasselman and Fulrath [154] have suggested that this particle spacing could help to decrease the size of the critical flaw. This is contrary to the critical flaw calculations where a_{cr} increases as the particle spacing decreases. For composites where the mean free path is less than the critical flaw size in the non-dispersed glass, Hasselman and Fulrath [154] suggest that substantial strengthening will occur. This condition was not met for the experimental work on the S glass composite so the hypothesis was not tested. The data in Figure 103 is quite similar to Hasselman and Fulrath's data for the glass - Al_2O_3 system [154]. Similar strength decreases were also measured by Bertolotti and Fulrath [158] for a glass containing spherical pores. In this case, however, the strength decreases tended to be much more abrupt especially for large pore distributions.

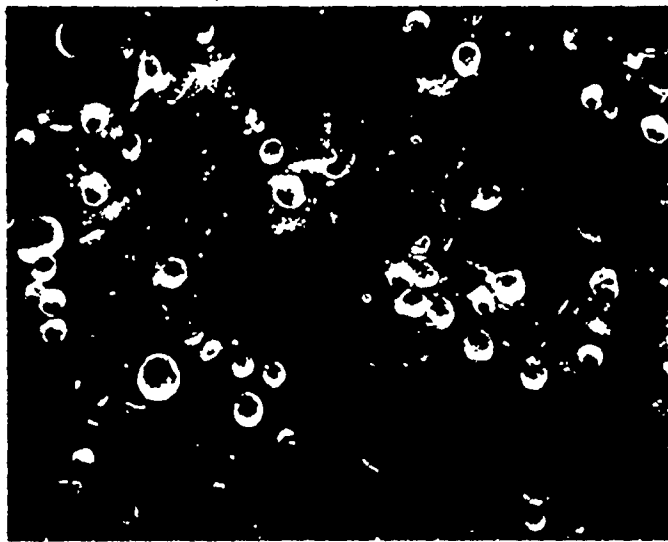
These arguments about limitation of the critical flaw size and the volume of flaw being stressed tend to be rather qualitative. A more logical approach is to consider the variation of all the parameters in the Griffith equation rather than isolating the critical flaw size as being the only important variable in controlling strength. In the former approach, strength is not considered a material property and it is more important to study the more fundamental parameters of E , ν and a_{cr} and

their variation with volume fraction. In this way, strength data are used mainly for critical flaw calculations although strength is still an important part of the design criterion.

In particulate composites, it is better to consider the particles themselves as the cause of failure. There will be an associated stress field around the particle and this will enhance the growth of any nearby flaws (section 3.4). In the S glass-nickel system, the stress field should be caused mainly by the difference in elastic properties. For a non-bonded system, the particles will be softer than the matrix ($\mu_p < \mu_m$) so that radial cracks are likely to form. These cracks can link particles and lead to extensive cracking and cause premature failure. This process is illustrated in Figure 45.

It can be seen from equation (3.30) that a substantial stress concentration ($K_m > K_0$) for the S glass-nickel system because the calculated critical flaw size for the non-dispersed glass ($a_{cr} = 0.19$ mm) is larger than the particle size (0.13 mm). In this way, it can be seen why the nickel particles increase the critical flaw size (Table 30).

Fractographic observations were made of the flexure samples in an effort to locate the fracture origins. For these composites, this endeavour was aided by the fracture surface steps as these lie parallel to the crack direction and on the opposite side of the particles from whence the crack approached (Figures 104-109). The general location of fracture origin can be determined quite readily by this technique but the exact nature of the flaw is more difficult to specify. All fractures start at or near the tensile surface and are associated with either a

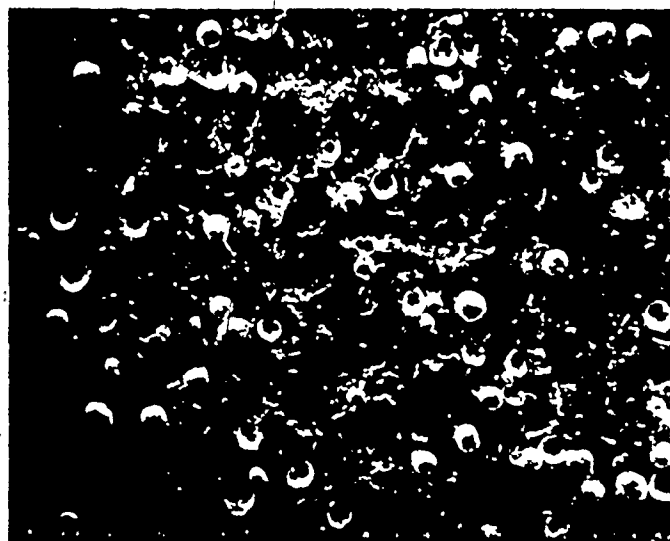


220

Figure 104. Fracture Surface in the Vicinity of the Failure Origin
S-Glass/6% Nickel.



Figure 105. Fracture Surface in the Vicinity of the Failure Origin, S Glass/6% Nickel.



320

Figure 106. Fracture Surface in the Vicinity of the Failure Origin,
S Glass/10% Nickel.

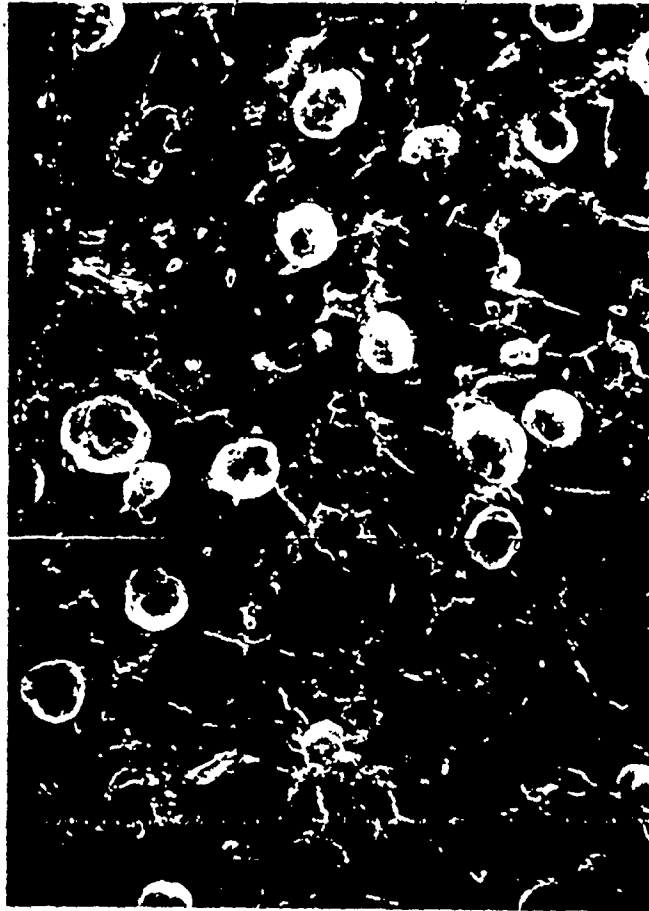
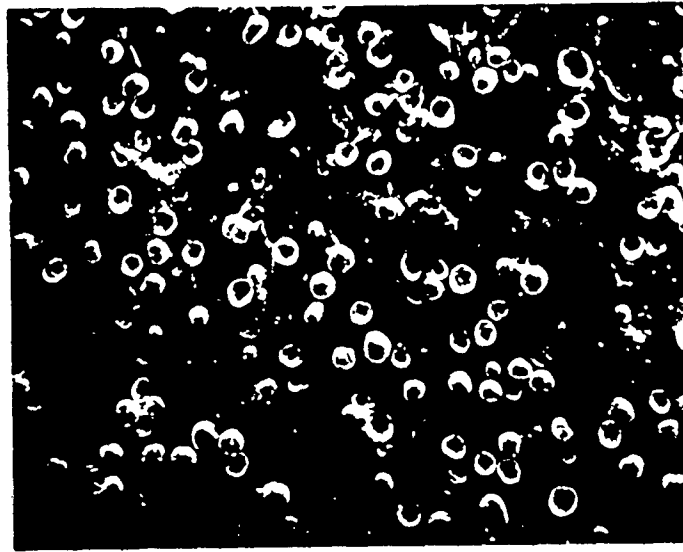
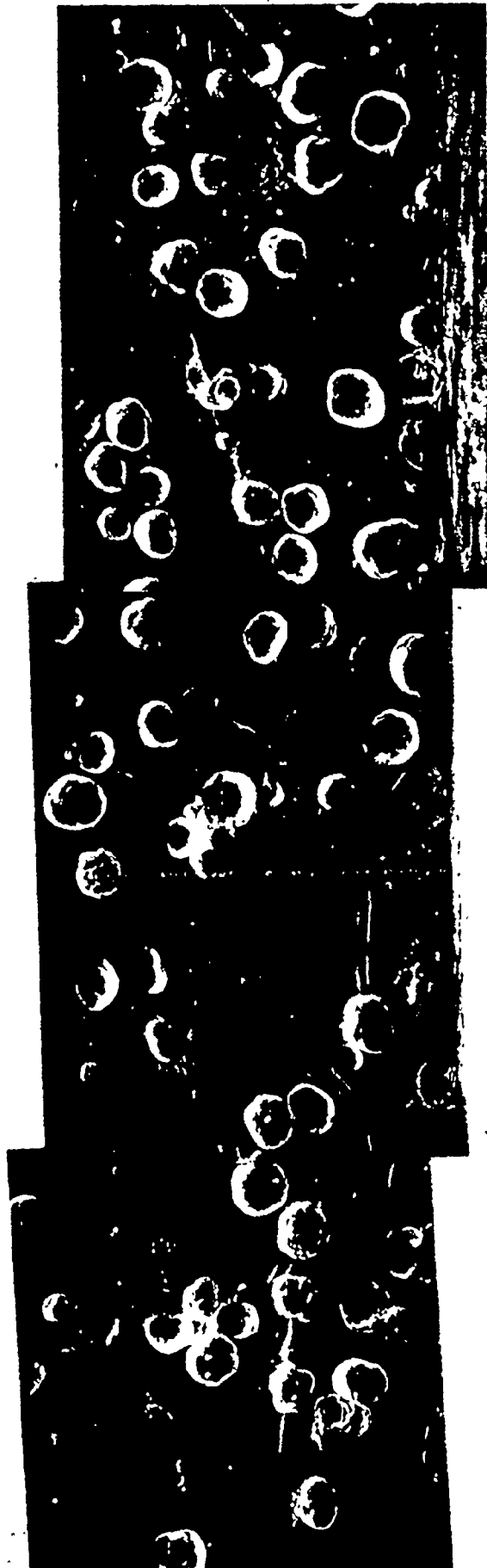


Figure 107. Fracture Surface in the Vicinity of the Failure Origin,
S Glass/10% Nickel.



360

Figure 108. Fracture Surface in the Vicinity of the Failure Origin,
S Glass/20% Nickel.



132

Figure 109. Fracture Surface in the Vicinity of the Failure Origin, S Glass/20% Nickel.

large particle or particles in contact. For example, in Figure 104 and 105, the fracture seems to have been initiated in the vicinity of two particles in contact in the lower right-hand corner.

For this non-bonded composite system, the particles can act themselves as stress concentrators and increase the size of the critical size. This increased flaw size is reflected in the strength decrease with increasing volume fraction of nickel.

5.7 Fractographic Observations

A study was made of the fracture surfaces of the S glass-nickel composites to identify the features involved in the fracture process. In particular, the specialized technique of ultrasonic fractography was used to yield information of crack velocity and shape in the vicinity of the particles.

5.7.1 Basic Fractography

Initial observations were made on S glass/2 Ni samples to identify the basic features. Figure 110 is a composite fractograph, that clearly identifies the fracture surface steps and the nickel spheres. The fracture surface is essentially planar as shown in a side view of the surface (Figure 111). In the vicinity of the particles, however, local perturbation of the fracture surface are observed (Figure 112). These perturbations consist of the fracture step (Figure 113) and the fracture ledge (Figure 114) which were discussed previously. A side view of the same ledge is shown in Figure 115. The side of the ledge near the particle is abrupt and is indicative of the attraction of the crack to the particle; as expected if the particle is behaving like a



150



Figure 110. SEM Composite Micrograph showing the Fracture Surface in a S Glass/2% Nickel Sample

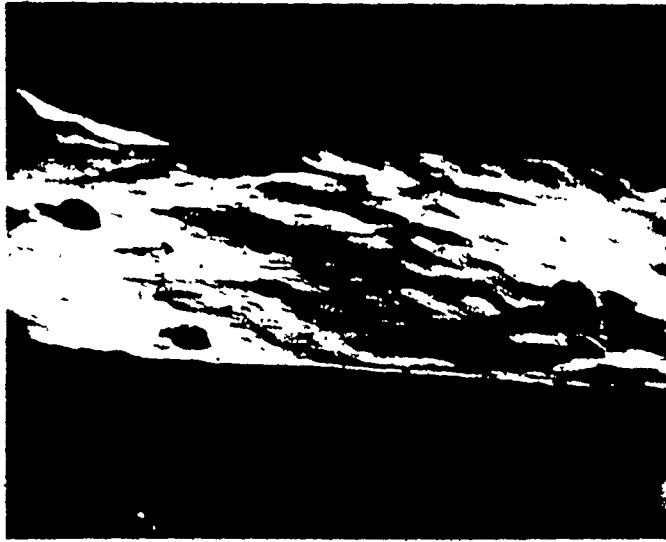


Figure 111. Side View of the Fracture Surface in a S Glass/2% Nickel Sample.

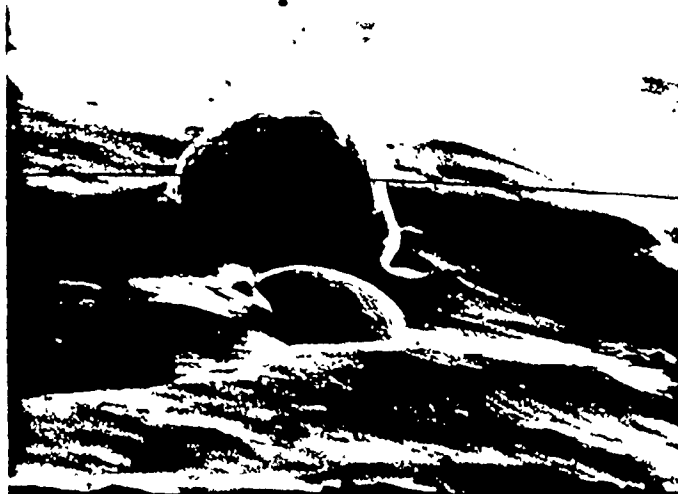


Figure 112. SEM Fractograph of Area around a Nickel Particle in a S Glass/2% Nickel Sample.



16

Figure 113. Close-up View of a Fracture Surface Step at the Rear of a Nickel Particle (S Glass/2% Ni)



16

Figure 114. Close-up View of Fracture Ledge in Front of a Nickel Particle (S Glass/2% Ni).

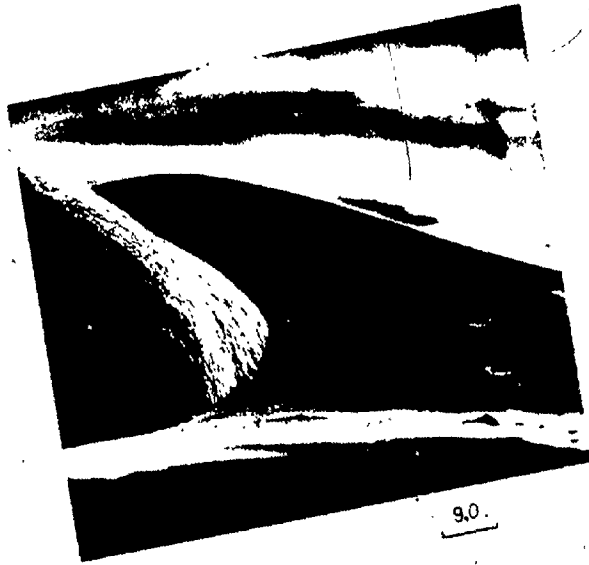


Figure 115. Side View of a Fracture Ledge in a S Glass/2% Ni Sample.

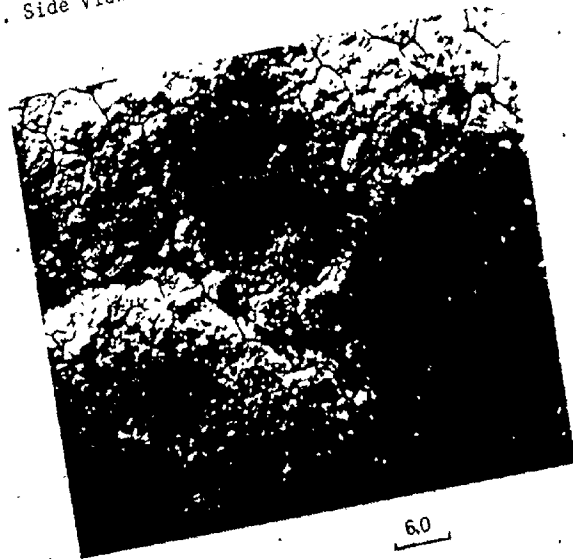


Figure 116. Surface of a Nickel Particle on a Fracture Surface (S Glass/2% Ni)

void. It appears that initially, the crack was seeking to avoid the particle probably because of a degree of bonding between the particle and the matrix. Stett and Fulrath [74] showed that improved bonding in this system by oxidizing the nickel, confined the crack to the matrix. The nickel particle surfaces show no evidence of glass debris after fracture (Figure 116) though the surface morphology is changed from the as-received particles. The surfaces appear etched and this must have occurred during the hot-pressing. A thin oxide film probably exists on the as-received nickel spheres and this could result in the development of a weak bond during fabrication. The fracture of this bond by the approaching crack front would cause the abrupt change in crack path as evidenced by the fracture ledge.

The fracture surface steps are probably a result of the interaction with the particle stress field. For example, mode II loading on the segmented cracks will alter their trajectory so that when these cracks reach the rear of the particle they are non-coplanar and need a secondary fracture to complete failure.

5.7.2 General Fractography

The basic fractographic observations were extended to encompass all the volume fractions used in this study. The same features were observed at all volume fractions (Figures 117 - 120) though the fracture ledges become less noticeable at higher volume fractions and are not so abundant. The fracture surface steps often connected particles at higher volume fractions because the interaction with other particles occurred before the segmented cracks could coalesce. As in the case of



130



Figure 117. Fracture Surface of a S_2 Glass/6% Nickel Sample.



150

Figure 118. Fracture Surface of a S Glass/10% Nickel Sample.



Fig. 14. Actin



160

301

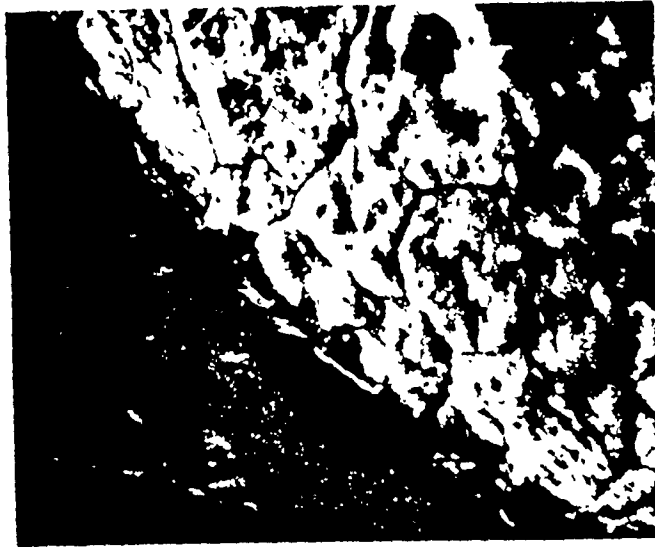
Figure 120. Fracture Surface of a S Glass/20% Nickel Sample.

cleavage steps, this behaviour probably gives rise to steps of greater height and hence a rougher fracture surface. There is no evidence of cracking at the glass-nickel interface (Figure 121). Figure 122 shows a side view of a nickel particle and gives a good indication of how the step affects the topography of the fracture surface.

5.7.3 Ultrasónic Fractography

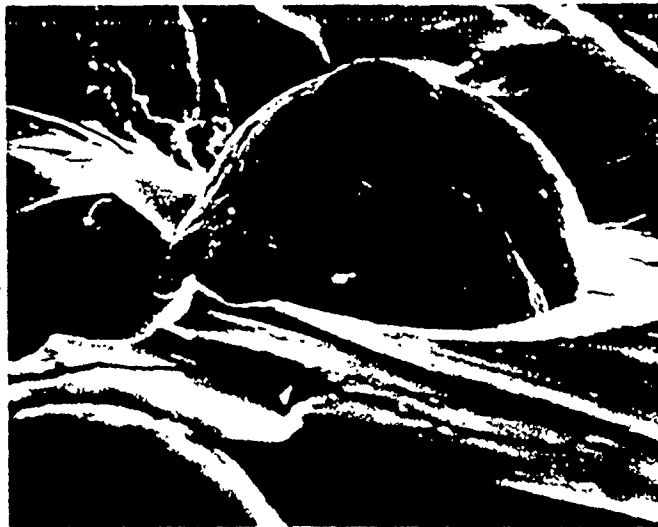
This technique has been used previously to measure crack velocities especially in the fast fracture regime. Figure 123 shows a modulated pyrex surface where the crack has moved from left to right. The velocity profile can be calculated from the ripple spacing. The frequency of the US waves for these experiments was 1.024 MHz. Interference microscopy allows the nature of the ripples to be more clearly defined and Figure 124 shows the pattern obtained for S glass. The three-dimensional, sinusoidal nature of the modulation is clear and furthermore, the spacing of the fringes allow the height of the ripples to be determined (0.6 - 0.7 μm).

As it was believed that the nickel spheres in the S glass composites acted as pseudovoids, some ultrasonic tests were performed on partially-fined S glass. These samples contain residual gas bubbles to simulate porosity. Figure 125 is an interference photograph showing the interaction between the crack front and such a pore. As the crack interacts with the pore, there is a change in crack shape. On the initial approach, the crack front is attracted to the void as expected by theoretical considerations (section 2.2.4). This attraction, which is a result of the increase in K_I at the crack tip, is reflected by a



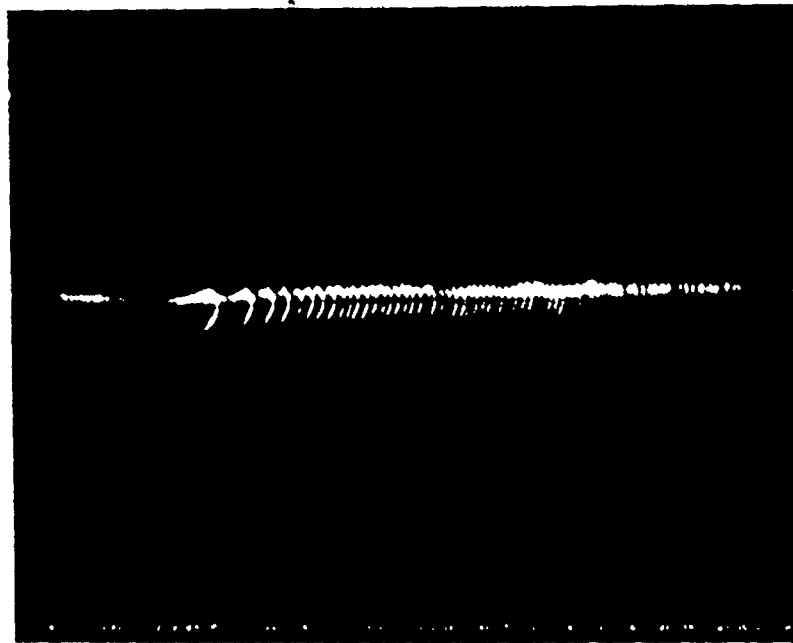
20

Figure 121. Example of Glass/Nickel Interface on a Composite Fracture Surface



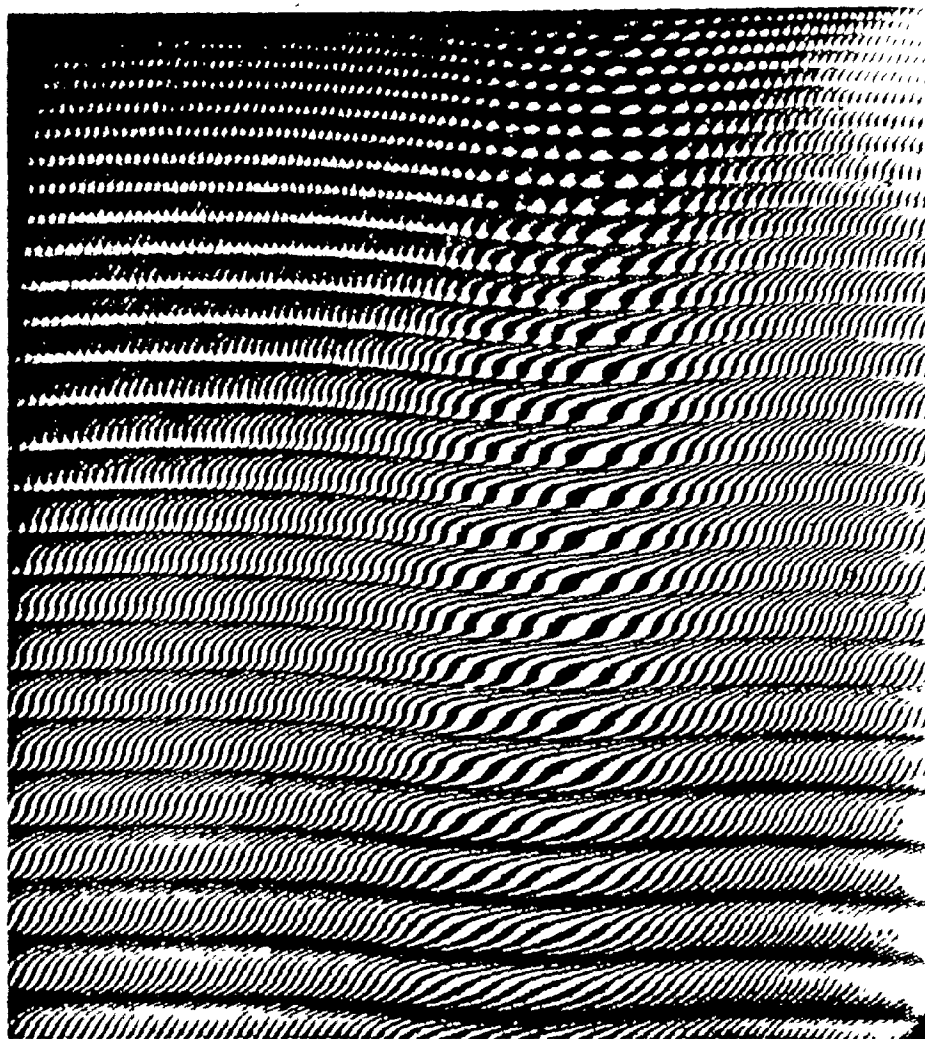
20

Figure 122. Side View of a Nickel Particle on Composite Fracture Surface



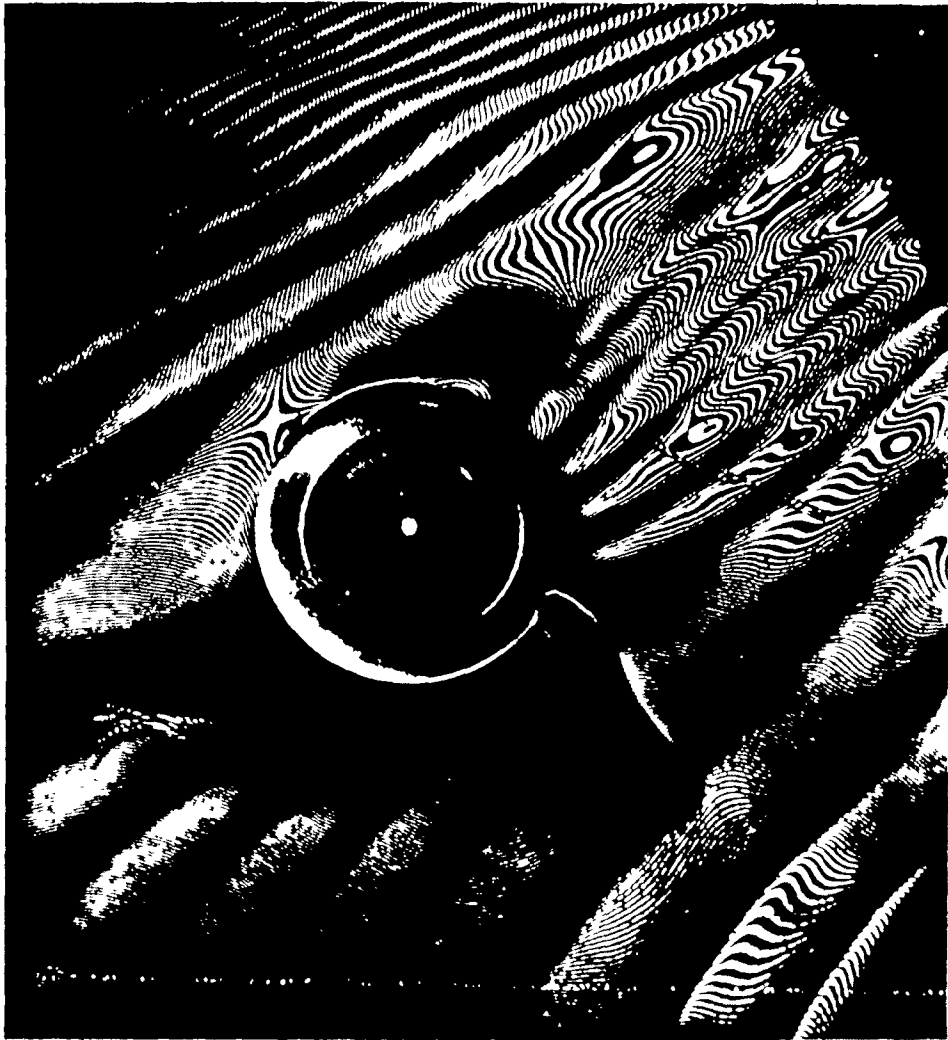
1600

Figure 123. Ultrasonically-Modulated Fracture Surface in a Pyrex Sample. Crack moved from Right to Left and the Micrograph shows the Deceleration of the Crack and its Arrest.



40

Figure 124. Optical Interference Micrograph of Ultrasonically-Modulated S Glass Fracture Surface.



100

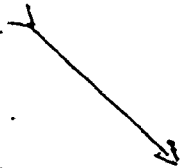


Figure 125. Optical Interference Micrograph of the Area around a Pore in an Ultrasonically-Modulated S Glass Sample.

local increase in crack velocity and hence a change in crack shape. As the crack segments to bypass the void, the change in crack shape continues, though the pore acts now to impede the crack motion. Finally, the crack front breaks away from the void, leaving a fracture surface step at its rear. The void does not act to pin the crack front in the sense used in the Evans' model, but behaves more like a penetrable obstacle. It is clear from Figure 125 that the topography of the fracture surface around the void is complex.

The changes of crack shape and velocity are clearer in the SEM composite (Figure 126). As the crack approaches the void, the local velocity increases from $\sim 5\text{m/s}$ to $\sim 30\text{m/s}$. During the bypassing process, the velocity decreases to a minimum ($\sim 5\text{m/s}$) at the centre of the void. In this position, the crack is again approximately planar. The crack velocity then increases and it breaks away from the void with a velocity of $\sim 80\text{m/s}$. In this figure, ultrasonic markings are also available within the fracture surface step and the secondary crack velocity is $\sim 5\text{m/s}$ i.e. an order of magnitude slower than that of the primary crack front in that region. This observation implies that the secondary fracture which occurs in the step formation must occur at some time after the major crack front has moved on. The interaction during the bypassing of the void is shown in more detail in Figure 127. There is evidence here of hackle-type features both at the front of the void and within the fracture step. The overall process is shown in Figure 128 and it can be seen that the major perturbation in crack shape is caused by the void and not the fracture step. Figure 129 shows in more detail, the increase in crack velocity as the crack approaches the void.

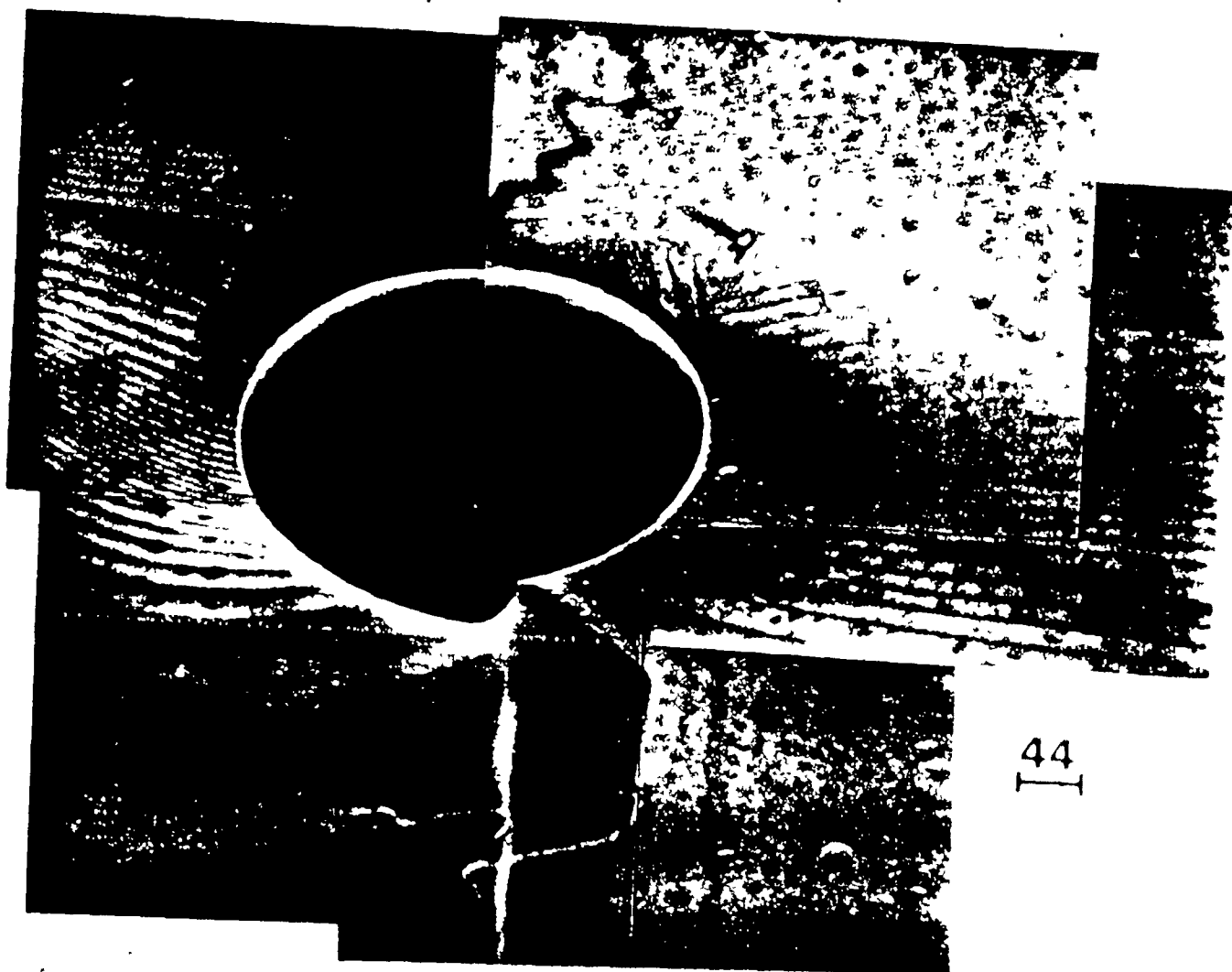


Figure 126. SEM Composite Micrograph of the Interaction between a Crack Front and a Pore in an Ultrasonically-Modulated S Glass Sample.

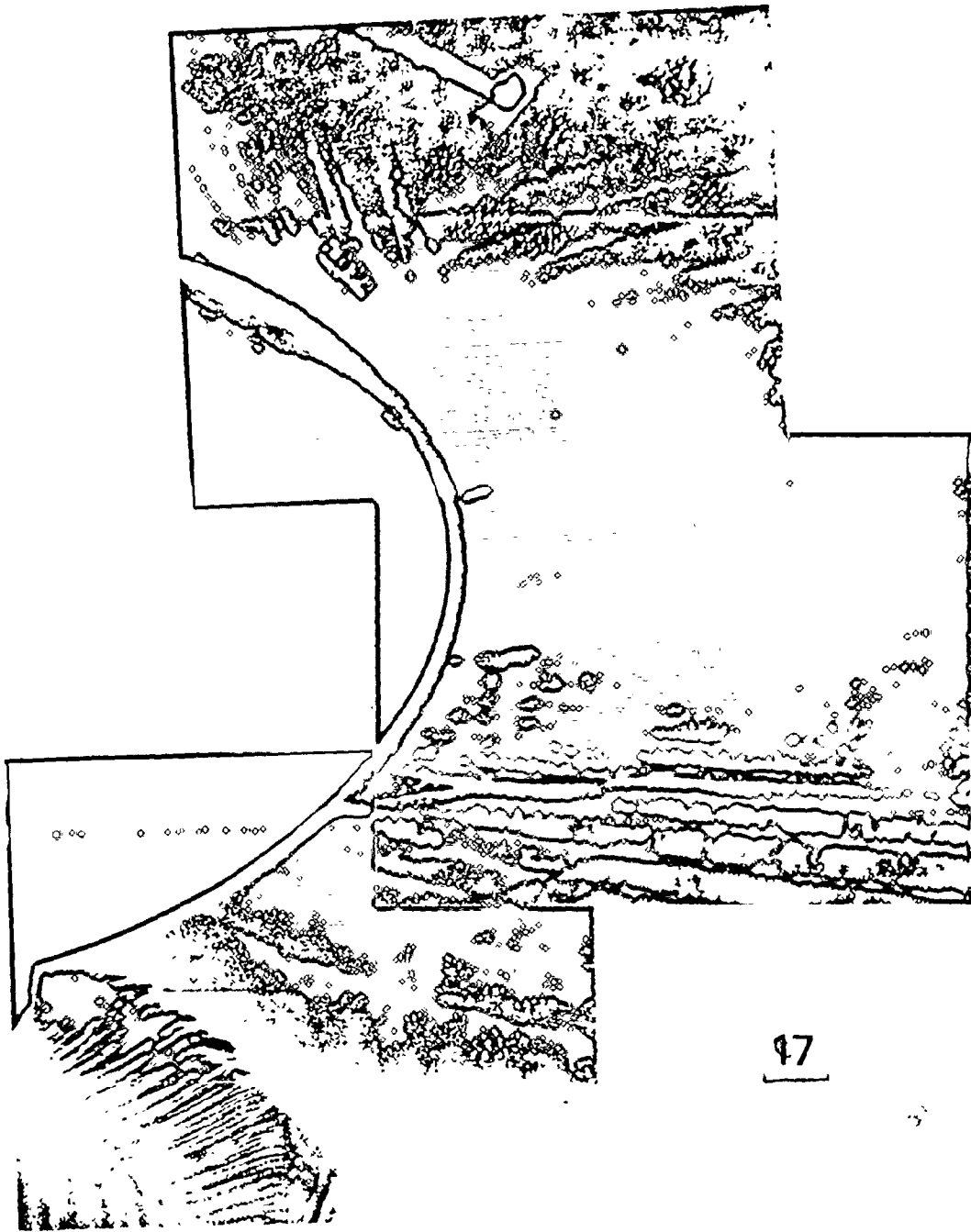
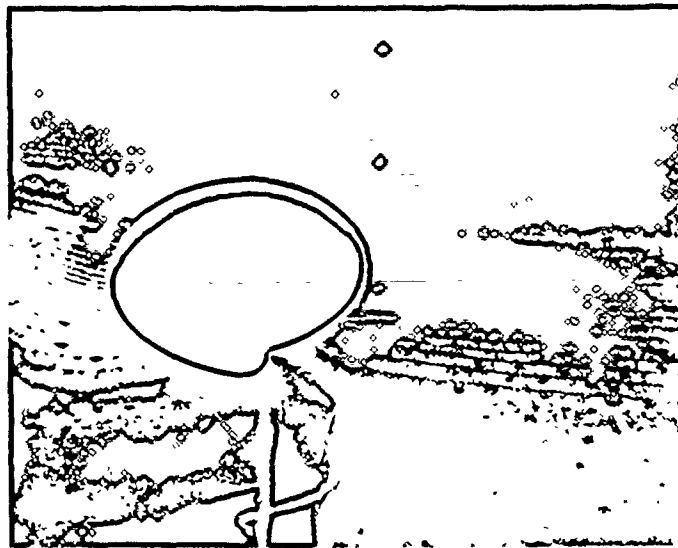
47

Figure 127. Close-Up View of the Ultrasonic Lines as a Crack By-Passes a Pore in S Glass.



85

Figure 128. Overall View of Crack-Pore Interaction in S Glass.



17

Figure 129. Increase in Crack Velocity as Crack approaches a Pore in S Glass.

Some final observations were made on the porous system using Nomarski interference microscopy. Figure 130 shows the crack interaction with a small void and Figure 131 with a larger void. The details of the surface topography are more clearly resolved than the SEM observations. In one of the partially-fined samples, a crack-inclusion interaction was observed (Figure 132). In this case, it appears that the inclusion does act to pin the crack.

For the S glass-nickel composites, the ultrasonic markings are very similar to those observed for the S glass-pore system. In Figure 133, it is evident that the crack bows as it bypasses the nickel particle even though the obstacle is penetrated and does not pin the crack front. The crack velocity is a minimum near the centre of the obstacle and the surface step morphology is very similar. In Figure 134, there is evidence of a slight attraction to the obstacle though the situation is complicated by the presence of the ledge. The effect is not as clear as in the glass-pore system.

As theoretical models are concerned with the crack shape at breakaway, as a function of interparticle spacing, an attempt was made to measure this function from the micrographs. The composite micrograph of Figure 135 shows a S glass - 6% nickel composite. Unfortunately, the ultrasonic markings are now unclear and less systematic, because of the acoustic impedance produced by the array of nickel obstacles.

The solution for the impingement of an elastic shear wave at a spherical obstacle is rather complex. An idea of the acoustic impedance



40

Figure 130. Crack Interaction with a Small Pore in S Glass
(Nomarski Interference)



Figure 131. Crack Interaction with Larger Pore in S Glass (Nomarski)

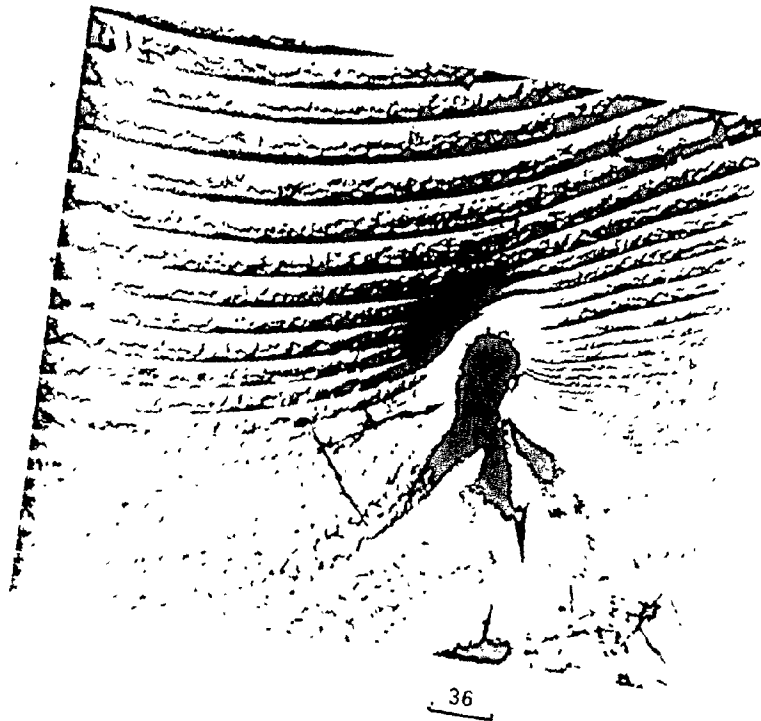


Figure 132. Crack Interaction with a Small Inclusion in a Partially-Fined S Glass Sample.



44

Figure 133. Crack Interaction with a Nickel Sphere in a S Glass/2%
.Nickel Sample.



12

Figure 134. Close-Up View as Crack By-Passes a Nickel Sphere.



40

Figure 135. SEM Micrograph of Modulated S Glass/6% Ni.

put forward by a coherent interface between dissimilar media to a normal longitudinal wave is more simple and it can be shown that the reflection factor (Z) is given by [201].

$$Z = \frac{\rho_2 c_2 - \rho_1 c_1}{\rho_2 c_2 + \rho_1 c_1} \quad (5.14)$$

where $\rho_{1,2}$ is the density and $c_{1,2}$ is the longitudinal wave velocity in the media 1 and 2. For the case of a glass-nickel interface a value of $Z = \sim 0.6$ is obtained. For the case of an incoherent interface, this value would be even higher. For a shear wave, the situation is further complicated by the possibility of total internal reflection above a certain critical angle of incidence and by the presence of both transverse and longitudinal, reflected and refracted waves. From the rough calculation, it can be seen that the nickel spheres can interfere strongly with the US waves making the modulation process much more difficult.

The fractographic observations were improved somewhat when Nomarski interference microscopy was used, though the depth of field of the rougher samples was not very good and did not lead to very clear micrographs. Figures 136 and 137 show some of the observations at higher volume fractions and it was possible to measure the crack shape at breakaway. The crack shape was measured using a parameter $(a/2c)^*$ which is illustrated in Figure 138 along with the results. The data are highly scattered but a general trend of increasing $(a/2c)$ as a function of decreasing interparticle spacing can be discerned.

To summarize these observations, it has been seen that the nickel particles act very similarly to pores in that they do not pin the crack

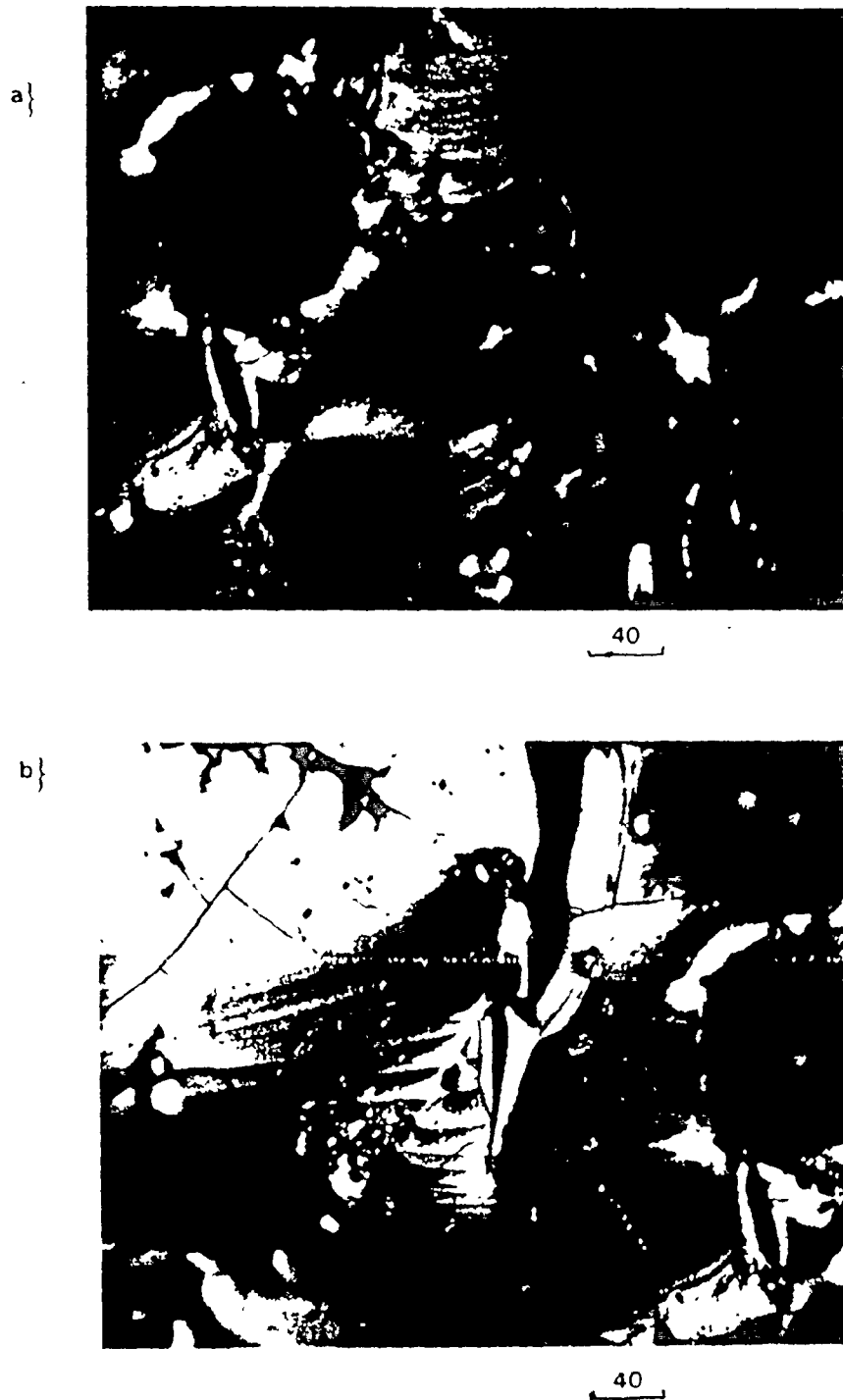


Figure 136. Crack-Particle Interactions in S Glass-Nickel Composites
a) 6 vol.% b) 10 vol.%

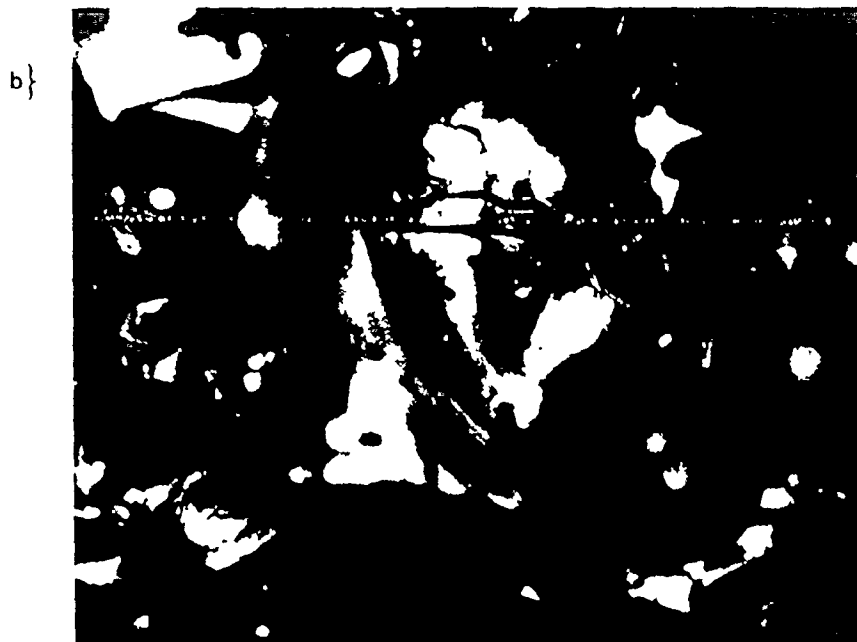


Figure 137. Crack-Particle Interactions in S Glass Composites
a) 15 vol.% b) 20 vol.%

front but they still afford an impedance to the crack motion. This impedance is reflected by a change in crack shape. The shape change is not predicted by the Evans' model and must be the result of processes not included in his model. For example, there is a change in stress state from plane stress at the interface to plane strain or some intermediate state within the glass. There will also be an interaction between the stress field around the inclusion and the crack front and in particular, the non-bonded particles may act to blunt the crack front locally and decrease the local stresses.

It is clear that the technique of ultrasonic fractography has the capability of allowing crack-particle interactions to be studied in great detail and changes in local crack velocity and crack shape to be quantitatively measured. In this way, this technique has a great potential for use in fundamental microstructural-interaction studies of brittle fracture.

5.8 Theoretical Aspects

The interaction of a crack front and an array of attractive obstacles can be thought of in three stages, i.e.,

- (i) The initial approach of the crack front to an isolated inclusion.
- (ii) The bowing process as the crack bypasses the inclusions.
- (iii) The formation of the fracture surface step as the crack breaks away.

These three effects will be discussed with respect to the glass-nickel system for comparison with the fractographic observations and the fracture

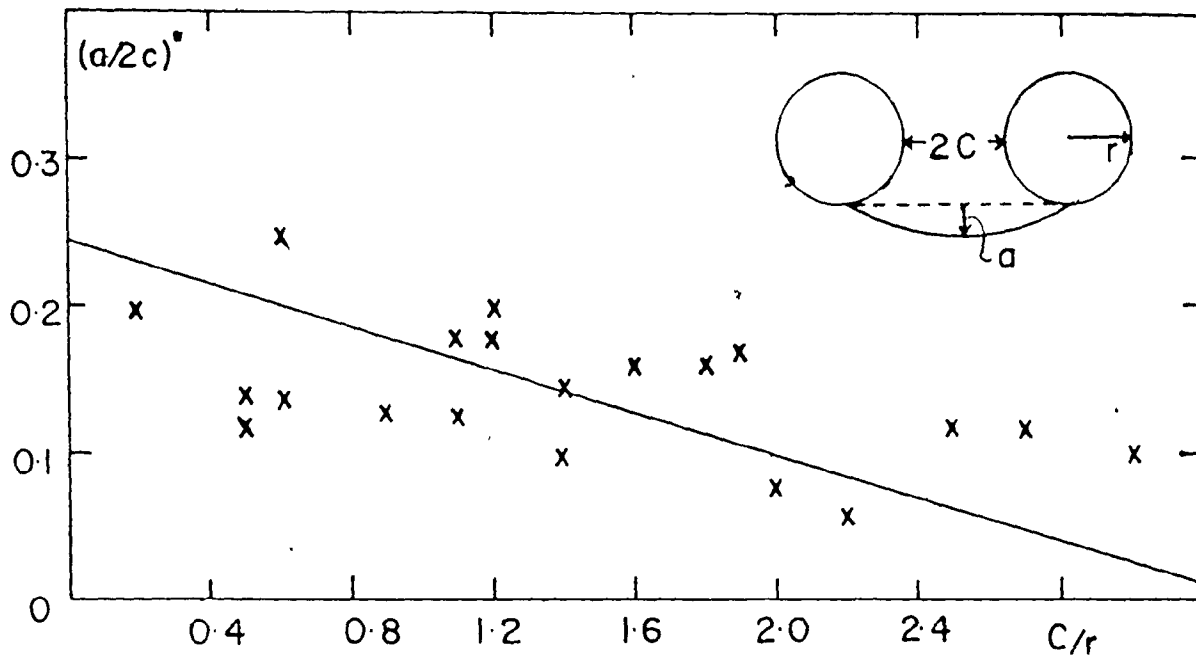


Figure 138. Observed Critical Crack Shape at Breakaway.

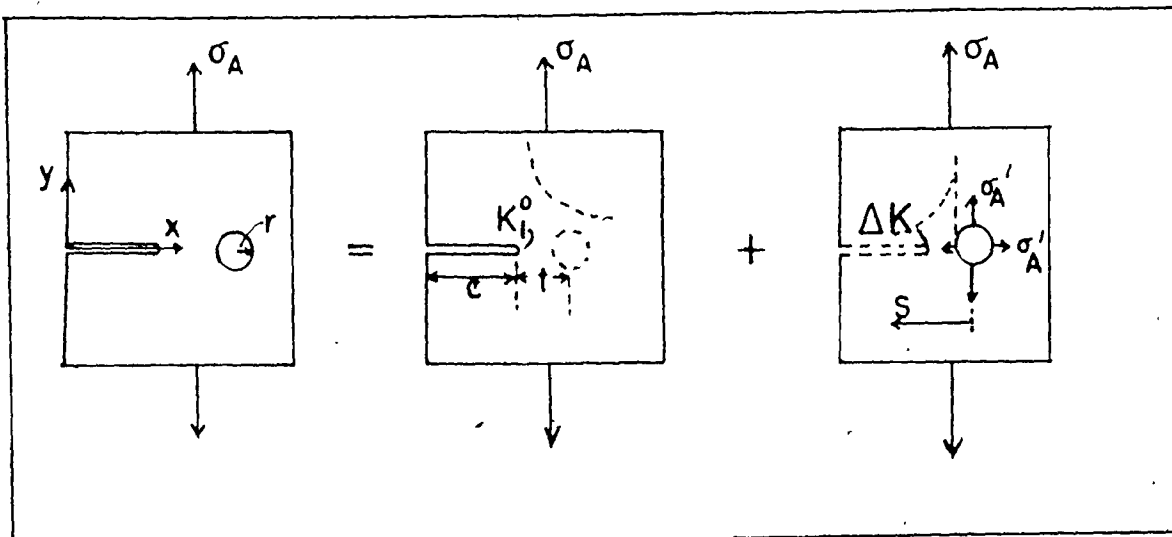


Figure 139. A Schematic Description of the Superposition Approach for a Crack Approaching an Elastic Disturbance.

surface energy measurements.

5.8.1 Crack Approach to an Elastic Disturbance

The interaction of a crack and an isolated inclusion was discussed previously (section 2.2.4) and it was predicted by various authors that a crack front can be attracted to soft particles or voids. In the US fractographic observations, the proof of this effect was established. Most authors have only considered small cracks and often their solutions break down for long cracks. Tirosh and Tetelman [72] have established a more comprehensive approach, though their first order analytical solution (equation 2.14) reduces to unity for large cracks ($R/c \approx 0$). For this case, the more complicated second order solution must be used.

An alternative approach will be outlined now, [202], as illustrated in Figure 139. This approach is similar to that of Tirosh and Tetelman [72] except that it uses a reverse procedure, by considering the stress field of the crack first and then considering the 'back-influence' of the obstacle on the crack. The third order solution should be negligible because for very long cracks the stress variation across the obstacle should be negligible. This approach proves to be simpler than that of Tirosh and Tetelman [72] and is given in an analytical form.

Consider a large, homogeneous isotropic body containing a crack (along the x axis), which is approaching a cylindrical disturbance. The crack is loaded in mode I and the cylindrical axis is perpendicular to the applied stress and the crack direction (i.e. along the Z axis), as shown in Figure 139. This type of geometry is common in composite

structures. This approach will only consider elastic structures but under this restriction, the interaction of microstructural stress concentrations and a crack front can be treated.

The stresses ahead of the crack are given from equation (2.7) by

$$\sigma_{xx} = \sigma_{yy} = \frac{K_I^0}{(2\pi(x - c))^{1/2}} \quad (5.15)$$

An inclusion placed at $(x - c) = t$, will be subjected to a biaxial stress (σ_A') given by

$$\sigma_A' = \frac{K_I^0}{(2\pi t)^{1/2}} \quad (5.16)$$

The elastic solution to the stress field for a cylindrical inclusion under biaxial tension (plane strain) is given by (Appendix A.4)

$$\sigma_{\theta\theta} = \sigma_A + A\sigma_A \left(\frac{r}{s}\right)^2 \quad (5.17)$$

where s is the distance from the centre of the inclusion (radius r) and

$$A = \frac{(1-2\nu_p)G_m - (1-2\nu_m)G_p}{(1-2\nu_p)G_m + G_p} \quad (5.18)$$

The solution is only valid for $r/s \leq 1$. For an inclusion acted on only by the stress field of the crack, the stress component in the y direction across $x = 0$, (σ_{yy}') is given by

$$\sigma_{yy}' = \sigma_A' + A\sigma_A' \left(\frac{r}{s}\right)^2 \quad (5.19)$$

The remote applied tension will also be acting on the inclusion but for situations where the crack tip is near the inclusion, the stress field due to σ_A' will be dominant. For these situations, the back influence

of the inclusion on the crack must be considered as an additional stress (σ_d) is now applied back to the crack. This additional stress is given by

$$\sigma_d = \sigma_{yy}' - \sigma_A' \quad (5.20)$$

$$= A \left(\frac{r}{s}\right)^2 \frac{K_I^0}{\sqrt{2\pi t}} \quad (5.21)$$

The additional stress will change the stress intensity at the crack tip to K_I' . The change in stress intensity $\Delta K (= K_I' - K_I^0)$, can be computed from a standard formula using

$$\Delta K = \int_0^c \frac{2\sigma_d(x,0)}{\pi^{1/2}} \left(\frac{c}{c^2 - x^2}\right)^{1/2} dx \quad (5.22)$$

The axes can be transformed to the centre of the particle using

$$s + x = t + c \quad (5.23)$$

In the approximation of large c , equation (5.22) becomes

$$\Delta K \approx \left(\frac{2}{\pi}\right)^{1/2} \int_t^\infty \frac{\sigma_d(s,0) ds}{(s-t)^{1/2}} \quad (5.24)$$

Substituting into this expression, the value of σ_d from equation (5.21)

$$\Delta K = \frac{AK_I^0 r^2}{\pi\sqrt{t}} \int_t^\infty \frac{ds}{s^2(s-t)^{1/2}} \quad (5.25)$$

$$= \frac{AK_I^0 r^2}{\pi\sqrt{t}} \left[\frac{(s-t)^{1/2}}{st} + \frac{1}{t^{3/2}} \tan^{-1} \left(\frac{s-t}{t}\right)^{1/2} \right]_t^\infty \quad (5.26)$$

$$= \frac{AK_I^0 r^2}{\pi\sqrt{t}} \left[\frac{\pi}{2t^{3/2}} \right] \quad (5.27)$$

$$= \frac{AK_I^0 r^2}{2t^2} \quad (5.28)$$

Finally, this can be rewritten as

$$\frac{K_I'}{K_I^0} = 1 + \frac{Ar^2}{2t^2} \quad (5.29)$$

The solution is illustrated in Figure 140 for the cases of a cylindrical hole ($A = 1$), a rigid, well-bonded inclusion ($A = 2\nu_m - 1$) and for a well-bonded nickel particle ($A = -0.486$). The elastic constant data are obtained from Ref. [74] and in particular $\nu_m = 0.2$. It can be seen that the value of A determines whether the stress field is attractive or repulsive. For $A > 0$ the field is attractive (soft particle) and for $A < 0$, it is repulsive (hard particles). For cracks located above or below the x axis, there will also be a shear stress component which can change the crack path (mode II loading). For hard particles this will lead to a tendency for a crack to avoid hard particles as shown experimentally by Tirosh and Tetelman [72] and as discussed in section 2.2.4.

For shorter crack lengths, the crack-inclusion interaction is much stronger but the solution of equation (5.29) can be seen as a limiting case for long crack lengths. The method can be generalized for other crack locations and crack sizes though its simplicity will be lost. The effect of mode II loading will also have to be included for these cases.

For non-bonded inclusions, the situation will revert to the solution for a cylindrical hole, because on the application of any biaxial stress, the inclusion will immediately separate from the matrix. The problem of internal stresses due to a difference in thermal expan-

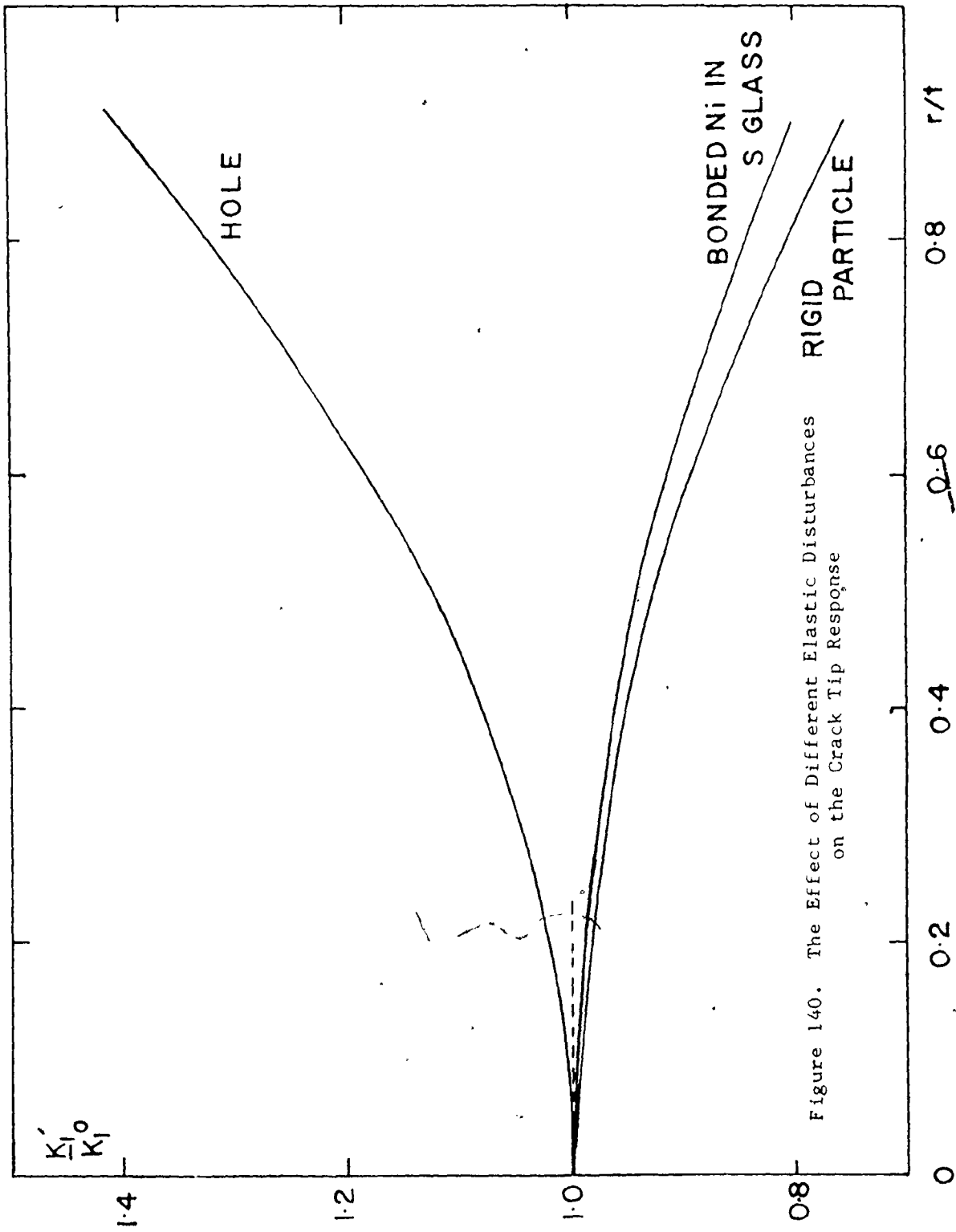


Figure 140. The Effect of Different Elastic Disturbances on the Crack Tip Response

sion coefficients of the two phases ($\Delta\alpha$) can also be treated. For this case, A is replaced by A' where

$$A' = A + 4 (\sigma_A/G_m)(\epsilon/r) \quad (5.30)$$

where ϵ is the misfit between the radius of the inclusion and the radius of the hole. For thermal expansion mismatch $\epsilon/r = \Delta\alpha \Delta T$ where ΔT is temperature difference.

For non-bonded particles, the situation is complicated because if $\epsilon < 0$, the inclusion will separate from the matrix. If $\epsilon = 0$, the inclusion will separate on the application of stress and for $\epsilon > 0$, the solution will be modified according to equation (5.30) until the applied stress is enough to overcome the misfit stress field. At this point; the inclusion will again separate from the matrix and act as a hole.

From the fractographic observations of Figure 129, the increase in crack velocity that is a result of increased K_I for a hole (Figure 140) can be approximately calculated and is shown in Figure 141.

5.8.2 The By-Pass Process

Once the crack has reached the obstacle, the situation is more complex and a more approximate approach has to be taken. For these considerations, it is assumed that the crack front is pinned by an array of obstacles and the critical stress intensity corresponds to the breakaway of the crack front from these obstacles. This situation corresponds to the measured values of K_{IC} or σ_c . For this situation, measurements of the crack shape at breakaway have already been made.

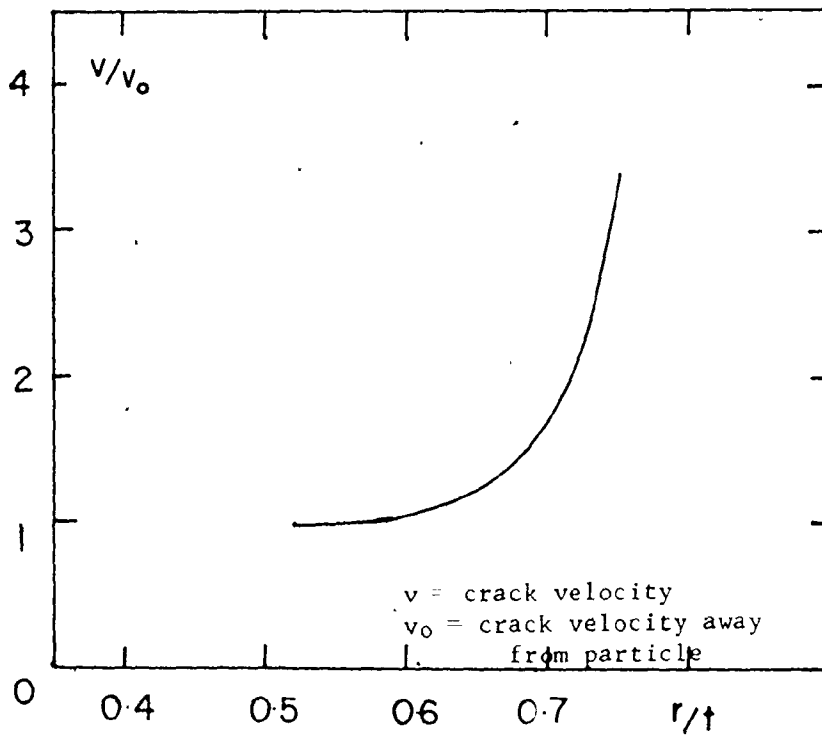


Figure 141. Maximum Increase in Crack Velocity Approaching a Pore in S Glass

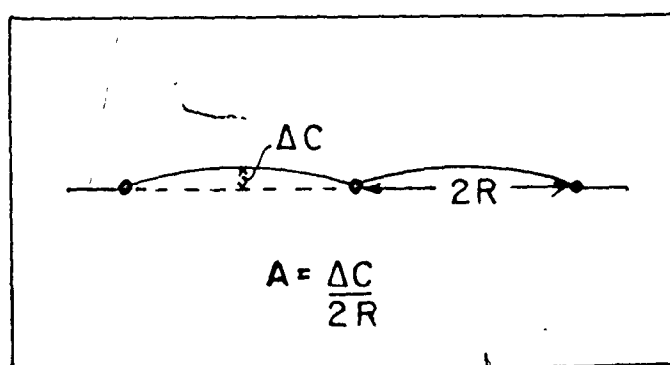


Figure 142. Definition of Crack Shape Factor from Lange (111)

A crack front is expected to remain straight unless there is some mechanism, by which there is a force acting locally against the crack motion. This force may act to pin or impede the motion of the crack. The variation in fracture resistance in particulate or fibrous composite may result in such a force.

Lange [111] approached the problem for the case of particulate composites by postulating that the crack has a line tension and that the crack shape at breakaway is semi-circular. The assumption that a crack has a line tension is rather tenuous and Evans [113] has shown that even if the idea is correct, the line tension is not constant. From the observations on the S glass-nickel composite, it is also clear that the crack shape at breakaway is not semi-circular. Evans [113] in his theoretical work, shows that the crack shape at breakaway varies with volume fraction even when the crack is pinned. Lange [111] gives a more general expression in his work for the increase in fracture surface energy as a function of crack shape, i.e.,

$$\gamma = \gamma_0 f'(A) + \frac{e^2}{d} g'(A) \quad (5.31)$$

where A is geometric factor which depends on crack shape as shown in Figure 142. Unfortunately, when $A < 1$, $f'(A)$ and $g'(A)$ can have negative values. It appears that the Lange model is open to question, although it does often correctly predict the observed functional relationship between γ and d , for many systems.

In the approach by Evans [113], the effect of pinning is introduced by considering the motion of secondary semi-circular and semi-elliptical cracks in the stress field of a primary crack. The distance

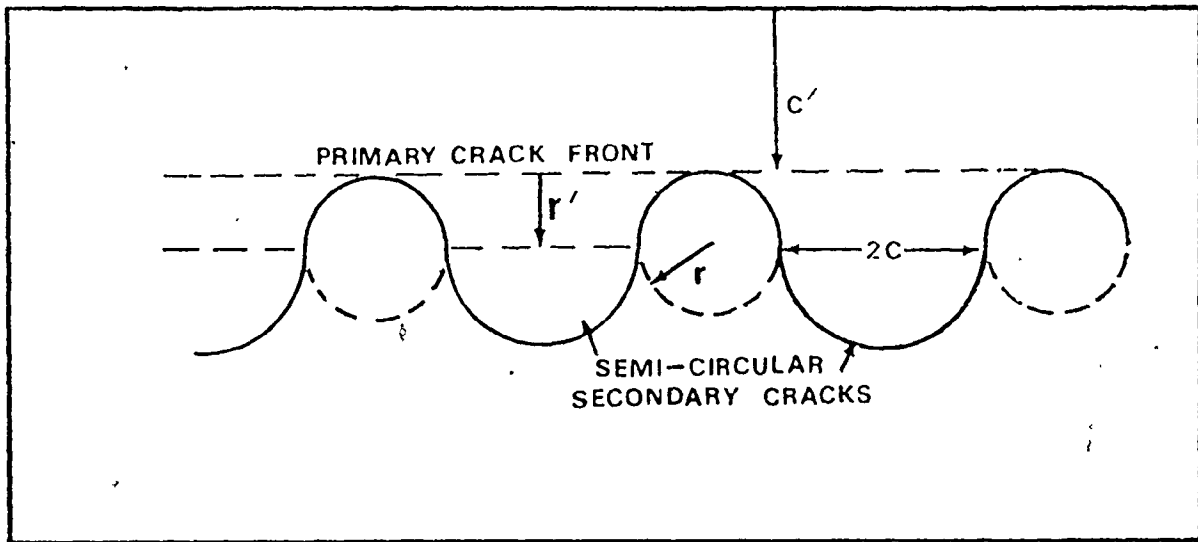


Figure 143. Evans' Model for the Interaction of a Crack with a Linear Array of Impenetrable Particles.

between the primary crack and the origin of the secondary cracks is denoted by r' , so that r' is a measure of the pinning ability of the particles. The Evans' model is illustrated in Figure 143. For the interaction of a crack with an array of voids or non-bonded particles $r' = 0$. For this case, the model by Evans' predicts no increase in fracture toughness and no change in crack shape. This is contrary to the observations made in the thesis as the crack shape is observed to change near the particles. The origin of this shape change may be caused by two factors, i.e., the variation from plane stress at the particle or void interface to plane strain within the matrix and local stress changes caused by the presence of the particle.

Consider a linear array of cylindrical voids with their cylindrical axes parallel to the crack front, as illustrated in Figure 144. The extension of a through-the-thickness surface crack of length C' is impeded by the array of voids so that the crack bows between the obstacles and generates small secondary cracks. For an increase in fracture toughness, the stress to move the secondary cracks must exceed that to move the primary crack (σ_C). For the case of an array of voids, the primary crack stress field will be changed because the voids act to blunt the crack. It can be seen that the secondary cracks move in a complex stress field but two limiting cases can be discerned, i.e., sharp and blunt primary cracks. For a sharp primary crack, the stress ahead of the crack and orthogonal to its plane is given by

$$\begin{aligned}\sigma_{yy} &= \sigma_A^S \left(1 + \frac{C'}{2x'}\right)^{1/2} \\ &\approx \sigma_A^S \left(\frac{C'}{2x'}\right)^{1/2} \quad \text{for } x' \ll C'\end{aligned} \quad (5.32)$$

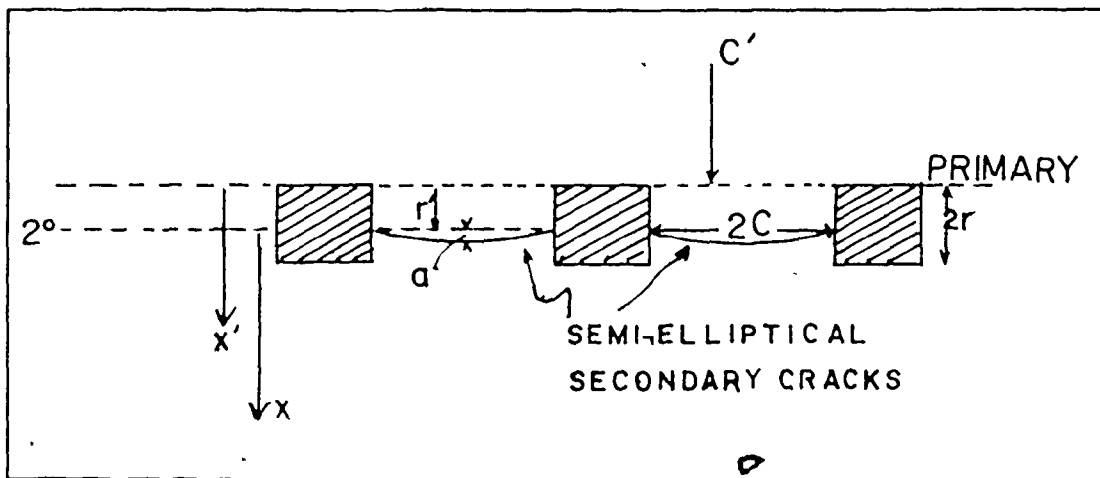


Figure 144. Model for Crack Blunting of a Crack Front by a Linear Array of Cylindrical Voids (or non-bonded particles)

For the case of crack pinning

$$x' = r' + x$$

so that equation (5.31) becomes

$$\sigma_{yy} = \sigma_A^s \left(\frac{C'}{2(r' + x)} \right)^{1/2} \quad (5.33)$$

For the case of no pinning ($r' = 0$)

$$\sigma_{yy} = \sigma_A^s \left(\frac{C}{2x} \right)^{1/2} \quad (5.34)$$

For a blunt primary crack, the stresses ahead of the crack are reduced so that using equation (5.13)

$$\sigma_{yy} = 2\sigma_A^s \left(\frac{C'}{\rho + 4x} \right)^{1/2} \quad (5.35)$$

Using a substitution $\rho = 4r'$ this last equation becomes

$$\sigma_{yy} = \sqrt{2} \sigma_A^s \left(\frac{C'}{2r' + 2x} \right)^{1/2} \quad (5.36)$$

which is the same form as equation (5.33). The impedance to the motion of the crack is reflected in a value of $r' > 0$. The approach of Evans can then be used to define the two limiting cases using equation (5.34) for the sharp primary crack and equation (5.36) for the blunt primary crack. The maximum value of ρ is given by $\rho = r$.

(i) Semi-circular Secondary Cracks

The condition to extend a semi-circular crack in the primary stress can be found using Sack's approach [203]. A flat, semi-circular crack orthogonal to the applied stress increases the elastic energy of a system (U) by

$$U = \frac{-2\alpha C^3}{3G} \int_0^{\pi/2} \sigma^2 \sin \theta d\theta \quad (5.37)$$

where $\alpha/G = 4(1-\nu^2)/E$ and θ is an oblate spheroidal coordinate. Evans [113] evaluates the mean stress acting on a semi-circular secondary crack using equation (5.31) and substitutes this into equation (5.37) to obtain

$$U = \frac{-8\alpha C^3 (\sigma_A^S)^2 k^2}{3\pi^2 G} \int_0^{\pi/2} [H(C, \theta, \beta)]^2 \sin \theta d\theta \quad (5.38)$$

where $\beta = \sin^{-1}(x/C \sin \theta)$, $k^2 = 1$ for a sharp primary crack and $k^2 = 2$ for a blunt crack. The integrand is given by

$$H(C, \theta, \beta) = \int_0^{\pi/2} \left(\frac{C'}{2r' + 2C \sin \theta \sin \beta} \right)^{1/2} d\beta \quad (5.39)$$

For the semi-circular crack to extend from C to $(C + dC)$, the equilibrium condition is given by

$$-\frac{dU}{dC} = 4\pi C \tau_0 \quad (5.40)$$

For $r' = 0$, the integration can be solved easily (Appendix A.7) to give

$$\left(\frac{\sigma_A^S}{\sigma_C} \right) = 1.30/k \quad (5.41)$$

The stress to move the primary crack in the absence of the voids (σ_C) is given by

$$\sigma_C = \left(\frac{2E\tau_0}{\pi(1-\nu^2)C'} \right)^{1/2} \quad (5.42)$$

Using this last equation and equation (5.40), equation (5.38) becomes

$$\left(\frac{\sigma_A^S}{\sigma_C} \right)^2 = \frac{3\pi^4 r'}{8k(3CF(C) + C^2 \partial F(C)/\partial C)} \quad (5.43)$$

where $F(C) = \int_0^{\pi/2} (H(C, \theta, \beta))^2 \sin \theta d\theta \quad (5.44)$

For finite values of r' , the integration in equation (5.43) can be solved numerically and is identical to that used in Appendix A.7 except for the factor of k . The solution is illustrated in Figure 145. For the two limiting cases of sharp ($r' = 0$) and blunt primary cracks, the solution is given in Figure 146 as a function of C/r . For semi-circular secondary cracks, the value of $\sigma_A^S/\sigma_C > 1$ for most values of C/r , indicating that an increase in toughness is possible under the assumptions so far.

(ii) Semi-elliptical Secondary Cracks

It is clear from the US fractographic observations that the assumption of semi-circular secondary cracks is incorrect. These conditions, can be transformed to consider semi-elliptical secondary cracks and in doing so, the crack shape at breakaway can be determined. The stress to extend a semi-elliptical secondary crack (σ_A^E) differs from that to move a semi-circular crack of the same depth (a). This stress ratio ($Z = \sigma_A^E/\sigma_A^S$) is given in Appendix A.7 and the crack shape at breakaway can be found using

$$\frac{d\sigma_A^E}{da} = \sigma_A^S \left(\frac{dZ}{da} \right) + Z \left(\frac{d\sigma_A^S}{da} \right) = 0 \quad (5.45)$$

The procedure is identical again to that in Appendix A.7 and the crack shape at breakaway $(a/2C)^*$ for the semi-elliptical cracks is illustrated in Figure 147 for the two cases and is then compared with the experimental data determined from US tests. It is found that the experimental results lie between the two limiting cases. For sharp cracks ($r' = 0$) the crack front is predicted to remain straight.

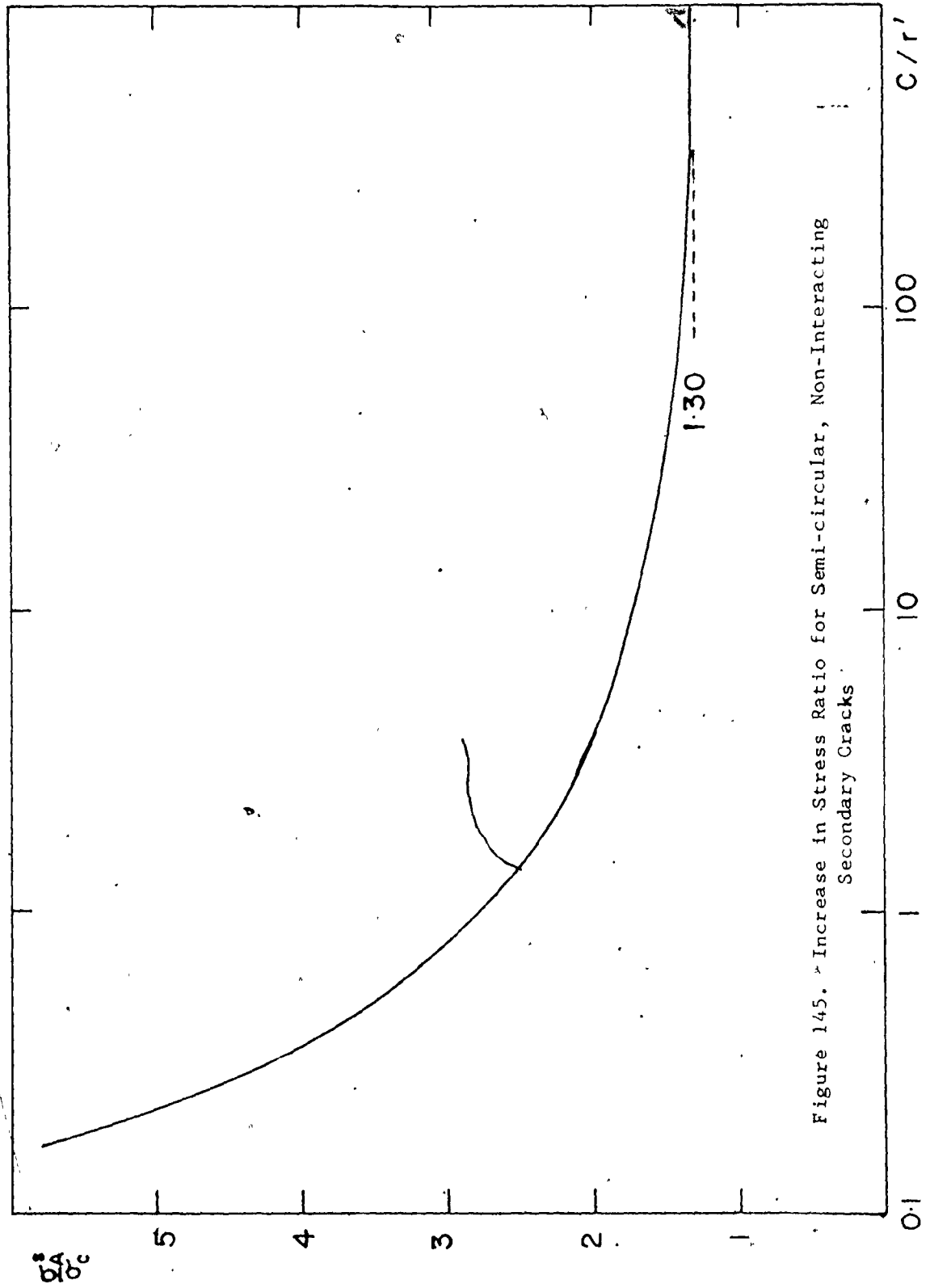


Figure 145. Increase in Stress Ratio for Semi-circular, Non-Interacting Secondary Cracks

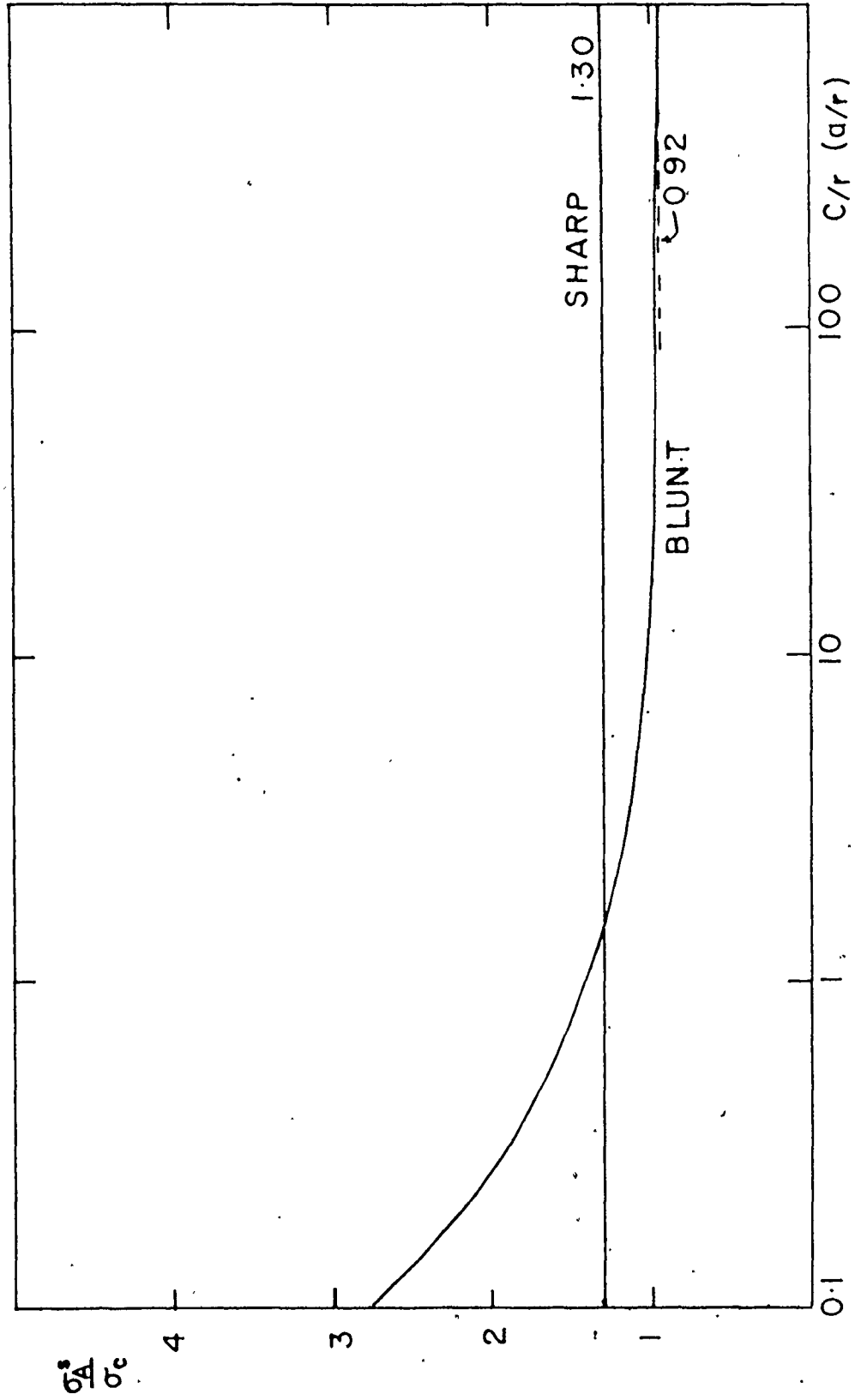


Figure 146. Stress to Move Semi-Circular Secondary Cracks Between an Array of Cylindrical Voids for Blunt and Sharp Primary Crack

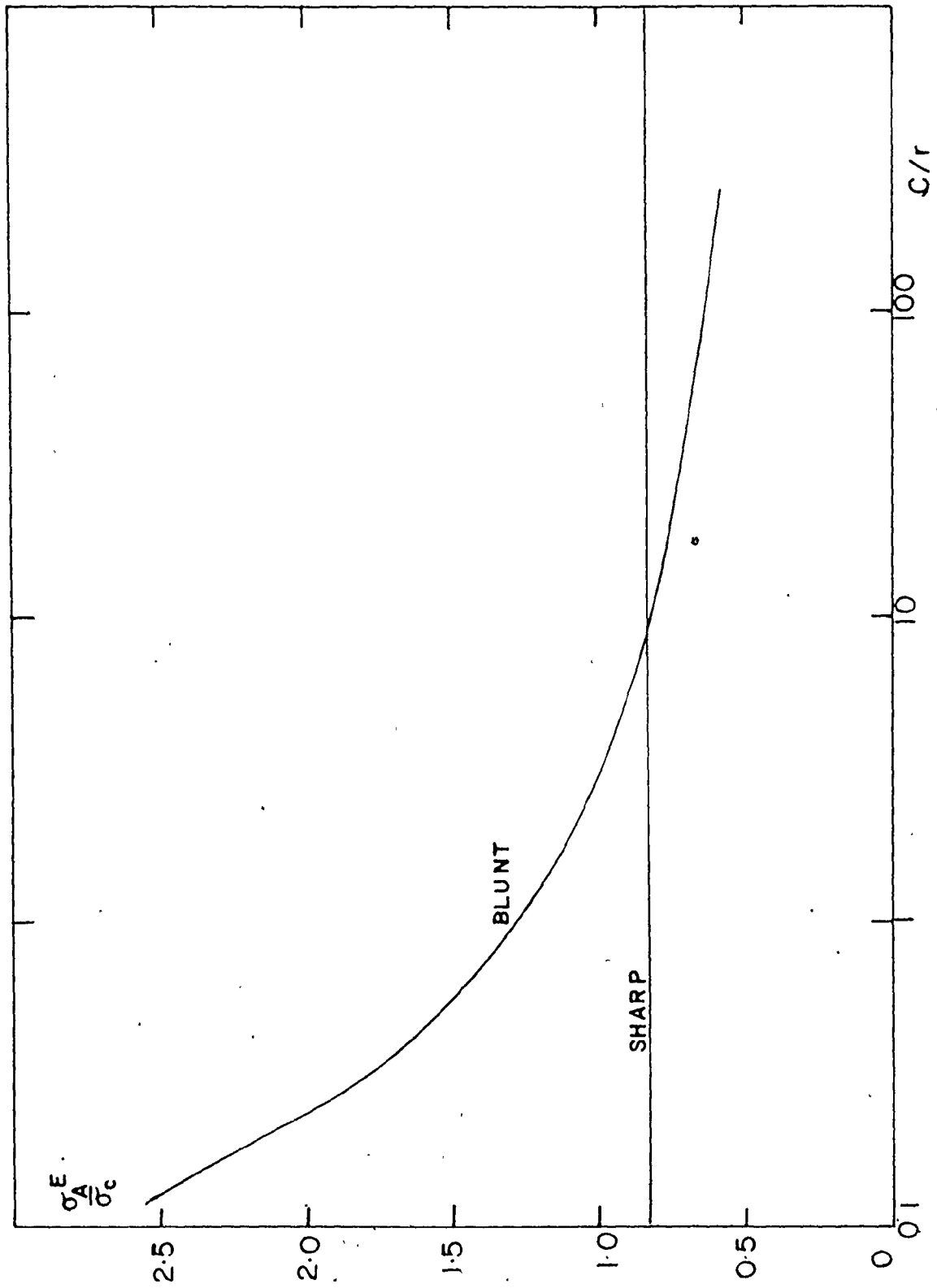


Figure 148. Stress to Move Semi-Elliptical Cracks Between Obstacles

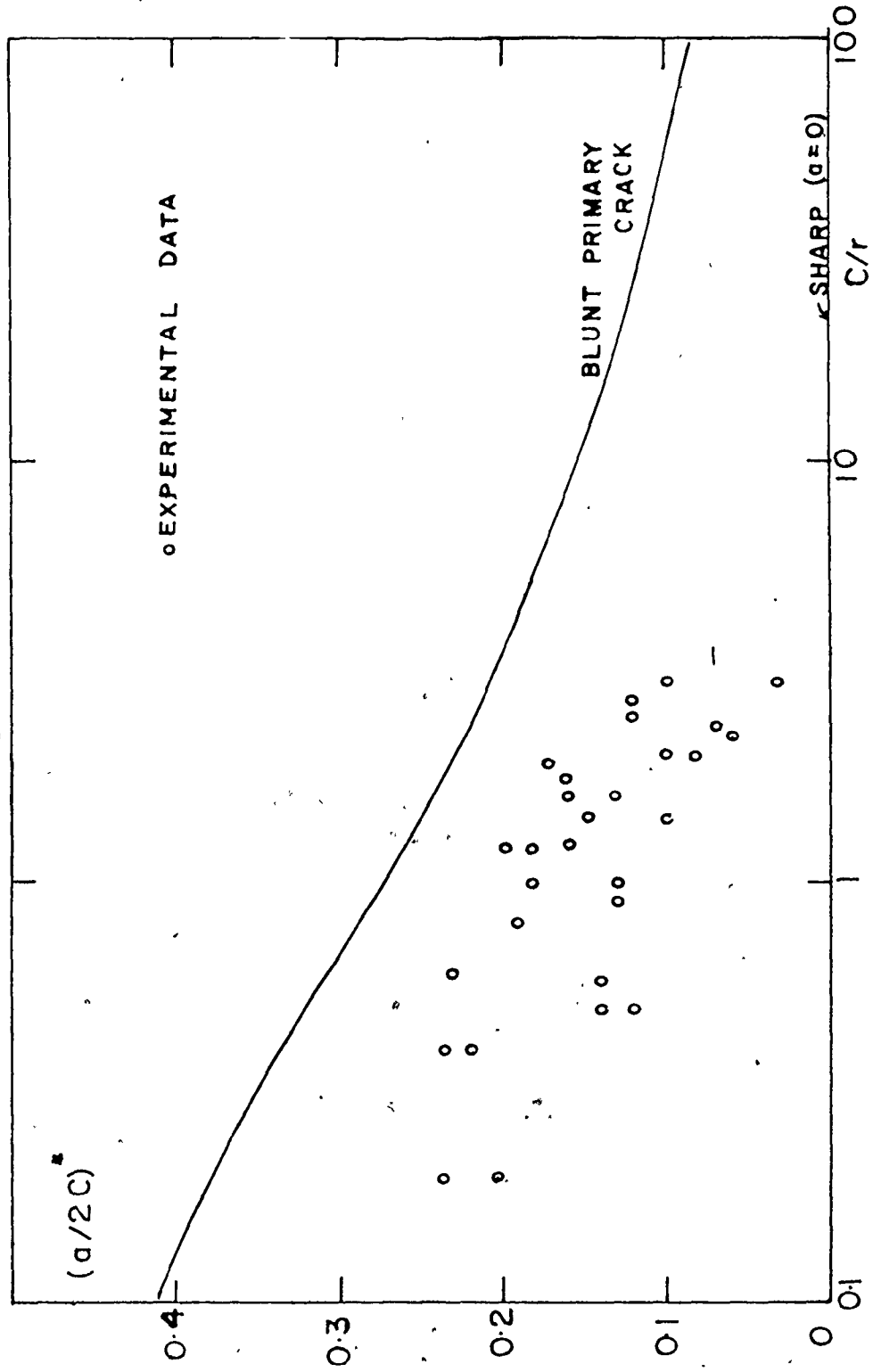


Figure 147: Crack Shape at Breakaway for Blunt And Sharp Primary Cracks and Compared to Data

Once the value of $(a/2C)^*$ is found, Z is known and the stress ratio (σ_A^E/σ_C) can be determined from the value of (σ_A^S/σ_C) for a semi-circular crack of equivalent depth (Figure 148). For sharp cracks with $r' = 0$, the stress ratio is approximately unity, indicating no increase in toughness. For values of $C/r < 8$, the value of σ_A^E/σ_C for blunt primary cracks is greater than that for sharp cracks. The value of σ_A^E/σ_C for sharp cracks is slightly less than unity and must be a result of the approximations made. It is expected that $\sigma_A^E/\sigma_C = 1$ for the case of no pinning. To correct for this, the values of σ_A^E/σ_C were normalized so that this condition was satisfied.

The increase in fracture surface energy is given by

$$\frac{\Sigma}{\Sigma_0} = \left(\frac{\sigma_A^E}{\sigma_C} \right)^2 (1 - \nu^2)^{-1} \quad (5.46)$$

where the $(1 - \nu^2)$ term corrects for the variation from plane stress at the void to plane strain in the matrix. The experimental and theoretical values of Σ/Σ_0 are compared in Figure 149. The experimental values do not lie between the limiting cases but the agreement is good considering the approximations.

For example, the non-bonded particles in S glass are spherical not cylindrical so that during the bowing process, the interparticle spacing increases from $2C$ to $2(C + r_0)$. This effect will tend to reduce the value of σ_A^E/σ_C especially at high volume fractions. The stress field between particles has not been included and again at high volume fractions, this should lead to interaction with another obstacle before the bowing is complete. This sort of effect could explain the

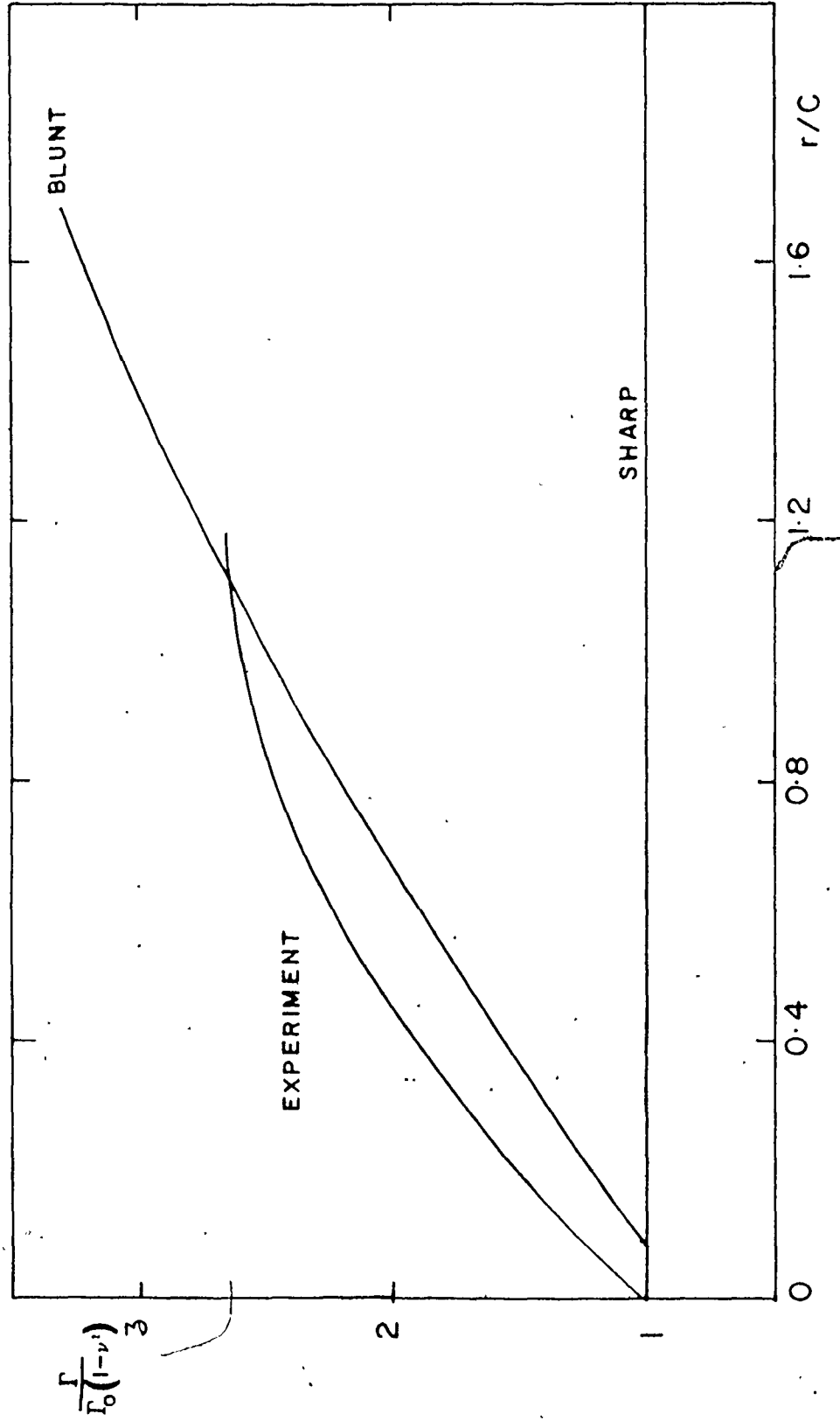


Figure 149. Comparison of Theoretical and Measured Values for Increase in Fracture Surface Energy - S Glass-Nickel Particulate System

maxima often observed in experimental determinations of τ/τ_0 in other particulate composites. Furthermore, at high volume fractions the pinning ability of the obstacle may be reduced. The absolute value of the interparticle spacing ($2C$) is somewhat in doubt and there are other mechanisms available that may increase τ/τ_0 e.g., the fracture surface steps. The interaction between adjacent bowing segments has also not been introduced. Evans [113] attempted to correct for this by assuming the secondary cracks were co-planar. This assumption is incorrect as, in general, the secondary cracks are generally non-coplanar as they break away from the particles.

For bonded particles, $r' > 0$ and substantial increases in τ/τ_0 could be obtained. For highly brittle composites, this effect could lead to a substantial contribution to τ . From these observations, the properties for a good brittle composite can be predicted. First, the obstacles must have the ability to pin the crack front so that the strength of the obstacles and the interface must be high. Secondly, the obstacles must 'attract' the crack front as otherwise the crack would simply stay in the matrix. For this situation the particles must be softer than the matrix or there must be some internal stress available to overcome the repulsion. Such systems may also exhibit high fracture strengths. Figure 150 shows a schematic representation of how the various effects may increase τ/τ_0 .

In fibrous microstructures or composites containing a ductile phase, the effect of crack pinning will not be so important as other mechanisms are available for fracture resistance.

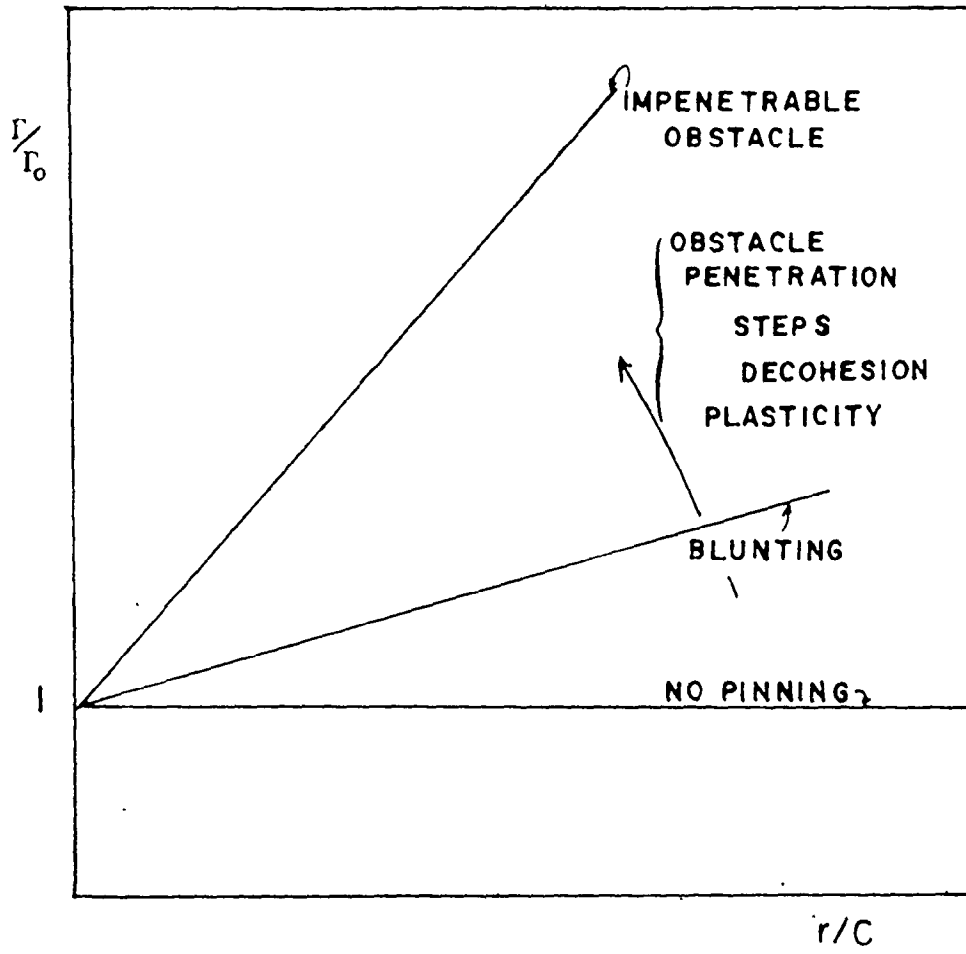
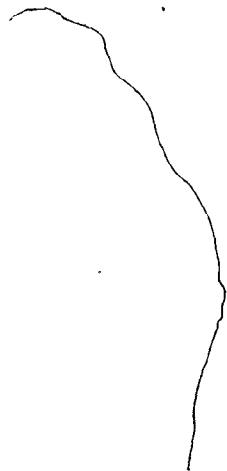


Figure 150. Schematic Representation of Different Energy-Absorbing Mechanisms in a Brittle Particulate System.



5.8.3 Fracture Surface Steps

As the crack breaks away from the nickel particles, it has been shown that fracture surface steps are formed at the rear of the particles. It was shown that the secondary fracture does not occur as the crack breaks away but at some later stage. The unbroken steps are therefore left as ligaments behind the crack front. This effect will restrain the opening of the crack faces. The effect on γ can be estimated from equation (5.11) by multiplying by the increased density of steps and the increased displacement needed to form the steps. Unfortunately, this information is not available from the experimental work. If these effects were to raise the fracture surface contribution by a factor of 20 or more, then this mechanism could become a major contribution to the fracture surface energy. The agreement in the last section between the theoretical predictions and experimental values of fracture surface energy would seem to indicate that the crack blunting effect remains the major mechanism while the formation of fracture surface steps could be an important secondary mechanism.

CHAPTER 6

CONCLUSIONS

Characterization of Materials and Test Technique

1. The hot pressing of the nickel spheres and S glass powder gave rise to samples with densities greater than 99% theoretical with negligible internal stress.
2. The stereological parameters were determined for the fabricated composite and it appeared that there was an increasing probability of interparticle contact with increasing volume fraction of nickel. Comparison of the nickel particle size distribution before and after fabrication and measurement of the contiguity ratio confirmed this effect. The effect on the stereological parameters was reasonably small indicating that there was only a small tendency for agglomeration and the fabricated samples could be considered well-dispersed.
3. The average interparticle spacing relevant to the interaction of a crack front with an array of obstacles was considered best described, to a first approximation, by the square root of the mean area per particle rather than the mean free path or nearest-neighbour distance. It was postulated that this interaction process is described by the average stereological parameters rather than any distribution extremes.
4. Fracture surface energy measurements were made on pyrex and window glass to test the accuracy and reliability of the test technique. Comparison with previous literature values for these materials showed

good agreement. There was a difference, however, depending on whether the experimental values were determined by load-crack length or load-deflection measurements. The load-crack length measurements were in better agreement with the literature. This accuracy, however, was sacrificed for the experimental benefits of the load-deflection approach.

Properties of S Glass-Nickel Sphere Composite

5. The Young's modulus data showed a decrease with increasing volume fraction of nickel. This effect is not predicted by most theoretical approaches but is consistent with a non-bonded glass-nickel interface.

6. The fracture surface energy for the glass-nickel system increases substantially with increasing nickel content. The increased surface area over that expected for planar crack extension was not sufficient to explain the observed variation in Γ . Other mechanisms such as the formation of the fracture surface steps, plastic deformation and decohesion of the particles were estimated to give only negligible contributions to the fracture surface energy values. If the fracture surface steps are left behind the major crack front as unbroken ligaments, the contribution by this mechanism can be substantially increased.

The alternative approach is to consider the increase in elastic energy of the system as the crack breaks away from the obstacles. For a non-bonded system, an increase in local fracture resistance could be obtained by crack blunting when the crack intersects the particles.

7. The fracture strength of the S glass-nickel composite system was

observed to decrease slightly with increasing nickel content. From these measurements, the critical flaw size can be calculated and was found to increase with increasing volume fraction of nickel. This effect is consistent with the particles themselves acting as nucleation sites for flaw generation. For non-bonded particles, extensive cracking is likely to occur between particles prior to failure.

Fractographic observations indicated that the fracture origin was often located near the tensile surface of the bend samples and in the vicinity of contacted nickel particles.

Fractography

8. Fractography was used to identify the features associated with the fracture of the particulate composites. The fracture surface was found to be reasonably planar except in the vicinity of the particles. Observations were often made of fracture ledges before the particles and fracture surface steps at the rear of the particle. The ledge is probably caused by failure of the glass-nickel interface, which may be weakly-bonded after fabrication. This failure will give rise to a sudden change in crack direction. At higher volume fractions of nickel, the ledges were observed to be less abundant while the fracture surface steps increased in number until they connected particles.

9. The technique of ultrasonic fractography was successfully applied to S glass, S glass containing residual spherical porosity and S glass-nickel composites, allowing local changes in crack velocity and crack shape to be studied.

10. For the glass-pore system, the crack is first attracted to the void and then the void impedes the local motion of the crack. Finally the crack breaks away leaving the fracture surface step at the rear of the particle. It was found that the fracture surface step broke sometime after the major crack front had passed that point, indicating the steps are left behind as unbroken ligaments. The voids do not act to pin the crack but rather to impede its motion.

11. For the glass-nickel composites, the change in crack shape is very similar to those observed for the glass-pore system. The initial attraction to the obstacle, however, is not as prominent. At higher volume fractions, the ultrasonic markings were difficult to distinguish but the crack shape at breakaway could be measured.

12. The technique of ultrasonic fractography has great potential for studying crack-microstructural interactions in detail.

Theoretical Aspects

13. A theoretical approach was formulated to predict the crack behaviour as it approaches a cylindrical elastic disturbance. It is shown that the crack will be attracted or repelled by the particle depending on whether the particle is softer (e.g. void, non-bonded particle) or harder than the matrix. This approach explains the observations of crack attraction

for the S glass-pore system and can be extended to deal with other crack locations or misfit stress fields.

14. A theoretical approach was formulated to predict the crack behaviour as it is blunted by an array of voids or non-bonded particles. This was done by considering two limiting cases, i.e., for a blunt and sharp primary crack. This approach predicts the crack shape at break-away for the two limiting cases and the experimental observations were found to lie between these limits. The increase in fracture surface energy can also be predicted and reasonable agreement is obtained with the experimental results. Therefore, it appears that the major contribution to fracture surface energy for this system is caused by the increase in elastic stored energy needed to overcome the local blunting of the crack front. This increased elastic energy is reflected by the change in crack shape.

15. The formation of the fracture surface steps will make a secondary contribution to the fracture surface energy as they are left behind the crack front as unbroken ligaments which restrain the crack opening.

L

SUMMARY FOR FUTURE WORK

The general approach of this thesis and in particular the technique of ultrasonic fractography has great potential for studying crack interactions in brittle composites. For particulate composites, the approach still needs further experimental clarifications, e.g.,

(i) Non-bonded glass composites

There is a need to establish the effects of particle size and shape on crack shape and the fracture toughness and to test the theoretical approach in this thesis.

(ii) Glass-pore system

There is a need to study the effects of pore volume fraction, size and shape on crack shape and fracture toughness in model glass-pore systems.

(iii) Well-bonded glass composite

The same technique should also be applied to well-bonded composites containing hard or soft particles. In particular, the indications are that attractive particles with the ability to pin the crack front could lead to substantial increases in fracture toughness. A practical example of this would be to study glass-ceramics. In this way, it should be possible to optimize the properties of a good particulate composite. The effect of internal stresses or crystalline matrices could also be included here.

There is some clarification needed to define more exactly the interparticle spacing for these crack-particle interactions and to assess the effect of the fracture surface steps.

Finally, the ultrasonic fractographic technique could also be used to study crack interactions near elastic disturbances and in particular the problem of crack trajectory near these particles.

BIBLIOGRAPHY

1. General References1.1 Glass Science

1. Pye, L.D., Stevens, H.J., and LaCourse, W.C., (eds), Introduction to Glass Science, Plenum Press, New York (1972).
2. Doremus, R.H., Glass Science, J. Wiley and Sons, New York (1973).
3. Holloway, D.G., The Physical Properties of Glass, Wykeham Science Series (24), Wykeham Publications, London (1972).

1.2 Microscopy

1. Murr, L.E., Electron Optical Applications in Material Science, McGraw-Hill, New York (1970).
2. Richardson, J.D., (ed), Optical Microscopy for the Materials Sciences, Dekker (1971).
3. Thornton, P.R., Scanning Electron Microscopy, Chapman and Hall, London (1968).
4. Rhines, F.N., and DeHoff, R.T., Quantitative Microscopy, McGraw Hill, New York (1968).
5. Underwood, E.E., Quantitative Stereology, Addison-Wesley, (1970).

1.3 Fracture

1. Tetelman, A.S., and McEvily, Jr., A.J., Fracture of Structural Materials, Wiley and Sons, New York (1967).

2. Knott, J.F., Fundamentals of Fracture Mechanics, Butterworths, London (1973).
3. Broek, D., Elementary Engineering Fracture Mechanics, Noordhoff, Leyden (1974).
4. Lawn, B.R., and Willshaw, T.R., Fracture of Brittle Solids, Cambridge University Press (1975).
5. Bradt, R.C., Hasselman, D.P.H. and Lange, F.F., (eds), Fracture Mechanics of Ceramics, Plenum Press, New York (1974).
6. The Iron and Steel Institute (London), Fracture Toughness, JISI 121 (1968).
7. Gordon, J.E., The Science of Strong Materials, Pelican Books, London (1968).
8. Liebowitz, H., Fracture: An Advanced Treatise, Academic Press, New York (1968), Vol. I - VII.
9. ASTM Special Tech. Pub., Nos 381, 410.
10. Kerhof, F., Bruchvorgange in Glasern, Deut. Glastechn. Ges., Frankfurt, A.M. (1970).
11. Kelly, A., Strong Solids, 2nd Edition, Clarendon Press, England (1973).
12. Cottrell, A.H., Mechanical Properties of Matter, Wiley and Sons, New York (1964).

1.4 Review Papers on Fracture of Brittle Materials

1. Davidge, R.W., Contemp. Phys. 10 (1969) 105.
2. Wiederhorn, S.M., in Ultra-Fine Grain Ceramics, (eds J.J. Burke et al), Syracuse University Press (1970).
3. Wiederhorn, S.M., NBS STP 303 (1968) 217.

4. Petch, N.J., in *Ceramics in Severe Environments* (ed W.W. Kriegel and H. Palmour III), *Mat. Sci. Res.*, 5 Plenum Press, New York (1971).
5. Davidge, R.W., and Evans, A.G., *Mat. Sci. Eng.*, 6 (1970) 280.
6. Smith, E., *Mat. Sci. Eng.*, 15 (1975) 3.
7. Wachtman, J.B. Jr., *J. Am. Ceram. Soc.* 57 (1974) 509.
8. Field, J.E., *Contemp Phys.*, 12 (1971) 1.

2. References

1. Secrist, D.R. and MacKenzie, J.D., Modern Aspects of the Vitreous State, Vol. 3, Chap. 6, Butterworths, London (1960).
2. Levin, E.M., et al., Phase Diagrams for Ceramists, The American Ceramic Society, Columbus (1956).
3. Manring, W.H., and Bauer, W.C., Glass Ind., 45 (1964) 354.
4. Buss, W., Glästech. Ber., 32 (1959) 89.
5. Riebling, E.F., J. Electrochem. Soc., 113 (1966) 920.
6. Kröger, C., Glästech. Ber. 25 (1952) 307.
7. Swarts, E.L., Introduction to Glass Science, pp. 273-327 Ed., Pye, L.D., et al, Plenum Press, New York (1972).
8. Kröger, C., and Goldman, N., Glästech. Ber., 35 (1962) 459.
9. Lange, F.F., J. Am. Ceram. Soc., 54 [12] (1971) 614.
10. Ritland, H.N., J. Am. Ceram. Soc., 39 [12] (1956) 403.
11. Sun, H.K., J. Am. Ceram. Soc., 30 (1947) 277.
12. Zachariasen, W.H., J. Am. Chem. Soc., 54 (1932) 3841.
13. Zachariasen, W.H., J. Chem. Phys., 3 (1935) 162.
14. Warren, B.E., and Briscoe, J., J. Am. Ceram. Soc., 21 (1938) 29.
15. Warren, B.E., X-Ray Diffraction, Addison-Wesley (1969).
16. Eckstein, B., Glästech. Ber., 36 (1963) 323.
17. Weyl, W.A., Coloured Glasses, Society of Glass Technology (1951).
18. Morey, G.W., The Properties of Glass (2nd Edition) Reinhold Pub. Corp., New York (1954).
19. Spriggs, R.M., High Temperature Oxides, Part III, ed. Alper, A.M., Academic Press, New York (1970).
20. Sahm, P.R., Powder Met. Int. 3 (1971) 1
Ibid 3 (1971) 96

21. Gazza, G.E., and Dutta, S.K., Am. Ceram. Soc. Bull., 49 (1970) 381.
22. Chaklader, A.C.D., J. Can. Ceram. Soc., 40 (1970) 19.
23. Rice, R.W., High Temperature Oxides, Part III, ed. Alper, A.M., Academic Press, New York (1970).
24. Ramquist, L., Powder Met., 9 (1966) 1.
25. Coble, R.L., Sintering and Related Phenomena, eds Kuczynski, G.C., et al, Gordon and Breach (1967).
26. Spriggs, R.M., and Dutta, S.K., Sintering and Related Phenomena, Mat. Sci. Res. Vol. 6, ed. Kuczynski, G.C., Plenum Press, New York (1973).
27. Murray, P., Livey, D.T., and Williams, J., in Ceramic Fabrication Processes, ed. Kingery, W.D., p. 147, J. Wiley and Sons, New York (1958).
28. Vasilos, T., J. Am. Ceram. Soc., 46 (1960) 493.
29. Chang, R., and Rhodes, C.G., *ibid.*, 45 (1962) 379.
30. Felton, E.J., *ibid* 44 (1961) 381.
31. Hashimoto, Y., M.S. Thesis, Univ. of California (1964).
32. Rossi, R.C., and Fulrath, R.M., J. Am. Ceram. Soc., 48 (1965) 558.
33. Spriggs, R.M., and Atteraaas, L., Ceramic Microstructures, ed. Pask, J.A., and Fulrath, R.M., J. Wiley and Sons, New York (1968).
34. Coble, R.L., J. Appl. Phys., 41 (1970) 4798.
35. Underwood, E.E., Stereologia, 3 [2] (1964) 5.
36. Underwood, E.E., Quantitative Stereology, Addison-Wesley (1970).
37. Fullman, R.L., Trans. AIME, 197 (1953) 447, 1267.
38. Saltykov, S.A., Stereometric Metallography, 2nd Edition, p. 446, Metallurgizdat, Moscow (1958).
39. Underwood, E.E., in Reference 33.

40. Hench, L.L., and Gould, R.W., Characterization of Ceramics, Marcel Dekker Inc., New York (1971).
41. Aitchison, J., and Brown, J.A.C., The Lognormal Distribution, Cambridge University Press (1969).
42. Herdan, G., Small Particle Statistics, Butterworths, London (1960).
43. Gurland, J., in Quantitative Microscopy, ed. Rhines, F.N., and DeHoff, R.T., McGraw-Hill, New York (1968).
44. Smith, C.S., and Guttman, L., Trans. AIME, 197 (1953) 81.
45. Gurland, J., Trans. AIME, 212 (1958) 452.
46. Forscher, F., J. Franklin Inst. 259 (1955) 107.
47. Ardell, A.J., Acta. Met., 20 (1972) 61.
48. Bansal, P.B., and Ardell, A.J., Metallography, 5 (1972) 97.
49. Brown, L.M., and Ham, R.K., Strengthening Mechanisms in Crystals, ed. Kelly, A., and Nicholson, R.B., Elsevier, Amsterdam (1971).
50. Tyson, W.R., Acta. Met., 11 (1963) 61.
51. Corti, C.W., Cotterill, P.C., and Fitzpatrick, G.A., Int. Met. Rev. 19 [182] (1974) 77.
52. Kocks, U.F., Phil. Mag., 13 (1966) 541.
53. Kocks, U.F., Acta. Met., 14 (1966) 1629.
54. Foreman, A.J.E., and Makin, F.J., Phil. Mag., 14 (1966) 911.
55. Orowan, E., Internal Stress in Metals and Alloys, p. 541, Inst. Metals, London (1948).
56. Lawn, B.R., and Willshaw, T.R., Fracture of Brittle Solids, Cambridge University Press, (1975).

57. Green, D.J., Report to AECL, December (1976).
58. Kelly, A., Strong Solids, 2nd edition, Clarendon Press, England (1973).
59. Griffith, A.A., Phil. Trans. Roy. Soc., (London), 221A (1920) 163.
60. Inglis, C.E., Inst. Naval Arch. Trans. 55 (1913) 219.
61. Glucklich, J., Eng. Fract. Mech., 3 [3] (1971) 333.
62. Orowan, E.; Repts. Prog. Phys., XII (1948) 185.
63. Dixon, J.R., Inst. Phys., Phys. Soc. Conf. Ser. No. 1 (1966)
64. Sih, G.C., Eng. Fract. Mech., 5 (1973) 365.
Ibid 5 (1974) 361.
65. Erdogan, F., and Sih, G.C., J. Basic Eng., 85 (1963) 519.
66. Wagoner, R.H., and Hirth, J.P., Submitted to Met. Trans.
September (1975).
67. Gell, M., and Smith, E., Acta. Met. 15 (1967) 253.
68. Sommer, E., Eng. Fract. Mech., 1 (1969) 539.
69. Lange, F.F., in Fracture and Fatigue of Composites, Composite Materials, Vol. 5, ed. Broutman, L.J., and Crock, R.H., Academic Press, New York (1973).
70. Tamate, O., Int. J. Fract. Mech., 4 (1968) 257.
71. Atkinson, C., Scripta. Met., 5 (1971) 653.
72. Tirosh, J. and Tetelman, A.S., Int. J. Fract. Mech., 12 [2] (1976) 187.
73. Erdogan, F., in Fracture Mechanics of Ceramics, ed. Bradt, R.C., et al., Plenum Press, New York (1974).
74. Stett, M.A., and Fulrath, R.M., J. Am. Ceram. Soc., 53 [1] (1970) 5.
75. Hancock, P., J. Mat. Sci., 10 (1975) 1230.

76. Hahn, G.T., Kanninen, M.F., Rosenfield, A.R., Ann. Rev. Mater. Sci. 2 (1972) 381.
77. Barenblatt, G., Advan. Appl. Mech., 7 (1962) 55.
78. Dugdale, D.S., J. Mech. Phys. Solids, 8 (1960) 100.
79. Hasselman, D.P.H., Krohn, D.A., Bradt, R.C., and Coppola, J.A., in Fracture Mechanics of Ceramics, ed. Bradt, R.C., et al. Plenum Press, New York (1974).
80. Bartenev, G.M., Paper A-25, 1st Int. Conf. Fracture, Vol. 1, Sendai, Japan (1965).
81. Plateau, J., Int. J. Fract., 4 (1968) 35.
82. Class, W.H., and Machlin, E.S., J. Am. Ceram. Soc., 49 (1966) 306.
83. Cook, J., and Gordon, J.E., Proc. Roy. Soc. (London) 282A (1964) 508.
84. Kaplan, M.F., Proc. Int. Conf. on Struct. of Concrete, Paper D1, London (1965).
85. Rosenfield, A.R., Hahn, G.T., and Hoagland, R.G., J. Rock. Mech., 5 (1973) 77.
86. Green, D.J., Nicholson, P.S., and Embury, J.D., J. Am. Ceram. Soc., 56 [12] (1973) 619.
87. Green, D.J., Nicholson, P.S., and Embury, J.D., in Fracture Mechanics of Ceramics, Vol. 2, ed. Bradt, R.C., et al., Plenum Press, New York (1974).
88. Kuszyk, J.A., and Bradt, R.C., J. Am. Ceram. Soc., 56 [8] (1973) 420.
89. Buessem, W.R., and Lange, F.F., Interceram., 15 [3] (1966) 229.
90. Claussen, N.E., J. Am. Ceram. Soc., 59 [1-2] (1976) 49.
91. Steeb, J., and Claussen, N.E., Presented at Ann. Meeting Am. Ceram. Soc., Cincinnati (1976).

92. Moavenzadeh, F., and Kuguel, R., J. Mater, 4 [3] (1969) 497.
93. Broutman, L.J., and Sahu, S., Mat. Sci. Eng., 8 (1971) 98.
94. Friedel, J., in Fracture 1959, ed. Averbach, B.L., et al. p. 498
Wiley, New York (1959).
95. Swain, M.V., Lawn, B.R., and Burns, S.J., J. Mat. Sci., 9 (1974) 175.
96. Lange, F.F., Phil. Mag. 16 (1967) 761.
97. Lange, F.F., and Lambe, K.A.D., Phil Mag., 18 (1968) 129.
98. Ahlquist, C.N., Acta. Met. 23 [2] (1975) 239.
99. Berry, J.P.; in Fracture Processes in Polymeric Solids, ed. Rosen, B.,
p. 172, Wiley, New York (1964).
100. Neuber, H., Kernspannungslehre, Springer, Berlin (1958).
101. Pabst, R.F., in Fracture Mechanics of Ceramics, ed. Bradt, R.C.,
et al. p. 555 (Vol. 2) Plenum Press, New York (1974).
102. Mendelson, M.I., and Fine, M.E., J. Am. Ceram. Soc., 57 [4]
(1974) 154.
103. Forwood, C.T., and Forty, A.J., Phil. Mag., 11 (1965) 1067.
104. Lange, F.F., Phil. Mag., 22 (1970) 983.
105. Briggs, A., courtesy photographs in Ref. [104].
106. Frechette, V.D., Introduction to Glass Science, ed. Pye, L.D.,
et. al. Plenum Press, New York (1972).
107. Ohlberg, S.M., Gelob, H.R., and Hollabough, C.M., J. Am. Ceram. Soc.,
45 (1962) 1.
108. Chaplin, C.R., J. Mater. Sci., 9 (1974) 329.
109. Kerkhof, F., and Sommer, E., Glastechn. Ber., 38 (1965) S.22.
110. Davidge, R.W., and Green, T.J., J. Mater. Sci. 3 (1968) 620.
111. Lange, F.F., Phil. Mag., 22 (1970) 983.
112. Thomson, R.B., Ann. Rev. Mater. Sci., 3 (1973) 31.

113. Evans, A.G., *Phil. Mag.*, 26 (1972) 1327.
114. Lange, F.F., in *Fracture and Fatigue of Composites*, ed. Broutman, L.J. and Krock, R.H., p. 1, Academic Press, New York (1973).
115. Kolsky, H., *Stress Waves in Solids*, Oxford University Press, England (1953).
116. Wachtman, J.B. Jr., in *Fracture Mechanics of Ceramics*, Vol. 2, ed., Bradt, R.C., et. al., p. 49, Plenum Press, New York (1974).
117. Mogford, I.L., *Met. Rev.*, 12 (1967) 49.
118. Krock, R.H., in *Modern Composite Materials*, eds. Broutman, L.J., and Krock, R.H., p. 455, Addison-Wesley, Reading, Mass. (1967).
119. Hashin, Z., *Appl. Mech. Rev.* 17 (1964) 1.
120. Paul, B., *Trans. Met. Soc. AIME*, 218 (1960) 36.
121. Hashin, Z., and Shtrikman, S., *J. Mech. Phys. Solids*, 11 (1963) 127.
122. Ishai, O., *Mag. Concr. Res.*, 17 (1965) 148. (Discussion of paper by U.J. Counto).
123. Rossi, R.C., *J. Am. Ceram. Soc.*, 52 (1969) 290.
124. Cohen, L.J., and Ishai, O., *J. Compos. Mater.*, 1 (1967) 390.
125. Sahu, S., and Broutman, L.J., *St. Louis Symp. Advan. Compos.* 5th April (1971).
126. Sundström, B., *Eng. Fract. Mech.*, 5 (1974) 483.
127. Sato, V., and Furakawa, J., *Rubber Chem. Technol.* 36 (1963) 1081.
128. Rice, R.W., *J. Am. Ceram. Soc.*, 58 (1975) 458.
129. Evans, A.G., in *Fracture Mechanics of Ceramics*, Vol. 1, ed. Bradt, R.C., et. al., p. 17, Plenum Press, New York (1974).
130. Wiederhorn, S.M., Shorb, A.M., and Moses, R.L., *J. Appl. Phys.*, 39 (1968) 1572.

131. Swanson, G.D., and Gross, G.E., J. Appl. Phys., 40 [11] (1969) 4684.
132. Srawley, J.E., and Gross, B., Mater. Res. Standards, 7 [4] (1967) 155.
133. Virkar, A.V., and Gordon, R.S., J. Am. Ceram. Soc., 59 [1-2] (1976) 68.
Ibid., 50 [11-12] (1975) 536.
134. Timoshenko, S.P., and Gere, J.M., Strength of Materials, Van Nostrand, Reinhold (1972).
135. Timoshenko, S.P., and Goodier, J.N., Theory of Elasticity, McGraw-Hill, New York (1951).
136. Gillis, P.P., and Gilman, J.J., J. Appl. Phys. 35 [3] (1964) 647.
137. Gillis, P.P., J. Appl. Phys., 36 [4] (1965) 1374.
138. Gillis, P.P., J. Appl. Phys., 39 (1968) 2149.
139. Kanninen, M.F., Int. J. Fracture, 9 [1] (1973) 83.
140. Cotterell, B., Int. J. Fract. Mech., 6 [2] (1970) 189.
141. Freed, C.N., and Krafft, J.M., J. Mater., 1 (1966) 770.
142. Hoagland, R.G., Trans. ASME, 89D (1967) 525.
143. Mostovoy, S., Crosley, P.B., and Ripling, E.J., J. Mater., 2 [3] (1967) 661.
144. Hoagland, R.G., Marshall, C.W., and Rosenfield, A.R., Mater. Sci. Eng., 15 (1974) 51.
145. Berry, J.P., J. Mech. Phys. Solids, 8 (1964) 194, 207.
146. Clausing, D.P., Int. J. Fract. Mech., 5 [3] (1969) 211.
147. Jaeger, J.C., and Cook, N.G.W., Fundamentals of Rock Mechanics, Methuen (1969).
148. Mai, Y.W., Int. J. Fract. Mech., 12 [1] (1976) 107.

149. Kanninen, M.F., *Int. J. Fract. Mech.*, 10 [3] (1974) 415.
150. Newnham, R.C., *Proc. Brit. Ceram. Soc.*, No. 25, (1975) 281.
151. Green, D.J., M.Sc. Thesis, McMaster University, Hamilton (1972).
152. Hoagland, R.G., *J. Am. Ceram. Soc.*, 59 [5-6] (1976) 189.
153. Marshall, C.W., and Rudnick, A., in *Fracture Mechanics of Ceramics*, Vol. 1, ed., Bradt, R.C., et. al., p. 69, Plenum Press, New York (1974).
154. Hasselman, D.P.H. and Fulrath, R.M., in *Ceramic Microstructures*, ed. Pask, J.A., and Fulrath, R.M., p. 343, Wiley, New York (1967).
155. Radford, K.C., *J. Mater. Sci.*, 6 (1971) 1286.
156. Lange, F.F., and Radford, K.C., *J. Mater. Sci.* 6 (1971) 1197.
157. Sahu, S., and Broutman, L.J., *Poly. Eng. and Sci.*, 12 (1972) 91.
158. Bertolotti, R.L., and Fulrath, R.M., *J. Am. Ceram. Soc.* 50 [11] (1967) 558.
159. Kenyon, A.S., *J. Colloid Interface Sci.*, 27 (1968) 761.
160. Binns, D.B., in *Science of Ceramics*, ed. Stewart, G.H., Vol. 1, p. 315, Academic Press, New York (1962).
161. Lange, F.F., in *Fracture Mechanics of Ceramics*, Vol. 2, ed. Bradt, R.C., et. al, p. 599, Plenum Press, New York (1974).
162. Evans, A.G., *J. Mater. Sci.*, 9 (1974) 1145.
163. Rice, R.W., in *Surfaces and Interfaces of Glass and Ceramics*, *Mater. Sci. Res. Vol. 7*, ed. Frechette, V.D., et. al., Plenum Press, New York (1974).
164. Rice, R.W., in *Fracture Mechanics of Ceramics*, Vol. 1, ed. Bradt, R.C., et. al., p. 323, Plenum Press, New York (1974).

165. Frechette, V.D., in Introduction to Glass Science, ed., Pye, L.D., et. al., p. 433, Plenum Press, New York (1972).
166. Holloway, D.G., The Physical Properties of Glass, Wykeham Science Series (No. 24), Wykeham Publications, London (1973).
167. Erdogan, F., in Fracture: An Advanced Treatise, Vol. II, ed., Liebowitz, H., Chapter 5, Academic Press, New York (1968).
168. Field, J.E., Contemp. Phys. 12 [1] (1971) 1.
169. Kerkhof, F., Bruchvorgänge in Gläsern, Deut. Glastechn. Ges., Frankfurt, A.M. (1970).
170. Dreizler, H., Dipl. Arb. Univ. Freiburg (1954) quoted in Ref. 169, p. 77.
171. Kerkhof, F., in Kurzzeitphysik, ed., Vollrath, K., and Thomer, G., p. 498, Springer, New York (1967).
172. Küppers, Z. Angew. Phys., 20 (1965) 88.
173. Schinker, M.G., J. Appl. Phys. 44 [3] (1973) 1105.
174. Greenwood, J.H., Int. J. Fract. Mech., 8 [2] (1972) 183.
175. Erdogan, F., in Fracture: An Advanced Treatise, Vol. II, ed. Liebowitz, H., Chapter 5, Academic Press, New York (1968).
176. Schardin, H., in Fracture 1959, ed. Averbach, B.L., et. al., p. 297, Wiley; New York (1959).
177. Kerkhof, F., Proc. 3rd Int. Congress on High Speed Photography; London, p. 194 (1956).
178. Kerkhof, F., Int. Conf. on Dynamic Crack Propagation, Lehigh University, Bethlehem (1972).
179. Kerkhof, F., Naturwiss, 40 (1953) 478.

180. Kerkhof, F., and Richter, H., Int. Conf. on Fracture, Brighton, p. 463 (1969).
181. Clark, A.B.J., and Irwin, G.R., Exptl. Mech., (1966).
182. Heyes, A.D., and Langdon, T.G., Nature, 221 (1969) 168.
183. Field, J.E., and Heyes, A.D., Proc. 7th Intern. Cong. High Speed Photography, ed. Helwich, O., p. 391, Zurich (1965).
184. Nason, D.O., M.S. Thesis, University of California, Berkeley (1962).
185. Greaves, R.H., and Wrighton, H., Practical Microscopical Metallography, p. 177, Chapman and Hall, London (1971).
186. Wiederhorn, S.M., and Bolz, L.H., J. Am. Ceram. Soc., 53 (1970) 543.
187. Kerkhof, F., and Schinker, M.G., Private Communication (1973).
188. Lowenheim, F.A., (ed), Modern Electroplating, Wiley, New York (1974).
189. Fairhurst, J., Private Communication (1972).
190. Selsing, J., J. Am. Ceram. Soc., 44 (1961) 419.
191. Wiederhorn, S.M., J. Am. Ceram. Soc., 52 (1969) 99.
192. Timoshenko, S.P., and Gere, J.M., Strength of Materials, Van Nostrand, Reinhold (1972).
193. Wiederhorn, S.M., Evans, A.G., and Roberts, D.E., in Fracture Mechanics of Ceramics, Vol. 2, ed. Bradt, R.C. et. al., p. 829, Plenum Press, New York. (1974).
194. Linger, K.R., and Holloway, D.G., Phil. Mag., 18 (1963) 1269.
195. Jaeger, J.C., and Cook, N.G.W., Fundamentals of Rock Mechanics, Methuen (1969).

196. Hasselman, D.P.H., and Fulrath, R.M., J. Am. Ceram. Soc., 47 (1964) 52.
197. Broek, D., Elementary Engineering Fracture Mechanics, p. 96.,
Noordhoff, Leyden (1974).
198. Hammond, J.C., B.Sc. (Hons.) Thesis, Sheffield Polytechnic, Great
Britain.
199. Yukawa, S., and McMullin, J.G., J. Basic Eng., 83 (1961) 877.
200. Weiss, V., ASME Paper No. 62, WA-270 (1962).
201. Garg, S.K., Svalbonas, V.; and Gurtman, G.A., Analysis of
Structural Composite Materials, p. 347, Dekker, New York (1973).
202. Hoagland, R.G., Private Communication, McMaster University (1975)
Khaund, A.K., Ph.D., Thesis Proposal, McMaster University (1975)
203. Sack, R.A., Proc. Phys. Soc., 58 (1946) 729.
204. Irwin, G.R., J. Appl. Mech., 24 (1957) 361.
205. Evans, A.G., and Graham, L.J., Acta Met., 23 (1975) 1303.
206. Antolovich, S.D., Shete, P.M., and Chanani, G.R., ASTM STP 514
(1972) p114.

APPENDIX

A.1 The Schwartz-Saltykov Method for Determining Particle Size Distributions from Polished Sections

For this method, a direct calculation of the number of particles in any size group may be made regardless of whether the number of particles in any other group is known or not. The number of groups required is not fixed, and only one table of coefficients is needed for any number of groups up to 15. A larger number of groups is rarely necessary.

The particle sizes may be broken down into as many groups as desired, depending on the accuracy required of the determination and whether it is convenient to make the measurements under the microscope or on a photomicrograph. A magnification may be selected so that the largest diameter D_{\max} can be expressed by an integer number of scalar units, preferably not less than 7 or 8.

Saltykov introduces the term Δ so that $D_{\max} = k\Delta$, where k is the number of groups. Thus, the diameter of particles in the first group is Δ , that of the second group is 2Δ etc. The nomenclature adopted for the size and numbers of sections and spheres is given in Table A.1. Those particles with diameters Δ can form sections only of the minimum size on the plane of polish (i.e., sections of the first group with diameters between 0 and Δ). Particles of diameter 2Δ can form sections of both group 1 and 2 in the plane of polish (i.e.

TABLE A.1 Definition of Terms Used in the Schwartz-Saltykov Method

Number of the Group	Diameter	Number per Unit Volume
Particles (j)		
1	Δ	$N_V(1)$
2	2Δ	$N_V(2)$
3	3Δ	$N_V(3)$
j	$j\Delta$	$N_V(j)$
k	$k\Delta$	$N_V(k)$
Sections (i)		
1	0 to Δ	$N_V(1)$
2	Δ to 2Δ	$N_V(2)$
3	2Δ to 3Δ	$N_V(3)$
i	$(i - 1)\Delta$ to $i\Delta$	$N_V(i)$
k	$(k - 1)\Delta$ to $k\Delta$	$N_V(k)$

from 0 to Δ and from Δ to 2Δ). Particles of maximum size form sections of all groups on the plane of polish. Therefore, in specifying the number of sections per mm^2 , N_A , it is necessary to designate both the section size and the particle size from which the section was derived. The notation adopted is according to the scheme in Table A.1 where the index j designates the group of particles which form the given sections on the plane of polish and the index i refers to the size group of the section. For example, $N_A(2,3)$ indicates the number of sections of the second size group (diameters Δ to 2Δ) formed exclusively by particles of the third size group (diameter 3Δ). The total number of sections of the i th size group may be written

$$N_A(i) = \sum_{j=1}^k N_A(i,j) \quad (\text{A.1})$$

Saltykov determined the general expression relating the number of sections observed on the plane of polish in unit area to the number of spheres in unit volume. The basic equation he derived for this relationship is given by

$$N_A(i,j) = N_V(j) \Delta \left[\sqrt{j^2 - (i-1)^2} - \sqrt{j^2 - i^2} \right] \quad (\text{A.2})$$

When the particle distribution is represented by spheres with discrete sizes, equation (A.2) is applied separately to each size group. By successive substitution of integer values of j and i , the coefficients in equation (A.2), relating the N_A 's to the N_V 's are determined. This procedure leads to i equations for $N_A(i)$ in terms of $N_V(j)$ which can be solved simultaneously to give

$$N_v(j) = \frac{\alpha(i)N_A(i) - \alpha(i+1)N_A(i+1) - \dots - \alpha(k)N_A(k)}{\Delta} \quad (\text{A.3})$$

where i and j vary from 1 to k and $\alpha(i)$ are coefficients. These coefficients have been calculated by Saltykov and are given in Table A.2. Although the coefficients can be used for any number of groups up to 15, groups of less than seven are not recommended.

If the measured number of sections of the smallest sizes be too low, a negative number of particles may be indicated in unit volume in the smallest size group. For this reason, special care must be used in counting sections of the smallest sizes. This analysis can be extended to particles of different shapes.

Reference.

Underwood, E.E., in Quantitative Microscopy, (ed) DeHoff, R.T., and Rhines, F.N., p. 149. McGraw-Hill, New York (1968).

TABLE A.2 Saltykov's Table of Coefficients for Calculating Particle Distributions from Diameters.

Coefficients, $\sigma(\pm)$

	$N_A(1)$	$N_A(2)$	$N_A(3)$	$N_A(4)$	$N_A(5)$	$N_A(6)$	$N_A(7)$	$N_A(8)$	$N_A(9)$	$N_A(10)$	$N_A(11)$	$N_A(12)$	$N_A(13)$	$N_A(14)$	$N_A(15)$
$N_V(1)$	+1 0000	0 1547	0 0380	0 0130	0 0081	0 0033	0 0020	0 0013	0 0009	0 0006	0 0005	0 0004	0 0003	0 0002	0 0001
$N_V(2)$		+0 5774	0 1529	0 0420	0 0171	0 0087	0 0051	0 0031	0 0021	0 0015	0 0010	0 0009	0 0006	0 0006	0 0004
$N_V(3)$			+0 4472	0 1382	0 0408	0 0178	0 0093	0 0057	0 0037	0 0020	0 0018	0 0013	0 0010	0 0007	0 0007
$N_V(4)$				+0 3779	0 1260	0 0386	0 0174	0 0095	0 0058	0 0038	0 0027	0 0020	0 0016	0 0012	0 0009
$N_V(5)$					+0 3333	0 1161	0 0366	0 0168	0 0094	0 0059	0 0040	0 0028	0 0021	0 0016	0 0013
$N_V(6)$						+0 3015	0 1081	0 0346	0 0163	0 0091	0 0058	0 0041	0 0028	0 0022	0 0016
$N_V(7)$							+0 2773	0 1016	0 0320	0 0155	0 0090	0 0057	0 0040	0 0029	0 0022
$N_V(8)$								+0 2582	0 0961	0 0319	0 0151	0 0088	0 0056	0 0039	0 0028
$N_V(9)$									+0 2425	0 0913	0 0301	0 0146	0 0085	0 0055	0 0039
$N_V(10)$										+0 2294	0 0872	0 0290	0 0140	0 0083	0 0054
$N_V(11)$											+0 2182	0 0236	0 0280	0 0130	0 0050
$N_V(12)$												+0 2085	0 0801	0 0270	0 0132
$N_V(13)$													+0 2000	0 0776	0 0261
$N_V(14)$														+0 1925	0 0750
$N_V(15)$															+0 1857
N_V	1 0000	0 4227	0 2583	0 1847	0 1433	0 1170	0 0988	0 0856	0 0753	0 0672	0 0610	0 0553	0 0511	0 0472	0 0441

A.2 Computer Program for Calculation of Nearest-Neighbour Distance for Finite Size Spheres (Bansal & Ardell)

In order to compute the nearest-neighbour distance from equation (1.29), a FORTRAN computer program was written as follows:

```

HWCG.                                                                 GREEN.D.J.
      EXTERNAL FCT
      COMMON/NAME 1/W,PI,IERMAX
      PI = 3.14159265
      Y = 0.01
      DO 100 I = 1,20
C      CALC. VOL. FRACTION
      V = Y*I
C      CALC. UPPER INTEGRATION LIMIT
      W = 6*V
C      CALC. LOWER INTEGRATION LIMIT
      ZERO = 0.0
C      CALL SUBROUTINE FOR NUMERICAL INTEGRATION (SSP LIBRARY
C      FCT = EXTERNAL FUNCTION, DEL = VALUE OF INTEGRAL
      CALL QG10 (ZERO,W,FCT,DEL)
C      RADIUS OF SPHERE = R
      R = 66.0
C      CALC. NEAREST NEIGHBOUR DISTANCE (DELTA)
      DELTA = R*((PI/2)+(DEL/(12*V)))
      WRITE (6,1000) V,DELTA,IERMAX
1000  FORMAT (2E20.5,F5.0)
C      IERMAX IS AN ERROR INDICATOR
100  CONTINUE
      STOP
      END
C      EXTERNAL FUNCTION FOR NUMERICAL INTEGRATION
      FUNCTION FCT(X)
      COMMON/NAME 1/W,PI,IERMAX
C      P IS INPUT GAMMA PARAMETER
      P = 0.5
      IERMAX = 0.0
C      CALL SUB ROUT. TO CALC. INCOMPLETE GAMMA FUNCTION, X IS VALUE
      TO WHICH GAMMA IS TO BE INTEG., PROB IS INTEGRAL VALUE (IMSL LIB)
      CALL MDGAM (X,P,PROB,IER)
      IF (IER.GT.IERMAX) IERMAX = IER
C      CALC. FCT(X), GAMMA(1/2) = SQRT PI
      ECT = SQRT(PI)*(1-PROB)
      FCT = ECT*EXP(X)/SQRT(W-X)
      RETURN
      END

```

A.3 Formation of Fracture Surface Steps

The atomically flat fracture surface is an ideal that is rarely approached in the fracture of brittle solids. Generally, the fracture surfaces exhibit a complex pattern of surface markings that are a visual record of the crack front disturbances. These local disturbances may enhance the stress concentration at the crack tip and hence lead to subsurface deformation. A most prevalent feature is the fracture surface step or cleavage step. These steps form when a crack front advances through a solid on more than one plane and as the material separates across the fracture interface, secondary fractures must occur between adjacent crack planes to produce a stepped crack profile. The steps thus formed lie closely parallel to the direction of the primary crack propagation.

The origin of these disturbances are manifold and some of the better known are as follows:

- (i) segmentation of the primary crack in order to by-pass an inclusion. The segmented cracks change plane as they interact with the stress field of the particles so that when they reach the rear of the particle they are non-coplanar and necessitate the secondary fracture to complete failure. The steps thus formed are sometimes referred to as fracture 'tails'.
- (ii) the main crack may form by the coalescence of a number of smaller cracks initiating from non-coplanar sources.
- (iii) a crack approaching its terminal velocity will tend to bifurcate onto adjacent planes.

(iv) an originally smooth crack experiencing a shear stress parallel to its front will tend to accommodate the disturbance by segmenting into partial fronts separated by 'lance-like' steps.

(v) a cleavage crack generally suffers a twist on intersecting a grain boundary and also segments.

(vi) Interaction of a cleavage crack with dislocations can produce microsteps which subsequently amalgamate into a 'river pattern' of macroscopic steps.

The formation of these steps locally impedes the motion of the crack and the separation mechanism will require the expenditure of extra fracture energy if only to create new surface area at the stress riser.

Swain et. al. have considered the stress state during step formation in order to identify the manner in which the material separates. In their work, they represented the process by considering the interaction of mutually opposed non-coplanar edge cracks. This is shown in Figure A.1 and they considered the growth of one crack in the stress field of the other crack. The stress field for crack 1 is given by equation (2.7). The stress intensity factors for crack 2 loaded by this stress field is given by

$$K_I \approx \left(\frac{2}{\pi}\right)^{1/2} \int_{x_c}^{\infty} \frac{\sigma_{yy}(x, y_c) dx}{(x-x_c)^{1/2}} + k_I^0$$

$$K_{II} \approx \left(\frac{2}{\pi}\right)^{1/2} \int_{x_c}^{\infty} \frac{\sigma_{xy}(x, y_c) dx}{(x-x_c)^{1/2}} \quad (A.4)$$

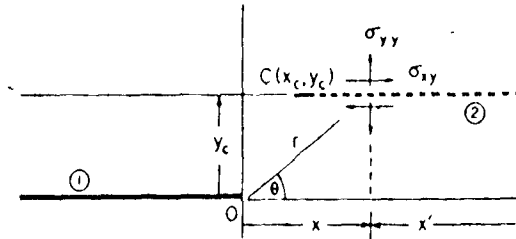


Figure A.1 Mutually Opposed Edge Cracks in Tensile Loading. Crack 1 is Pre-Existent at Tip Position 0; Crack 2 at Tip Position C advances through the Field of Crack 2.

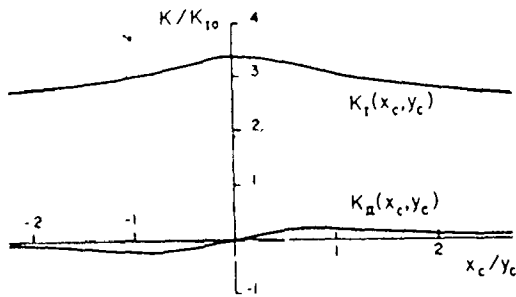


Figure A.2 Stress Intensity Factors for Crack 2 as a Function of the Tip-Separation Co-Ordinate x_c .

The solution is shown in Figure A.2 and illustrates the magnitude of the interaction. K_I is shown to be dominant as the cracks approach. It is also seen that there is a mode II contribution which tends to alter the crack path. This tendency should manifest itself as an initial repulsion and then attraction of crack 2 to crack 1. The ratio of K_{II}/K_I is, however, very small and may not be sufficient to deflect the crack until there is considerable overlap. For cleavage fractures, changes in crack path may be even more difficult.

From their work, Swain et. al. consider the most likely step separation mechanism will be one where there is a considerable overlap and this mechanism is consistent with many fractographic and X-ray diffraction microscopy observations.

The stresses which occur during overlap have been discussed by Lange in his photoelastic study. This work indicates the tendency for attraction between the cracks increases as the overlap increases. For conchoidal fractures, the two cracks will deviate from their symmetry planes till one or both connect. This process should be more difficult for cleavage fractures. In this case, greater overlap should occur until the resolved tensile stresses on orthogonal cleavage planes are sufficient to cause failure.

References

- Swain, M.V., Lawn, B.R., and Burns, S.J., J. Mater. Sci., 9 (1974) 175.
Lange, F.F., Int. J. Fract., 4 (1968) 287.

A.4 Stress Fields around Cylindrical and Spherical Inclusions.

Second phase inclusions in an elastic matrix give rise to a stress field around the inclusions due to the differences in elastic properties between the matrix and the inclusion. This stress field can interact with nearby defects such as cracks and lead to substantial influences on crack nucleation and growth.

Goodier has solved the equations of elasticity for cylindrical and spherical inclusions subjected to a uniform tensile stress at infinity in an elastic matrix. The matrix is assumed to be infinite in extent, ideally elastic, isotropic and homogeneous. Similar restrictions also apply to the inclusion except that it is assumed small. The elastic disturbance is confined to the neighbourhood of the inclusion and it was found that at about 4 diameters away from the inclusion, the perturbation to the stress field is less than 1%. In consequence, the results are valid for inclusions at least 4 diameters or more away from a boundary or from other inclusions or flaws. In polycrystalline materials, the solution will be only valid only when the inclusion size is large compared to the grain size. The solutions were found to be independent of inclusion size but dependent on inclusion shape. Goodier produced solutions for cylindrical and spherical inclusions.

A.4.1 Cylindrical Inclusions.

The solutions to the elasticity equations for cylindrical inclusions under plane stress or plane strain are given by

$$\begin{aligned}
\sigma_{rr} &= 2G_m \left\{ \frac{-A}{r^2} + \left[\frac{3B}{r^4} - \frac{2C}{r^2} \right] \cos 2\theta \right\} + \frac{\sigma_A}{2} (1 + \cos 2\theta) \\
\sigma_{\theta\theta} &= 2G_m \left\{ \frac{A}{r^2} - \frac{3B}{r^4} \cos 2\theta \right\} + \frac{\sigma_A}{2} (1 - \cos 2\theta) \\
\sigma_{r\theta} &= 2G_m \left\{ \left(\frac{3B}{r^4} - \frac{C}{r^2} \right) \sin 2\theta \right\} - \frac{\sigma_A}{2} \sin 2\theta
\end{aligned} \tag{A.5}$$

where

$$\begin{aligned}
A &= \frac{\sigma_A a^2}{4G_m} \left\{ \frac{(1 - 2\nu_p) G_m - (1 - 2\nu_m) G_p}{(1 - 2\nu_p) G_m + G_p} \right\} \\
B &= \frac{\sigma_A a^4}{4G_m} \left\{ \frac{G_m - G_p}{G_m + (3 - 4\nu_m) G_p} \right\} \\
C &= \frac{\sigma_A a^2}{2G_m} \left\{ \frac{G_m - G_p}{G_m + (3 - 4\nu_m) G_p} \right\}
\end{aligned} \tag{A.6}$$

G_m and G_p are the shear moduli of the matrix and the inclusion respectively and the co-ordinate system is shown in Figure A.3. The solution for the displacement fields are also available in Goodier's original paper. For cylindrical voids a maximum elastic stress concentration of 3 occurs at $\theta=90^\circ$ and $r=a$ in $\sigma_{\theta\theta}$.

A.4.2 Spherical Inclusions.

The stress field for a spherical inclusion is given by

$$\begin{aligned}
\sigma_{rr} &= 2G_m \left\{ \frac{2A}{r^3} - \frac{2\nu_m}{1-2\nu_m} \left(\frac{C}{r^3} \right) + \frac{12}{r^5} \frac{B}{r^5} + \left[\frac{-2(5-\nu_m)}{1-2\nu_m} \frac{C}{r^3} + \frac{36}{r^5} \frac{B}{r^5} \right] \cos 2\theta \right\} \\
&\quad + \frac{\sigma_A}{2} (1 + \cos 2\theta) \\
\sigma_{\theta\theta} &= 2G_m \left\{ \frac{-A}{r^3} - \frac{2\nu_m}{1-2\nu_m} \left(\frac{C}{r^3} \right) - \frac{3B}{r^5} + \left[\frac{C}{r^3} - \frac{21B}{r^5} \right] \cos 2\theta \right\} + \frac{\sigma_A}{2} (1 - \cos 2\theta) \\
\sigma_{r\theta} &= 2G_m \left\{ -\frac{2(1+\nu_m)}{1-2\nu_m} \left(\frac{C}{r^3} \right) + \frac{24B}{r^5} \right\} \sin 2\theta - \frac{\sigma_A}{2} \sin 2\theta \\
\sigma_{\psi\psi} &= -(\sigma_{rr} - \sigma_{\theta\theta})
\end{aligned} \tag{A.7}$$

where

$$\begin{aligned}
A &= \frac{-\sigma_A a^3}{8G_m} \left[\frac{G_m - G_p}{(7-5\nu_m)G_m + (8-10\nu_m)G_p} \right] \frac{(1-2\nu_p)(6-5\nu_m)2G_m + (3+19\nu_p - 20\nu_m\nu_p)G_p}{(1-2\nu_p)2G_m + (1+\nu_p)G_p} \\
&\quad + \frac{\sigma_A a^3}{4G_m} \left(\frac{((1-\nu_m)(1+\nu_p)/(1+\nu_m) - \nu_p)G_p - (1-2\nu_p)G_m}{(1-2\nu_p)2G_m + (1+\nu_p)G_p} \right)
\end{aligned}$$

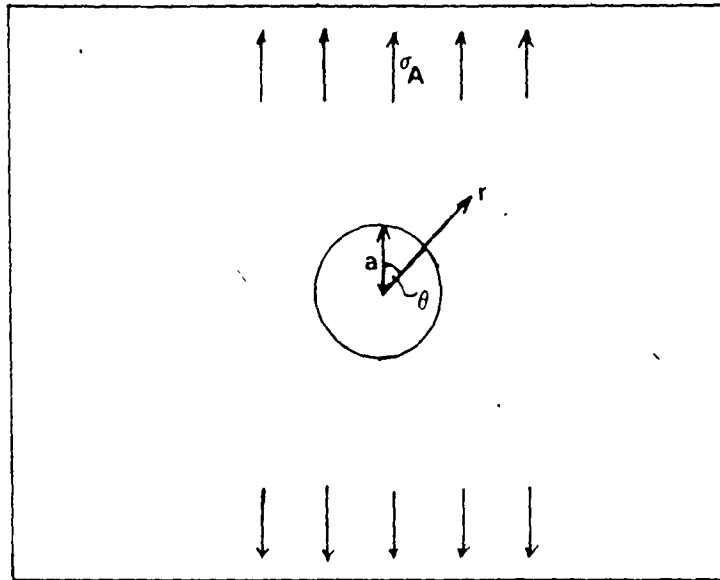


Figure A.3 Co-ordinate System Used in Stress Analysis Solution for Cylindrical Inclusion.

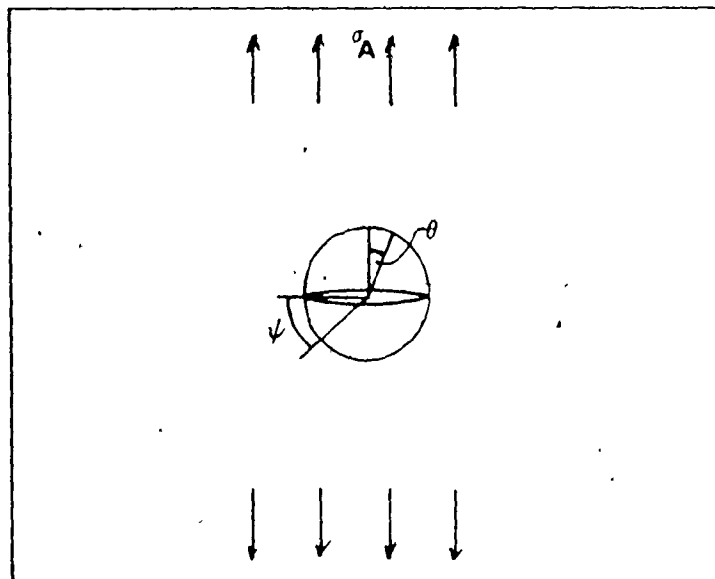


Figure A.4 Co-ordinate System Used in Stress Analysis Solution for Spherical Inclusion.

$$\begin{aligned}
 B &= \frac{\sigma_A}{8G_m} a^5 \left\{ \frac{G_m - G_p}{(7-5\nu_m)G_m + (8-10\nu_m)G_p} \right\} \\
 C &= \frac{\sigma_A}{8G_m} a^3 \left\{ \frac{5(1-2\nu_m)(G_m - G_p)}{(7-5\nu_m)G_m + (8-10\nu_m)G_p} \right\}
 \end{aligned} \tag{A.8}$$

The co-ordinate system is shown in Figure A.4. For $\nu_m = 1/3$, the maximum elastic stress concentration for a spherical void is given by

$\sigma_{\theta\theta} = 2 \frac{1}{16} \sigma_A$ along the equator of the void. The displacement fields are given in the original Goodier paper.

A.4.3 Stress Contours.

To illustrate these solutions, iso-stress contours have been drawn using a computer for the two systems of relevance to this thesis, i.e., a glass-void system and the S glass-nickel system. To simplify the procedure, only cylindrical inclusions have been considered. The data for the elastic constants were taken from the work of Stett and Fulrath (Ref. 74). The stress contours are shown in Figures A.5 to A.9.

The solutions for cylindrical inclusions have also been discussed by Muskhelishvili and this work also includes the effect of misfit stress fields. Southwell and Gough have treated the case of spherical cavities.

References.

1. Goodier, J. N., J. Appl. Mech. Trans. ASME, 55A (1933) 39
2. Muskhelishvili, N. I., Some Problems of the Mathematical Theory of Elasticity, p210, Noordhoff, Holland (1953)
3. Southwell, R. V., and Gough, H. J., Phil. Mag.; 1 (1926) 71

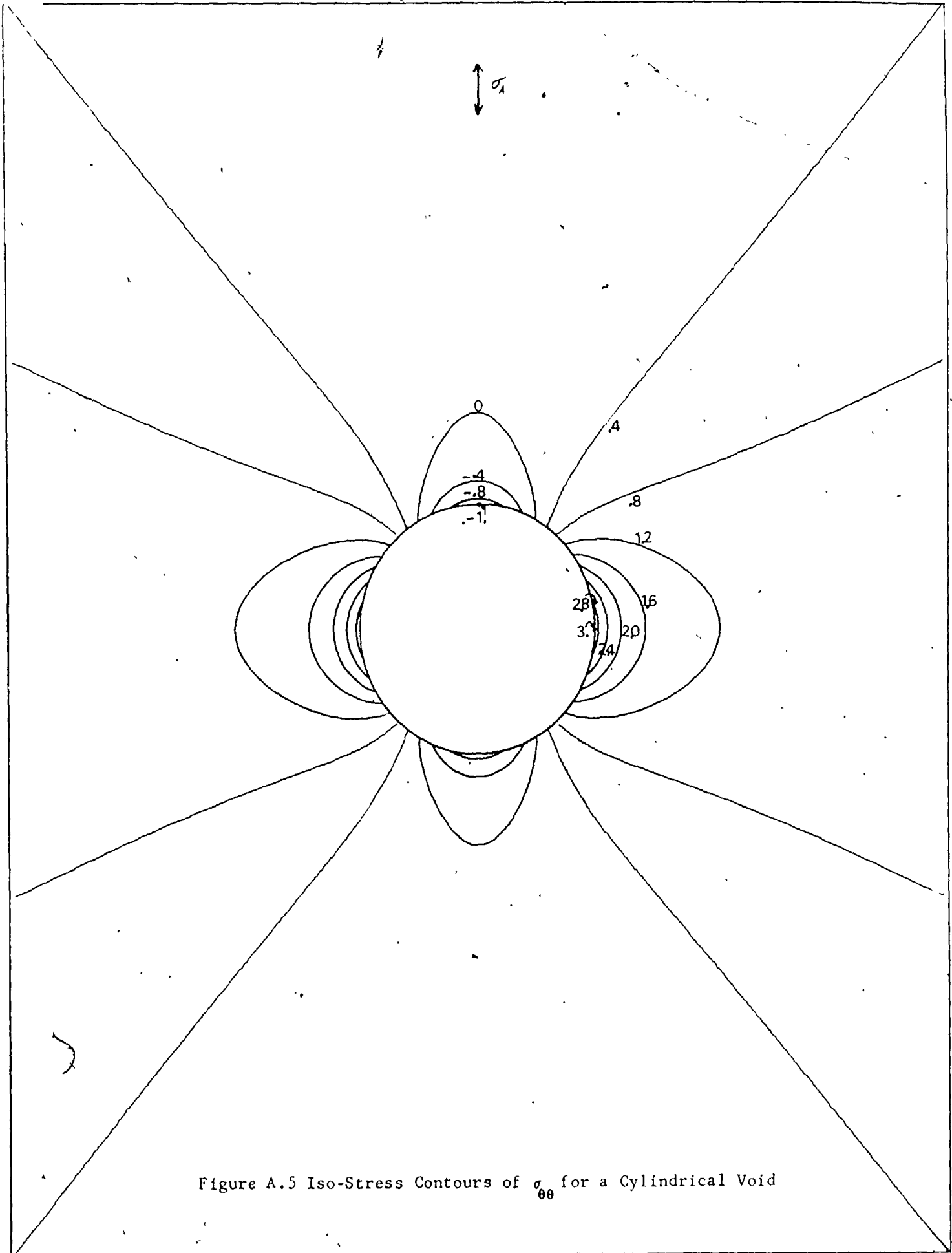


Figure A.5 Iso-Stress Contours of σ_{00} for a Cylindrical Void

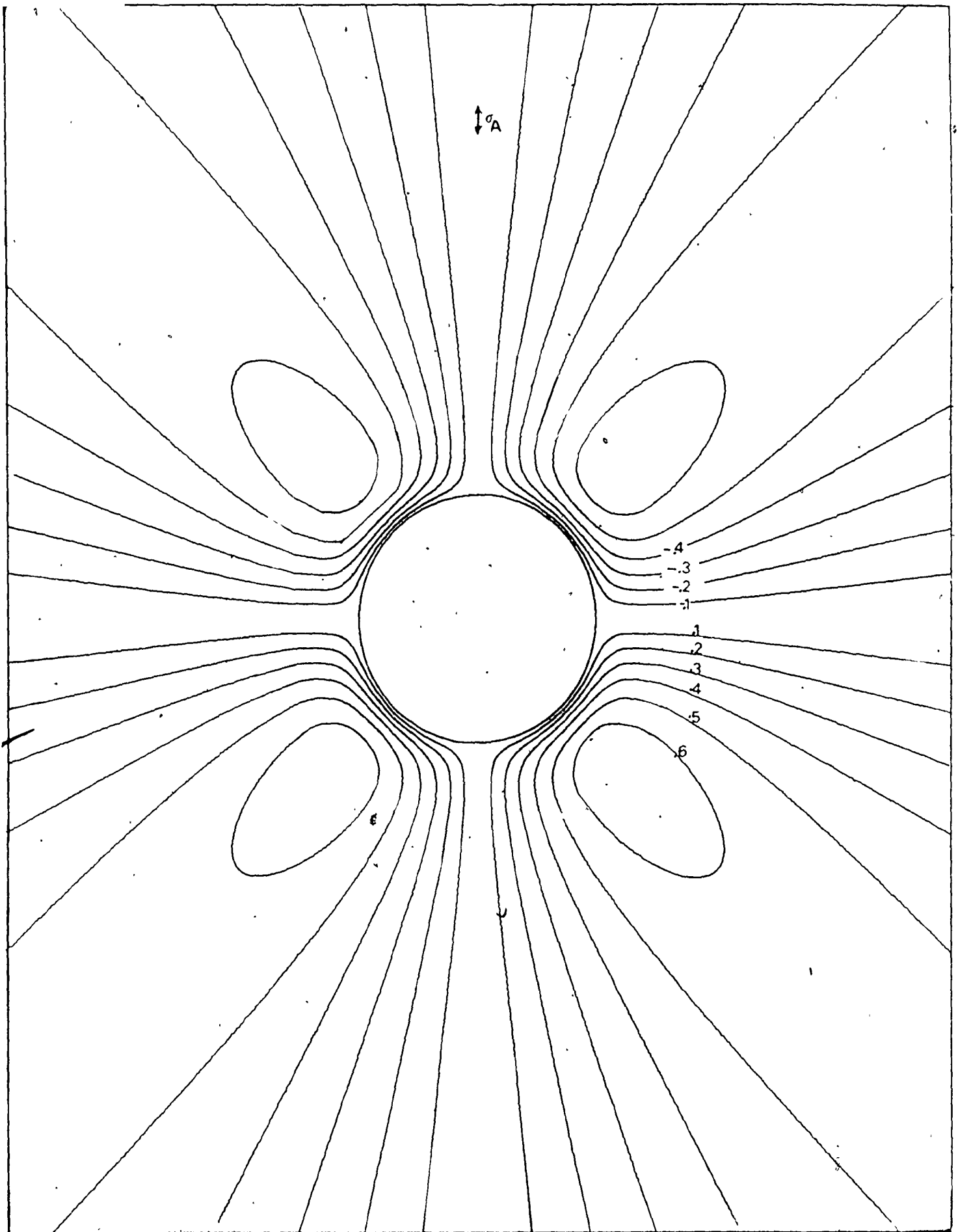


Figure A.6 Iso-Stress Contours of σ_{r0} for a Cylindrical Void.

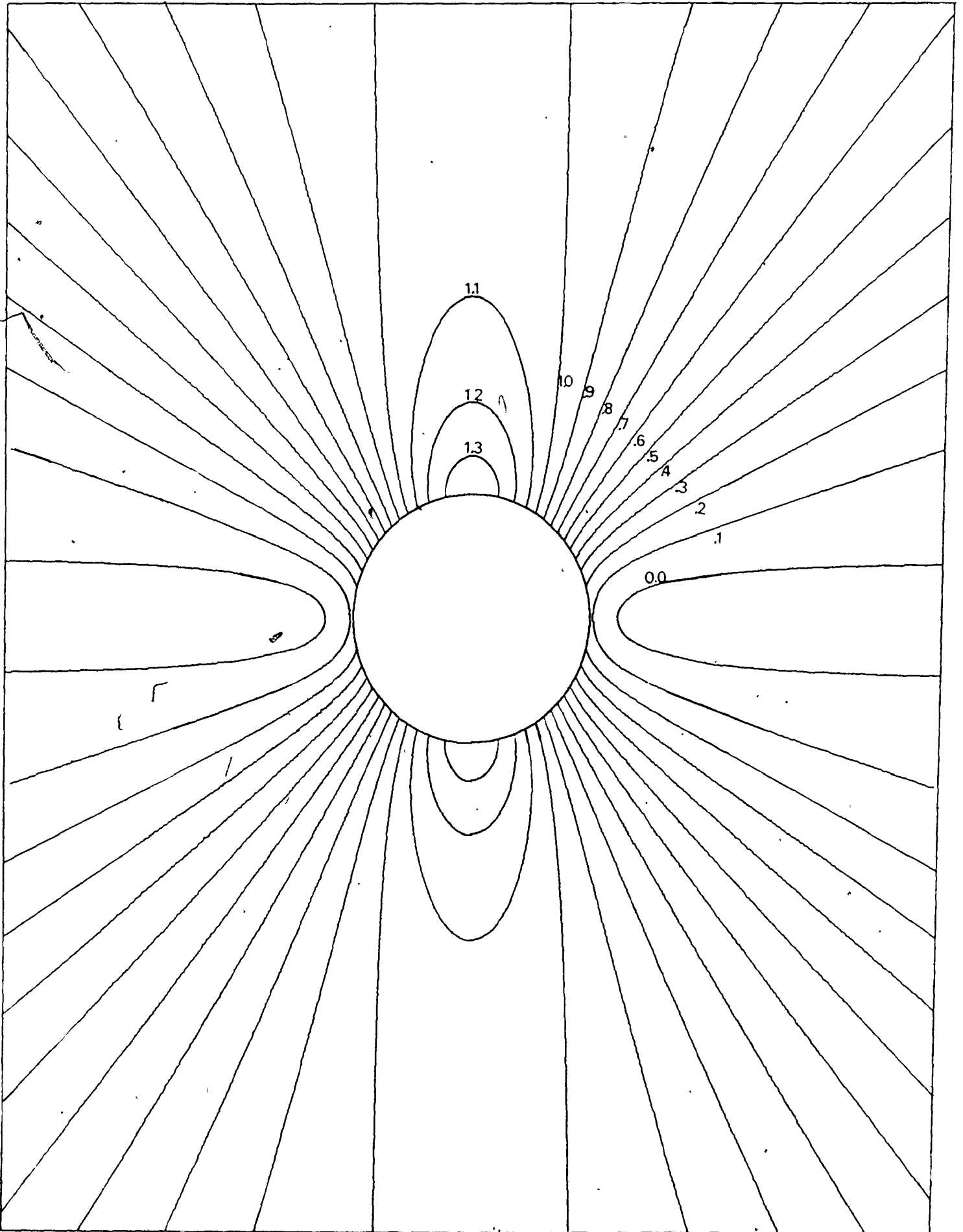


Figure A.7 Iso-Stress Contours of σ_{rr} for a Cylinder in S.C.I.a

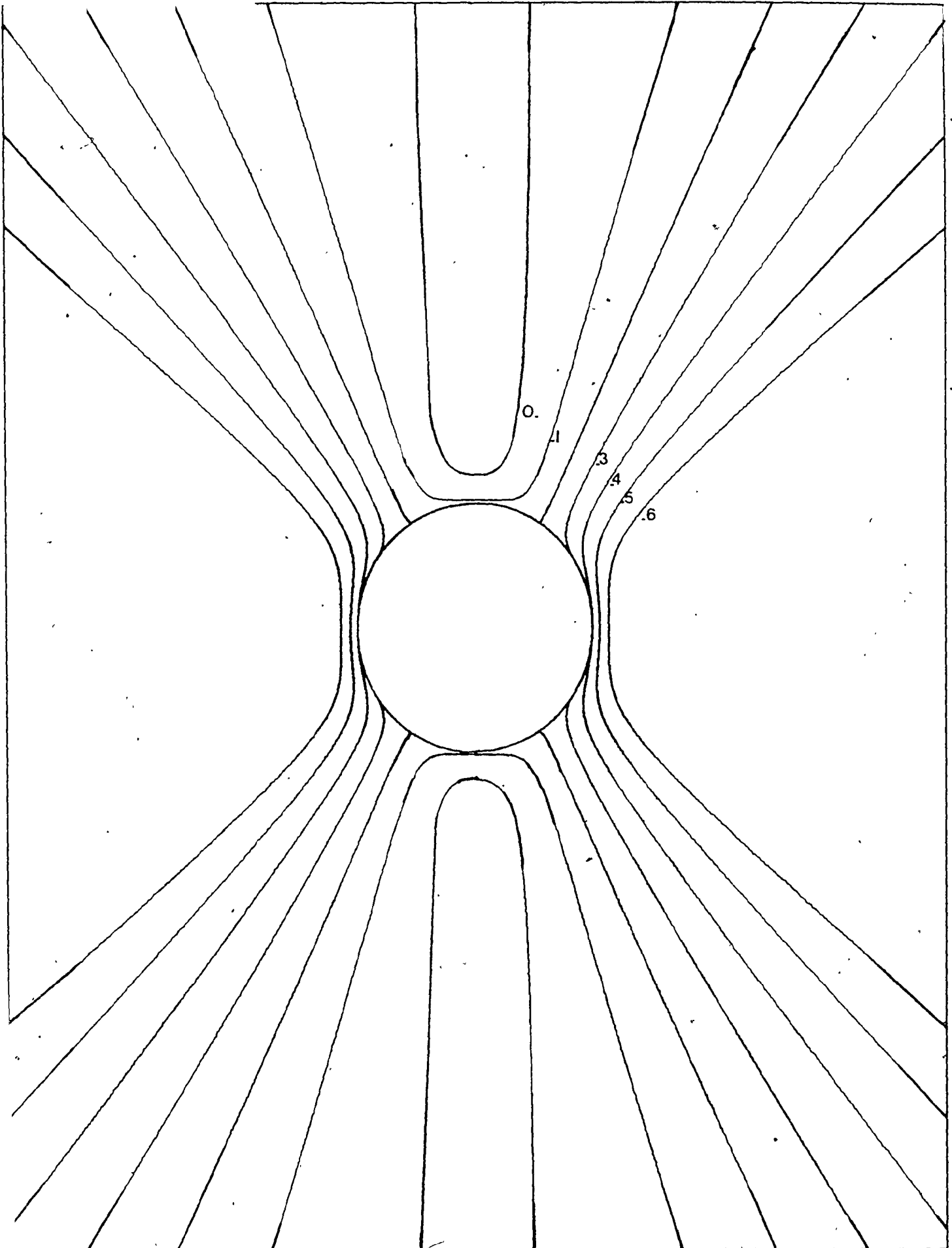


Figure A.8 Iso-Stress Contours of σ_{00} for a Nickel Cylinder in

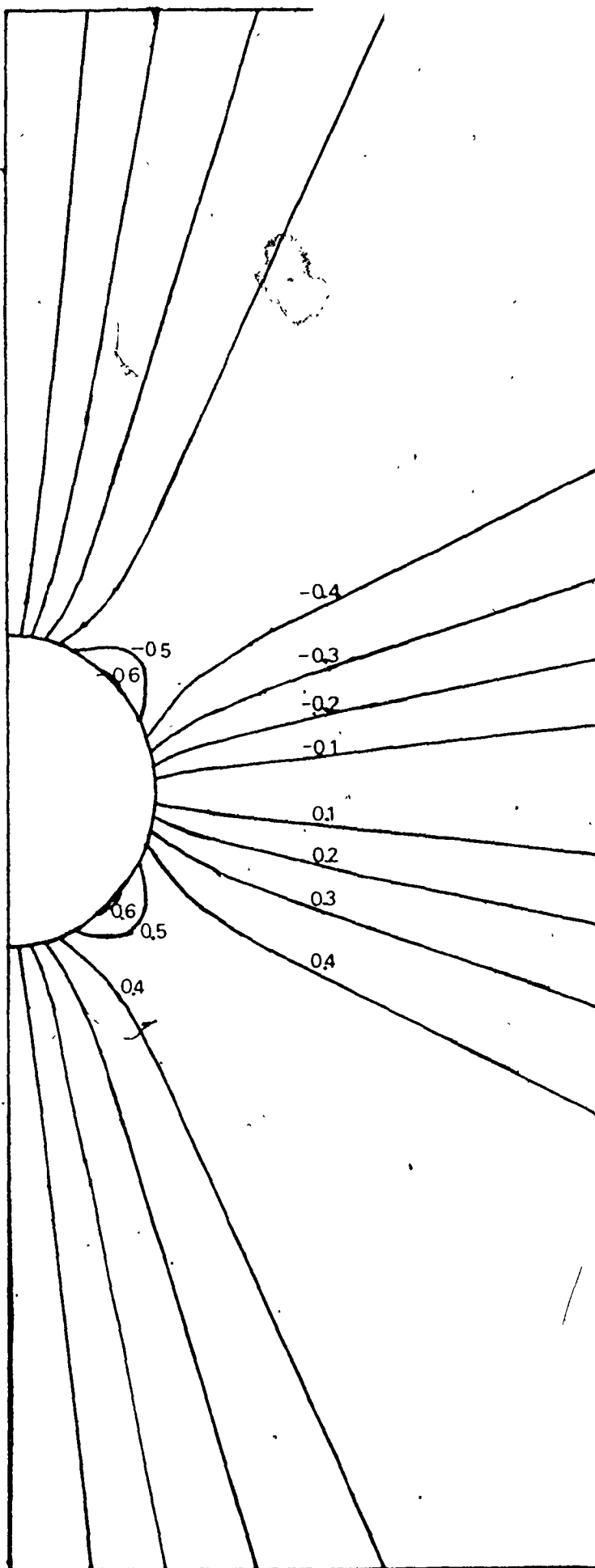


Figure A.9 Iso-Stress Contours ($\sigma_{r\theta}$) for Ni Cylinder

A.5 Microcrack Zones

Brittle materials often contain weak interfaces and when subjected to the high stresses in the vicinity of the crack tip, these interfaces may fail. Thus a microcrack zone is produced near the crack tip. This process effectively increases the opening displacement needed for fracture and as such may be an important energy absorption mechanism in brittle materials.

A theoretical model was developed to describe this dissipative process by assuming that the interface will fail when the stress normal to the interface reaches some critical value (σ_T) as illustrated in Figure A.10. For grain boundary cracking, the formation of the cracks will depend on the orientation of the boundary but the limit of this cracking will be defined by the iso-stress contour for the greater principal stress ($=\sigma_T$) as shown in Figure A.11.

For particulate composites, the interface between the matrix and the particle may also be a source of weakness leading to a decohesion zone near the crack tip when a stress is applied. In this case, provided the particles are small, there should always be some part of each particle interface (within the zone) normal to the greater principal stress. It can be considered to a first approximation that all the particles within the zone will decohere. For large particles, the situation is more complicated and some particles may only partially decohere. The decohesion problem for an inclusion subjected to a uniform tensile stress has been discussed by Sundstrom and he shows

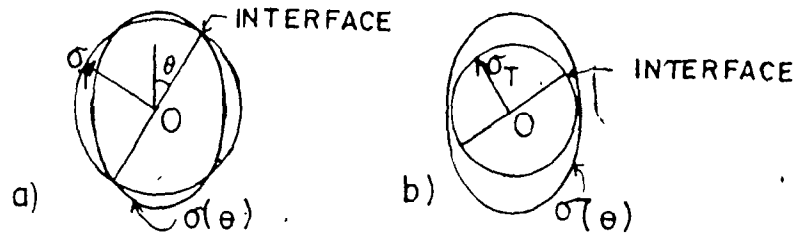


Figure A.10 Schematic Representation of Stress Variation around a Point O ($\sigma(\theta)$) and the Stress Needed to Break an Interface (σ_T) that Lies at an Angle θ to the Applied Stress. a) Interface Not Failed b) Interface Failed.

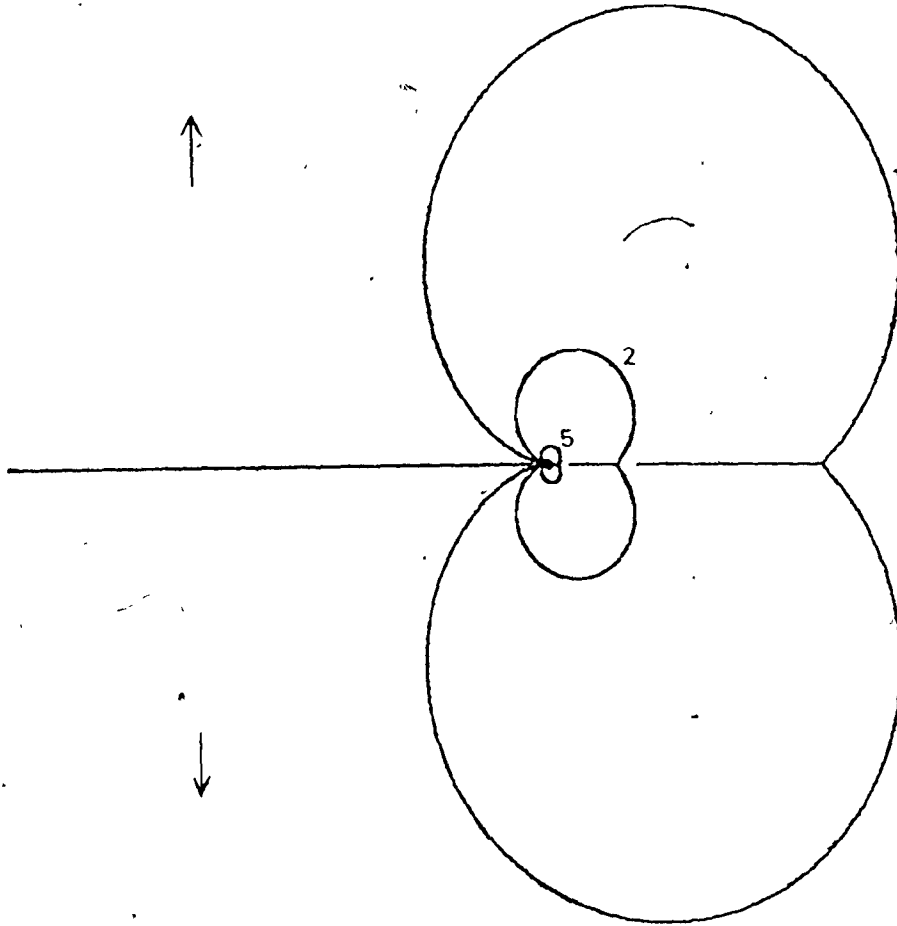


Figure A.11 Iso-Stress Contours for the Greater Principal Stresses around a Crack Tip.

that the interfacial crack may arrest before the particle is completely decohesed. In the vicinity of crack tips, the stress field is triaxial so that complete decohesion is more likely.

The theoretical model was submitted and accepted for publication. A copy is included with this appendix.

The formation of microcracks in a material is generally reflected in anomalously low elastic moduli, hysteresis effects in many mechanical properties, increased permeability, low notch sensitivity, low thermal diffusivity, good thermal shock resistance and low strength. A similar concept to the model has been adopted for polymeric materials where crazes are observed to form along the minor principal stress trajectories, i.e., normal to the major principal stress.

References

- Sundstrom, B., Engg. Fract. Mech., 6 (1974) 483.
Hoagland, R.G., Embury, J.D., and Green, D.J., Scripta. Met. 9 (1975) 907.
Green, D.J., M.Sc. Thesis, McMaster University, Hamilton (1972).

PREVIOUSLY COPYRIGHTED MATERIAL IN

A.5., LEAVES 388-390, AND A.6.2.-A.6.9.,

LEAVES 392-398, NOT MICROFILMED.

- A.5. On the Density of Microcracks Formed During the Fracture of Ceramics, by R.G. Hoagland, Battelle, Columbus Laboratories, Columbus, Ohio, U.S.A., and J.D. Embury and D.J. Green, McMaster University, Hamilton, Ontario, Canada. Scripta METALLURGICA, Vol. 9, pp. 907-909, 1975.
- A.6.2. Forwood, C.T., Phil. Mag., 17 (1968) 657
- A.6.3. Wambach, A., Trachte, K., and DiBenedetto, A., J. Comp. Mater., 2 (1968) 266.
- A.6.4. Lange, F.F., and Radford, K.C., J. Mater. Sci., 6 (1971).
- A.6.5. Broutman, L.J., and Sahu, S., Mater. Sci. Engg., 8 (1971) 98.
- A.6.6. Mallick, P.K., and Broutman, L.J., Mater. Sci. Engg., 18 (1975) 63.
- A.6.7. Hing, P., Proc. Brit. Ceram. Soc., No. 25 (1975) 13.
- A.6.8. Hing, P., and Groves, G.W., J. Mater. Sci., 7 (1972) 427.
- A.6.9. Hing, P., and Groves, G.W., J. Mater. Sci., 7 (1972) 422.

A.6 Fracture of Brittle Particulate Composites

There has been numerous studies on the fracture of brittle particulate composites and some of these works will be briefly reviewed here.

A.6.1 R.M. Fulrath and Co-workers (Berkeley)

This group at Berkeley has studied the strength and Young's modulus of many model glass-crystal and glass-pore systems as a function of particle size, volume fraction, internal stress and interfacial bonding. The elastic constant data for these systems were shown to agree with theoretical predictions. The strength variation for these systems was postulated to be controlled by the particles acting to limit the size of the critical flaw and by the size of the particle or void compared to the critical flaw size. Much of this work was reviewed by Hasselman and Fulrath (Ceramic Microstructures, Wiley, New York (1968)) and the work was extended by Bertolotti and Fulrath (J. Am. Ceram. Soc., 50 (1967) 558), Stett and Fulrath (J. Am. Ceram. Soc., 53 (1970) 5, and Nivas and Fulrath (J. Am. Ceram. Soc., 53 (1970) 188.

For the majority of this work, no attempt was made to measure the fracture surface energy and so in a sense the ideas are incomplete. The postulate that the particles act to reduce the critical flaw size has been criticized by many workers, who have shown that the particle can increase the critical flaw size by acting as sites for crack nucleation.

An attempt was recently made by Bishwas and Fulrath (J. Am. Ceram. Soc., 58 (1975) 526) to measure some of the fracture surface energy values and it was shown that the γ values increased for a glass-nonspherical Al_2O_3 system but not for a glass-spherical W system.

Other References (not referred to in thesis or this appendix)

1. Forward, C.T., and Forty, A.J., *Phil. Mag.*, 11 (1965) 1067.
2. Radford, K.C., *J. Mater. Sci.*, 6 (1971) 1286.
3. Bethge, H., *Phys. Status Solidi*, 2 (1962) 814.
4. Frey, W.J., and MacKenzie, J.D., *J. Mater. Sci.*, 2 (1967) 124.
5. Veevers, K., and Rotsey, W.B., *J. Mater. Sci.*, 1 (1966) 346.
6. Miyata, N., and Jinno, H., *J. Mater. Sci.* 7 (1972) 973.
7. Sahu, S., and Broutman, L.J., *Polym. Engg. Sci.*, 12 (1972) 91.
8. Brassell, G.W., and Wischmann, K.B., *J. Mater. Sci.* 9 (1974) 307.
9. Tummala, R.R., and Friedberg, A.L., *J. Am. Ceram. Soc.*, 52 (1969) 228.
10. Gupta, T.K., *J. Mater. Sci.*, 9 (1974) 1585.
11. Agarwal, B.D., Panizza, G.A., and Broutman, L.J., *J. Am. Ceram. Soc.*, 54 (1971) 620.
12. Nielsen, L.E., *J. Appl. Polym. Sci.*, 10 (1966) 97.
13. Groves, G.W., in *Strengthening Methods in Crystals* (ed.) Kelly, A., and Nicholson, R.B., p. 403, Halsted Wiley Press (1971).
14. Mendelson, M.I., and Fine, M.E., in *Fracture Mechanics of Ceramics*, Vol. 2, ed. Bradt, R.C., et. al. p. 527, Plenum Press, New York (1974).
15. Bansal, G.K., and Heuer, A.H., *ibid*, p. 677.

A.7 Re-analyses of the Evans' Model

A. G. EVANS, *Phil. Mag.*, 26 (1972) 1327

Evans has taken a fracture mechanical approach to the interaction of a crack front with a linear array of impenetrable obstacles (Figure A.12). In his calculations, he considers the stress needed to propagate the primary crack (σ_c) and the stress needed to propagate secondary cracks between the obstacles (σ_a). For a contribution of this mechanism to the fracture toughness of the composite, $\sigma_a > \sigma_c$. Evans analyses three situations, where the secondary cracks are assumed to be

- (i) semi-circular and non-interacting
- (ii) semi-elliptical and non-interacting
- (iii) semi-elliptical and interacting.

Within the approximations of his model, there are several criticisms that can be made.

A.7.1 Semi-circular, Non-interacting Secondary Cracks.

Evans used the analysis derived by Sack, in which it is shown that a flat semi-circular crack, orthogonal to an applied stress (σ) increases the elastic energy of a system (U) by

$$U = - \frac{2aC^3}{3G} \int_0^{\pi/2} \sigma^2 \sin\theta \, d\theta \quad (\text{A.9})$$

where G is the bulk modulus, a is a constant such that $a/G = 4(1-\nu^2)/E$ and θ is an oblate spheroidal co-ordinate.

In order to calculate the stress applied to the secondary crack at breakaway, an assumption must be made about the position of

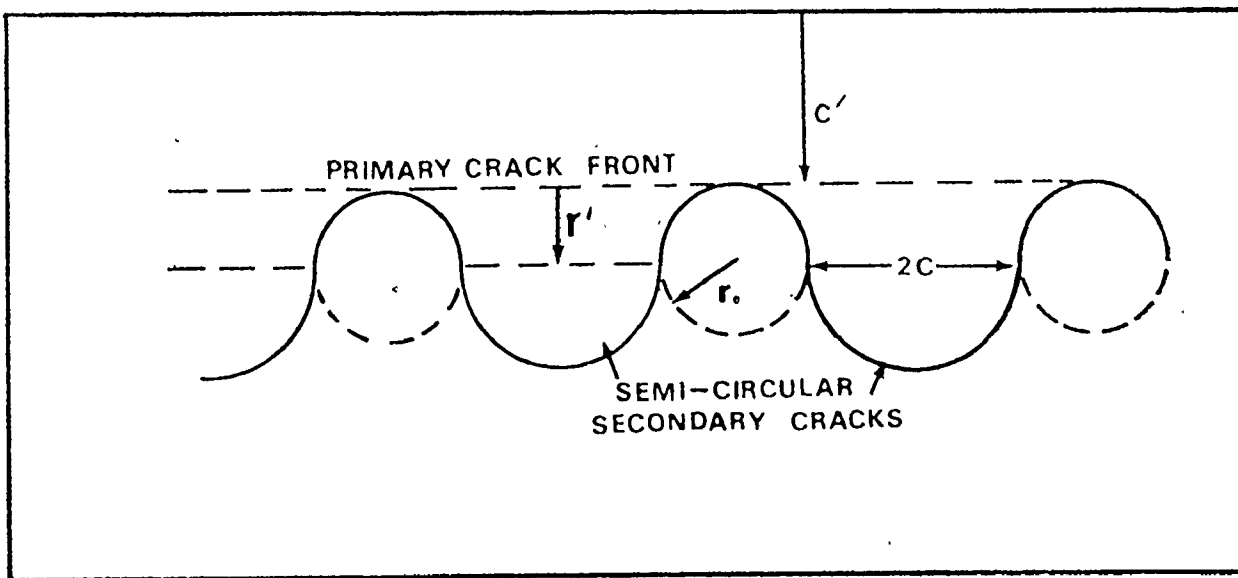


Figure A.12 Model Used by Evans for the Interaction of a Crack with an Array of Impenetrable Obstacles.

maximum stress. Evans assumes that the maximum stress occurs at breakaway, i.e., once the origin of the secondary crack has extended beyond the obstacle ($r' = 2r_0$). This assumption is questionable and it may be that the maximum stress position is a function of obstacle shape and the amount of interaction between the secondary cracks. These points will be amplified later but initially only rectangular obstacles will be treated (Figure A.12). In this case there is no change in the interparticle spacing ($2C$) as the secondary cracks move. With Evans' assumption about the maximum stress position, the origin of the secondary cracks will then be at $r' = 2r_0$. In his mathematics, however, he bases his calculation on $r' = r_0$. This error reduces the magnitude of his theoretically predicted 'line tension' effects.

An attempt was made to reproduce Evans' results without defining the maximum stress position, using $r' = \beta r_0$, where β is a constant with values between 0 and 2 and represents the strength of the pinning forces. The value $\beta = 1$ corresponds to the Evans' calculation. In this way failure of the obstacle or a maximum stress position before $r' = 2r_0$ can be introduced into the calculation. Considerable effort was made to make the analysis, which involves numerical integration of double integrals and their derivatives as accurate as possible. The results and implications of this re-analysis differ slightly from those of Evans. The origin of these differences is not clear.

The first step in the Evans' calculation is to calculate the stress acting on the secondary crack. The stress ahead of the main crack and orthogonal to its plane (σ_{yy}) is given by

$$\sigma_{yy} = \sigma_a^s (1 + C'/2x')^{\frac{1}{2}} \quad (\text{A.10})$$

provided x' is much larger than the crack tip radius. At the maximum stress position, this equation becomes

$$\sigma_{yy} = \sigma_a^s \left[1 + \frac{C'}{2r' + 2x_2} \right]^{\frac{1}{2}} \quad (\text{A.11})$$

$$= \sigma_a^s \left[1 + \frac{C'}{2r' + 2C \sin \theta \sin \beta} \right]^{\frac{1}{2}} \quad (\text{A.12})$$

provided r' is greater than the dimensions of the plastic zone. Evans then shows the mean stress acting over the secondary crack ($\bar{\sigma}$) is given by

$$\bar{\sigma} = \frac{2\sigma_a^s}{\pi} (H(C, \theta, \beta)) \quad (\text{A.13})$$

$$\text{where } H(C, \theta, \beta) = \int_0^{\pi/2} \left[1 + \frac{C'}{2r' + 2C \sin \theta \sin \beta} \right]^{\frac{1}{2}} d\beta \quad (\text{A.14})$$

This stress when substituted into equation (A.9) gives an increase in elastic energy of

$$U = \frac{-8aC^3 (\sigma_a^s)^2}{3\pi^2 G} \int_0^{\pi/2} (H(C, \theta, \beta))^2 \sin \theta d\theta - U_0 \quad (\text{A.15})$$

where U_0 is the contribution to strain energy for the crack surfaces between the obstacles.

In order to calculate the stress for crack extension from C to $(C + dC)$, the equilibrium condition can be used, i.e.,

$$-\frac{dU}{dC} \geq 4\pi C \Gamma \quad (\text{A.16})$$

Differentiation of equation (A.15) and substitution into equation

(A.16) gives

$$\left(\frac{\sigma_a^s}{\sigma_c} \right)^2 = \frac{3\pi^4}{8(3VF(C) + V^2 r' dF(C)/dC)} \quad (\text{A.17})$$

$$\text{where } F(C) = \int_0^{\pi/2} (H(C, \theta, \beta))^2 \sin\theta d\theta \quad (\text{A.18})$$

$$r' \frac{dF(C)}{dC} = \int_0^{\pi/2} \left[H(C, \theta, \beta) \cdot \int_0^{\pi/2} \left(1 + \frac{W}{1+V\sin\theta\sin\beta} \right)^{-\frac{1}{2}} \cdot \frac{\sin\theta\sin\beta}{(1+V\sin\theta\sin\beta)^2} d\beta \right] \sin\theta d\theta \quad (\text{A.19})$$

$$W = C'/2r' \quad \text{and } V = C/r' \quad (\text{A.20})$$

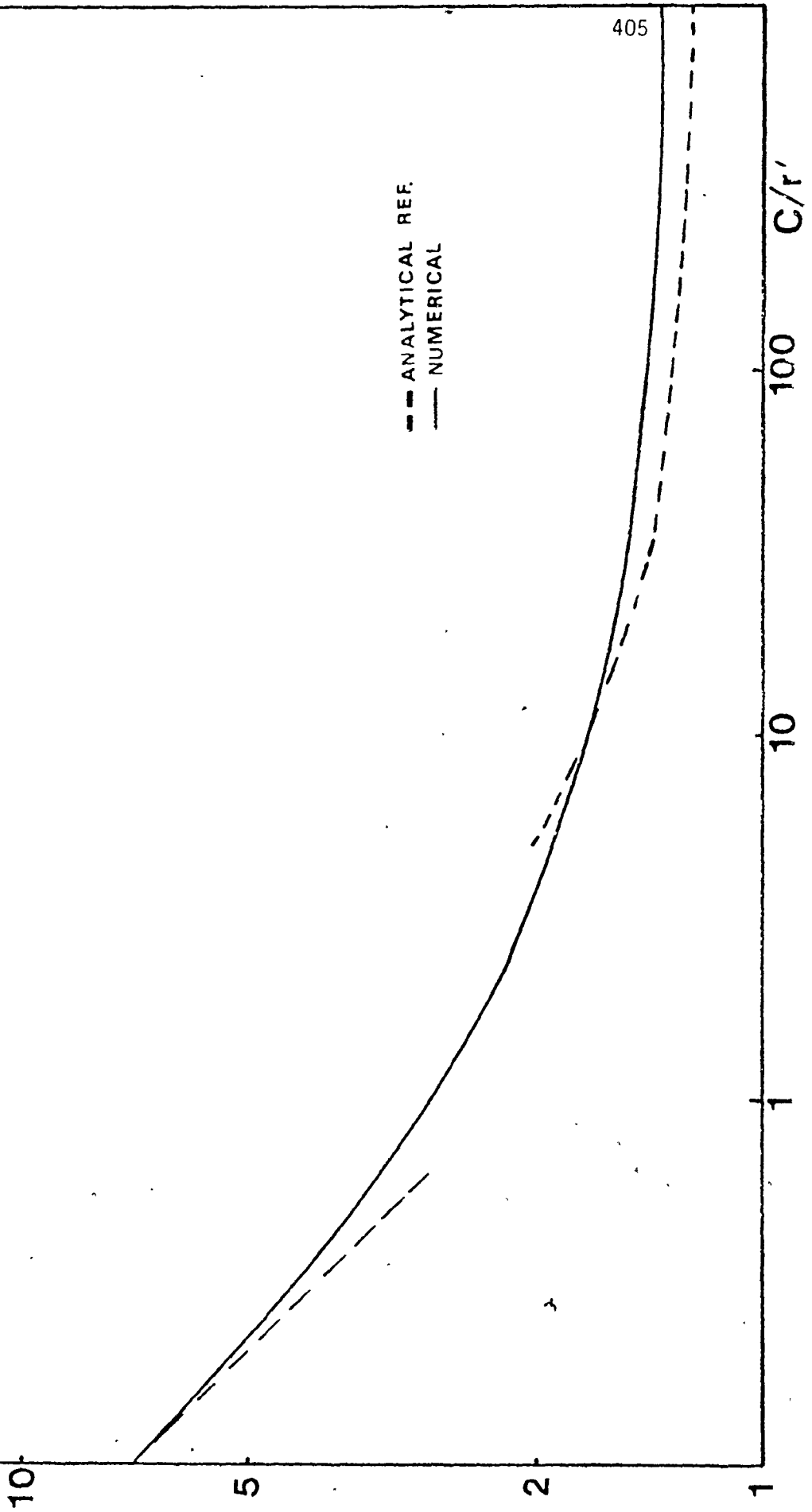
The increment in crack length does not affect U_0 so that $dU_0/dC = 0$.

The crack extension stress cannot be evaluated analytically though Evans gives approximate analytical solutions that are within ~10% of the numerical solutions for $V < 1/5$ and $V > 5$. The numerical solutions evaluated in this work for $W \gg V$ are shown in Figure A.13. As Evans indicates, the values of σ_a^s are greater than σ_c for all values of C/r' and an increase in toughness due to the crack-particle interaction is expected for semi-circular, non-interacting secondary cracks. This contribution increases as the value of r' (or β) increases (Figure A.14) i.e., as the strength of the pinning increases. The maximum contribution will occur for $r' = 2r_0$.

It is worth considering at this point, the effect of obstacle shape, e.g., circular obstacles. In this case the interparticle spacing is not constant. The effect on the stress ratio is shown in Figure A.15 and it can be seen that the maximum stress position now lies between $r' = r_0$ and $r' = 2r_0$ depending on the value of C/r_0 . In this way, it can be seen that obstacle shape plays a role in determining the maximum stress position. Furthermore, it is also clear that crack interactions

$\frac{\sigma}{\sigma_c}$

Figure A.13 Stress to Move Semi-Circular Secondary Cracks between an Array of Obstacles as a Function of Obstacle Spacing and Amount of Pinning



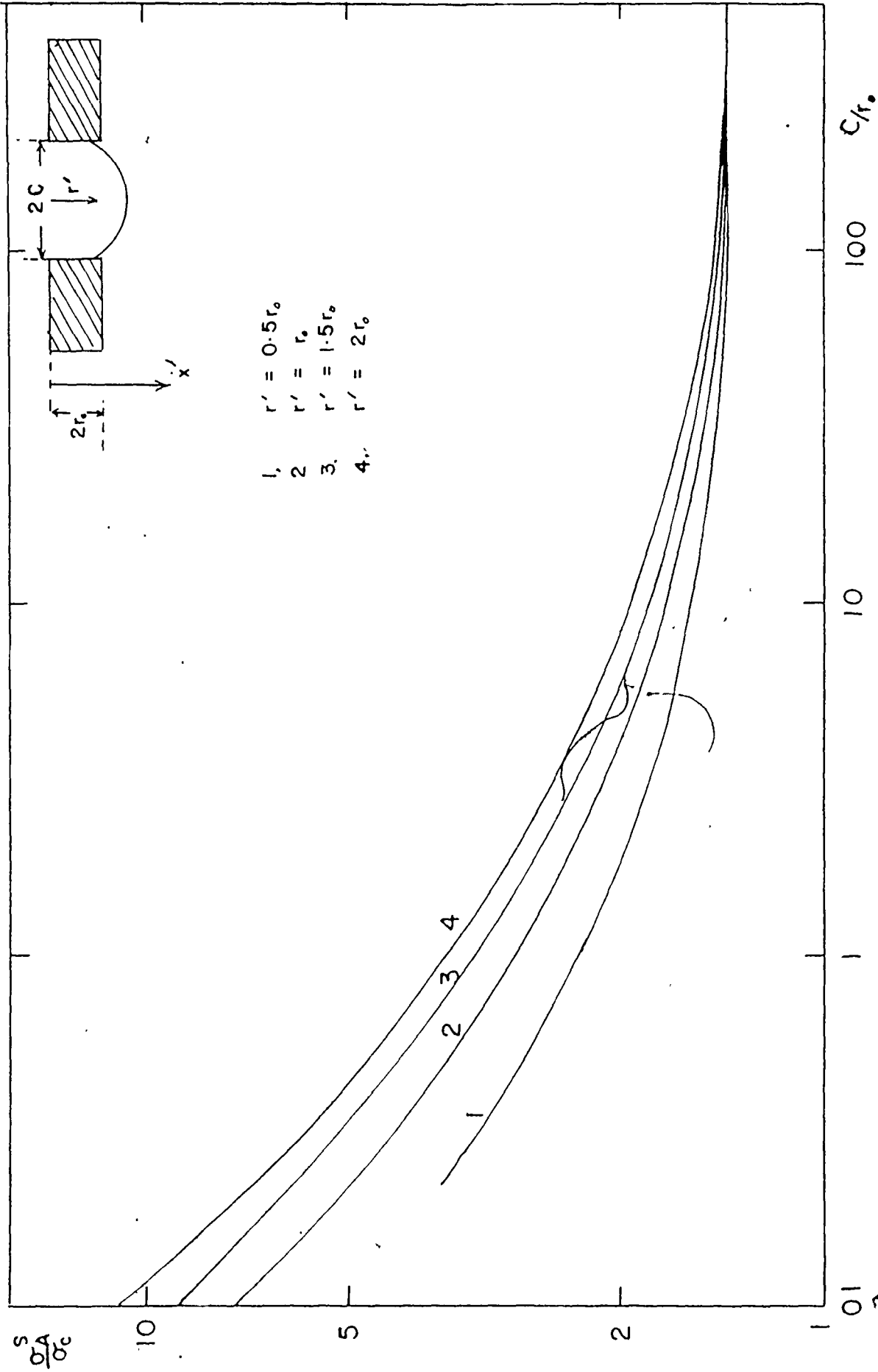


Figure A.14 Stress to Move Semi-Circular Cracks Between Rectangular Obstacles as a Function of Particle Size and Spacing

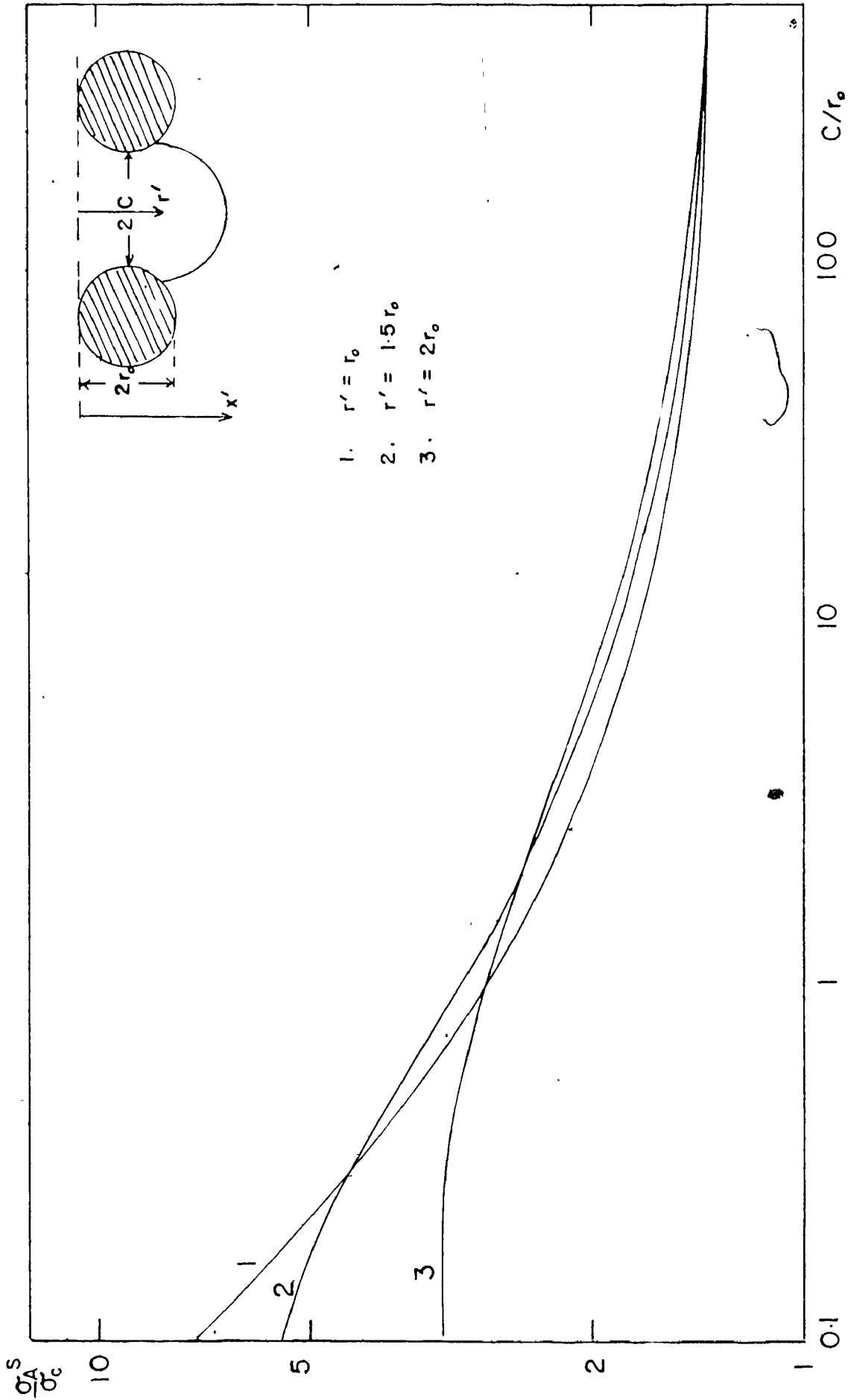


Figure A.15 Stress to Move Semi-Circular Cracks Between Spherical Obstacles as a Function of Particle Size and Spacing

will play an important role here because as the secondary crack origin moves to $r' = 2r_0$, the stress fields from neighbouring cracks will overlap considerably. The two cases of rectangular and circular obstacles can be seen as limiting cases when obstacle shape is considered. In general, there will be a compromise between increasing r' and the increased crack interaction. Failure of the interface or particle before the maximum stress position will also reduce the toughness as r' can again be less than $2r_0$.

It is useful to evaluate the limiting condition for $C/r' = \infty$. For large values of C , no interaction is expected because the particles are too widely spaced. For values of $r' = 0$, there is no pinning and again no interaction is expected. This latter situation corresponds to crack interaction with a void or non-bonded particle. Recognizing from equation (A.14) that $C'/C \sin \theta \sin \beta \ll 1$, it follows that

$$U = \frac{-4a(\sigma_a^s)^2 C^2 C'}{3\pi^2 G} \int_0^{\pi/2} \left[\int_0^{\pi/2} \sin^{-\frac{1}{2}} \beta d\beta \right]^2 d\theta \quad (\text{A.21})$$

$$\text{Now } \int_0^{\pi/2} \sin^{-\frac{1}{2}} \beta d\beta = \frac{1}{2} B\left(\frac{1}{2}, \frac{1}{2}\right) = \frac{(\Gamma(\frac{1}{2}))^2}{2\sqrt{2}\pi} = \frac{(3.626)^2}{2\sqrt{2}\pi} \quad (\text{A.22})$$

where $B(x, y)$ is the Beta Function and $\Gamma(\)$ is the Gamma Function so

$$U = \frac{-4.586}{\pi} (a/G)(\sigma_a^s)^2 C' C^2 \quad (\text{A.23})$$

$$\text{and } \frac{dU}{dC} = \frac{9.173}{\pi} (a/G)(\sigma_a^s)^2 C' C = 4\pi C \Gamma \quad (\text{A.24})$$

$$\text{Substituting } \sigma_c^2 = \frac{2E\Gamma}{\pi(1-\nu^2)C'} \quad (\text{A.25})$$

the limiting condition becomes

$$\left(\frac{\sigma_a^s}{\sigma_c}\right) = 1.30 \quad (\text{A.26})$$

It can be seen that the limiting condition still gives $\sigma_a^s > \sigma_c$ but this effect is a result of the assumption of semi-circular cracks. It will be shown in the next section, that allowing the crack shape to become semi-elliptical gives a condition of $\sigma_a^s \sim \sigma_c$ for $r_0/C = 0$, i.e., infinitely-spaced obstacles or no pinning does not affect the material's toughness, which is intuitively expected as the correct limiting condition.

A.7.2 Semi-elliptical, Non-interacting Secondary Cracks.

It is not immediately apparent that the shape of the crack at breakaway should be semi-circular. Evans, therefore, attempted to correct his results to semi-elliptical conditions. The stress to extend a semi-elliptical crack (σ_a^e) differs from the stress to extend a semi-circular crack of the same depth.

For a semi-circular crack, radius a , under a uniform tensile stress, the stress intensity factor is given by

$$K_I = \sigma_a^s \sqrt{a} \cdot \frac{2}{\sqrt{\pi}} \quad (\text{A.27})$$

For a semi-elliptical crack, width $2C$ and depth a , under a uniform tensile stress, the stress intensity factor is given by

$$K_I = \frac{\sigma_a^e \sqrt{\pi a}}{E(k_1)} \quad \text{for } a \leq c \quad (\text{A.28})$$

where $E(k_1)$ is the complete elliptical integral of the second kind and k_1 is its modulus such that

$$k_1 = \sqrt{1 - (a/c)^2} \quad (\text{A.29})$$

The stress ratio Z is therefore given by

$$Z = 2E(k_1)/\pi \quad (\text{A.30})$$

The value of Z is plotted in Figure A.16 as a function of $a/2C$.

Approximate values for σ_a^e may be obtained by combining Z with σ_a^s determined for semi-circular cracks of equivalent depth. The approximate stress can be obtained from Figure A.13 using a/r' as the coordinate instead of C/r' . It should be remembered the stress ratio is determined for the case of a uniform tensile stress and not the stresses at the tip of a 'through-the-thickness' crack.

Before the above procedure can be carried out, it is necessary to determine the dimensions of the semi-elliptical crack at each stage of bowing. For each increment in crack length (da), the increment in stress ($d\sigma_a^e$) will be the minimum possible needed to attain the increase in length. Therefore,

$$\frac{d\sigma_a^e}{da} = \sigma_a \left(\frac{dZ}{da} \right) + Z \left(\frac{d\sigma_a^s}{da} \right) \sim 0 \quad (\text{A.31})$$

The solution of this equation allows the shape of the semi-ellipse to be determined. The procedure involves obtaining the slopes of Figures A.13 and A.16. This was done by differentiating equations A.17 and A.30 with respect to a . The slope of Figure A.13 (n) is given by

$$n = \frac{d\sigma_a^s}{da} \left[\frac{r'}{C} \right] \quad (\text{A.32})$$

From the differentiation, one obtains

$$n = -\sqrt{\frac{3\pi^4}{32}} \left\{ \frac{\int_0^{\pi/2} (3F(C) - 5VdF(C)/dC + (V)^2 r'^2 d^2F(C)/dC^2) \sin\theta d\theta}{\left[\int_0^{\pi/2} (3VF(C) - V^2 r' dF(C)/dC) \sin\theta d\theta \right]^{3/2}} \right\} \quad (\text{A.33})$$

where $r'^2 \frac{d^2(F(C))}{dC^2} = \int_0^{\pi/2} \left[\int_0^{\pi/2} \frac{1}{2} \left[\frac{\sin\theta \sin\beta}{(1+V\sin\theta \sin\beta)^{3/2}} d\beta \right]^2 + \right.$

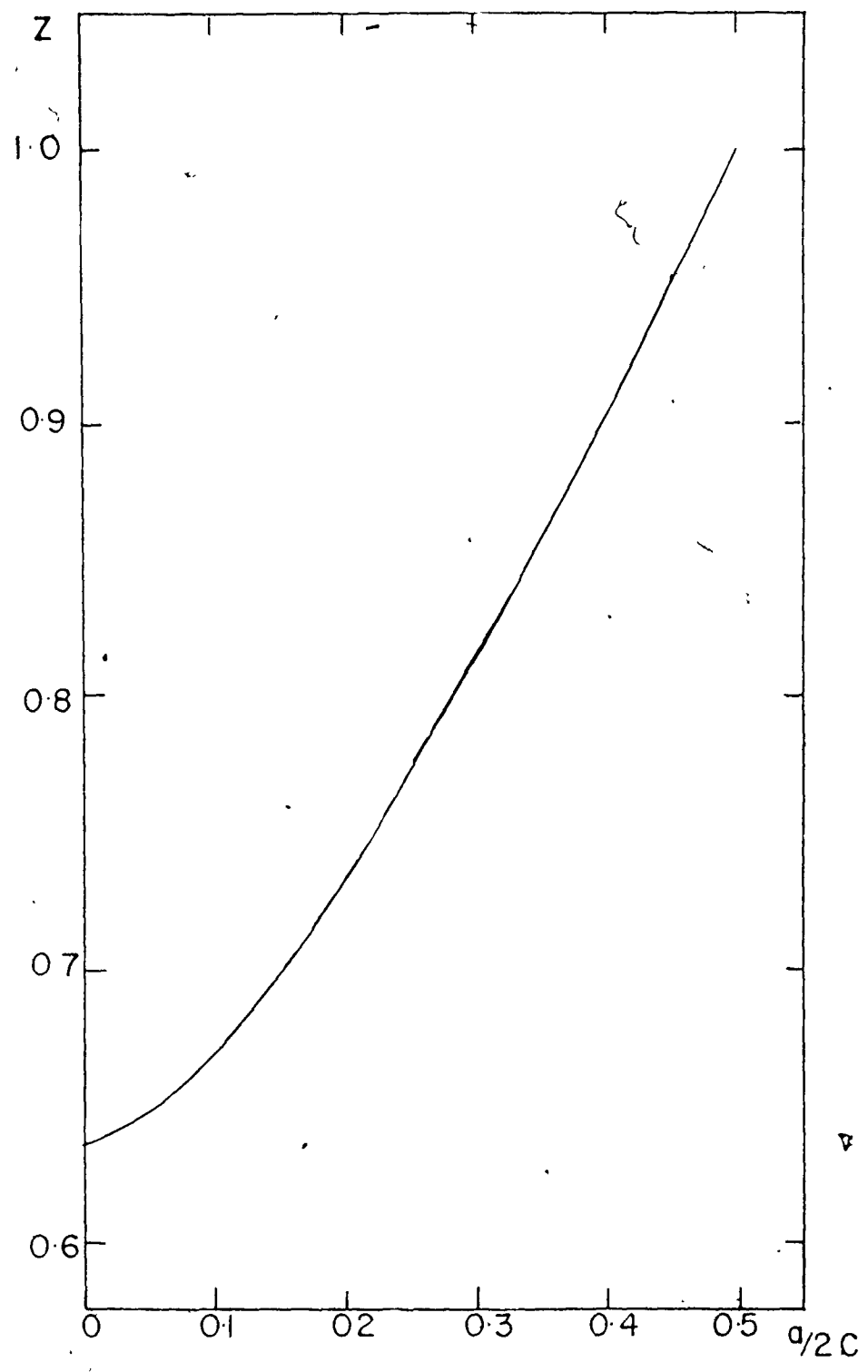


Figure A.16 Ellipse Shape Parameter Z as a Function of Elliptical Axes

$$\int_0^{\pi/2} (1+V\sin\theta\sin\beta)^{-\frac{1}{2}} d\beta \cdot \int_0^{\pi/2} \frac{3}{2} \left[\frac{\sin\theta\sin\beta}{(1+V\sin\theta\sin\beta)^{5/4}} \right]^2 d\beta \Big] \sin\theta d\theta \quad (\text{A.33})$$

The values of n are plotted in Figure A.17 as a function of a/r' .

The slope of Figure A.16 (q) is given by

$$q = \frac{dZ}{da} \cdot 2C = \frac{2aK(k_1)}{\pi c} \quad (\text{A.34})$$

where $K(k_1)$ is the complete elliptical integral of the first kind. Now putting

$$p = 2nZ \left[\frac{C}{r'} \right] \left[\frac{\sigma_c}{\sigma_a} s \right] \quad (\text{A.35})$$

and plotting p and q as a function of $a/2C$, equation (A.31) will be satisfied where $p = q$. This will then give the critical value of $a/2C$. The results are shown in Figure A.18. In this figure the p and q values are substantially different from those of Evans. The general trend is that $a/2C$ at breakaway decreases as C/r' increases. These results differ from Evans in that values of $a/2C > 0.5$ are not obtained. For elliptical cracks under a uniform tensile stress, K_I is greatest at the tip of the minor axis, so that a crack is expected to grow towards the semi-circular condition. Once the crack is semi-circular, K_I is constant along the whole crack front, so that further growth as a semi-circular crack is expected. In this way, it is not expected that $a > c$. For this particular model the stress field is not uniform but drops off with distance from the primary crack front so in reality the semi-circular condition should be even more unlikely. The critical values of $a/2C$ at breakaway are shown in Figure A.19 as a function of C/r' . The previous comments are in agreement with the analysis i.e., as $r'/C \rightarrow 0$, the crack

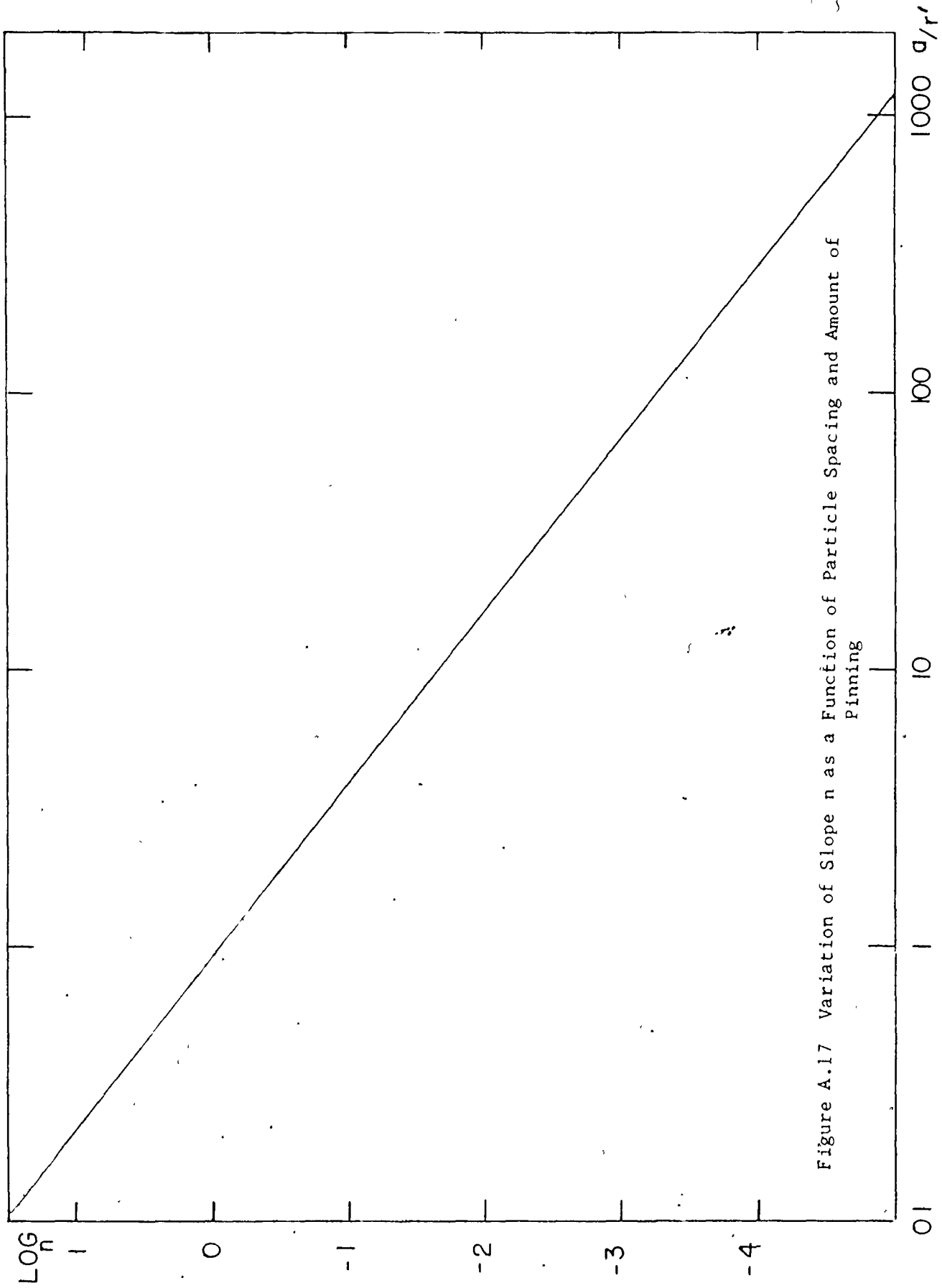


Figure A.17 Variation of Slope n as a Function of Particle Spacing and Amount of Pinning

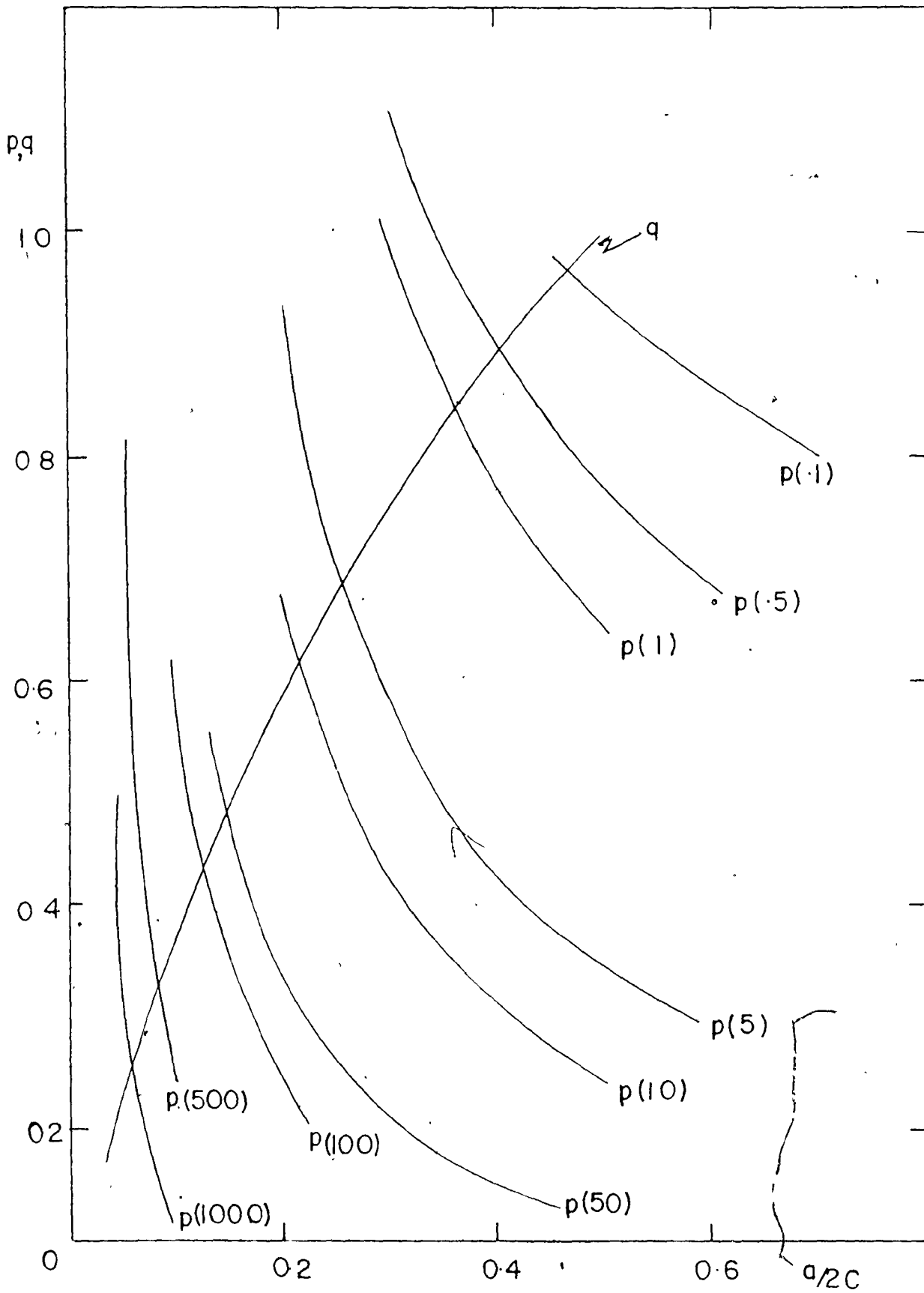


Figure A.18 Determination of Crack Shape at Breakaway.

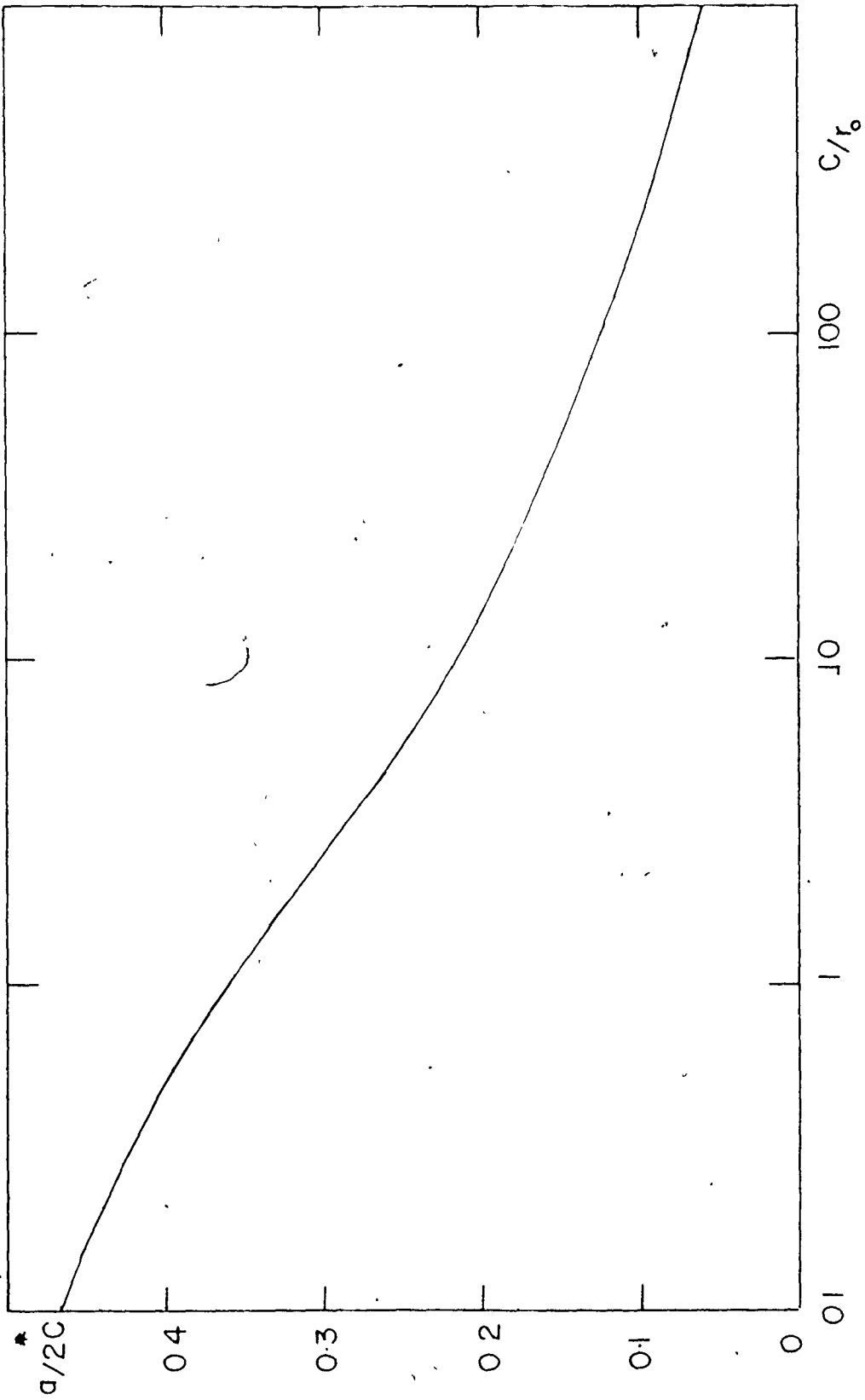


Figure A.19 Variation of Crack Shape at Breakaway with Obstacle Size and Spacing

should remain straight while for large r'/C the semi-circular crack becomes the limiting condition.

The critical values of $a/2C$ were then used to determine σ_a^s/σ_c for a semi-circular crack of equivalent depth (a) and the value of Z for the corresponding semi-elliptical crack. The product of these two parameters will give the stress ratio σ_a^e/σ_c and the results are shown in Figure A.20. The correction is largest for large values of C/r' as the secondary cracks are furthest from the semi-elliptical condition. The value of σ_a^e/σ_c is \sim unity for these large values of C/r' . This is to be expected as at these values of C/r' , the primary crack should not 'see' the obstacles. The asymptotic value is actually slightly less than unity and this is probably due to the approximation used in determining Z for a non-uniform tensile field. The calculations show that there is still a substantial contribution to fracture toughness for finite values of r'/C with semi-elliptical, non-interacting secondary cracks.

Finally Evans tries to evaluate the effect of secondary crack interactions by assuming that they are coplanar. This assumption is questionable because fracture surface steps are generally formed at the rear of the obstacles indicating that the secondary cracks are actually non-coplanar. For this reason no attempt was made to evaluate the crack interaction term in this re-analysis.

A.7.3 Summary

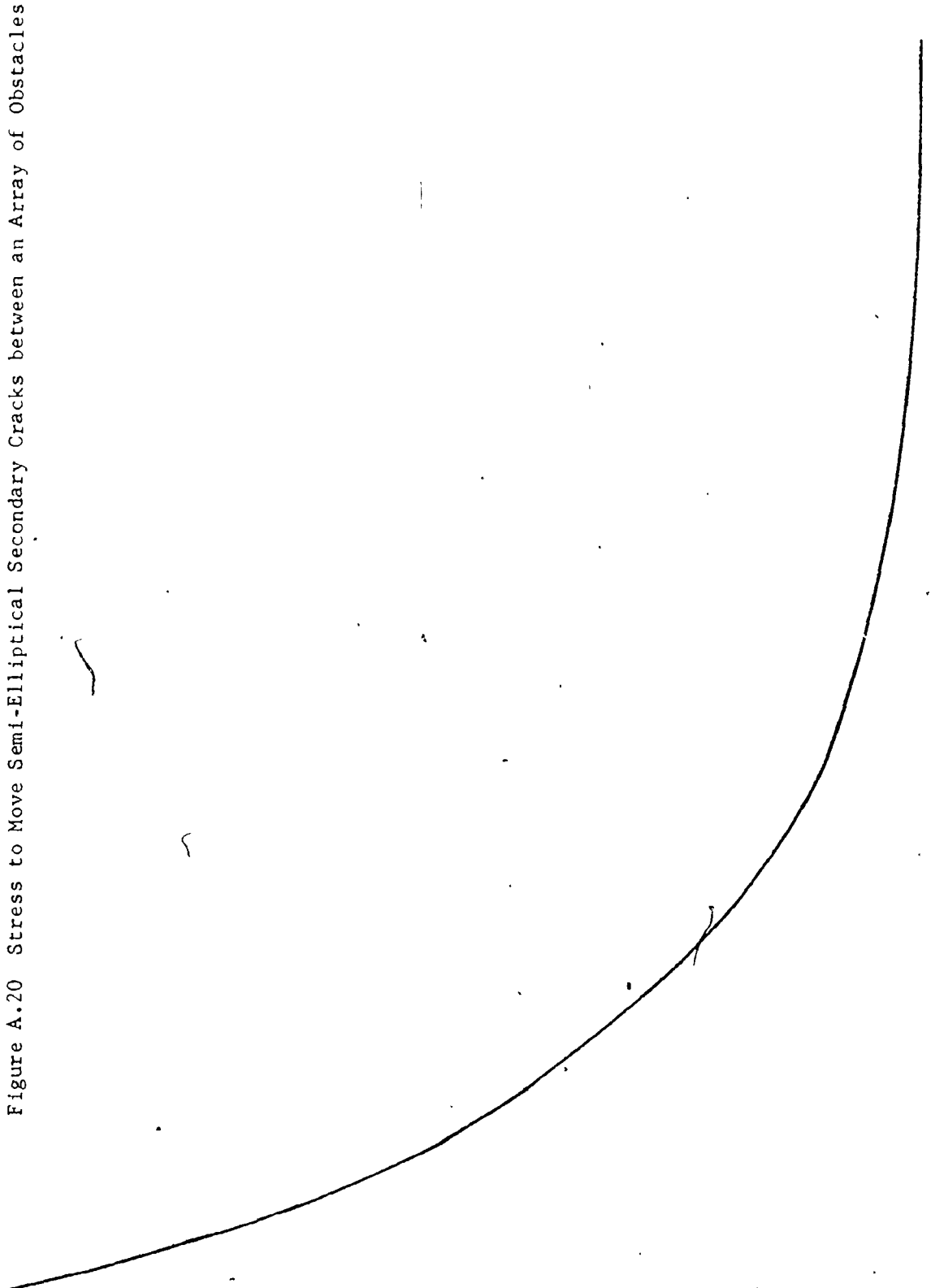
The magnitude of the contribution to toughness in this re-analysis was found to be greater than that found by Evans because a value of $r' = 2r_0$ was used rather than $r' = r_0$. Evans compared his predictions with experimental determinations of Γ for particulate

Figure A.20 Stress to Move Semi-Elliptical Secondary Cracks between an Array of Obstacles

$$\frac{E}{\sigma_c} \frac{dA}{dc}$$

6
5
4
3
2
1

1
10
100
1000
C/r'



composites. The agreement is only reasonable and as discussed in Chapter 2 of the thesis the relationship between the interparticle spacing and V_v is open to question. Evans used the data of Lange, who interprets the interparticle spacing $2C$ as the mean free path. In the thesis it was shown that $2C$ is probably less than the mean free path, so that the comparison with the literature becomes even worse. Figure A.21 shows the comparison with the data of Lange using this re-analysis and a value of $2C$ defined by equation (5.3).

In general, it appears that the Evans' approach predicts a contribution to toughness greater than usually observed. This effect is probably due to obstacle or interface failure before the maximum stress position. As pointed out by Evans the chance of penetration of brittle obstacles probably increases as r'/C increases. For failure of the particle or interface $\beta < 2$. This effect may also explain the maxima observed in some of the experimental data. For coherent ductile obstacles the impenetrability should increase but plastic flow will also make a contribution to the toughness. Similarly, in fibrous composites, there is other more important energy absorbing mechanisms.

In all of this work, the stress field of the particle has been ignored and it may be an important omission. Also, at high volume fractions, interaction with another particle can occur before the maximum stress position is reached.

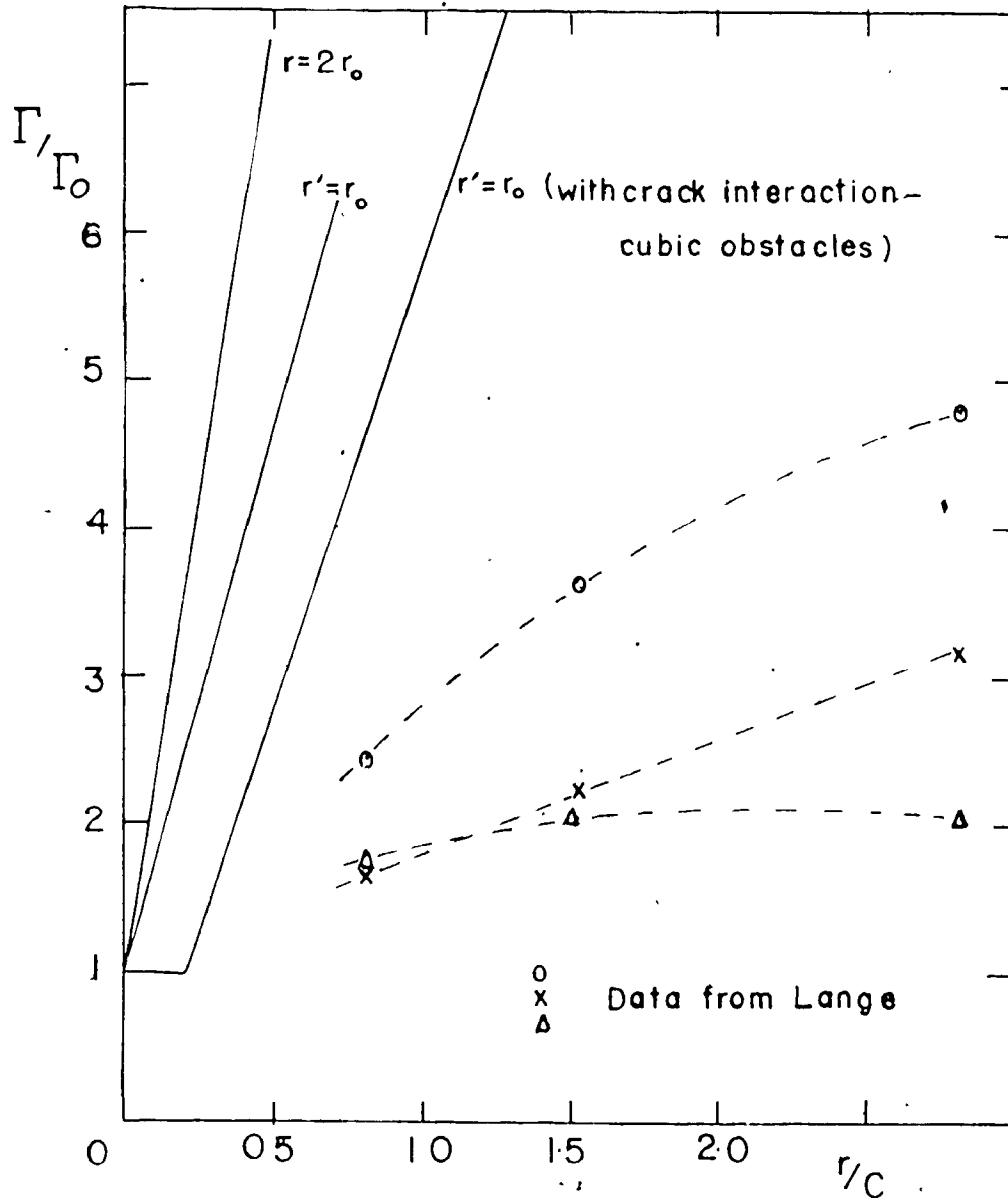


Figure A.21 Comparison of Experimental Work of Lange with Theoretical Predictions from the Evan's Model

A.8 Density Measurements

Density is an important parameter in many mathematical expressions where volume or weight of a sample is being considered. It is expressed as the ratio of the total mass of a sample to its total volume (e.g. kg/m^3). The mass is generally determined by weighing, and the volume by calculation from the mass and density of water (or other fluid) displaced by the sample. This method has long been in use and is simple, direct and accurate if done carefully. For large samples, it allows the bulk or apparent density to be determined, while for finely-ground specimens, it allows the theoretical density to be measured.

A.8.1 Method

(i) Apparent or Bulk Density

Weigh a clean, dry sample in air (greater than 1g) to find its unsaturated weight (W_D). Place the sample in a beaker of boiling distilled water to remove entrapped air and to fill the open pores. Cool the sample and water down to room temperature and determine the saturated weight of the sample (W_S). The sample is then suspended in a beaker of distilled water so that it is totally submerged. Determine the weight of the submerged sample (W_{SS}) and the temperature of the water. The density of the water (ρ_L) can be found from the literature as a function of temperature.

The bulk density (ρ_b) can be calculated from

$$\rho_b = \frac{W_D \times \rho_L}{W_S - W_{SS}}$$

and the apparent density (ρ_a) from

$$\rho_a = \frac{W_D \times \rho_L}{W_D - W_{SS}}$$

The step-by-step procedures can vary slightly and ASTM has a variety of standard test methods.

(ii) True Density

This method requires a pycnometer, which is a glass flask fitted with a ground glass stopper that is pierced lengthwise by a capillary opening. A thermometer is sometimes an integral part of the stopper so that the mercury reservoir is in contact with the liquid. The pycnometer has a precise fluid volume when properly filled. The procedure is as follows:

Weigh a clean dry pycnometer in air (W_a). Add about 10g of finely ground sample and clean the outside of any spilled powder. Weigh the pycnometer, including its stopper and contents (W_d). Fill the pycnometer about half full with distilled water washing into the flask any powder adhering to the inside of the neck. Remove entrapped air by gentle boiling of the water for several minutes with frequent, gentle agitation of the contents to prevent loss by foaming.

Cool the pycnometer and its contents to room temperature, and then add enough boiled, cooled distilled water at room temperature to fill the pycnometer. Insert the stopper and seat it carefully. Thoroughly dry and clean the outside of the flask with a dry cloth. Weigh the pycnometer and its contents (W_c) and determine the temperature.

Finally, remove the powder from the pycnometer and clean it. Fill the pycnometer with boiled, cooled distilled water at the same temperature as before, insert the stopper and dry the outside with a cloth. Weigh the pycnometer and the water (W_w).

The theoretical density (ρ_t) can be calculated from

$$\rho_t = \frac{\rho_L (W_d - W_a)}{(W_d - W_a) - (W_c - W_w)}$$

The method is very precise if volumes and weights are carefully measured. A weighing error of 1 mg on a 10g powder sample gives an error in theoretical density of only 0.3 kg/m³. The calibration of the pycnometer can be very important but errors may also be introduced by non-representative sampling. The distilled water may be replaced by other liquids such as toluene, m-xylene or carbon tetrachloride for more accurate determinations. This method for determining particle density does not give the average density of the particles because samples may not contain equal masses of particles of all densities represented. The values obtained are weighted with respect to the relative masses of the particles and the harmonic mean density may be more exact terminology.